INVESTIGATIONS ON PRESSURE CASTING AND EXTRUSION PROCESSING PARAMETERS ON THERMO- MECHANICAL PROPERTIES OF LOW EXPANDING CERAMICS

A thesis
submitted for the degree of

DOCTOR OF PHILOSOPHY
in
MATERIALS ENGINEERING

by

Papitha Ramanathan

School of Engineering Sciences and Technology
University of Hyderabad
Hyderabad- 500 046
India
2014

Dedicated to my
Loving parents
Mr. M. Ramanathan &
Mrs. R. Lakshmi

DECLARATION

I hereby declare that the matter embodied in this thesis entitled, "**Investigations on Pressure Casting and Extrusion Processing Parameters on Thermo- Mechanical Properties of Low Expanding Ceramics**" submitted to University of Hyderabad for the award of **Doctor of Philosophy** in **Materials Engineering** is a record of original research work carried out by me under the supervision of **Dr. Roy Johnson,** Scientist F and Team Leader, Centre for Ceramic Processing, International Advanced Research Centre for Powder Metallurgy and New Materials (ARC-I), An autonomous R&D Centre of Department of Science & Technology, Govt. of India, Hyderabad and **Dr. Dibakar Das,** Associate Professor, School of Engineering Sciences and Technology, University of Hyderabad. To the best of my knowledge, this work is not submitted for any degree in any University or Institute.

(PAPITHA R)

Place: Hyderabad
Date: 31-03-2014

INTERNATIONAL ADVANCED RESEARCH CENTRE FOR POWDER METALLURGY AND NEW MATERIALS
(An Autonomous Research & Development Centre of Department of Science &Technology, Govt. of India)
ARCI
Balapur P.O. HYDERABAD-500 005 (A.P), INDIA

Dr. ROY JOHNSON,
Scientist F & Team leader,
Center for Ceramic Processing

CERTIFICATE

This is to certify that the work contained in this thesis entitled, "**Investigations on Pressure Casting and Extrusion Processing Parameters on Thermo- Mechanical Properties of Low Expanding Ceramics** ", has been carried out by **Ms. Papitha R** under my supervision and the same has not been submitted for the award of research degree of any university.

(Roy Johnson)
Research Supervisor

Place: Hyderabad
Date: 31-03-2014

Forwarded

DIRECTOR

SCHOOL OF ENGINEERING SCIENCES AND TECHNOLOGY (SEST),

UNIVERSITY OF HYDERABAD,
HYDERABAD 500046, INDIA

CERTIFICATE

This is to certify that the work contained in this thesis entitled, "**Investigations on Pressure Casting and Extrusion Processing Parameters on Thermo- Mechanical Properties of Low Expanding Ceramics**", has been carried out by **Ms. Papitha. R** under my supervision and the same has not been submitted for the award of research degree of any university.

(DR. DIBAKAR DAS)
Research Co-Supervisor

Place: Hyderabad
Date: 31-03-2014

DEAN
School of Engineering Sciences and Technology
University of Hyderabad

Table of Contents

Chapter I: Introduction

Chapter II : Synthesis and Physico-Chemical Characterization of Aluminum Titanate

Chapter-III: Thermal Stability Studies on Preformed AT and TAT-5

Chapter-IV: Evaluation of Thermo-Mechanical Properties of AT And TAT-5 Specimens

Chapter-V: Shaping of TAT-5 Formulation into Components

Chapter- VI :Pressure Assisted and Conventional Slip Casting of TAT-5 Formulation based green components

Acknowledgements

I wish to express my heartful thanks to **Dr. G. Sundararajan**, **Director,** ARCI for providing me an excellent opportunity to carry out this research work at ARCI and also for providing necessary facilities and guidance without which I could not have been completed my work successfully. I am also grateful to **Prof. K. Sundaraman**, **DEAN**, School of Engineering Sciences and Technology (SEST), University of Hyderabad, Hyderabad, for their immense support and encouragement, and timely advice during this course of work.

I express my deep sense of gratitude to **Dr. Roy Johnson**, Scientist F and Team Leader, Center for Ceramic Processing, ARCI, Hyderabad, Research Supervisor of this research of work. He gave me great encouragement, confidence as well as the freedom to think while carrying out this work. His valuable guidance and constant encouragement, excellent technical discussions and valuable advices are the motive force leading to the successful completion of this work. I take this opportunity to express my utmost gratitude to him. He has been more than a guide and philosopher to me.

It has been indeed a great privilege for me to have **Dr. Dibakar Das**, Associate Professor, School of Engineering Sciences and Technology (SEST), University of Hyderabad, Hyderabad as my Co-Supervisor. I express my deep sense of gratitude for his valuable guidance throughout the course of this work. His valuable guidance and constant encouragement, adept technical discussions and relentless advice were much needed to complete this part of research work. I take this opportunity to express my heartfelt thanks to him.

My special thanks are to **Dr. S. V. Joshi,** Additional Director and **Dr. G. Padmanabham,** Associate Director, ARCI for their constant encouragements, timely suggestions during the course of my research at ARCI.

I m also thankful to Dr. Y. S. Rao, Sc ‘E’ for suggestions during pressure slip casting of samples which is one of the significant parts of this thesis. My thanks are to Dr. M. B. Suresh, Sc ‘D’, ARCI, suggestions during the XRD analysis in my project period.

I am grateful to, Mr. R. Senthil Kumar, Sc ‘D’, Ms. Papiya Biswas, Sc ‘C’, Mr. Pandu Ramavath, Sc ‘C’ and Dr. K. Rajeswari, PDF of ARCI, for extending their cooperation as and when required.

I would like to thank Mr. N. Ravi, Sc ‘D’ for his cooperation in mechanical testing of the samples and Dr. Dibynedu Chakravarty, Sc ‘D’ of ARCI, for spark plasma sintering of the specimens carried out during the study.

My thanks are to Mr. Mahender, TO ‘C’, Mr. A. Rajasekhar Reddy, TO ‘A’, Mr. G. V. R. Reddy, TO ‘C’ and Mr. K. Ramesh Reddy, TA ‘B’ and in-particular technicians Mr. Venkata Rao, Mr. K. V. Ramana, Mr. S. Ahmed, Mr. M. Satyanand, Mr. B. Subramanyam and Mr. M. Lingaiah of ARCI and all the technical staff of School of Engineering Sciences and Technology, University of Hyderabad for their kind help during my project work.

I would also like to express my thanks to Dr. M.Vijayakumar, Scientist G and Head, Ceramic Composite Group, DMRL, Hyderabad for his guidance and permission to utilize the HMOR facility and Mr. Visewara Rao, Technical Officer for the suggestions during the experimentation.

I express my sincere thanks to all faculty members of School of Engineering Sciences and Technology (SEST), University of Hyderabad, for their help during the course of work.

I am also indebted to my classmates and friends for their constant encouragement, cooperation and support.

I indebted to my parents, Shri M. Ramanathan and R. Lakshmi and my brother R. Pradeep whom always been a source of strength to me, without their moral support and concern, I would not have reached this stage.

Place: Hyderabad **PAPITHA R**
Date: 31-03-2014

Synopsis

Aluminum titanate (Al_2TiO_5) is an emerging engineering ceramics gaining relevance recently in view of its significant application potential such as new generation diesel particulate filter, foundary crucibles, lancing tubes etc [1-4]. Additionally, aluminum titanate has also been proposed as chemical anchoring and coefficient of thermal expansion compensating additives for NiO-ZrO_2 SOFC anode [5-5]. Aluminum titanate exhibits high temperature capability due to its high melting point of 1850°C and low coefficient of thermal expansion of ~ 1x 10^{-5}/ °C (30-1000 °C) leading to excellent thermal shock resistance. Though aluminum titanate is proposed as a candidate material for many applications, basic drawbacks of poor mechanical properties and thermal stability in the temperature regime of 900-1280°C [7-9], limits the effective utilization of this material for various thermo structural and functional applications. Present study, therefore attempts to identify various critical issues and to provide solutions on a scientific and technological point of view. Various aspects investigated in the present research study are briefly described in the synopsis report.

First chapter of the thesis started with introduction and overview on low expanding materials with the focus on evolution of aluminum titanate ceramics over the years and the present status. A thorough literature survey revealed that there is renewed interest in aluminum titanate ceramics and especially since 2007, which is peaked during 2009. Fig 1 shows status on

aluminum titanate research during 1998 to 2013.

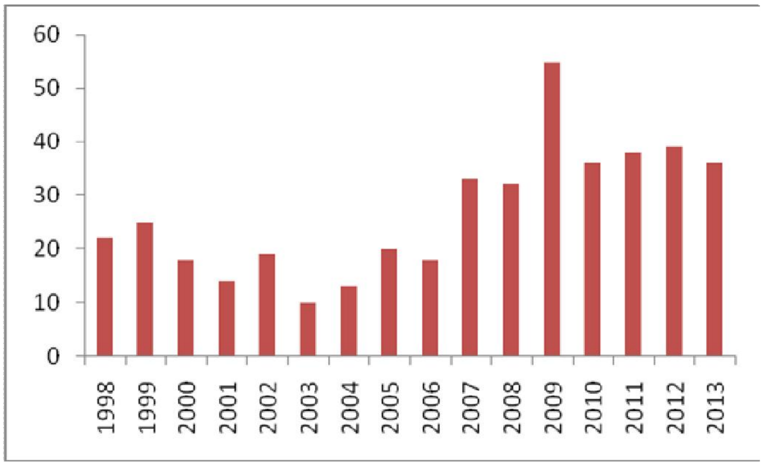

Fig 1 R & D publications 1998- 2013 (scopus survey: SCI Journals)

A consistent number of 35-40 publications are seen to appear in SCI Journals during 2010-2013. The chapter ends with the motivation to undertake the study and the approved scopes of the work are as follows,

Scope of the study

- Selection of raw materials and identification of process and parameters for synthesis of stiochiometric Al_2TiO_5 ceramics.

- Identification of critical issues that hinder the technological applications based on the literature survey.

- Optimization of synthesis parameters, selection of type and concentration of additives to address the inherent poor sinterability and low mechanical properties and simultaneously retaining the low thermal expansion values with good thermal stability.

- Evaluation of thermal stability by conventional and spark plasma sintering and thermal treatments conditions.
- Characterization of the samples for thermal properties such as thermal expansion, thermal hysteresis, high temperature XRD and thermal conductivity.
- Characterization of the samples for mechanical properties such as flexural strength (ambient and high temperature), hardness and compression strength behaviour.
- Correlation of thermo-mechanical properties with respect to newly developed formulation and processing parameters.
- Extrusion processing of newly developed formulation, with high strength and thermal stability, into honeycomb structures and its thermo-mechanical properties evaluation.
- Investigation on pressure slip casting of the newly developed formulation and its comparative evaluation with respect to cold isostatic pressing and conventional slip casting

Chapter 2 deals with synthesis and characterization of Al_2TiO_5. The various synthesis routes employed by earlier researchers were ranked based on the selected attributes and solid state synthesis is identified as a viable process, as the thesis is envisaged to have application development also. The raw materials were selected and are characterised for the phase analysis, particle size and surface area by X-ray diffraction, dynamic light scattering (DLS) and Brunauer–Emmett–Teller surface area (BETSA) techniques respectively. Compositions were formulated in the molar ratio of alumina and titania (1:1) according to the equation:

$\mathbf{Al_2O_3 + TiO_2 \longrightarrow Al_2TiO_5}$, and uni-axially compacted to green density of 2.38 g/cc (58.33% of theoretical density) under compaction pressure of 500 MPa. The compacts were sintered at 1500°C for a duration one hour and the maximum density observed was 3.32 g/cc (87% of TD) as shown in Fig 2(a). The reasons for crystallographic volume expansion due to formation of Al_2TiO_5 is obvious from the dilatometric curves shown in Fig 2(b). A decrease in density beyond 1500°C has been evaluated and it was observed that there is an increase in phase content (from 92.5% to 94.5%) which in turn resulted in excessive microcracking (Fig 2(c)-(d)).

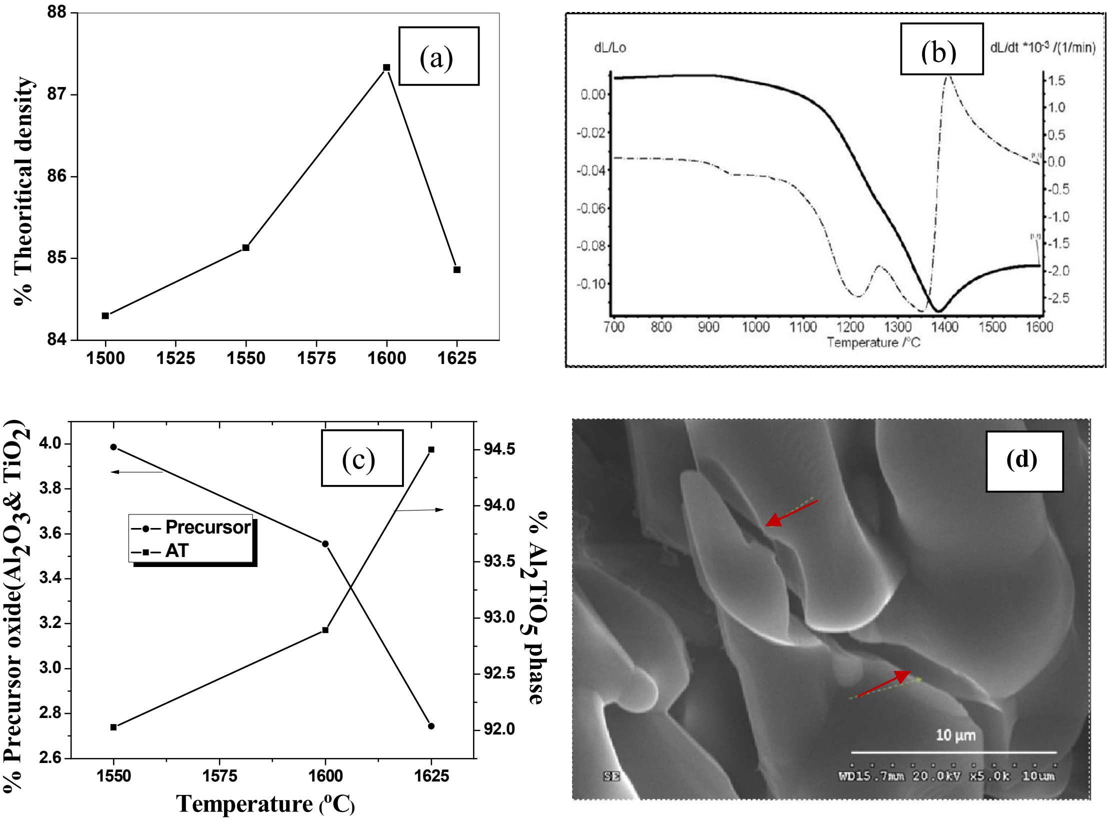

Fig 2 (a) Density variation with sintering temperature, (b) Dilatometric curve of the Al_2TiO_5 precursors green samples and (c) Al_2TiO_5 phase evolution with increasing temperature and (d) SEM microstructure of insitu sintered aluminum titanate at 1525°C

In an attempt to further densify the pellets Al_2TiO_5 powder was preformed through calcination of precursors oxides at 1400°C which has resulted in phase formation ~ 90%. The preformed powder was granulated, using PVA as a binder and were shaped into pellets by uniaxial die compaction under identical conditions. However, the green density was marginally low ~ 2.05 g/cc (51.3%TD). Sintering of the green pellets resulted in 5% increase in sintered density, compared to that obtained by sintering of the precursor oxides. The final density was limited to 92% of theoretical density. The poor densities demonstrated by both the approaches necessitated investigations on additives. Oxides such as MgO, ZrO_2, Fe_2O_3, SiO_2, $ZrSiO_4$ are reported to be effective in densification and improving the thermal stability. However, they need to be added in large volumes, deteriorating the thermal properties and long term stability. Doping with complex oxides such as, spodumene ($LiAlSiO_4$), mullite ($3Al_2O_3.2SiO_2$), cordierite ($Mg_2Al_4Si_5O_{18}$) and feldspar ($KAlSi_3O_8$) have resulted either enhancement in mechanical properties or lowering of CTE [10-13].

Two new additives such as, kaolinite ($2Al_2O_3.3SiO_2.2H_2O$) and talc ($Mg_3Si_4O_{10}(OH)_2$) were employed in the present study. The samples were designate with kaolinite addition of 2.88wt%, 5.8wt% and 8.8wt% as KAT-2.88, KAT-5.8 and KAT-8.8 and samples with talc addition of 2.5wt%, 5wt% and 7.5% were designated as TAT-2.5, TAT-5 and TAT-7.5 respectively. The kaolinite and talc follows a unique decomposition path, which forms reactive amorphous oxides, which in turn enhances the expected substitutions and diffusion promoting sintering. Not only the type, but also concentration of additives is found to play

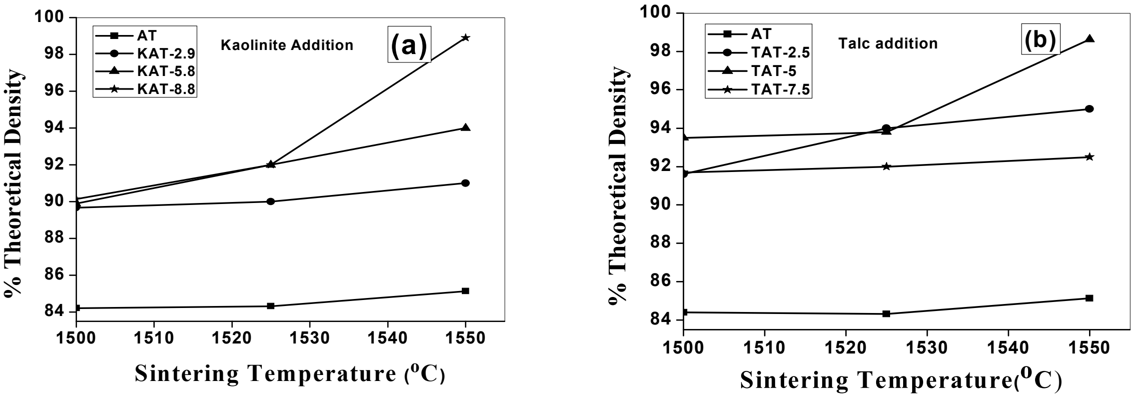

Fig 3 Density variation with temperature of (a) AT, KAT-2.88, KAT-5.8 and KAT-8.8 and (b) AT, TAT-2.5, TAT-5 and TAT-7.5

Kaolinite addition has resulted in a maximum density of ~ 99%TD at 1550°C with an additive concentration of 8.8wt %. On the other hand, the talc addition has exhibited a density of ~99%TD at 1550°C with a lower concentration of 5wt%. A temperature beyond 1550°C, in selected concentrations of the additives has shown no improvement in the densification. In view of above, the talc was selected as a suitable additive with an optimum concentration of 5wt% and the sintering temperature of 1550°C was chosen to prepare the samples (designated as TAT-5) for further investigations. (*Published in Journal of Applied Ceramic technology, DOI: 10.1111/ijac.12092, (2013) 1-10 and Journal of Ceramics, 214794, (2013) 1-9*).

The new TAT-5 formulation prepared under optimised conditions was evaluated for thermal stability with respect to the eutectoid decomposition and has been described in **Chapter 3**. The eutectoid phase decomposition is studied under Conventional Ramp and Hold (CRH) parameters at a heating rate of 4°C/min to the peak temperatures of 1000°C and 1100°C for 5 and 10 hours in air along with pure Al_2TiO_5 samples (designated as AT). Though no decomposition (estimated as % AT phase retained) revealed, by XRD studies, at 1000°C for both samples, a decomposition of 5% and 21% was observed for AT samples at 1100°C soaked for 5 and 10 hrs respectively (Fig 4(a)). However, no decomposition of the corresponding precursor oxides (Al_2O_3 and TiO_2) of Al_2TiO_5 was observed in case of TAT-5 samples.

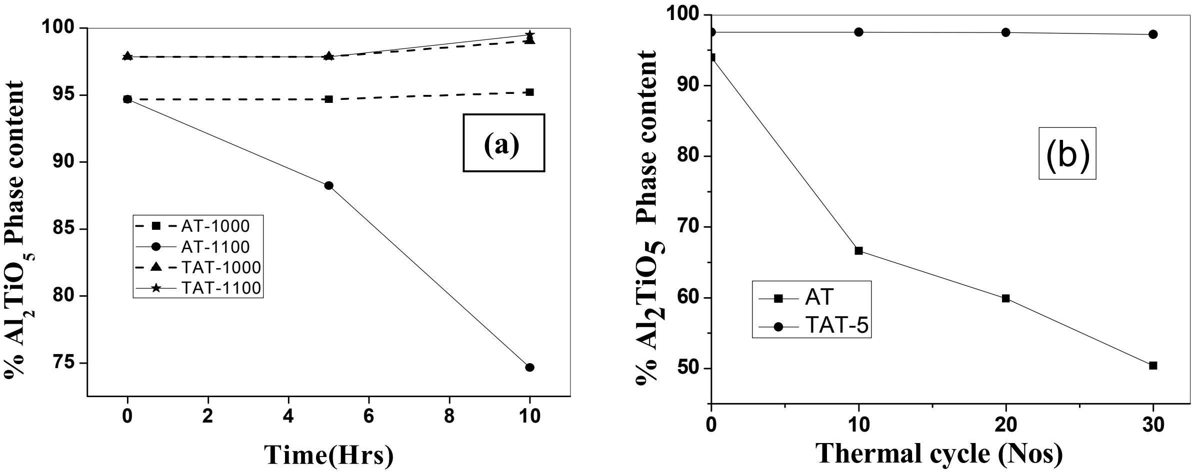

Fig 4 The % Al_2TiO_5 phase content in AT & TAT-5 as a function of (a) soaking time at 1000 °C and 1100°C and (b) thermal cycling at 1200°C upto 30 cycles

Further, in order to evaluate the thermal stability under realistic application trials these samples were subjected to thermal cycling experiments with typical parameters of cycling from 28°C to 1200°C at a maximum heating rate of 100°C/min, with a 10 minutes dwell time for 10, 20 and 30 cycles. A decomposition of ~ 35%, 43% and 54% was observed for AT samples for 10, 20 and 30 cycles respectively (Fig 4(b)). However, TAT-5 samples do not indicated any decomposition even at 30 cycles.

In order to elucidate, the mechanisms of eutectoid decomposition of Al_2TiO_5 phase, dilatometric studies were conducted and were correlated with high temperature XRD data. Unlike in the case of TAT-5 samples, a clear slope change as shown in Fig 5(a), was observed for AT samples in the temperature regime of 1000-1200°C, signifying the proposed decomposition. Similarly, the high temperature XRD data as shown in Fig 5(b), revealed an appearance of a new and metastable phase at $2\theta=40^{o}$, confirming a new phase (not confirming with precursor oxides or there combination or aluminum titanate) appearing which in turn decomposes to precursors oxides.

In Al_2TiO_5 structure each Al^{3+} and Ti^{4+} cations are surrounded by six oxygen ions forming distorted AlO_5 or TiO_5 octahedra forming (001) oriented double chain. The dimensional decrease observed in dilatometric studies may impart elastic strain in the matrix. It may be regarded as the strain energy surpasses the chemical driving force (ΔG) in the temperature regime of 1000°C–1200°C leading to spontaneous decomposition. (*Published in Journal of Ceramic International, 40[1], (2014)459-555*)

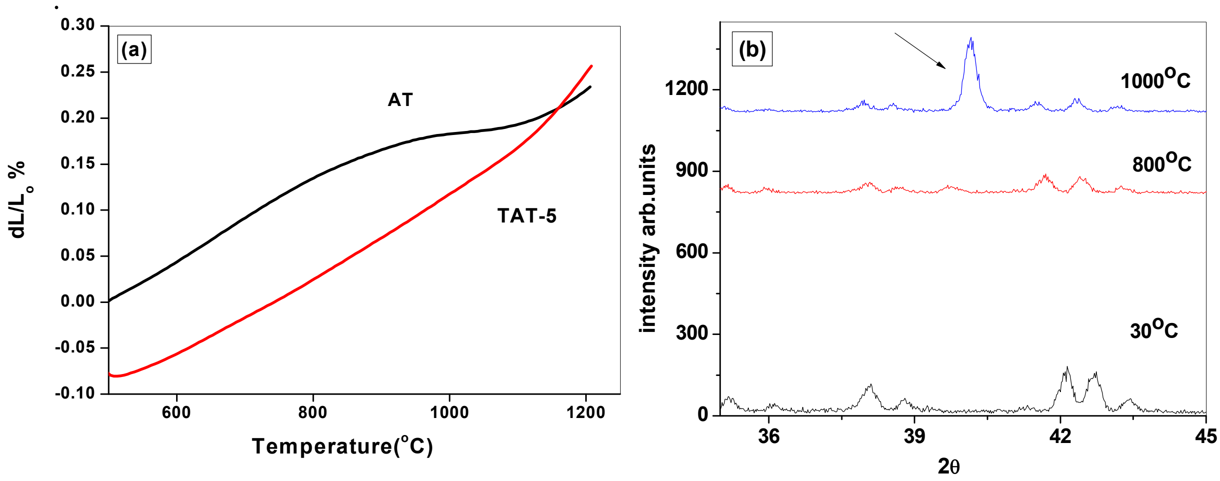

Fig 5 (a) Dilatometric curve of AT and TAT-5 samples and (b) XRD Patterns recorded for AT sample at 30, 800 and 1000°C

The elimination of eutectoid decomposition in TAT-5 specimens, exhibiting thermal stability as a consequence of magnesium silicate doping can be ascribed to larger ‘c’ constant which corresponds to the height of the distorted (MO_5) octahedra in the AT lattice. The expanded c direction as minimises the distortion of the AT lattice leading to the enhanced stability of the TAT-5 specimens, as reported by earlier researchers [8, 11].

For scientific curiosity, the decomposition of Al_2TiO_5 phase has also been studied under Spark plasma sintering (SPS) conditions and reported for the first time in the literature. The SPS runs were carried out at a heating rate of 200°C/min, to peak temperatures of 1400°C with dwell time of 3 minutes and a pressure of 50 MPa to study the decomposition of AT and TAT-5 samples respectively. In comparison to TAT-5 samples which exhibited decomposition to 50% of precursor oxides, the AT samples undergone 100% decomposition during SPS conditions. Decomposition of Al_2TiO_5 phase in SPS conditions can possibly be attributed to plasma generated in the initial stages of SPS condition that produces the reactive surfaces and extremely high heating rate of 200°C/min under argon atmosphere. (*Published in Journal of Ceramic International, 40[1], (2014)459-555*).

The advantages of the newly developed TAT-5 formulations were thoroughly investigated for thermo-mechanical properties and has systematically been presented in **Chapter 4**. The enhancement of thermal expansion with additives being a critical problem, dilatometric studies are carried out to ensure the CTE values are in the target range of $<1x\ 10^{-5}/^{o}C$. The dilatometric results clearly indicated no change in CTE value which can be attributed to the unique microcracking behavior in the matrix. The microcracking modify the thermal anisotropy of the material which are root cause for the microcracking. In order to confirm and correlate this observation thermal hysteresis differential expansion was recorded while heating and cooling of the samples in a dilatometer. A typical hysteresis recorded for AT and TAT-5 samples are shown in Fig 6(a). A large hysteresis area 95 cm^2 for TAT-5 samples, correlates well with the low CTE value of $0.42x\ 10^{-5}/^{o}C$ observed for TAT-5 samples. The unique microcracking behavior found to affect the thermal conductivity behavior as well. Increasing thermal conductivity beyond 300-400°C is related to the increased heat transfer paths due to microcrack healing (Fig 6(b)). (*Published in Journal of Processing and application of ceramics, 7 [3] (2013) 143–145*).

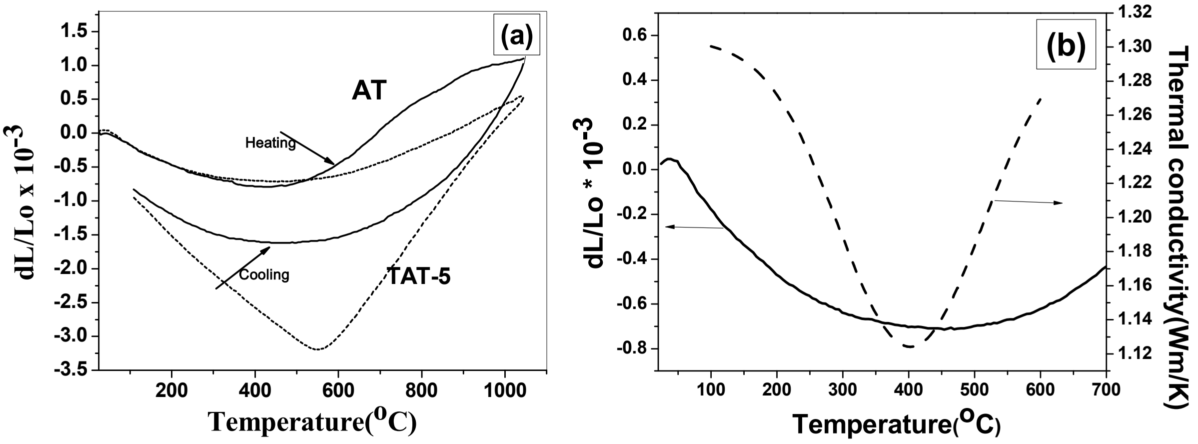

Fig 6 (a) Hysteresis of AT and TAT-5 samples and (b) Correlation of thermal expansion and thermal conductivity behavior as a function of temperature for TAT-5 samples

The samples are also characterized for mechanical properties, such as flexural strength at ambient and high temperature, hardness and compressive strength. An increase in room temperature flexural strength by 19% at 500°C and a maximum increase of 159% at 1200°C are obtained for TAT-5 samples shown in Fig 6(c). Enhancement in flexural strength, σ_f and CTE, α beyond 400°C correlated well and can be attributed to thermally activated microcrack blunting. Further, an identical increasing trend in σ_f and α with temperatures reveals the increasing extent of thermally activated microcrack blunting at elevated temperatures upto1200°C.

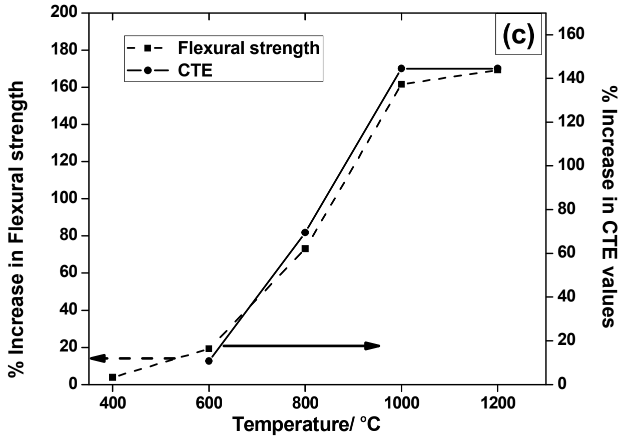

Fig 6(c) % increase in CTE and flexural strength as a function of temperature for TAT-5

In order to evaluate the adaptability of the newly developed formulation (TAT-5) which has exhibited desired properties were subjected to shaping into components using advanced ceramic processing techniques. **Chapter 5**, discusses on the extrusion processing of the TAT-5 formulation into honeycomb structures. However, the scope was limited to establish the extrudability looking towards the future potential as a proposed next generation particulate filters. The formulation was made into an extrudable dough with the binder and plastisizers which imparted a shear thinning behaviour is shown in Fig 7(a).

The study employed a honeycomb die designed and developed by the proprietary techniques of ARCI for the extrusion processing. An extrusion rate of 100 mm/min was employed and the defect free honeycomb extrudates were microwave dried and sintered as per the optimised sintering schedule. A typical sintered TAT-5 honeycomb with 525 channels/square inch is depicted in Fig 7(b). Further, the honeycomb sample was characterised and the relative density was found to be 0.38. (*Published in Trans Indian Inst Met. DOI 10.1007/s12555-011-0095-3 (2011)*)

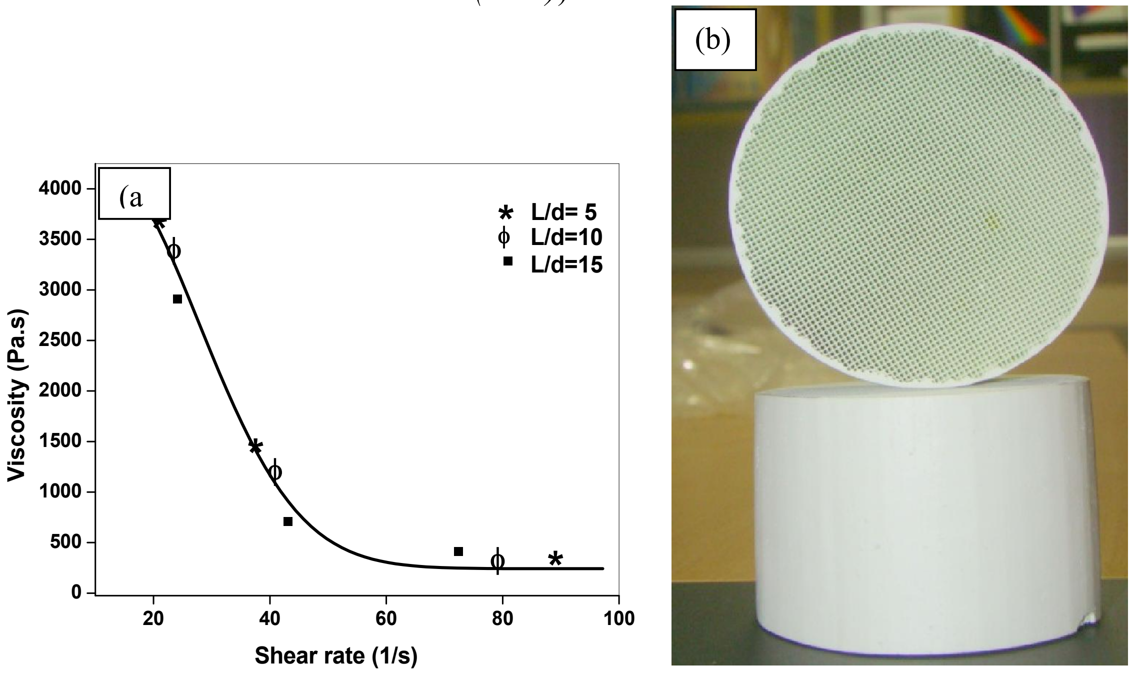

Fig 7 (a) Plot of viscosity versus shear rate of TAT-5 formulation and (b) sintered TAT-5 honeycomb

Chapter 5 deals with a comparative evaluation of the different shaping techniques for the TAT-5 formulation, cold isostatic pressing (CIP), conventional slip casting (CSC) and pressure slip casting (PSC), a relatively new processing technique, have been compared. Pressure casting machine employed during the study along with the polymer mould (fabricated by the proprietary techniques of SAMA) and fitted with the pressure casting machine is shown in Fig 8(a) is shown in Fig 8(a). Pressure casting presently is well established in the traditional ceramic processing. In the area of advanced ceramics PSC has resulted in limited success. Unlike traditional clay based ceramics, advanced ceramics cause improper alignment of particles and mechanical interlocking, resulting in serious problems while demoulding. The precursor-powder mixtures were made into slurry and suitability for pressure casting is established through rheological studies and typical rheological behavior of the slurry is shown in Fig 8(b). The slurry was subjected to pressure casting as per the pressure casting cycles as depicted in Fig 8(c). As it is evident from Fig 8(c), a typical pressure casting cycle consists of filling of the slurry into the mold, pressuring slip to form first layer followed by pressurization to form full cast and finally draining of excess slip. The cast with high green strength can be demoulded instantaneously by air percolated through the porous mould under pressure. A disc cast out of the TAT-5 formulation is shown in Fig 8(d).

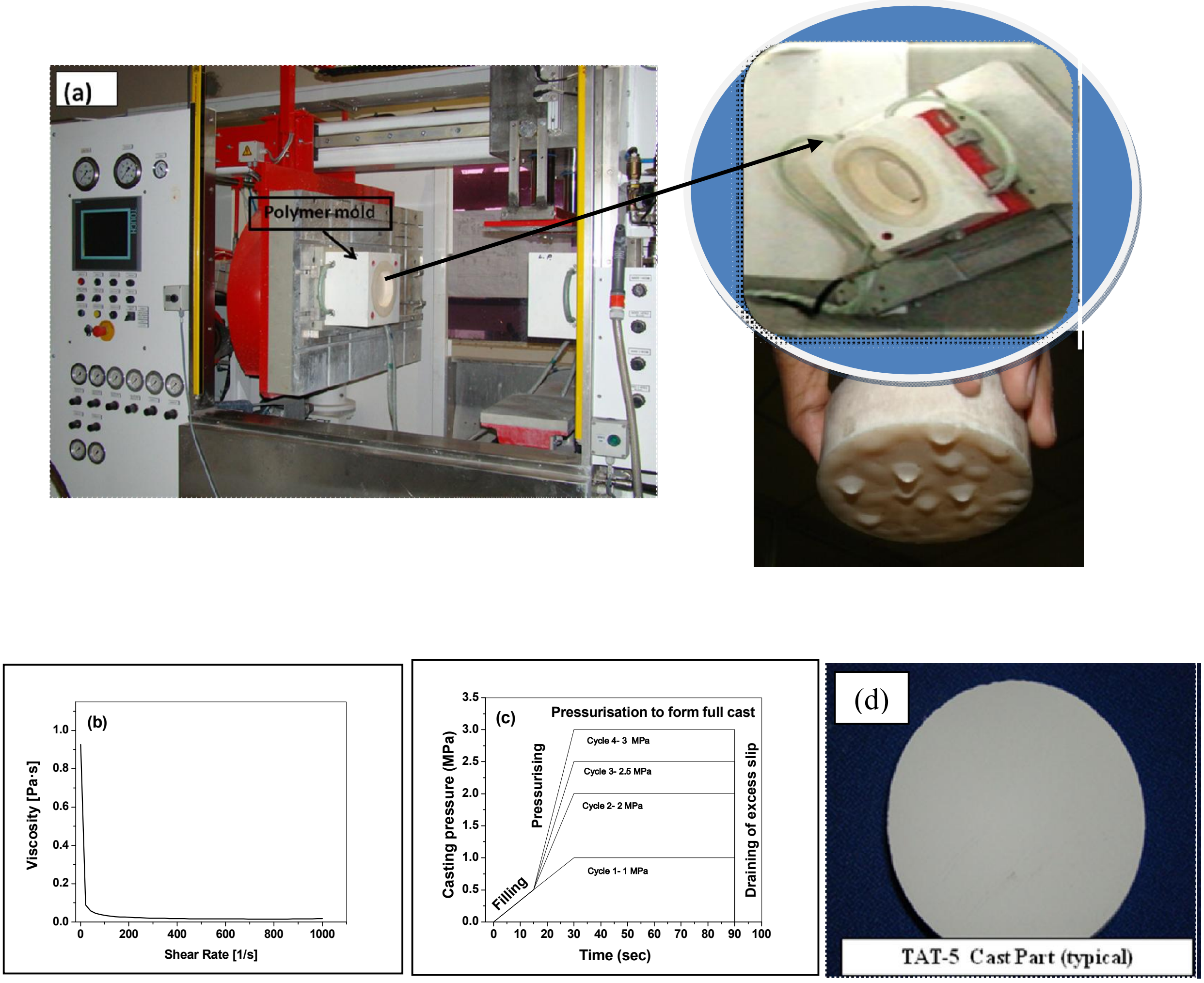

Fig 8 (a) Pressure casting machine, (b) viscosity versus shear rates of the TAT-5 slurry (c) Pressure casting cycle and (d) Cast part (Typical)

In order to clearly bring out the advantages of pressurization of a slurry for the consolidation into a cast, cold isostatic pressing of the dried granules was also carried out. It was observed that in dry condition (for CIPing) a compaction pressure of 100 MPa was required to achieve a green density ≥ 50% of the TD. However, for slurry under pressure (PSC) only 2 MPa of pressure is adequate to achieve similar green density (~50% of the TD). Studies were also carried out to demonstrate the effect of pressure on consolidation of the slurry by subjecting the same slurry for conventional slip casting (CSC). However, the green densities were limited only to ~50% of TD for CSC. (*Published in Journal of Processing and application of ceramics, 7 [4] (2013)159-555*)

References

1. T. Boger, J. Jamison, J. Warkins, N. Golomb, C. Warren and A. Heibel, Next generation aluminum titanate filter for light duty diesel applications, SAE. Int. doi:10.4271/2011-01-0815, 1-13 (2011).
2. J. Adler, Ceramic diesel particulate filters, Int. J. Appl. Ceram. Technol., 2 [5] 429–439 (2005).
3. C.H. Chen and H. Awaji, Temperature dependence of mechanical properties of aluminium titanate ceramics, J. Eur. Ceram. Soc., 27, 13-18 (2007).
4. H. C. Kim, K. S. Lee , O. S. Kweon, G. C. Aneziris and I. J. Kim, Crack healing, reopening and thermal expansion behaviour of Al_2TiO_5 ceramics at high temperature, J. Eur. Ceram. Soc., 27, 1431-1434 (2007).
5. C.H. Law and S.W. Sofie, Anchoring of infiltratred nickel electro-catalyst by addition of aluminum titanate, ECS Transactions, 28, 217-225 (2010).
6. Y.B. Matus, L.C. De Jonghe, C.P. Jacobson and S.J. Visco, Metal-supported solid oxide fuel cell membranes for rapid thermal cycling, Solid State Ionics, 175, 443–449 (2005).
7. E. Kato, K. Daimon, and J. Takahashi. Decomposition Temperature of β- Al2TiO5, J.Am. Ceram. Soc. 53, 355-359 (1980).
8. V. Buscaglia, P. Nanni, G. Battilana, G. Aliprandi and C. Carry, Reaction sintering of Aluminium titanate: I - Effect of MgO addition, J. Eur. Ceram. Soc. 13, 411-417 (1994).
9. M. Low, Z. Oo and B. H. O. Connor, Effect of atmospheres on the thermal stability of aluminium titanate, Phys B. 385–385, 502-504 (2005).
10. T. Korim, Effect of Mg^{2+} and Fe^{3+} ion on formation mechanism of aluminum titanate, Ceram. Int., 35, 1571-1575 (2009).
11. L. Jiang, X. Y. Chen, G. M. Han, M. Yu, Effect of additives on properties of aluminium titanate ceramics, Transactions of Nonferrous Met. Soc., 21, 1574-1579 (2011).
12. A. Yoleva, S. Djambazo, D. Arsenov, V. Hristo, Effect of SiO_2 addition on thermal hysteresis of aluminum titanate, J. Univ. Chem. Tech. Met. 45 [3] 259-274 (2010).
13. M. Tahazaksi, M. Fukuda, H. Fukuda and T. Yoko. Preparation, structure, and properties of thermally and mechanically improved aluminium titanate ceramics doped with alkali feldspar, J. Am. Ceram. Soc., 85 [12] 3025-30 (2002).

List of publications from thesis work

1. High temperature flexural strength and thermal stability of near zero expanding doped aluminum titanate ceramics for DPF Applications, Papitha R, M. Buchi Suresh, Dibakar Das, Roy Johnson, Journal of Applied Ceramic technology, DOI: 10.1111/ijac.12092, 1-10 (2013).

2. Eutectoid decomposition of aluminum titanate (Al_2TiO_5) ceramics under spark plasma (SPS) and conventional (CRH) thermal treatments, Papitha R, Buchi Suresh M, Chakravarty D, Swarnakar A, Dibakar Das and Roy Johnson, Journal of Ceramic International, 40[1], 559-555, (2014).

3. Effect of micro-cracking on the thermal conductivity and thermal expansion of tialite (Al_2TiO_5) ceramics, Papitha R, M. Buchi Suresh, Dibakar Das and Roy Johnson, Journal of Processing and application of ceramics, 7 [3] 143–145 (2013).

4. Mineral oxide doped aluminum titanate ceramics with improved thermo-mechanical properties, R. Papitha, M. Buchi Suresh, Dibakar Das and Roy Johnson, Journal of Ceramics, 214794, 1-9 (2013).

5. Rheological studies on aqueous alumina extrusion mixes, M. Swathi, R. Papitha, U. S. Hareesh, B. P. Saha, R. Johnson and M. Vijayakumar, Trans Indian Inst Met. DOI 10.1007/s12555-011-0095-3 (2011).

6. Pressure Slip Casting and Cold Isostatic Pressing of Aluminum Titanate Green Ceramics: A comparative Evaluation, R.Papitha , M.B. Suresh, Y.S. Rao, B.P. Saha, Dibakar Das and Roy Johnson, Journal of processing and application of ceramics, 7 [4],159–155(2013).

Conference Presentations:

1. Pressure slip casting of aluminum titanate ceramics, R.Papitha, M.B. Suresh, Y.S. Rao, Dibakar Das and Roy Johnson, at **International conference on ceramic science** 77thAnnual convention of Indian Ceramic Society, December (2013) at Jameshadpur.

2. Effect of low temperature thermal cycling on thermo-mechanical properties of aluminum titanate ceramics, R. Papitha, M.B. Suresh, N.Ravi, Dibakar Das and Roy Johnson, at 75thAnnual convention of Indian Ceramic Society, January (2013) at Ahemahbad.

(**Awarded second best paper presentation**)

List of figures

Chapter I:

Chapter II:

Chapter III:

Chapter IV:

Chapter V:

Chapter V:

List of tables

Chapter I:

Chapter II:

Chapter II:

Chapter IV:

Chapter V:

Chapter VI:

Chapter - I

Introduction

1.0 Introduction

Over the past few decades, on account of their unique combination of properties, ceramic materials enabled significant technological advancements in vital sectors. As ceramics can be engineered to exhibit diverse properties to carry out a variety of functions the significance and scope of ceramics is expected to grow continuously in modern times. However, the ceramics are inherently brittle in nature because of the presence of covalent and ionic bonding in them. Strong bonding in ceramics leads to limited yield, which results in significant stress concentration to develop at the crack tip and cause the crack tip to propagate with low expended energy resulting in low fracture toughness. At elevated temperature though the yielding is improved, thermal stresses develop because of the thermal expansion/contraction mismatch in the multiphase materials or anisotropy in the single phase materials [1-5].

Noncubic ceramics with high thermal expansion anisotropy have long been known to spontaneously microcrack upon cooling. The cracking, which occurs along the grain boundaries, becomes progressively less severe with decreasing grain size and below a certain critical grain size it is no longer observed. Ceramics on subjecting them to extreme thermal environments suffers transient thermal stresses due to thermal gradient leading to catastrophic failure. Thermal stresses are mainly originated from poor thermal conductivity in most of the ceramics. As the yield point of ceramics are quite high they have tendency not to yield under thermal stresses causing catastrophic crack propagation and thermal shock resistance related fracture. It is well known that thermal stresses can be well correlated with restraint of the thermal expansion by the surrounding structure of thermal gradient originating within matrix itself. Hence, the low expanding coefficient ceramic material becomes a preferable option for thermo-structural applications. Zero or close to zero thermal expanding materials will be ideal candidate to eliminate thermal stresses developed while subjecting to thermal shocks [4-7].

Controlling the thermal expansion is the key for a wide variety of applications like cookware for oven to freezer, electronic devices, dental applications, zero-expansion heat sinks, engine components, spark plugs, catalyst supports, high performance optical mirror substrates, etc [8-17]. Though, greater challenges exist in engineering the material towards achieving the low expansion, there are not only scientific but also technological motivations for investigations in detail in this direction. One of the approaches is to develop basic understanding on crystal structures as well as chemistry of the material, which exhibit intrinsically low thermal expansion and synthesize structural analogues [18]. Additionally, engineering the microstructure of the anisotropic crystallographic families lead to low bulk thermal expansion values [19-20]. Another approach which can be successfully employed is to identify suitable dopants based on the crystallographic tolerances within the thermodynamic limits to control the thermal properties of the material or to simultaneously reduce the expansion close to zero and to enhance other desirable properties [21-22].

1.1 Thermal Expansion: A brief Overview

A classification of ceramic materials based on their coefficient of thermal expansion (α) is proposed by Hummel [23]. According to this arbitrary classification, ceramic material can be classified as (i) high expanding group where $\alpha > 8 \times 10^{-6}$ /^{o}C (ii) intermediate expanding group : $2 < \alpha < 8 \times 10^{-6}$ /^{o}C and (iii) low expanding group : $\alpha \leq 2 \times 10^{-6}$ /^{o}C (this group includes negative expanding ceramic as well). It is well known that for technical applications, the expansion or the contraction of materials in use are deleterious for its effective performance and durability necessitating engineering of expansion values close to zero. Though chemical composition and structure can be correlated with the thermal expansion behaviour of materials, unlike physical properties, there are several anomalies in approximating thermal expansion behaviour through the quantitative estimation.

The earlier studies on thermal expansion behaviour of normal materials trace back to Einstein's paper on specific heat of materials [24]. Later Grueneisen [25], based on lattice dynamics and theoretical analysis, attempted to predict the thermal expansion behaviour of materials. Further, Grueneisen, based on thermodynamics and assumptions of Debye [26] coined the relation,

$$\alpha_r = \gamma K_o C_\upsilon / \upsilon \qquad \text{.............} \ (1.1)$$

where α_r is the volume coefficient of thermal expansion, γ is the Grueneisen constant, K_o is the compressibility, C_υ is the specific heat at constant volume and υ is the molar volume. A correlation was found between the low expansion of the material corresponding with its bond strength from the equation (1.1).

An inverse proportionality of the bond-length expansion to the square of the bond strength of homodesmic crystals was put forwarded by Megaw (1938) [27]. According to this thermal expansion of MgO is estimated to be around one fourth that of the isostructural phases of NaCl and found to have a good agreement of thermal expansions exhibited by ionic solids. However, discrepancies exist in case of phases with cations of low charge and high coordination. McKinstry [28], employed X-ray and dilatometric methods to elucidate, the thermal expansion behavior of alkali halides crystalline solutions and brought out limitations of such approaches. Further, studies of Megaw [29] correlated crystal structure with the thermal expansion, where-in electrostatic sharing and tilting effects of the polyhedra that form the network structures were incorporated. However, these observations could not be generalized due to the discrepancy associated with different systems. For a large variety of cubic and close packed materials the product αT_m (where α is the coefficient of thermal expansion and (T_m) melting temperature) is reported to be constant based on empirical ideas of Van Uitert [30-33]. Hazen& Prewitt [34] further correlated α with the existence of first coordination polyhedra and reported that metal-oxygen bonds with cation of the same charge had approximately the same α (e.g. octahedrally coordinated divalent cations Fe,Mg, Ni, Mn, Co, Ca, Sr and Ba all had $\alpha = 14 \times 10^{-6}$ /°C).

Thermal expansion of a material can be either intrinsic or extrinsic. Intrinsic thermal expansion is based on the changes of crystallographic unit cell axes with respect to temperature. Intrinsic thermal expansion can be isotropic or anisotropic. Isotropic materials show the same magnitude of thermal expansion in all dimensions of the unit cell and they are cubic or amorphous. On the other hand; anisotropic materials have different magnitude of thermal expansion along the different unit cell axes. When a single phase ceramic made of an anisotropic material is heated, micro cracks may from, because of the different expansion behavior of the unit cell axes. If the thermal expansion of a ceramic body is measured directly, these micro cracks affect the overall thermal expansion of the ceramic body on repeated heat treatments.

Thermal energy assimilation, in case of solids, is through the increase in vibration energy of atoms. It is well known that the vibrations of adjacent atoms are based on the nature of atomic bonding leading to lattice waves termed phonons, which transfer energy through the material. With increase in temperature the average distance between the atoms increases leading to thermal expansion. When temperature raises, the changes in dimensions in length of the solid is given by linear coefficient of thermal expansion 'α' and is defined as $\alpha = dl/L_0 = \alpha\ (T_2 - T_1)$. Fig. 1.1 illustrates simple potential energy curve and trough in the potential energy curve corresponds to the equilibrium interatomic spacing at 0 K. Heating of the sample result in the raising of vibrational energy and the width of the curve is proportional to the vibrational amplitude behaviour of the atoms and the average interatomic distance is represented by the mean position, which increases with temperature. If interatomic distances are large and well of the potential energy curve is deep and narrow, as in the case of material with strong bond energies, the interatomic separation with raise of temperature is small yielding small 'α' value. However, for the material having small bond energies interatomic spacing increases with temperature raise leading to large 'α' value [35].

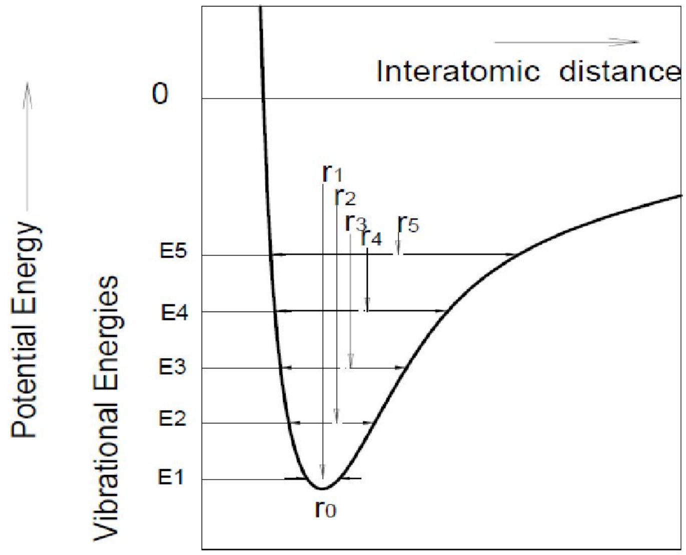

Fig 1.1 Inter-atomic energy separation curve for two atoms (Materials display steep curve with a deep trough have low 'α')

1.2 Low Expanding Ceramics: Fundamental basis for low thermal expansion anisotropic ceramics

Very low thermal expansion coefficients can be achieved through distinct features of non-cubic highly anisotropic ceramic crystal structures and aspect involves crystal chemistry at the unit cell level. In the case of the polycrystalline ceramic, when grains oriented randomly, the volume coefficient of thermal expansion is found to be a function of the sum of the unit cell principal axial thermal expansion coefficients. The relationship for an orthorhombic, such as pseudobrookites, β_v regarded as

$$\beta_v = \alpha_a + \alpha_b + \alpha_c \qquad \text{.............} \ (1.2)$$

Where, β_v is the volume coefficient of thermal expansion and the α_a, α_b and α_c are the principal axial thermal expansion coefficients of the crystallographic axes a, b and c. In case of rhombohedral (hexagonal) or anisotropic tetragonal crystal structure, β_v can be regarded as

$$\beta_v = 2\alpha_a + \alpha_c \qquad \text{.............} \ (1.3)$$

since $\alpha_a = \alpha_b$. This also applies for the crystal structures like sodium zirconium phosphate etc.

Thermally anisotropic crystal structures exhibits positive or negative principal axial thermal expansion coefficients. Hence, it is essential to examine the thermal expansion coefficients in case of all members of an isostructural family and chemically design a solid solution where principal axial thermal expansion coefficients equal to zero. Bayer [36, 37] has discussed this unit cell "alloying" concept for the pseudobrookite structure, while both Ota and Yamai [38] and Roy et.al [13] have addressed it for the sodium zirconium phosphate structure. The concept of designing unit cell level solid solution to achieve the desired thermal expansion values is considered to be a novel concept. However, could not be applied in general, as the zero coefficient of thermal expansion could not be achieved based on the prediction.

Generally, the principal axial thermal expansion coefficients equals to zero, when considered as the sum of both positive and negative values of principal axial thermal expansion coefficients. Because of this positive and negative principal axial thermal expansion, it generates extremely high internal micromechanical stresses along the grain boundaries during cooling [39]. Lazlo [40] has termed these internal microstresses as tensellated stresses. Buessem and Lange [41] and McPherson [42] have also described these internal micromechanical stresses for anisotropic ceramics. The internal stresses caused due to the anisotropy can lead to the grain boundary microcracking resulting in poor mechanical properties. This happens especially cooling from the process temperature. It is reported that microcracking can be effectively controlled by engineering the grain size of the ceramic matrix as reported by Kuszyk and Bradt [43].

In the earlier studies, Kuszyk and Bradt [43] prepared a series of $MgTi_2O_5$, a thermally anisotropic pseudobrookite ceramic with different grain size in order to evaluate the effect of grain size in their thermal behaviour. They concluded that, lesser microcracking with high structural integrity is possible with fine grain microstructure. However, coarse grained microstructures exhibited severe microcracking along the grain boundaries. A critical grain size for microcracking through an energy balance, where the volume dependence of the elastic strain energy was contrasted to an areal surface energy for grain boundary fracture. A reasonably good theoretical estimate of the critical grains size for microcracking could be predicated and found to be in good agreement with the experimental validation through their studies. On defining the critical grain size for the onset of internal microcracking for polycrystalline ceramic, it is possible through the advanced processing technique to engineer the grain size to defined critical values. Such engineered ceramics is expected to have good mechanical strength and structural properties and can be effectively used for harsh environment with thermal stresses.

The polycrystalline ceramics once crosses beyond the critical grain size that is the larger grain size are formed during processing at elevated temperature. On cooling of this ceramics extensive microcracking will occur throughout the matrix which substantially reduces the mechanical properties. Due to the excessive microcraking linear coefficient of the thermal expansion will approach close to zero or even zero. The mechanism, operative in achieving such low thermal expansion can be attributed to initial compensation of expansion, through microcrack closure while heating. Once the microcracks closures is completed which generally occurs at modest temperature, then expansion follows according to the chemical composition.

Thermal hysteresis is one of the inherent behaviors of the microcracked polycrystalline ceramic. Buessem, et.al [44] first reported thermal hysteresis of Al_2TiO_5 ceramics and further, studies of Kuszyk and Bradt [43] in $MgTi_2O_5$ also revealed the existence of thermal hysteresis. Thermal cycling of these heavily cracked ceramics may results in affecting the hysteresis area and even thermal expansion behaviour. Other inherent property of these microcracked ceramics include excellent thermal insulating properties [45].

A comprehensive study on low expanding polycrystalline ceramics and empirical examination by Rustam Roy et al.[13], revealed anomalies exists in many cases of low expanding ceramics, some of the structural features that contributes to these anomalies are listed below,

- The changes in the bond lengths associated with the strongly bonded polyhedron linked in three dimensions to minimize thermal expansion behavior.
- Lattice with an open structure with large openings or channels in the structure would enable accommodate, partially, thermal energy in transverse vibrations perpendicular to the bond directions.
- Structures with ferromagnetic or ferroelectric microdomains, the distribution of which changes over a temperature range thus compensating for the dimensional changes caused by thermal energy.

The most widely used materials for low expanding applications are listed below with their corresponding coefficient of thermal expansion values and working temperature range.

Table 1.1 List of low expanding materials

Material	Formulation	Average CTE x 10^{-6} /°C	Temperature Ranges
Spodumene, Lithium Aluminium Silicate (LAS)	Li_2O-Al_2O_3-$4SiO_2$	0.9	25 – 400°C
Cordierite, indalite	$2MgO$-$3Al_2O_3$-$5SiO_2$	1.4	25 -800°C
Tialite (Aluminum Titanate)	Al_2TiO_5	1.4	25 -1000°C
Silica glass	SiO_2	0.05 to -0.03	25 -800°C
Aluminosilicate glass	Al_2O_3-SiO_2	0.5	25 -800°C
NZP Family	$NaZr_2P_3O_{12}$	0.63	25 -500°C
Invar	FeNi alloy	0.12	25 -100°C

1.3 Aluminum Titanate Ceramics

Aluminum Titanate ceramics (Al_2TiO_5, designated as AT) are synthetic materials of potential interest for many thermo-structural applications owing to their high melting point, low thermal conductivity and excellent thermal shock resistance. Al_2O_3 -TiO_2 phase diagram is shown in Fig 1.2. It is evident that AT is formed by a solid state reaction of equimolar mixtures of Al_2O_3 and TiO_2 in the range 1360–1400°C and its melting point is around 1860°C. Further, it shows the existence of two allotropic forms of aluminum titanate: α- Al_2TiO_5 and β- Al_2TiO_5. α- Al_2TiO_5 is a high temperature phase, stable between 1820°C and the melting point at 1870°C and β- Al_2TiO_5, a low temperature phase stable from room temperature up to around 750°C and from 1300°C up to inversion temperature 1820°C. It is also evident that < 1300°C, Al_2TiO_5 undergoes decomposition into Al_2O_3 and TiO_2 [46, 47].

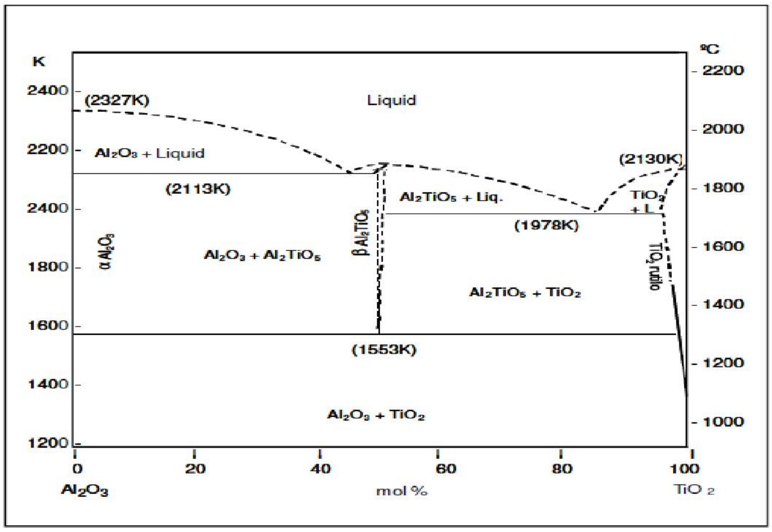

Fig 1.2 Phase diagram of Al_2O_3: TiO_2 system [Lange et.al (1952)]

1.3.1 Crystal structure and anisotropy

The structure of aluminum titanate is isomorphous with mineral pseudobrookite ($M^{2/3+}Ti^{4+}O_5$) structure crystallizing in the orthorhombic (face centered) space group with lattice parameters of *a* = 9.436Å, *b* = 9.648 Å, and *c* = 3.557 Å. In this structure each Al^{3+} or Ti^{4+} cation is surrounded by six oxygen ions forming distorted oxygen octahedra [48,49]. The arrangement of Al^{3+} or Ti^{4+}ions in octahedra is shown in Fig 1.3.

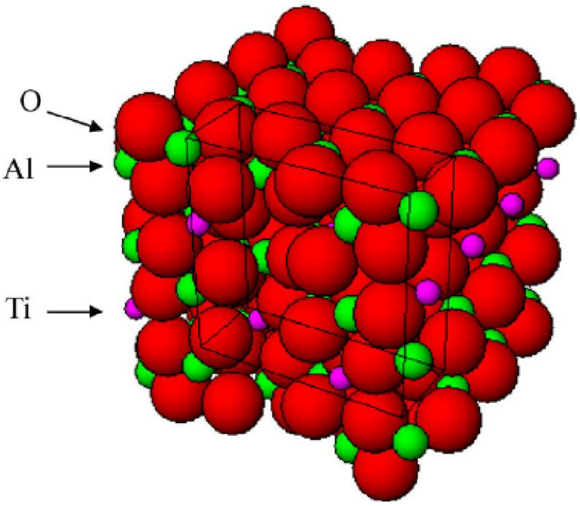

Fig 1.3 The arrangement of Al and Ti ions in AT crystal structure [R.D.Skala (2009)]

Aluminum titanate, due to its inherent orthorhombic crystal structures is highly anisotropic. The thermal expansion of the principal axes of the single AT crystal is shown in Fig.1.4(a). Thermal expansion values from RT-1000°C for crystallographic axes of α_a, α_b and α_c are estimated to be 11.8, 19.4 and -2.6 x 10^{-6}/°C respectively. It is evident that on heating the structure will expand along a and b dimensions and contract in the c dimension. The presence of corner shared polyhedra and structural holes in the pseudobrookite based orthorhombic unit cell (Fig 1.4(b)) along the principal c – axis may be the probable reason for negative expansion. Additionally, equalization of bond lengths leading to the tilting of polyhedra that reduces distortions when heated may also contribute to the low expansion values [44, 50-53].

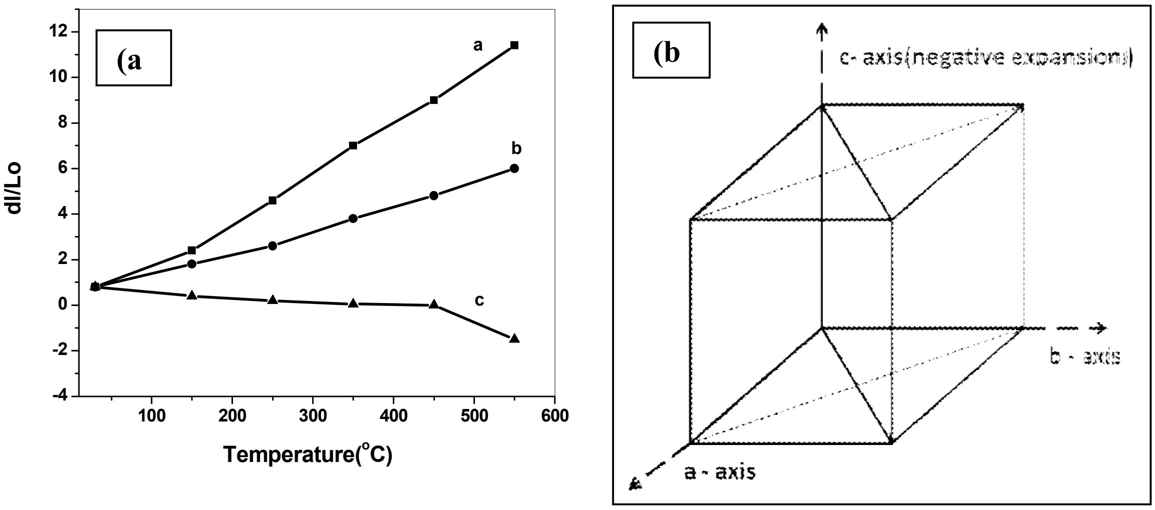

Fig 1.4 (a)Thermal Expansion of principal axis a, b and c and (b) orthorhombic unit cell showing the principal axes

1.3.2 Anisotropy induced micro-cracking

Based on the sum of the thermal expansions of principal axes α_a, α_b and α_c the bulk thermal expansion of sintered polycrystalline aluminum titanate is expected to be 9.7 x 10^{-6}/°C, however, it exhibits lower expansion value of ~1 x 10^{-6}/°C [53]. This anomaly in the thermal expansion behavior can be explained due to the anisotropy induced microcracking. Thermal anisotropy originates from differential orientation of AT crystal domains. During cooling process, after sintering the individual crystal domain in the AT bulk ceramics shrinks anisotropically. This induces internal stresses, promotes the breakdown of the grain boundaries, which causes a decrease in the structural integrity of the polycrystalline ceramics [54-64]. Typical micrographs exhibiting the microcracks are shown in Fig. 1.5.

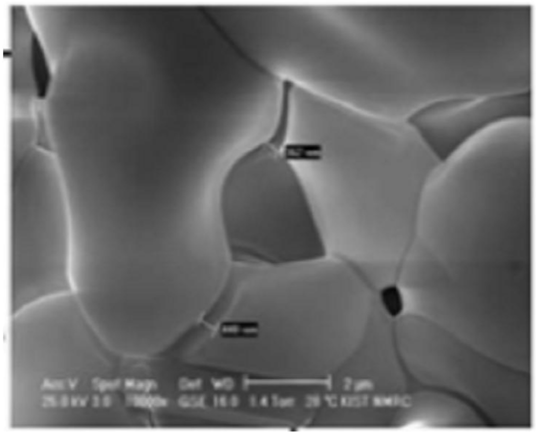

Fig 1.5 Micrograph of Al_2TiO_5 exhibiting the microcracks [I.K. Jim(2010)]

1.3.3 Properties of aluminum titanate

The typical properties of aluminum titanate are listed in Table 1.2. It is evident that aluminum titanate as a ceramic material possess inherent thermal properties that makes it a potential candidate for various engineering applications. The major applications of aluminum titanate being used on commercial basis or explored widely are listed below.

- Catalyst filter / wall flow trap for diesel exhaust particulates
- Exhaust Port liners for engine manifolds
- Non ferrous melt handling crucibles in foundries
- Kiln furnitures / Insulations plates for furnace
- Thermal expansion control / chemical anchoring additive for SOFC anodes

Table 1.2 Typical properties of aluminum titanate ceramics

Properties	Nominal values	References
Chemical formula	Al_2TiO_5 [Al_2O_3-56%, TiO_2-44%]	S.Lang (1952)
Density(g/cm^3)	3.7	Holcombe (1973) Busgalia (1994)
Crystal structure	Orthorhombic	Morsin (1972)
Melting point(°C)	1860	S.Lang (1952)
Thermal expansion values (x10^{-6}/°C), 30-1000°C	$\alpha = \sim 1$	Morsin (1972) Thomas (1991)
Thermal conductivity, k (Wm/K)	1.5-2.5	Stingl (1986)
Hardness, Hv (GPa)	5	Wohlfromn (1990)
Bending strength, σ (MPa)	4-20	Milosevski (1995)
Elastic Modulus, E (GPa)	12-18 10-20	Stingl (1986) Cleveland (1978)
Application temperature(°C)	1500	S.Lang (1952)
Corrosion resistance	Good	Holcombe (1973)
Contact angle (nonwettability with aluminium melt)	135	Holcombe (1973)

1.3.4 Applications of aluminum titanate

Catalyst filter/ wall flow trap for diesel exhaust particulates

Respirable soot particulates of diesel exhaust are considered to be a hazardous material causing several health issues and hence the particulate emission of diesel engines are the subject of strong legislative regulation in recent years. Recent developments of diesel particulate filters (DPFs) for diesel engines have shown that ceramic materials are well suited to the harsh requirements of exhaust after treatment. A honeycomb structure is preferred for treating exhaust gases because it is lightweight and has a reduced back-pressure drop across the filter. Diesel particulate filters of different designs and materials are available with SiC and cordierite based formulations. While application of cordierite is limited by its melting temperature (1450ºC) and lower heat capacity and SiC suffers from exorbitant cost and poor thermal shock resistance due to its higher thermal expansion. AT offers high potential due to its much higher melting point, superior heat capacity and also at par or more thermal shock resistance to silicon carbide.

Hence, AT is considered as the next generation light duty diesel filter material to meet future exhaust norms. Application of AT as catalyst substrates as well as wall flow filters are being explored [63-65]. Typical AT catalyst filters and wall flow filters are shown in Fig 1.6 (a)-(c) respectively.

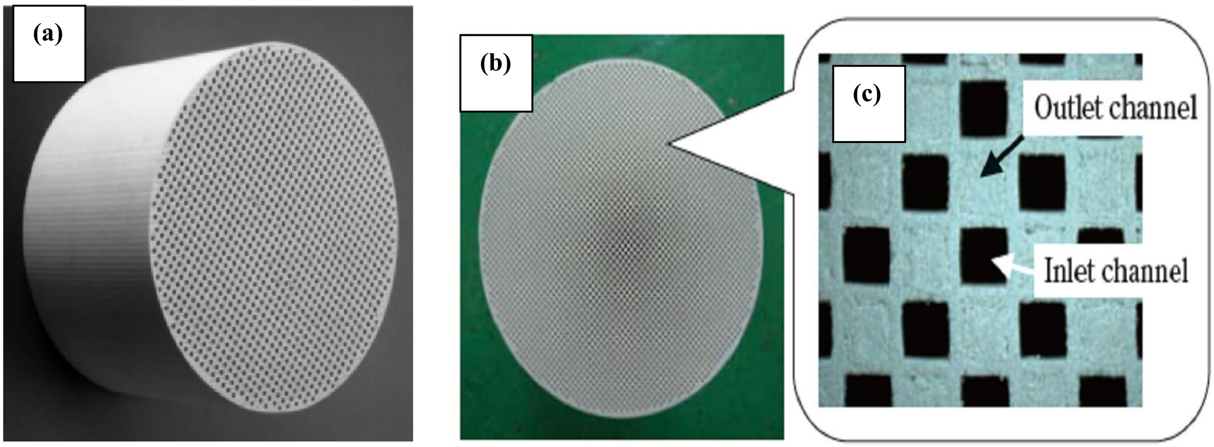

Fig 1.6 Typical AT (a) catalyst filters and (b)-(c) wall flow filters [Sumitomo kagaku, vol. 2011-II]

Non ferrous melt handling crucibles in foundries

Specific advantage of AT in handling non ferrous melt, crucibles, tubes, riser tubes, lancing tubes etc in foundries [66-67] (various AT foundry parts are shown in Fig 1.7) in comparison to other potential candidate such as cast iron, dense fused silica and silicon nitride are listed below:

- Long durability
- Non-wetting and corrosion resistance
- Thermal shock resistance

- Low thermal expansion coefficient
- No coating required
- Good thermal insulation

Fig 1.7 Foundry AT tools [www.Blashceramics.com]

Aluminum titanate has also been explored as insulation plates, high temperature light weight kiln furnitures etc by major manufactures based on the potential thermal properties. Recently, aluminum titanate has also been proposed by NASA as a additive for enhancing thermal stability of NiO-zirconia anode material through thermal expansion compensation [69-70]. Though aluminum titanate is commercially used or explored for various applications major benefits of outstanding thermal properties are offset because of the poor mechanical properties, which not only invoked scientific but also technological quest for addressing the issues. An overview of the earlier work on aluminum titanate ceramics based on the detailed literature survey are shown below[71-103].

1.3.6 Aluminum Titanate: Brief Overview

A research trend in terms of R & D publications during 1998- 2013 (scopus survey: SCI Journals) is presented in Fig 1.8. A renewed interest in AT research is indicated by the increasing trend in R& D Publications in recent years. The published literature, as peaked almost close to the recent previous years signifying, continued increasing interest in AT R &D.

Bachmann et.al [71] (1948), reported lower thermal expansion of conventionally prepared AT ceramics obtained by reactive sintering of Al_2O_3 and TiO_2 powders, which is lower than that of the vitreous silica. Lang et. al [46] (1952) studied the Al_2O_3 - TiO_2 equilibrium diagram and concluded the existence of two allotropic forms of aluminum titanate: α-Al_2TiO_5, a high temperature phase, stable between 1820°C and the melting point a 1860+10ºC and β- Al_2TiO_5, a low temperature phase stable from room temperature up to ≈ 750ºC and from 1300°C up to inversion temperature 1820°C (at intermediate values, it has instability and decomposes to Al_2O_3 + TiO_2). The transformation between both phases is spontaneous and reversible. It was also concluded that it is almost impossible to obtain α-Al_2TiO_5 at room temperature.

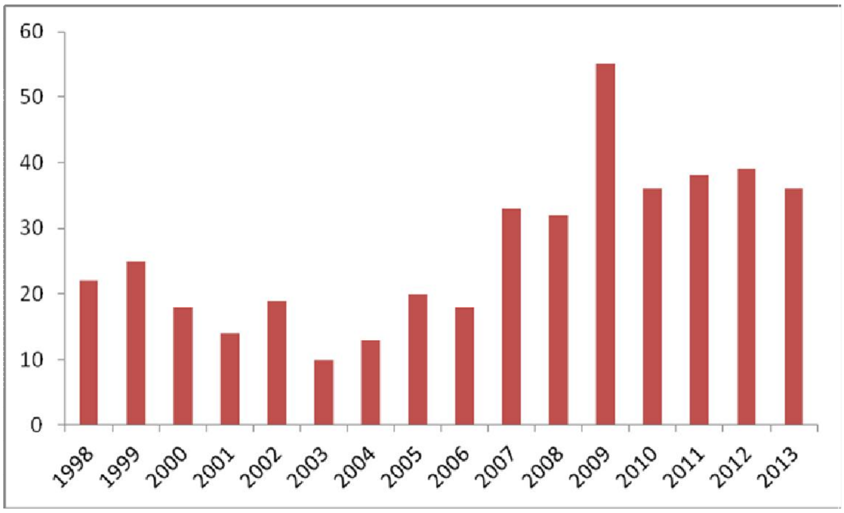

Fig 1.8 R & D publications 1998- 2013 (scopus survey: SCI Journals)

Austin et.al [72] (1953) elucidated the crystal structure of AT and reported it to be isomorphous with mineral pseudobrookite which crystallizes in the orthorhombic symmetry with space group Bbmm. Morosin and Lynch [48] (1972), by x-ray diffraction study, claimed a disordered arrangement for Al and Ti cations in Al_2TiO_5 lattice. The two metal sites M1 (Ti, Al) and M2 (Ti, Al) have octahedral coordination, with each site surrounded by six oxygen atoms. In considering the angles between the oxygen atoms on the plane of the metal atom, the structure can be considered distorted octahedra. The angles between the oxygen atoms at the vertices of the octahedra and the metal atom also show a distortion for both octahedra. Hamano et.al [73] (1985) demonstrated the crack propagation of Al_2TiO_5 ceramics. It revealed that microcracks increase the resistance to crack propagation on fracture by mechanisms involving crack deflection, branching and blunting. Ohya et.al [74] (1988) demonstrated the crack healing and increase in bending strength for Mg doped aluminum titanate ceramics at high temperature.

Epicier et.al [51] (1990) showed that the arrangement in Mg-doped aluminum titanate. It can be assumed that the well-known stabilizing effect of Al_2TiO_5 by Mg addition is due to a reduction of the distortion of atomic coordination polyhedra, responsible for the high thermal expansion anisotropy of pure aluminum titanate. Since the structure of the Mg-Al_2TiO_5 solid solution appears to be correctly described with atomic positions equal to those refined in the case of pure aluminum titanate. Wohlfromn et.al [75] (1990) studied the effect of both solid solution of MgO and second phases (mullite, ZrO_2) on properties of Al_2TiO_5 by SEM and TEM. The solid solutions are made by solid state synthesis. It is found that Mg in Al_2TiO_5 lattice, not only effect the ordering in the cationic lattice, order-disorder phenomena but also sets up an in the system. Thomas et.al [76] (1991) showed the effect of ZrO_2 addition on Al_2TiO_5 system by solid state synthesis. It was found that strength of Al_2TiO_5 system improved with its addition. Djambazov et.al [77] (1994) studied the stabilization of Al_2TiO_5 with CaF_2, SiO_2 or kaolin and MgO additives. It was found that stabilization of Al_2TiO_5 improved in MgO and CaF_2 solid solutions. Busgalia et.al [78] (1994) studied the sintering of Al_2TiO_5 with MgO. The lower density of the titanate (3.7 g/cm^3), in comparison with the equimolar $A1_2O_3/TiO_2$ mixture (4.1 g/cm^3), is responsible for the volume increase and the expansion rate is related to the Al_2TiO_5 formation later. With MgO in Al_2TiO_5 resulted in a strong reduction of the titanate grain sizes with a subsequent increase in the final density. Grimes et.al [79] (1994) studied, defect formation structure in Al_2TiO_5 and its influence on structural stability. The study suggests that Al_2TiO_5 in cationic disordered. The schottky and Frenkel defects are neglibe and cluster of vacany defects are strongly bonded.

Busgalia et.al [80](1994) studied the sintering of Al_2TiO_5 with MgO using different alumina powders. It was conclude that nature of alumina determines the formation of Al_2TiO_5 and residual oxides. They also explained the formation mechanism of Al_2TiO_5. In densification of aluminum titanate three different consecutive processes can be identified:(i) Initial contraction due to the densification of the starting oxide mixture;(ii) Expansion as a consequence of Al_2TiO_5 formation (Volume expansion of 10-11%) (iii) Second contraction due to Al_2TiO_5 sintering. Zabicky et.al [62] (1995) studied the thermal anisotropy of tialite and it depends on processing and nature of precursors. Ohya et.al [57](1996) studied the thermal anisotropy of tialite by measuring the crack volume. It was concluded that the specimens with low bulk density have a smaller difference between sintering and crack onset temperature.

Busgalia et.al [81](1997) studied the decomposition of Al_2TiO_5 and MgO doped Al_2TiO_5.The enthalpy of reaction Al_2TiO_5 is, in fact, considerably negative, and formation of Al_2TiO_5 becomes feasible only at high temperature. This is because of the contribution of the configurational entropy resulting from disordered distribution of Al^{3+} and Ti^{4+} ions in the cationic sublattices. This is confirmed by studies of Navrotsky [83] and Morosin and Lynch [48] from X-ray diffractometry (XRD) and by Wohlfromm et. al [76. from high-resolution transmission electron microscopy (HRTEM). The isostructural compounds Fe_2TiO_5 and $MgTi_2O5$ show similar behavior and in general, all the oxides with the orthorhombic pseudobrookite structure can be considered as ''entropy-stabilized'' high-temperature phases. $MgTi_2O5$ decomposes to $MgTiO_3$ + TiO_2 below ~700°C and Fe_2TiO_5 to Fe_2O_3 + TiO_2 below 565°C. The decomposition rate of Al_2TiO_5 below 800°–900°C is found to be very low. Nucleation and growth of a solid inclusion in a solid matrix involves strain energies related to the change of molar volume. So the decomposition proceeds with ~10% volume decrease, with significant tensile stresses developed in the matrix. The elastic strain energy Δ G $_{strain}$ has to be compared with the chemical driving force Δ G $_{chem}$, because random nucleation of the reaction products does not occur unless, $\Delta G_{chem} \geq \Delta G_{strain}$. Although the elastic strain energy can be considered almost temperature independent, the chemical driving force per unit volume is approximately proportional to the degree of supercooling $T - T_d$, because Δ G $_{chem}$ = 0 at T - T_d. The available chemical driving force is far below the strain energy, in the range 1000 – 1100°C, where decomposition of solid solution is more rapid. As a consequence, formation of the decomposition products occurs only at a limited number of sites, the above conditon ($\Delta G_{chem} \geq \Delta G_{strain}$) is locally verified probably because of the presence of impurities and/or glassy phases. A similar behavior has been observed for the formation of Al_2TiO_5 by solid-state reaction of Al_2O_3 and TiO_2 powders in the temperature range 1553 to ~1700 K [80-83].

Liu et.al [84] (1999) prepared Al_2TiO_5 with MgO and Fe_2O_3, explained the improvement in stability. The AlO_6 octahedron in AT is distorted as it shows a tendency for tetrahedral coordination. It was suggested that the Al^{3+} (ionic radius=0.053 nm) is slightly too small for the octahedral site, whereas, Fe^{3+} (ionic radius=0.064 nm) and Mg^{2+} (ionic radius= 0.078 nm) fit in well. The similarity of the Fe^{3+} cation size to Ti^{4+} (ionic radius=0.068 nm) involves a higher thermal stability because the octahedra are much less distorted than that of AT or to a lesser extent than that of $MgTi_2O_5$.

Nagano et.al [85] (1999) prepared Al_2TiO_5 with various additives like low expanding glass, barium salts and ZrO_2. It was found that addition of barium salts and ZrO_2 suppress the thermal decomposition but increase its expansion value. Takahasi et.al [86] (2002) prepared Al_2TiO_5 with alkali feldspar and it was found to, effectively, improve the mechanical and thermal properties. Tsetsekou [87] (2005), studies the tialite ceramics with doping of various oxides like MgO and feldspar which led to improved thermal and mechanical properties. In 2005, application of Al_2TiO_5 as Diesel Particulate Filter (DPF) was proposed by Corning. Developed formulation based on AT material has higher thermal shock resistance than silicon carbide [64-65].

Low et.al [88] (2006) studied the effect of atmosphere on decomposition of Al_2TiO_5. Rate of phase decomposition of Al_2TiO_5 is dependent on the atmosphere or oxygen partial pressure during isothermal ageing. Chen et.al [66] (2007) explains the temperature dependence of physical and mechanical properties in Al_2TiO_5. The influence of temperature on microcrack morphology changes in Al_2TiO_5. Kim et.al [89] (2007) explains crack healing mechanism, the morphology of microcracks in Al_2TiO_5 ceramics shows remarkable temperature dependence. As the temperature increases up to 700°C, the microcracks at the grain boundaries close up. The different parts of the hysteresis behaviour are as follows,

- At temperatures less than 500°C, the microstructure is held together by the crystals in the *a* direction of the lattice which contract upon heating.
- At ~500°C, the bulk thermal expansion coefficient increases slightly as the lattice expands towards *b* and *c* direction upon heating. The microcracks close partially, with little effect on the bulk dimensions of the body
- The microcracks close as the material expands. Expansion in the direction is substantially less than in the *c* direction.
- The true bulk thermal expansion of the material is the slope of the line tangent to the curve at this point. Each individual grain acts as a single crystal with changing dimension.
- Intergranular and intragranular microcracks begin to form due to large thermal expansion anisotropy in 3 crystallographic directions.

- The lattice direction *a* expands upon cooling and *b* and *c* directions contract. The *a* direction which has no microcracking, dominates on cooling to relieve the stress place upon it

Oikonomou et.al [90] (2007) studied the stabilization of Al_2TiO_5 presence of Fe_2O_3. Decomposition of AT was altered to the very small size of aluminium (Al^{3+} ionic radius = 0.053 nm). The available thermal energy permits aluminium to migrate from its site resulting to a structural dissolution to rutile and corundum. On the contrary, iron cations (Fe^{3+} ionic radius = 0.064 nm) fit in very well to the lattice site thus reducing the decomposition reaction rate to a minimum. The presence of Fe_2O_3 in the system results in decreasing the reaction temperature for the formation of Al_2TiO_5, while the rate of Al_2TiO_5 formation is increased. Thus, the addition of Fe_2O_3 has a catalytic effect on the kinetics of the Al_2TiO_5 forming reaction. In 2008, AT was used in light-duty vehicles and is being increasingly deployed for heavy-duty diesel applications. Regeneration conditions and the regeneration efficiency are evaluated for AT as a filter which exhibits improvement in testing by 2009 [91,92].

Skala et.al [49](2009) explains room and high temperature crystal structure of Al_2TiO_5 ceramics. As the temperature increases, it is seen that the site occupancies of the Al atoms within the M1 and M2 sites increases. The largest increase in site occupancies of Al for both the M1 and M2 sites occurs when the temperature increases from 800 to 1200°C. This temperature range is also the range in which Al_2TiO_5 decomposes into its constituent phases, namely alumina and rutile. The changes in Al and Ti sites may indicate that these are “pre-transformation” or pre-eutectoid changes at the atomic scale that may enhance subsequent eutectoid decomposition on cooling. It is also interesting to note that this increase in the occupancy of the Al atoms and the temperature range over which it occurs coincides with the temperature range over which Al_2TiO_5 decomposes to its constituent materials, i.e. alumina and rutile. This is accompanied by an expansion of the unit-cell of Al_2TiO_5 as the temperature is increased. It is proposed that, as the material is heated through this temperature range, the crystal system contracts, so much so that it effectively expel the Ti atom from the structure leaving the aluminium in place to form alumina.

Naghizadeh et.al [93](2009), studied that addition of 2.5 wt.% Fe_2O_3 to a fine mixture of aluminum hydrate and rutile resulted in decreasing the tialite formation temperature from temperatures over 1280ºC down to 1150ºC. Korim et.al [94] (2009) explained the effect of additives on formation of aluminum titanate ceramics by addition of MgO and Fe_2O_3. Replacement of Al^{3+} for Mg^{2+}, led to the assumption that possibly two Al^{3+} is replaced by one Mg^{2+} and one Ti^{4+}-ions together in order to preserve the charge neutrality. Mg^{2+} and Fe^{3+} ions build in the crystal lattice of Al_2TiO_5 forming solid solution series that possible. Naderi et.al [95] (2009) explained the effect of talc on sintering of aluminum titanate. A talc addition leads to the formation of AT around 1200ºC. The bulk density and tialite content is high at 1650ºC with solid solutions of MgO (94%TD). Yoleva et.al [96] (2010) demonstrates that addition of SiO_2 has both stabilizing and densification effect on Al_2TiO_5 but higher amount addition leads to higher thermal expansion. Brunno et.al [97] (2010) proposed the mechanisms to explain the apparent anomalous behavior of the Al_2TiO_5 under compression. It was established with a modeling; that under compression changes are observed more in c lattice followed by a lattice parameter. Low et.al [98-99] (2010) studied thermal stability and self-recovery in aluminum titanate. It was found that process of decomposition in AT is reversible, whereby self-recovery when it is re-heated above 1300°C. Lan et.al [100] (2011), explained the effect of additives on properties of aluminum titanate ceramics by addition of MgO, SiO_2 and Fe_2O_3. The stability of Al_2TiO_5 can be reflected by its lattice constant c, shown in Fig 1.9. The larger the lattice constant c, the more stable AT. By MgO and Fe_2O_3, a decrease in the distortion of octahedral of AT ceramics.

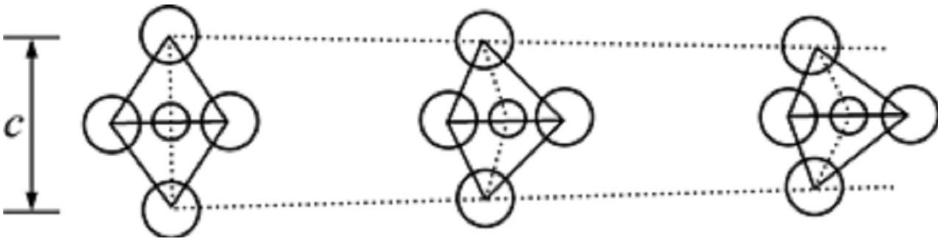

Fig 1.9 The schematic of crystal structure showing lattice constant 'c' variation

In 2011, next generation aluminum titanate filters for light duty, including the needs for advanced after treatment system (EU5 systems). It was founded that AT filter exhibited higher soot mass limit [65]. In diesel engines, innovative aluminum titanate based-diesel particulate filter having asymmetric hexagonal cell geometry are made in 2012 to enhance the efficiency. In current scenario (2013), AT filter new product family can help address specific requirements for the Indian market are presented for BS-1V regulations [101-103].

1.4 Motivation of the study:

From a vast literature on R&D carried out on AT ceramics, it is evident that AT is an important technical ceramics due to it's superior properties such as,

- ☐ Near zero expanding ceramic < 1.0 x 10^{-6}/°C (30 – 1000°C),
- ☐ High refractoriness (1860°C),
- ☐ Application temperatures upto 1500°C,
- ☐ High chemical inertness

However, aluminum titanate exhibits poor mechanical properties due to its low sinterability and extensive microcracking results from the crystallographic thermal expansion anisotropy. This limits the use of aluminum titanate ceramics in engineering applications in spite of its low thermal expansion value of <1.0 x 10^{-6}/°C (RT-1000°C).

Inherent eutectoid decomposition of aluminum titanate (Al_2TiO_5) ceramics in the temperature regime of 800-1200°C limits the application temperatures, though the refractoriness is very high (1860°C).

Hence, it is important to understand the scientific issues in depth to cater the above technological issues and to engineer the AT ceramics through unique processing techniques with/without an additional phases. Successful development of AT ceramics processed with adequate strength and thermal stability, in combination with its inherent low CTE values is required for its commercial applications. This will provide opportunities to address the challenges involved in developing several AT based industrial applications.

1.5 Objectives of the study

- Selection of raw materials and identification of process and parameters for synthesis of stiochiometric Al_2TiO_5 ceramics and optimization of parameters, dopant chemistry approaches to address the inherent poor mechanical properties and poor sinterability while retaining the low thermal expansion values with good thermal stability
- Characterization of the samples for thermal properties such as thermal expansion, thermal hysteresis, thermal stability, high temperature XRD and thermal conductivity
- Characterization of the samples for mechanical properties such as flexural strength (room and high temperature), hardness and compressive strength behaviour
- Correlation of thermo-mechanical properties with respect to formulation and processing parameters
- Extrusion processing of newly developed formulation with high strength and thermal stability into honeycomb structures and its thermo-mechanical properties evaluation
- Investigation on pressure slip casting of the newly developed formulation and its comparative evaluation with respect to cold isostatic pressing and conventional slip casting

1.6 References

1.W.D. Kingery, Introduction to ceramics. John Wiley and Sons: New York, (1976).

2.J.S. Reed, Principles of Ceramics Processing, 2nd edition Wiley, New York, (1995).

3.M.N. Rahaman, Ceramic Processing and Sintering, Marcel Dekker Inc., New York (1995).

4.M.W. Barosum, Fundamental of ceramics, McGraw-Hill, (1997).

5.C.B. Carter, N.G. Norton, Ceramic materials and science and engineering, (2007).

6.M. Sakai and R.C. Bradt, Fracture toughness testing of brittle materials, Int. Mat. Rev., 38[2], 53-78 (1993).

7.F.A. Hummel, Low expansion ceramics, Interceram, 33[1], 27-30 (1984).

8.R. Roy, D.K. Agrawal and H.A. M/cKinstry, Very low thermal expansion coefficient materials, Ann. Rev.Mat. Sci. 19, 59-81(1989).

9.S.Y. Limaye, New low thermal expansion materials for high use temperatures, Materials and processing report, 4, 1-2 (1989).

10. J.P. Ray and D.L. Hinckman, Ceramic gas turbine heat exchanger development, Corning.

11. C.J. Rahnke and L.R. Rossi, Automotive gas turbine ceramic regenerator design and reliability program, ERDA COO-2630-34 (1975).

12. A.J. Sherman, R.H. Tuffias and R.B. Kaplan, Refractory ceramic foams: A novel, new high temperature structure, Ceram. Bull., 70[6], 1025-1029 (1991).

13. F.Z. James, E. Paul and C.Z. Elizabeth, Porous ceramics for gas filtration, Am. Ceram. Soc. Bull., 70[1], 108-111 (1991).

14. I.G. Talmy and D.A. Haught, Ceramics- for advanced radome applications, NSWC TR89-162, (1989).

15. L.G. Van Uitert, Relations between melting point, glass transition temperature and thermal expansion for inorganic crystals and glasses. J.A.P. 50[12,] 8052-8066 (1979).

16. R.M. Hazen and L.W. Finger, Comparative crystal chemistry, J.S. Wiley, NewYork (1981).

17. F.A. Hummel, Thermal expansion properties of natural lithia minerals, Foote prints, 20, 3-11 (1948).

18. J.P. Boilot, J.P. Salanic, G. Desplancer and D.L. Potier, Mater. Res. Bull., 14, 1469-1477 (19).

19. J. Alamo and R. Roy, Ultra low-expansion ceramics in the system Na_2O-$ZrO_2P_2O_5$-SiO_2, J.Am.Ceram.Soc., 67, C78-79 (1984).

20. R. Roy, D.K. Agrawal and J. Alamo and R.A. Roy, [CTP]: A new structural family of near-zero expansion ceramics, Mater. Res. Bull., 19, 471-477 (1984).

21. D.K. Agrawal and V.S. Stubocan, Synthesis and sintering of $Ca_{0.5}Zr_2P_3O_{12}$ -a low thermal expansion material, Mater. Res.Bull, 20, 199-106 (1985).

22. G.E. Lenain, H.A. McKinstry, S.Y. Limaye and A. Woodworld, Low thermal expansion of alkali-zirconium phosphates, Mater. Res.Bull, 19, 1451-1456 (1984).

23. F.A. Hummel, Electronic and newer ceramics, Chap V, VI, VII. Chicago: Industrial (1959).

24. Albert Einstein, Physics and reality, Journal of the Franklin Institute, 221 [3], 349-382 (1936).

25. E. Gruneneisen, Ann.Phys, 26, 211-218 (1908).

26. P. Debye, The early days of lattice dynamics, Lattice Dynamics, 9-13 (1965).

27. H.D. Megaw, The thermal expansion of crystals in relation to their structure, Kristallogr. Bd., 100, 58-76 (1938).

28. H.H. McKinstry, Thermal expansion of certain alkali halides and their solid solutions. PhD thesis, Penn State Univ., University Park, (1960).

29. H.D. Megaw, Crystal structures and thermal expansion, Mater.Res.Bull., 6, 1007-1018 (1971).

30. L.G. Van Uitert, H.M. O Bryan, M.E. Lines, H.J Guggenheim and G. Zydzik, Thermal expansion — An empirical correlation, Mater.Res.Bull, 12, 261-268 (1977).

31. L.G. Van Uitert, H.M. O Bryan, M.E.Lines, H.J Guggenheim and G. Zydzik, Correlation of the thermal expansion coefficients of rare earth and transition metal oxides and fluorides, Mater.Res.Bull., 12, 307-314 (1977).

32. L.G. Van Uitert, The effect of bond length and ionicity on the thermal expansion of tetrahedral semiconductors, Mater.Res.Bull., 12, 315-320 (1977).

33. L.G. Van Uitert, Relations between melting point, glass transition temperature and thermal expansion for inorganic crystals and glasses, J. Appl, Phys., 50, 8052-61 (1979).

34. R.M. Hazen and C.T. Prewitt, Effects of temperature and pressure on interatomic distances in oxygen-based minerals, Am.Mineral, 62, 309-315 (1977).

35. S.L. Kakani, Materials science,pp-403 ISBN (13) : 978-81-224-2656-4 (2002).

36. G. Bayer, Thermal expansion characteristics and stability of pseudobrookite compounds, Me3O5, J. Less. Common metals, 24[3] 129-138 (1971).

37. G. Bayer, Thermal expansion anisotropy of oxides compounds, Proc. Brit. Ceram. Soc. 22, 39-53(1972).

38. T. Ota and I. Yamai, Thermal expansion behaviour of NZP-type compounds, J.Am. Ceram, Soc. 69[1], 1-6 (1986).

39. J.J. Cleveland and R.C. Bradt, Grain size microcracking relations for pseudobrookites oxides, J.Am.Ceram.Soc. 76[2] 487-491 (1993).

40. F. Lazlo, Tensellated stresses, J. Iron Steel Inst. London, 147[1] 173-189 (1943).

41. W.R. Buessem and F.F. Lange, Residual stresses in anisotropic ceramics, Interceram, 15[3] 229-232 (1996).

42. R. McPherson, Intercrystalline thermal stressess in polycrystalline rutile, J. Aus .Ceram. Soc, 3[2], 43-52 (1967).

43. J.A. Kuszyk and R.C. Bradt, Influence of grain size on effects of thermal expansion anisotropy in $MgTi_2O_5$, J. Am. Ceram.Soc., 56[8], 420-423 (1973).

44. W.R. Buessem, N.R. Thielke and R.V. Sarakauskas, Thermal expansion hysteresis of Al_2TiO_5, Ceramic Age, 60[5], 38-40 (1952).

45. H.J. Siebeneck and D.P.H. Hasselman, J.J. Cleveland and R.C. Bradt, Effect of microcracking on the thermal diffusivity of Fe_2TiO_5. J. Am. Ceram. Soc. 59 [5-6], 241-246 (1976).

46. S. Lang, C. Fillmore and L. Maxwell. The system berlia-alumina-titania: Phase relation and General physical properties of three components porcelain (1952).

47. D. Golberg, On the systems formed by alumina with several trivalent and tetravalent metal oxides, in particular titanium oxide, Rev. Int. Hautes Temp. Refract., 5, 181-194 (1968).

48. B. Morosin and R.W. Lynch, Structure studies on Al_2TiO_5 at room temperature and at 600°C, Acta cryst B, 28, 1040-1046 (1972).

49. R.D. Skala, D. Li and I.M. Low, Diffraction, structure and phase stability studies on aluminium titanate, J. Euro. Ceram. Soc. 29, 67-75 (2009).

50. C.E. Holcombe and A.L. Coffey, Calculated X-Ray Powder Diffraction Data for β-Al_2TiO_5, J. Am. Ceram. Soc. 56 [4] 220 -221(1973).

51. T. Epicier, G. Thomas, H. Wohlfromm and J. Moya, High resolution electron microscopy of the cationic disorder in Al_2TiO_5,. J. Mater. Res. 6 [1] 138-145 (1991).

52. H. Thomas and R. Stevens. Alumina Titanate - A Literature review. Part. Engineering properties and thermal Stability; Br. Cer. Trans. J. 88, 184-190 (1989).

53. I.J. Kim, Thermal stability of Al_2TiO_5 ceramics for new diesel particulate filter applications- A literature review, J. Ceram. Pro. Res. 11[4] 411-418 (2010).

54. S.M. Meybodi, H.B. Bafrooei, T.Y. Ohya and Z. Nakagawa, Grain boundary microcracking due to thermal expansion anisotropy in aluminium titanate ceramics, J. Am. Ceram. Soc., 70 [8], 184-186 (1987).

55. Y. Ohya and Z. Nakagawa, Grain boundary microcracking due to thermal expansion anisotropy in aluminium titanate ceramics, J. Am. Ceram. Soc., 70, 184-186 (1987).

56. L. Stanciu, J.R. Groza, M. Zaharescu, Microstructural investigations on Aluminum titanate ceramics (1965).

57. Y. Ohya, Measurement of crack volume by using dilatometer, J. Mater. Sci., 31, 1555-1559 (1996).

58. D.P. Hasselman and J.P. Singh, Analysis of thermal stress resistance of microcracked Brittle Ceramics, Bull. Am. Cer. Soc. 58 [9], 856-860 (1979).

59. M. Milosevski, O. Ondracek, R. Milisevska, D. Spaseska and A. Dimeska, Thermal expansion and mechanical properties of Al2TiO5 – SiO2 system. Ceramics Charting The Future. (Edit. P. Vicenzini, Techna Srl.) 1875-1882 (1995).

60. M. Milosevski, Thermal diffusivity of Al_2TiO_5, $CaTiO_3$ and $BaTiO_3$, Science of Sintering, 29 [2] 105-112 (1997).

61. P. Stingl, J. Heinrich and J. Huber, Proceedings of the 2nd International Symposium of ceramic Materials and Component Engines, Lübeck - *Travemunde (FRG)* April (1986). (Ed) W. Bunk and H. Hausner. DKG Bad Honned 369.

62. J. Zabickyl, G. Kimmel, J. Yaaran and L. Zevinl, Thermal anisotropy of tialite (Al_2TiO_5) by powder XRD, Peragmon nano str. Matls., 6, 675-678 (1995).

63. J. Adler, Ceramic Diesel Particulate Filters, Int. J. Appl. Ceram. Technol., 2 [6], 429–439 (2005).

64. S. Ogunwumi, P. Tepesch, T. Chapman, C. Warren, Aluminum titanate compositions for diesel particulate filters, SAE. Int., doi:10.4271/2005-01-0583 (2005).

65. T. Boger, J. Jamison, J. Warkins, N. Golomb, C. Warren and A. Heibel, Next generation aluminum titanate filter for light duty diesel applications, SAE. Int., doi:10.4271/2011-01-0816 (2011).

66. C.H. Chen and H. Awaji, Temperature dependence of mechanical properties of aluminium titanate ceramics, J. Eur. Ceram. Soc., 27, 13-18 (2007).

67. C.E. Holcombe and G.L. Powell, The reaction of alumina titanate crucibles with molten uranium, J. Nuc. matls., 49, 238-240 (1973/74).

68. Bender and B. Jeffrey, NASA technical report, 20050186595, (2004).

69. C.H. Law and S.W. Sofie, Anchoring of infiltratred nickel electro-catalyst by addition of aluminum titanate, ECS Transactions, 28[11], 217-226 (2010).

70. Y.B. Matus, L.C. De Jonghe, C.P. Jacobson and S.J. Visco, Metal-supported solid oxide fuel cell membranes for rapid thermal cycling, Solid State Ionics 176, 443–449 (2005).

71. J.L. Bachmann, Investigations of properties of aluminium oxide and some aluminuos materials, Ph.D Thesis, Pennsylvania State University (1948).

72. A.E. Austin and C.M. Schwartz, The crystal structure of aluminium titanate. Acta Crystallogr., 6, 812–813 (1953).

73. K. Hamano, Y. Ohya, and Z. Nakagawa, Crack propagation resistance of aluminium titanate ceramics, Int. J. High. Tech. Ceram., 1[2] 129–137 (1985).

74. Y. Ohya, Z. Nakagawa and K. Hamano, Crack healing and bending strength of aluminum titanate ceramics at high temperature, J. Am. Ceram. Soc., 71[5], C 232-233 (1988).

75. H. Wohlfromm, T.S. Moya and P. Pena, Effect of $ZrSiO_4$ and MgO Additions on reaction sintering and properties of Al_2TiO_5 based materials. J. Mater. Sci., 25, 3753-3764 (1990).

76. H.A.J. Thomas, R. Stevens and E. Gilbart, Effect of zirconia additions on the reaction sintering of aluminum titanate, J. Mater Sci., 26, 3613-3616(1991).

77. S. Djambazov, D. Lepkova and I. Ivanov, A study of the stabilization of aluminium titanate, J. Mater. Sci, 29, 2521-25(1994).

78. V. Buscaglia, P. Nanni, G. Battilana, G. Aliprandi and C. Carry. Reaction sintering of Aluminium Titanate: I - Effect of MgO addition, J. Euro. Ceram. Soc., 13, 419-426 (1994).

79. R.W. Grimes and J. Pilling, Defect formation in Al_2TiO_5 and its influence on structure stability. J. Mater. Sci., 29, 2245–2249 (1994).

80. V. Buscaglia, P. Nanni, G. Battilana, G. Aliprandi and C. Carry. Reaction sintering of aluminium titanate: I - Effect of different alumina powder, J. Euro. Ceram. Soc., 13, 419-426 (1994).

81. V. Buscaglia, F. Carracciolo, M Leoni, P Nanni, M Viviani, and J Lematre, Synthesis, Sintering and Expansion of $Al_{0.8}Mg_{0.6}Ti_{2.1}O_5$ Low thermal expansion material resistent to thermal decomposition, J. Mater. Sci., 32, 6525-6531 (1997).

82. E. Kato, K. Daimon, and J. Takahashi, Decomposition Temperature of β- Al_2TiO_5, J.Am. Ceram. Soc,. 63, 355-356 (1980).

83. A. Navrostky, Thermodynamics of formation of some compounds with the pseudobrookite structure and of the $FeTi_2O_5$-Ti_3O_5 solid-solutions series, American Mineralogist 60, 249-256 (1975).

84. T.S. Liu and D.S. Perera, Long-term thermal stability and mechanical properties of aluminium titanate at 1000-1200C, J.Mat.Sci, 35, 995-1001(1998).

85. M. Nagano, S. Nagashima, H. Maeda and A. Kato, Sintering behavior of Al_2TiO_5 base ceramics and their thermal properties, Ceram Int., 25, 281-289 (1999).

86. M. Tahazaksi, M. Fukuda, H. Fukuda and T. Yoko, Preparation, structure, and properties of thermally and mechanically improved aluminium titanate ceramics doped with alkali feldspar, J. Am. Ceram. Soc., 85 [12], 3025-30 (2002).

87. A. Tsetsekou. A comparison study of tialite ceramics doped with various oxide materials and tialite–mullite composites: microstructural, thermal and mechanical properties, J. Euro. Ceram. Soc. 25, 335–348 (2005).

88. I. M. Low, Z. Oo and B. H. O. Connor, Effect of atmospheres on the thermal stability of aluminium titanate, Physica B., 385–386 [1] 502-504 (2006).

89. H. C. Kim, K. S. Lee, O. S. Kweon, C. G. Aneziris and I. J. Kim. Crack healing, reopening and thermal expansion behavior of Al_2TiO_5 ceramics at high temperature, J. Euro. Ceram. Soc., 27, 1431-1434 (2007).

90. P. Oikonomou, Ch. Dedeloudis, C.J. Stournaras, Ch. Ftikos, Stabilized tialite-mullite composites with low thermal expansion and high strength for catalytic converters, J. Euro. Ceram. Soc., 27, 3475-82 (2007).

91. D. Rose, O.A Pittner, C. Jaskula, T. Boger, T. Glasson and V.M. Da Costa, On road durability and field experience obtained with an aluminum titanate diesel particulate filter, SAE Technical papers (2007).

92. T. Boger, D. Rose, I. Tilgner, A.K Heibel, Regeneration strategies for an enhanced thermal management of oxide diesel particulate filters, SAE Technical papers (2009)

93. R. Naghizadeh and H. R. Rezaie, The influence of composition, cooling rate and atmosphere on the synthesis and thermal stability of aluminium titanate, Mater Sci & Engg B., 157, 20-25 (2009).

94. T. Korim. Effect of Mg^{2+} and Fe^{3+} ion on formation mechanism of aluminum titanate, Ceram. Int., 35, 1671-1675 (2009).

95. G. Naderi, H. R. Rezaie, S.F. Ali, R. Naghizadeh and S. Atashgar, The effect of talc on the reaction sintering, microstructure and physical properties of Al_2TiO_5 based ceramics, J. Ceram. Process. Res., 10[1] 16-20 (2009).

96. Y. Djambazo and A. Hristo, Effect of SiO_2 addition on thermal hysteresis of aluminum titanate, J. University of Chemical Technology and Metallurgy 45[3] 269-274 (2010).

97. G. Bruno, A. Efremov, B. Wheaton, I. Bobrikov, V. G. Simkin and S. Misture. Micro- and macroscopic thermal expansion of stabilized aluminium titanate, J. Euro. Ceram. Soc., 30, 2555–2562 (2010).

98. I.M. Low and Z.Oo, Reformation of phase composition in decomposed aluminium titanate, Mater. Chem. & Phy., 111, 9–12 (2008).

99. I.M. Low and W.K. Pang, In situ diffraction study of self-recovery in vacuum decomposed Al_2TiO_5, J. Aus. Ceram. Soc. 49[1] 48 – 52 (2013).

100. J. Lan, C. Xiao-Yan, H. Guo-Ming and M. Yu, Effect of additives on properties of aluminium titanate ceramics, Trans. Nonferrous Met. Soc. 21, 1574-1579 (2011).

101. Iwasaki and T. Shibuta, Durability investigation on aluminum titanate-diesel particulate filter having asymmetric hexagonal cell design, SAE Technical papers (2013).

102. D. Rose, J.A. Jamison, T. Boger and R. Kataria, Light duty diesel exhaust gas after treatment challenges and technologies for post BS-IV regulations, SAE Technical papers (2013).

103. T. Boger, D. Rose, I.C. Tilgner and A.K. Heibel, Regeneration strategies for an enhanced thermal management of oxide diesel particulate filters, SAE Technical papers (2013).

Chapter- II

Synthesis and Physico-Chemical Characterization of Aluminum Titanate

2.0 Introduction

Present chapter deals with various routes followed for the synthesis of aluminum titanate (Al_2TiO_5) ceramics. The various synthesis routes that is followed as been discussed and the various methods are ranked based critical attributes. Out of various methods ranked, solid state synthesis is found to be more adaptable and followed below as described.

2.1 Synthesis of Aluminum Titanate

2.1.1 Solid-State Reaction

This conventional processing is most direct method for preparing the multi-component mixed oxide ceramic system. This process mainly involves mixing of raw materials according to the stoichiometric ratio and solid-state reaction at desired temperature to form the phase pure oxides. The solid-state reactions typically result in the formation of aggregates (hard agglomerations) that require a milling process to reduce the particle size to the submicron level. Though homogeneity and purity of the powder are issues, this conventional process has still been widely used in industry for producing ceramic powders due to its simplicity and low cost. Conventionally, Al_2TiO_5 powders are prepared by solid-state reactions in a mixture of Al_2O_3 and TiO_2 powders in stoichiometric proportions. The Al_2O_3 - TiO_2 equilibrium phase diagram studied by Lang et al.[1] which has already been discussed in the previous chapter (Fig 1.2). The mole fraction of Al_2O_3 : TiO_2 for the stoichiometric composition of 0.56:0.44. As discussed, the phase diagram shows the existence of two allotropic forms of aluminum titanate: α- Al_2TiO_5, a high temperature

---

- **Part of the work being published in International Journal of Applied Ceramic Technology (JACT), DOI: 10.1111/ijac.12092, (2013)1-10.**
- **Part of the work being published in Journal of Ceramics, 214794, (2013)1-9.**
- **Secured second best in paper presentation in 76th Annual session of Indian Ceramic Society (ICS), 2013.**

phase, stable between 1820°C and the melting point at 1860±10°C and β-Al_2TiO_5, a low temperature phase stable from room temperature up to ~ 750°C and from 1300°C up to inversion temperature 1820°C (at intermediate values, it has instability and decomposes to Al_2O_3 + TiO_2).

Several attempts have been made for the solid state synthesis of Al_2TiO_5. Busgalia et al. [2] synthesized aluminum titanate from titania (particle size-1µm, rutile phase powders) and alumina with varying specifications. Alumina (particle size of 1µm, α-phase) and reactive alumina (particle size=0.5µm, γ- phase) were used as precursor oxides. Precursor compacts of alumina (α -phase) with particle size of 1µm, resulted in high green density of 62% of theoretical density (TD) but alumina powders(γ- phase) with particle size of 0.5µm, resulted in a very low green density of 47% TD. Authors attributed the low green densities observed with reactive alumina to the agglomeration during mixing. Compacts, with green densities of 62 % and 47 % of TD, on sintering in a conventional furnace at 1550°C for 6 hours have resulted in sintered densities of 83% and 66% TD respectively. Lower sintered densities at 1550°C were attributed to the offset of sintering by the volume expansion by Al_2TiO_5 formation.

Takahasi et al. [3] studied Al_2TiO_5 ceramic formation from alumina (α-phase) and titania (rutile phase). The precursors oxides are molded under pressure of 60 MPa. TG-DSC phase formation studies with green bodies indicated Al_2TiO_5 phase formation temperature at 1384°C. The green bodies are further sintered in conventional sintering furnace at peak temperature of 1600°C for 2 hours duration. The sintered bodies exhibited a sintered density of 83.64%TD. The authors attributed low sintered samples mainly due to volume expansion and extensive microcracking.

Kim et al. [4] prepared aluminum titanate from alumina (purity-99.5%) and titania (purity-99%). The precursor mixture were calcined at 1000 °C for 1 hour duration followed by pulverised to a particle size of 3-5µm. The calcined powders were further made into compacts at 150 MPa pressure. The green compacts were sintered at 1600°C for 6 hours duration in conventional sintering furnace. The sintered samples reported to have a 93.2% TD. The relatively higher sintered density of 93.2%TD in comparison to earlier reported studies could be due to initial calcination and extensive duration of solid state reaction.

2.1.2 Co Precipitation From Solution

Co-precipitation from the precursor sol solution is one of the well practiced wet chemical techniques for the preparation of ceramic oxides. It consists of preparation of an aqueous solution and using a precipitating agent. The precipitated product is separated from the liquid by filtration, dried and further thermally decomposed to the desired compound. Several parameters, such as pH, mixing rates, temperature and concentration have to be controlled to produce satisfactory results. The composition control, purity and morphology of the resulting products are reported to be good. However, different rates of precipitation of each individual compound may lead to microscopic inhomogeneity and agglomerates are generally formed during calcination, as with other solution techniques. By controlling the synthesis conditions, this method can produce stoichiometric ceramic powders of high purity and fine particle size at a relatively moderate cost and is currently applied widely to make ceramic powders.

Thomas et al. [5] synthesized aluminum titanate powder by co-precipitation. An ultra fine mixture of alumina and titania is prepared by coprecipitating the combined isopropoxides into a water/alcohol solution. The dried co-precipitate powder was calcined at 950°C, which resulted in equimolar mixture of α-alumina and titania (rutile phase). The powders were compacted by wet bag isopressing at 200 MPa. Sintering studies of compacts were done by using a dilatometer at a heating rate of 5°C min^{-1} upto 1500°C. The dilatometric curve have not formed a plateau signifying lower final density.

Nagano et al. [6] reported co-precipitation of aluminum titanate powder. Al_2TiO_5 precursor was obtained by a co-precipitation of the sulfates ([$Al_2(SO_4)_3$ and [$TiOSO_4$]) in the proportion of 1:1 and with addition of NH_4OH solutions. The precipitate was rinsed and dried in a vacuum at 70°C and was calcined in air at 1000°C for duration of 1 hour. The calcined powders were compacted and sintered at 1500°C, resulted in 92%TD and complete Al_2TiO_5 phase formation. Authors emphasized the importance of calcination temperature of aluminium titanate powder.

2.1.3 Combustion Synthesis

Combustion synthesis process is used to produce homogeneous, very fine, crystalline and unagglomerated multicomponent oxide ceramic powders, without any intermediate decomposition and/or calcining steps. The method exploits an exothermic, usually very rapid and self sustaining chemical reaction between the desired metal salts and a suitable organic fuel, which is ignited at a temperature much lower than the actual phase transformation temperature.

Segadaes et al. [7] discussed the combustion synthesis of aluminium titanate powder. The aluminium titanate powder was made with $A1(NO_3)_2.9H_2O$ and $Ti[O.CH(CH_3)_2]_4$, as cation precursors, urea $CO(NH_2)_2$ as fuel and $NH_4.NO_3$ as combustion aid. The precursors were taken according to the stoichiometric ratio and melted in a wide-mouth vitreous silica basin by rapid heating up to ~300°C on a hot-plate. When the liquid thickened and began frothing, the basin was transferred to a muffle furnace preheated at 500°C where ignition took place. The combustion reaction lasted for less than 1 min. The as-prepared combustion reaction product was uniaxially pressed at ~500 MPa (60% relative green density) into pellets, which were then sintered in air at 1500°C (10ºC min^{-1}) for duration of 2 hours, in a Super Kanthal electric furnace. It was inferred by the authors that combustion synthesis yields very fine crystallite size which is responsible for low phase formation temperature. And also gave rise to highly dense fine-grained and single-phase polycrystals, thus reducing the tendency to microcracking and decomposition during fabrication.

2.1.4 Hydrothermal Synthesis

Hydrothermal synthesis is a process that utilizes single or heterogeneous phase reactions in aqueous media at elevated temperature (T>25ºC) and pressure (P>100 kPa) to crystallize ceramic materials directly from solution. However, researchers also use this term to describe processes conducted at ambient conditions. Syntheses are usually conducted at autogeneous pressure, which corresponds to the saturated vapour pressure of the solution at the specified temperature and composition of the hydrothermal solution. Upper limits of hydrothermal synthesis extend to over 1000ºC and 500 MPa pressure. Hydrothermal methods are more environmentally benign than many other synthesis methods, which can be attributed in part to energy conserving low processing temperatures, absence of milling, ability to recycle waste, and safe and convenient disposal of waste that cannot be recycled.

The low reaction temperatures also avoid other problems encountered with high temperature processes, for example poor stoichiometric control due to volatilization of components.

Zaharescu et al. [8] synthesized aluminium titanate by hydrothermal process. The required amount of aluminum isopropoxide and titanium isopropoxide was homogenized in propyl alcohol. The atomic ratio of Al : Ti was kept 2 : 1. The final solution was aged for 2 hours at 70°C, by refluxing under N_2 atmosphere. A definite amount of solution was transferred into a Teflon-lined pressure vessel, which was sealed and heated. Then solution was dried for the removal of the volatile compounds and water and subjected subsequently to hydrothermal treatment after adding the corresponding amount of water at the required pH. The hydrothermal treatment conditions are carried out at different temperatures 150°C and 190°C. The hydrothermal powder was recovered by filtration, then dried at 110°C for 12 hours. The sample treated at 190°C shown higher Al_2TiO_5 phase content than 150°C thermal treated powder. The samples are sintered at 1300°C exhibited 78.7% TD with 8.8% open porosity. Authors attributed the high porosity of the ceramic bodies to the high porosity of the precursor powders, by formation of the transient alumina during the thermal treatment, as well as by the aluminum titanate formation that has lower density as the initial oxides.

A relative comparison of process with respect to powder quality is shown in Table 2.1. Though there are several advantages for co-precipitation, hydrothermal and combustion synthesis techniques, there are issues related to scale up and processing. As the present study is aimed towards the development of few products followed by application. The solid state reaction, which is widely practiced on commercial scale is selected as standard for powder synthesis in the present study.

Table 2.1 Al_2TiO_5 Powder synthesis route comparison

Properties	Solid state	Co-precipitation	Combustion	Hydrothermal
Compositional control	excellent	excellent	excellent	excellent
Morphology control	moderate	excellent	excellent	excellent
Powder reactivity	poor	excellent	poor	excellent
Particle size (nm)	~1000	~100	~100	~100
Purity(%)	>99	> 99.5	> 99	> 99
Secondary calcination step (carbon removal)	no	no	yes	no
Status of development	commercialized widely used	commercialized	R&D/pilot scale	R&D/pilot scale

2.2 Experimental Procedure

2.2.1 Characterization of Alumina and Titania Precursor Oxides (Solid State Reaction)

Commercially procured alumina powder ($\alpha+\gamma$-Al_2O_3, Baikowski, France) and titania (TiO_2, Qualigens, India) were used for the processing of the specimens. The powders were characterized for phase analysis using X-ray Diffraction Technique (XRD) and particle size by Dynamic Light Scattering (DLS). Surface area of the powder has been analyzed using BET nitrogen adsorption method (BETSA) respectively. The details of the measurements are discussed below. The process was based on supplier specification with respect to chemical composition.

2.2.1.1 Phase identification by X-Ray Diffraction

Phase analyses of the as received powders were performed by X-ray diffraction (XRD) (Bruker AXS GmbH, Karlsruhe, Germany) using CuKα radiation in Bruker D8 Advanced system. The XRD system was equipped with LynxEye^{TM} (Bruker AXS) 1-dimensional compound silicon strip detector for high quality diffraction data. The powder samples were loaded on a non-diffracting sample holder placed in the Bragg-Brentano diffractometer setup.

The recorded XRD profiles (raw data) were normalized to 100% in each case. The background correction as well as Kα_2 stripping using Rachinger's method was performed prior to the phase analysis using search-match program with ICDD-PDF4+ database. Identification of the crystalline phase was based on comparison of the observed d-spacing and relative intensities with those of a reference material pattern compiled in the ICDD database.

The X-ray diffraction pattern for alumina and titania samples used in the present study are shown in Fig 2.1 (a) and (b) respectively. It is evident from the XRD patterns that the alumina powder sample shows α and γ phase of alumina with α-Al_2O_3 as a major phase. However, the XRD patterns of TiO_2 exhibited single phase of anatase.

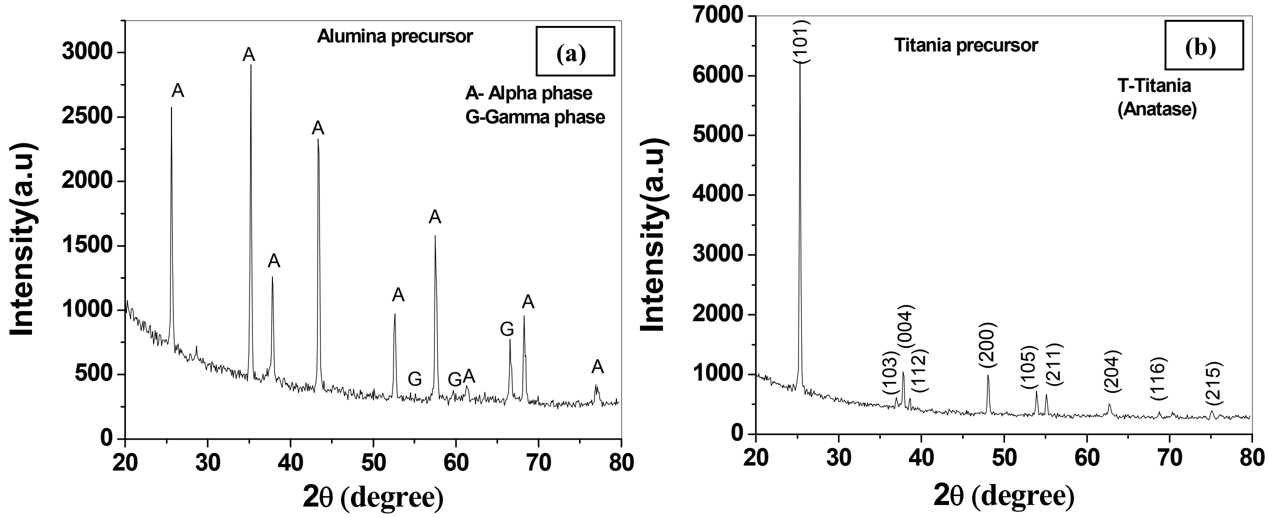

Fig 2.1 XRD Pattern of the (a) alumina and (b) titania samples

2.2.1.2 Particle size analysis by Dynamic Light Scattering

Particle size analysis of the as received powders was carried out using Photon Correlation Spectroscopic measurements. Photon Correlation Spectroscopy is based on the measurement of the velocity of particles diffusing due to Brownian motion. The random movement of particles in a liquid media due to the inter-particle collision is known as Brownian motion. This motion causes fluctuations of the local concentration of the particles resulting in local in-homogeneities in the refractive index of the material. This in turn leads to Rayleigh scattering spectrum with line width Γ (defined as the half-width at half-maximum), which is proportional to the diffusion coefficient D of the particles (2.1):

$\Gamma = Dk^2$ (2.1)

Where $k = (4\pi n/\lambda) \sin(\theta/2)$, n is the refractive index, λ the laser wavelength, and θ the scattering angle. Assuming the particles to be spherical and non-interacting, one can obtain the mean radius 'r' from the Stokes-Einstein equation (2.2):

$D = K_BT/(6\Pi\eta r)$ (2.2)

D – Diffusion coefficient, K_B-Boltzmann constant, T - absolute temperature, r – particle radius, and η – Coefficient of viscosity of the medium.

Particle size analysis was carried out by dispersing 0.05 gram of as received powder in 100 ml de-ionized water using dispersant Darvan 821A i.e., ammonium polyacrylate (R. T. Vanderbilt Co., Inc., Norwalk, CT, USA). Suspensions were ultrasonicated for 15 minutes using Sonics (VCX 750, Sonics & Materials Inc., Newtown CT, USA) to ensure the homogeneity and filled into the glass cuvette. The well dispersed suspensions, based on zeta measurements, were subjected to dynamic light scattering (DLS) measurements using a Nanosizer (Malvern, UK) and particle size distribution curve is shown in Fig 2.2 (a) and (b).

An average particle size of 315 nm with a particle size distribution ranging from 200 to 600 nm for alumina and an average particle size of 355 nm with a particle size distribution ranging from 150 to 550 nm for titania are exhibited by the measurements.

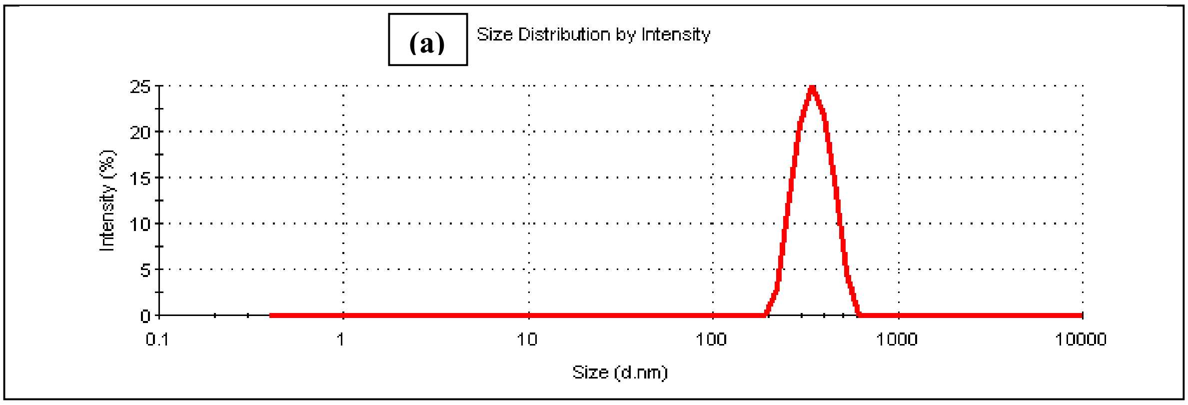

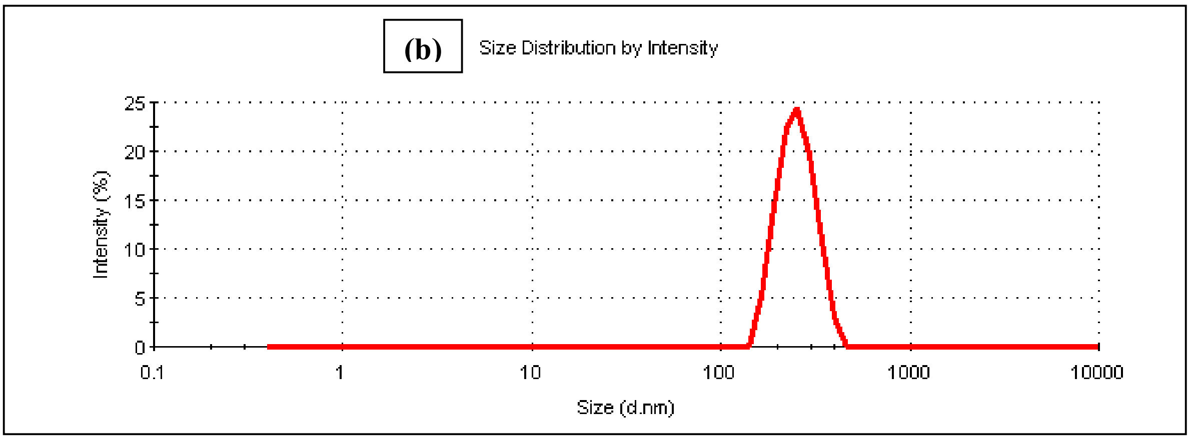

Fig 2.2 Particle size distribution curve (a) alumina and (b) titania samples

2.2.1.3 BET Surface area analysis

Surface area measurements were carried out by BET surface area analyzer (Micromeritics Instruments Corp, ASAP 2020, Norcross GA, USA), which works on the principle of static volumetric technique, introducing consecutive known doses of adsorbate (nitrogen) inside the sample holder kept at liquid nitrogen temperature (77K). This facilitates adsorption on sample surface once a dose of gas is injected, the pressure slowly decreases until an equilibrium pressure is established in the manifold.

BET theory is an extension of the Langmuir theory for monolayer molecular adsorption to multilayer adsorption with the following assumptions: (a) gas molecules physically adsorb on a solid surface in infinite layers; (b) there is no interaction between each adsorption layer. The resulting adsorption isotherm, known as **BET equation** as per the name of the Scientists, Brunauer, Emmett, and Teller, is expressed as (2.3):

$$\frac{1}{[Q(P_0/P-1)]}=\frac{C-1}{Q_mC}\left(\frac{P}{P_0}\right)+\frac{1}{Q_mC} \qquad (2.3)$$

Where, P and P_0 are the equilibrium and the saturation pressure of adsorbates at the temperature of adsorption, Q is the adsorbed gas quantity, and Q_m is the monolayer adsorbed gas quantity. C is the BET constant, which is expressed by the equation (2.4):

$$C=\exp\left(\frac{E_1-E_L}{RT}\right) \qquad (2.4)$$

E_l is the heat of adsorption for the first layer, and E_L is that for the second and consecutive layers and is equal to the heat of liquefaction.

Equation (2.3) is an adsorption isotherm and can be plotted as a straight line with 1 / Q [(P_0 / P) − 1] on the y-axis and φ = P / P_0 on the x-axis. This plot is called a BET plot. The linear relationship of this equation is maintained only in the range of $0.05 < P / P_0 < 0.35$. Relative pressure, quantity of nitrogen adsorbed and 1 / Q [(P_0 / P) − 1] obtained through BET analysis is shown in Table 2.2 (a) and (b) and the plot of 1/ [Q (P_0/P-1)] against (P/P_0) is shown in Fig 2.3.

Table 2.2 (a) Relative pressure, gas quantity adsorbed and 1 / Q [(P_0 / P) − 1] obtained from BET experiment of alumina powder

Relative Pressure (P/P_0)	**Gas quantity Adsorbed, Q (cm^3/g STP)**	**1/[Q(P_0/P-1)]**
0.066	4.62	0.015
0.082	4.8	0.188
0.107	5.05	0.023
0.13	5.28	0.028
0.155	5.5	0.033
0.178	5.7	0.038
0.203	5.92	0.043
0.227	6.13	0.048
0.251	6.33	0.053

Table 2.2.(b) Relative pressure, gas quantity adsorbed and $1 / Q\,[(P_0 / P) - 1]$ obtained from BET experiment of titania powder

Relative Pressure (P/P_0)	**Gas quantity Adsorbed, Q (cm^3/g STP)**	**$1/[Q(P_0/P-1)]$**
0.067	2.39	0.029
0.083	2.47	0.036
0.107	2.58	0.046
0.13	2.68	0.056
0.155	2.78	0.066
0.179	2.88	0.076
0.203	2.98	0.085
0.228	3.08	0.096
0.251	3.17	0.105

From the BET plot, the value of the slope A and the y-intercept I were estimated and the monolayer adsorbed gas quantity Q_m and the BET constant C were determined using the following equation (2.5 & 2.6):

$$Q_m = \frac{1}{A + I} \tag{2.5}$$

$$C = 1 + \frac{A}{I} \tag{2.6}$$

Further the total surface area S_{total} and a specific surface area S were evaluated by the following equations (2.7):

$$S_{BET,total} = \frac{(Q_m Ns)}{V} \tag{2.7}$$

where Q_m is in units of volume which are also the units of the molar volume of the adsorbate gas nitrogen

$$S_{BET} = \frac{S_{total}}{a} \tag{2.8}$$

N: Avogadro's number, (6.02×10^{23} mol^{-1})
s: adsorption cross section of the adsorbing species [$16(A°)^2$]
V: molar volume of nitrogen and a: mass of alumina and titania powders respectively (0.36g and 0.58g)

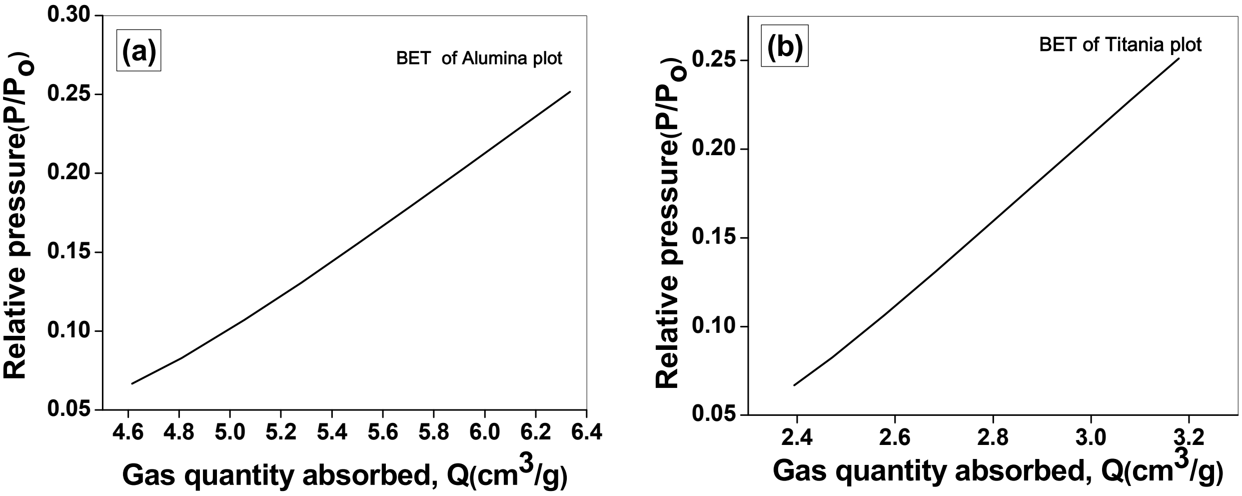

Fig 2.3 BET plots of (a) alumina and (b) titania samples

BET Surface area of the alumina and titania samples were estimated to be 21.3 m^2/g and 10.6 m^2/g respectively.

2.1.4 Chemical composition (Supplier specification)

Alumina used in the present study is 99.5% pure with 0.05% MgO and in case of titania powder it is 99% pure with minor quantity of Fe_2O_3.

2.2.2 Compaction Processing of AT precursors Powders

2.2.2.1 Preparation of AT precursors granules

Alumina and titania powder were accurately weighed and mixed according to the stoichiometry as per the reaction mentioned in equation [$\mathbf{Al_2O_3 + TiO_2 \longrightarrow Al_2TiO_5}$]. The precursor mix was blended with 2wt% PVA (Polyvinyl alcohol) with respect to the powder content and mixed homogeneously with 25% of water to form a semisolid mix. This semisolid mix, in a partially dry condition, are forced through a SS- 316 wire mesh of ASTM size (-) 30 and granules of the required size for compaction are extracted from the dried product by sieving using ASTM mesh size (-) 60 and (+) 100.

2.2.2.2 Design and fabrication of the Die

Engineering design of the die along with the dimensional details are shown in Fig 2.4 (a) and the actual die used for compaction is shown in Fig 2.4 (b).

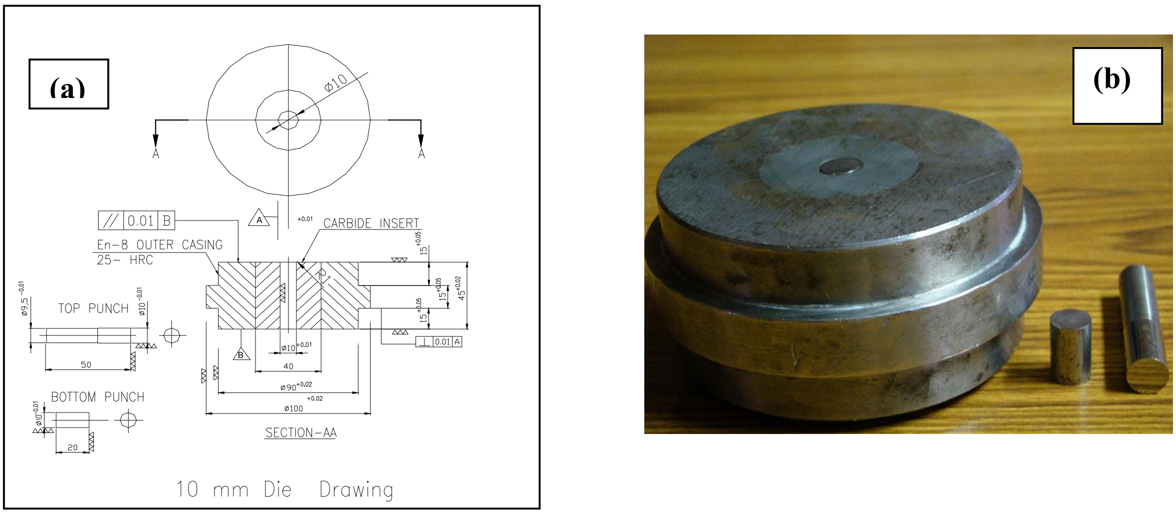

Fig 2.4 (a) Engineering drawing of the Compaction Die and (b) compaction die along with bottom and top punches

2.2.2.3 Compaction of the granules into pellets

Precursors granules were compacted inorder to study the insitu formation of AT and also the sinterability. Compaction experiments are carried out with 0.8 gm of the precursor granules filled in a compaction die. The compaction was carried out using hydraulic press (Peeco Industries, Calcutta) in Fig 2.5(a). Granules were compacted at a constant ram rate of 1mm/min under pressures varying from 300 to 700 MPa. The green pellets are shown in Fig 2.5(b) and green densities of the pellets were calculated by dimensional method.

Dimensions of the samples were measured using a digital Vernier caliper and weight of the pellets was determined using an analytical balance. Percentage theoretical density was calculated by the rule of mixtures. The compaction pressure and percentage theoretical density is presented in Table 2.3 and corresponding plots are given in Fig 2.5 (c). Table 2.3, shows the green density of the samples increases with the increasing compaction pressure.

Table 2.3 Compaction pressure, specimen dimensions and green density of the samples

Compaction Pressure (MPa)	**Dimensions (mm)**		**Weight (g)**	**Green density (g/cc)**	**Average green density (%TD)**
	Diameter	**Thickness**			
300	10.00	4.5	0.8	2.23	
		4.52	0.8	2.24	
		4.52	0.8	2.24	54.7
400	10.00	4.46	0.8	2.3	
		4.46	0.8	2.3	
		4.46	0.8	2.3	56.5
500	10.00	4.35	0.8	2.38	
		4.38	0.8	2.38	
		4.38	0.8	2.38	58.2
600	10.00	4.21	0.8	2.4	
		4.21	0.8	2.4	
		4.25	0.8	2.4	59.2
700	10.00	4.16	0.8	2.5	
		4.16	0.8	2.5	
		4.18	0.8	2.5	60.1

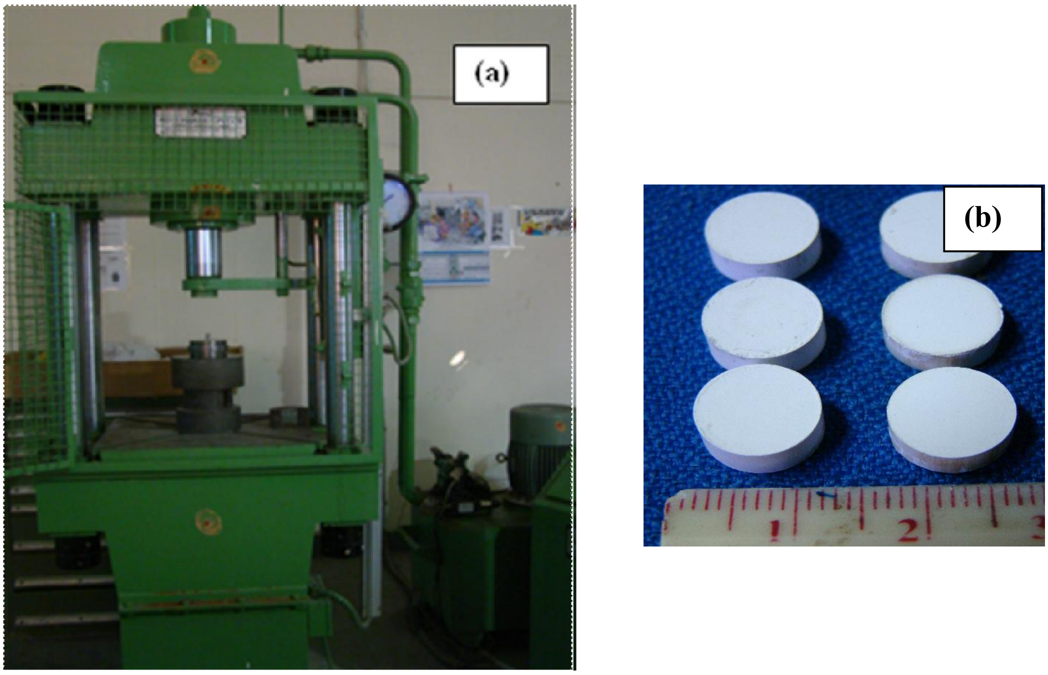

Fig 2.5 (a) Hydraulic press and (b) Green pellets

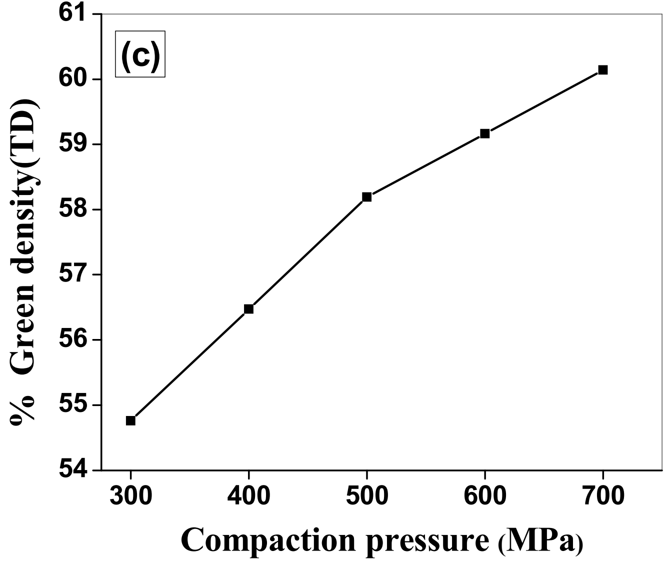

Fig 2.5(c) Compaction pressure versus % green density of AT precursors

2.2.3 Studies on Evolution of Al_2TiO_5 Phase Through Differential Scanning Calorimetry

Thermal analysis technique is widely used to characterize the thermal events that occur during thermal treatment of ceramic. This technique offers understanding on decomposition, crystallization and its associated exothermic and endothermic changes.

Generally, binder burnout plays an important role in achieving defect free ceramic components where STA are extensively used. In the present study, simultaneous thermal analyzer (STA 449 F3, Netzsch, Germany) is used for DSC analysis (Fig 2.6(a)). STA is provided with platinum heating element and S-type thermocouple for sensing the temperature.

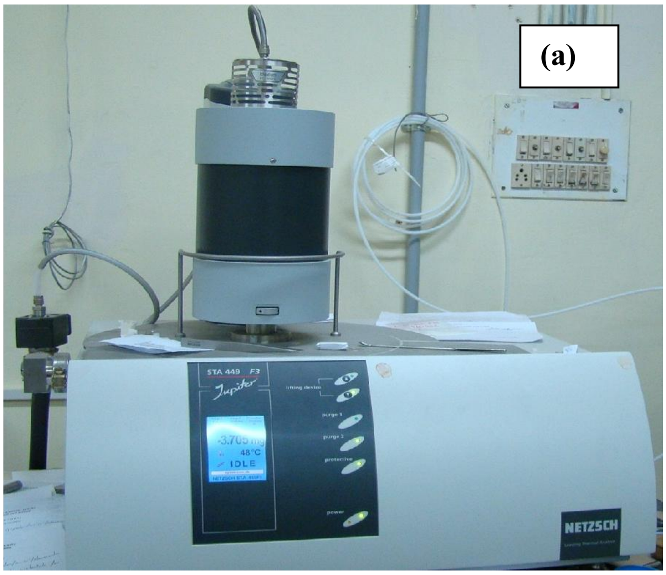

Fig 2.6(a) STA thermal analyser used for investigating the thermal changes of the AT precursor

For conducting the analysis 67.045 mg of the AT precursor was placed in an alumina crucible and heated from room temperature to 1550 °C at a heating rate of 5°C/min. The purge gas used was nitrogen for protecting heating elements during reactions, at a flow rate of 50 ml per min.

DSC curves recorded on the green compacts from room temperature to 1550°C is shown in Fig 2.6(b). It is evident that (Fig 2.6(b)) the evolution of endothermic DSC peaks around 780°C may be due to metastable low temperature anatase phase transformation into the more stable rutile form. Another DSC peak at 1070°C corresponds to cubic γ-alumina to hexagonal α-alumina as the initial raw material contains 15-20% of γ-phase. After this transformation there is a major endothermic DSC peak at 1356°C due to solid state reactions leading to the formation of Al_2TiO_5 phase. Beyond 1400°C there are no further major thermal events.

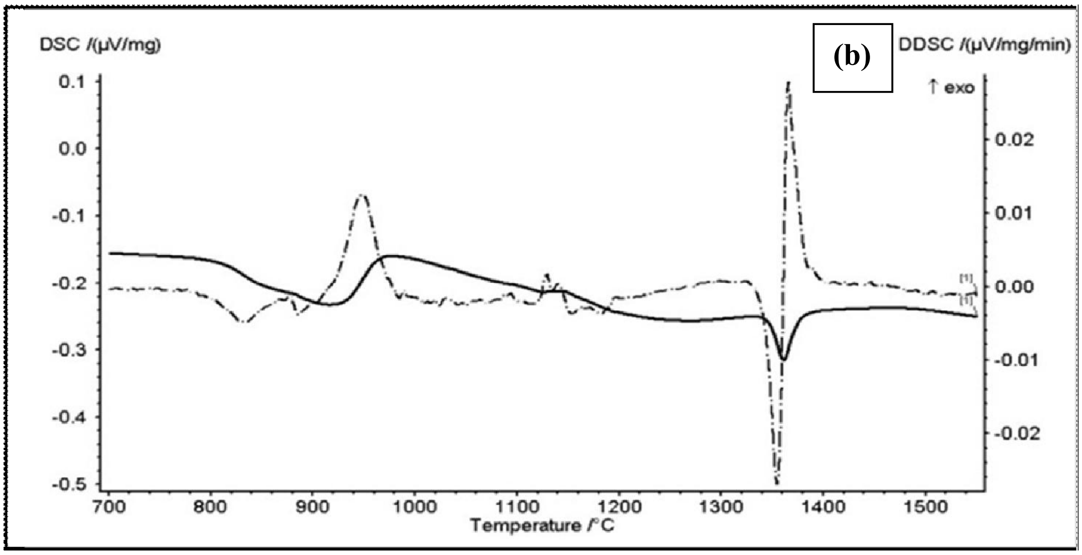

Fig 2.6(b) DSC curves of the Al_2TiO_5 precursor green samples

2.2.4 Formation and Densification of Al_2TiO_5

2.2.4.1 Formation and densification of Al_2TiO_5 through Dilatometric studies

Dilatometric analysis are carried out essentially to track sintering behaviour of green bodies which signifies slope changes in the appropriate sintering regions. In the present study, single pushrod dilatometer (Model No. 402C, Netzsch, Germany) was used for the analysis. The furnace is provided with graphite heating element and S-type thermocouple with sample temperature control. Aluminum titanate precursor pellets made into dimensions of 10 mm diameter and 5 mm thickness were subjected to dilatometric measurements (ASTM E228-11).

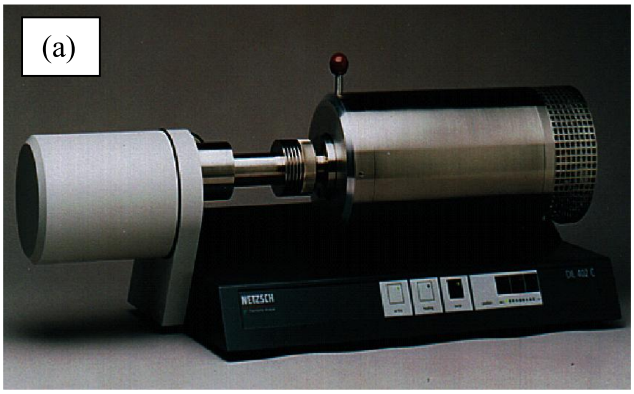

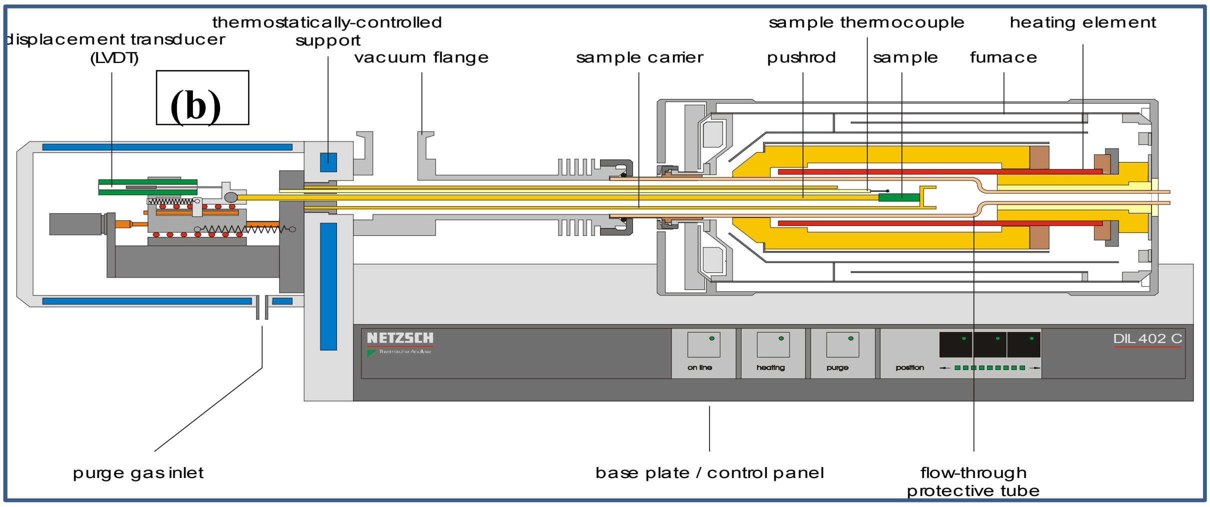

Fig 2.7 (a) Dilatometer and (b) Schematic (cross-section) diagram of dilatometer used for the measurements

Photograph and schematic (cross-section) diagram of the components of the dilatometer are presented in Fig 2.7 (a) and (b) respectively. Sintering curves for AT precursors was recorded from room temperature to 1550°C at a heating rate of 5°C/min. Alumina sample holder was calibrated and single pushrod was employed for the measurements.

Sintering curve (Fig 2.8) shows the start of sintering shrinkage around 1100°C, which reach a maximum followed by a significant expansion corresponding to Al_2TiO_5 formation and it is more evident with the first derivative presented in Fig 2.8. These observations compliments with DSC events observed at 1070°C and 1356°C.

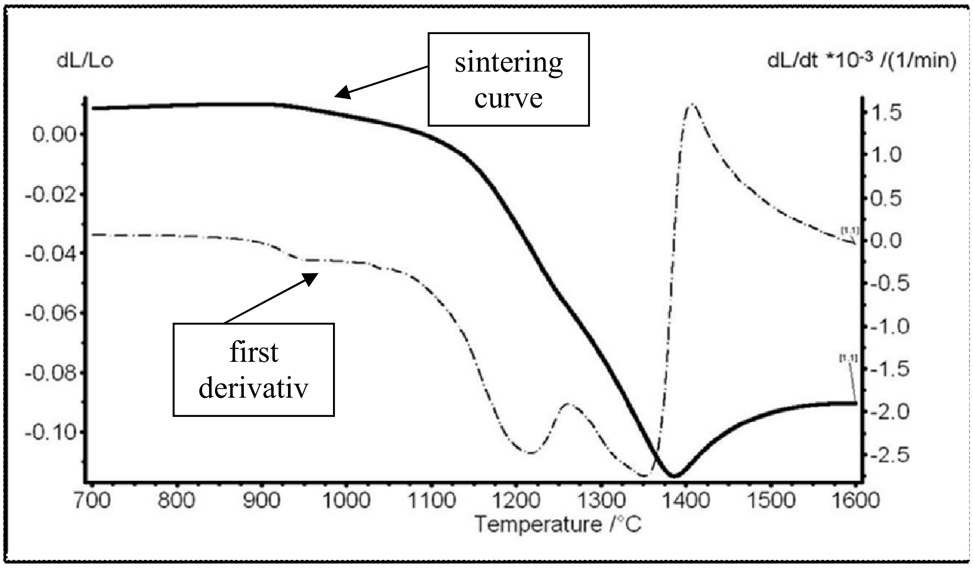

Fig 2.8 The dilatometric curve of the Al_2TiO_5 precursors green samples

2.2.4.2 Sintering of compacts by Conventional ramp hold (CRH)

The green pellets compacted from AT precursors granules were subjected to sintering in a high temperature furnace PID controller with molybdenum disilicide heating elements (Nabertherm, Germany). Sintering schedule employed for the samples are shown in Fig 2.9 ((a)-(c)).

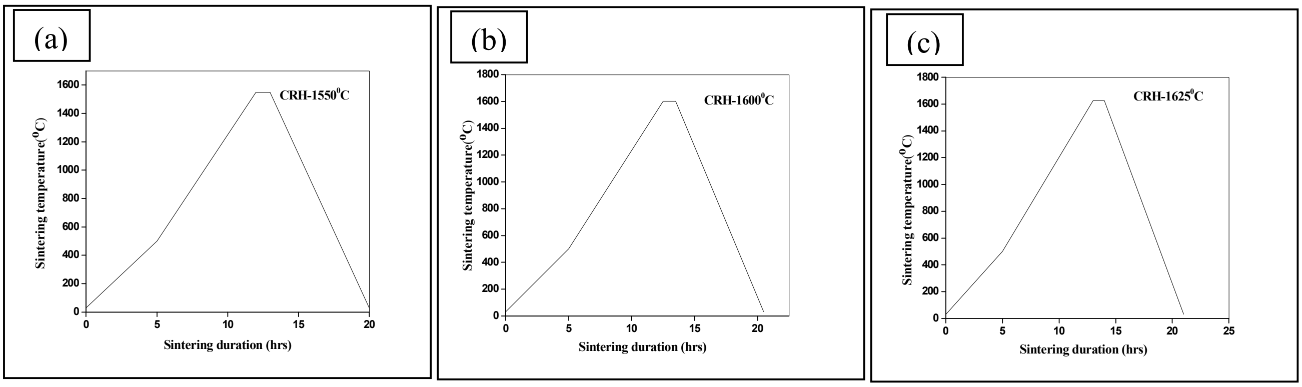

Fig 2.9 Sintering schedule profiles employed to sinter Al_2TiO_5 precursor pellet by CRH sintering method (a) 1550°C, (b) 1600°C and (c) 1625°C

The low ramp rate of 90^{o}C/hour was adopted up to 500^{o}C so as to remove the binder effectively without leading to the distortions of the sample. Further the heating rate is increased to 150^{o}C/hour till it reaches a temperature of 1400, 1500, 1550, 1600 and 1625°C and further the samples were soaked for 1 hour at each temperature.

2.2.5 Characterization of Sintered Compacts

The sintered pellets formed from AT precursors were characterized for their phase formation, critical properties such as density, porosity, water absorption and grain size analysis as discussed below.

2.2.5.1 X-ray diffraction studies

Fig 2.10 (a) shows the X-ray diffraction patterns (XRD) of precursor oxides heat treated at 1400, 1500, 1550, 1600 and 1625°C and the corresponding phase evolution is shown in Fig 2.10 (b).

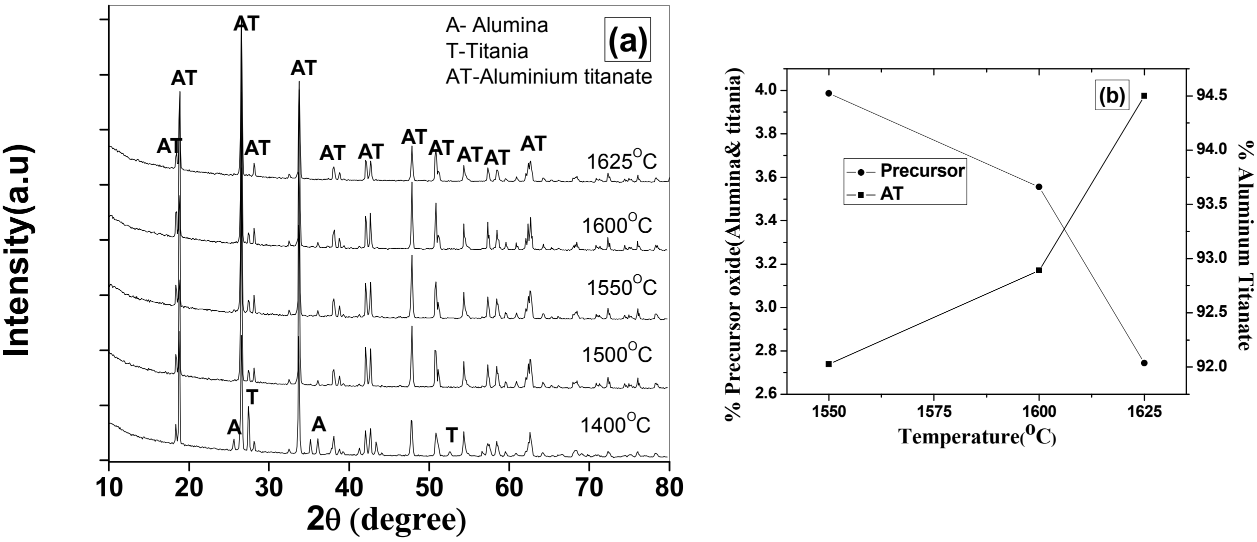

Fig 2.10 (a) X-ray diffraction patterns of alumina and titania specimens sintered at 1400, 1500, 1550, 1600 and 1625°C and (b) variation of Al_2TiO_5 phase content

Temperatures below 1500°C, Al_2TiO_5 (designated as AT) formation is significantly low indicating necessity of high temperatures of 1550, 1600 and 1625°C for the phase formation. It is clear that as the temperature increases from 1550°C to 1625°C, Al_2TiO_5 phase increased from 92 to 95% .

2.2.5.2 Bulk density, porosity and water absorption measurements

The determination of the density of the sintered pellets is based on Archimedes principle using water as medium. Bulk density, porosity and water absorption of the sintered sample was measured by adopting the ASTM C73 procedure using an analytical balance with density measuring kit. The weight of the samples were first taken in air (D) followed by boiling the same sample in distilled water for about 40 min. The samples were cooled to room temperature. The saturated weight (W) and the suspended weight in water (S) were measured accurately. The bulk density, water absorption and percentage porosity were calculated using following formulae:

Bulk Density = D/(W-S)

Water Absorption = (W-D)/D

Apparent Porosity = (W-D)/(W-S)

Table 2.4 Sintering parameters and results of the CRH sintered Al_2TiO_5 samples

Specimen Identity	**Sintering temperature (°C)**	**Dwell Time (hr)**	**Density (g/cc)**	**%TD**	**Porosity (%)**	**Water absorption (%)**
1 2 3	1550	1	3.15 3.15 3.154 **3.152**	**85.1**	**16**	**5.6**
1 2 3	1600	1	3.23 3.23 3.22 **3.226**	**87.3**	**11.9**	**4.1**
1 2 3	1625	1	3.14 3.14 3.16 **3.154**	**84.9**	**16.4**	**6.2**

The density, percentage theoretical density and porosity values of the samples sintered at 1550°C, 1600°C and 1625°C are shown in Table 2.4. It is evident (Fig 2.11) that a maximum percentage theoretical of 85 - 87 %, density in the temperature range of 1550 – 1600°C and a further decrease in the density to 84% on further increasing the sintering temperature to 1625°C is observed. This can be attributed to extensive microcracking present in the sample, which will be discussed in subsequent section.

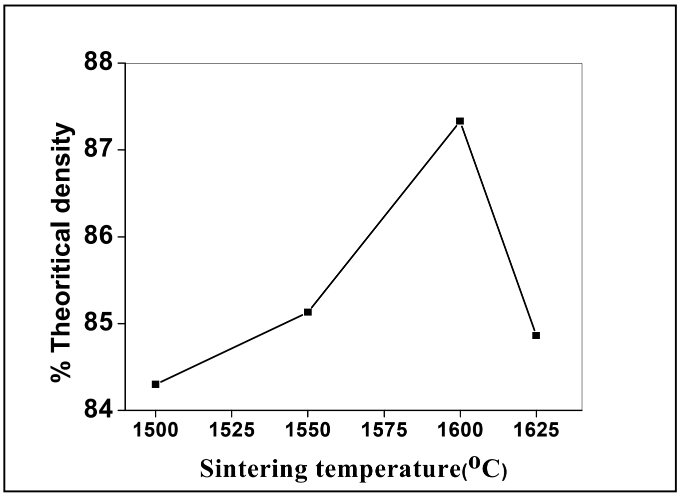

Fig 2.11 Dependence of density sintering temperature of Al_2TiO_5 specimens sintered by CRH sintering method

2.2.6 Microstructural Characterization

2.2.6.1 Ceramographic specimen preparation for microstructural characterization

The sample sintered at 1550ºC, 1600°C and 1625°C, which exhibited more than 90% Al_2TiO_5 phase, are studied for microstructural characterization. Ceramographic specimen preparation normally requires a specific sequence of operation such as sectioning, mounting, grinding, polishing and etching. Further to obtain an accurate interpretation of a microstructure the prepared specimen should be representative of the material being examined. Representative samples were cut from the parent piece of a sintered aluminium titanate samples using a diamond cutter (Isomet Model No. 11-1280-250, Buehler, Lake IL, USA.). The cut samples were coarse ground to remove deformation produced during sectioning and to make flat surface.

Mounting and polishing

The cut samples were mounted in acrylate based resin moulds. An automatic grinding and polishing machine (Struers, Tegraforce -5, Germany) used for grinding and polishing the sample. Mounted samples were placed in the sample holder and was ground using polishing disc of SiC grit size 120 µm and number of revolutions were fixed at 250 per minute The ground samples were further polished using diamond suspensions of 15, 9, 6, 3 and 1 µm particle size to achieve the required surface finish. The samples were cleaned and are examined under optical microscope for scratches, stains, and other imperfection.

Thermal etching

Polished samples were removed from the mount, cleaned with acetone and thermally etched at 150°C below sintering temperature with soaking time of 30 minutes in a laboratory furnace.

2.2.6.2 SEM Analysis

The polished and thermally etched Al_2TiO_5 samples were gold coated using ion sputtering device to make the sample electrically conductive. The samples were fixed onto the carbon tape, which is pasted on the sample holder. Silver paste was applied to minimize charging effects.

Microstructural analysis was carried out using FSEM at an accelerating voltage of 20kV at magnifications ranging from 2K - 20K. The micrographs of AT, with different sintering temperatures of magnification 5K are shown in Fig 2.12.

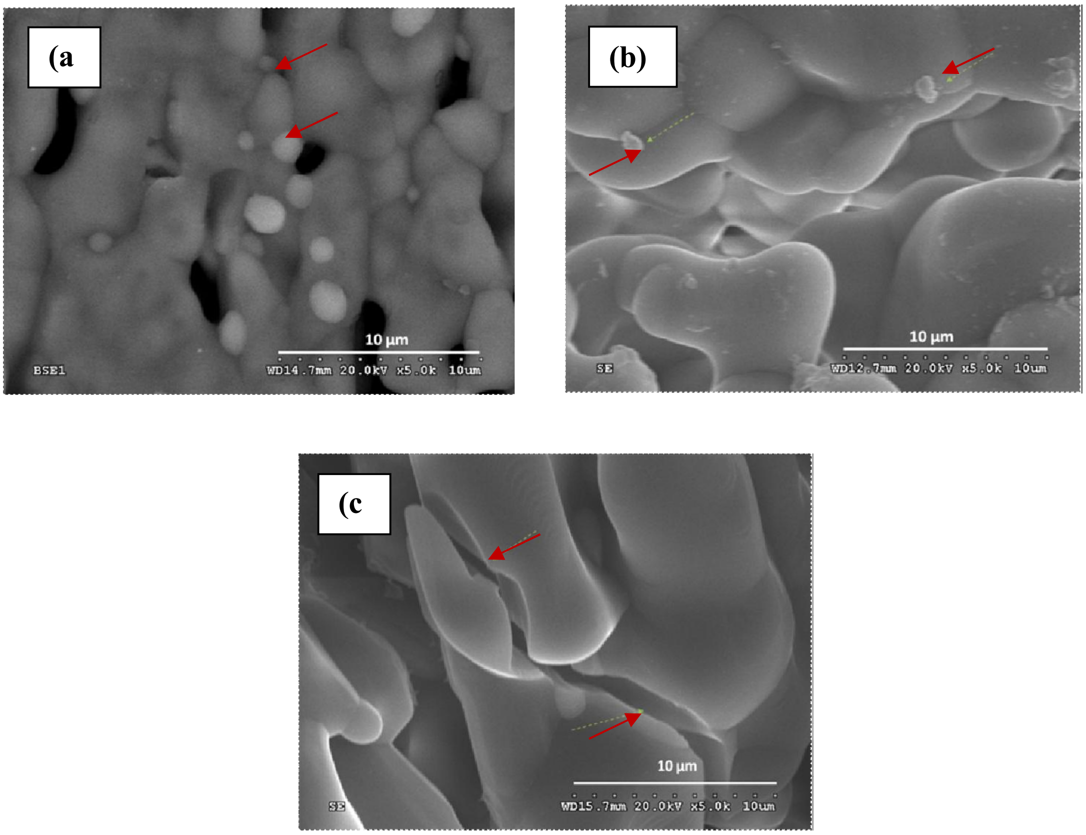

Fig 2.12 SEM Microstructure of the Al_2TiO_5 samples sintered at (a)1550°C, (b)1600°C and (c)1625°C (arrow marks indicates the microcracks)

Fig 2.12 (a)-(c) shows the microstructure of the samples sintered at 1550°C, 1600°C and 1625°C, respectively. The microstructure of samples sintered at 1550°C and 1600°C (Fig 2.12 (a)-(b)) exhibits porous structure with unreacted precursor oxides revealing the process progression towards the formation of AT through nucleation and growth of Al_2TiO_5 grains. There are traces of unreacted precursor oxide particles embedded along the grain and grain boundaries. It is obvious from the BSE image of 1550°C sintered sample, that the brighter ones corresponds to alumina grains and grey colored grains belongs to aluminum titanate, with small amount of dark grey titania grains, which is further confirmed by EDS analysis shown in Fig 2.12(a). As the temperature increases to 1625°C, precursor oxides completely disappear as is evident from the increase in percentage

Al_2TiO_5 phase (Fig 2.10). Table 2.5 shows the AT samples with their corresponding density and grain size with respect to the sintering temperatures. In addition to the above an increase in grain size and enhancement in microcrack density of are also evident for 1625°C sintered samples.

Table 2.5 The AT samples with their corresponding density and grain size

Sr.No	Sintering temperature(°C)	Density (g/cm^3)	Grain size (µm)
1	1550	3.1	3.8
2	1600	3.2	6
3	1625	3.1	7.1

2.3 Densification and Sintering Strategies

It is evident that the maximum density that could be achieved is only around 87 %. A close look at dilatometric sintering curve (Fig 2.8) reveals that dilatometric sintering of the $A1_2O_3 : TiO_2$ matrix starts at 1100°C and stops at 1400°C followed by an expansion related to Al_2TiO_5 formation. After the maximum temperature of shrinkage the expansion offsets the matrix densification which is the reason for the poor densification. Various approaches to address this issue of poor density are as follows:

(i) Sintering of pre-formed Al_2TiO_5 (solid state) powder

(ii) Sintering through selected additives in $A1_2O_3 : TiO_2$ matrix

2.3.1 Sintering of Preformed Al_2TiO_5 (solid state) Powder

Alumina and titania powder were accurately weighed and mixed according to the stoichiometry and homogeneously mixed with water to form a semisolid mix. The semisolid mix was calcined at 1400°C as per the formation temperature of DSC curve and further confirmed by XRD studies. The calcined powder in a partially dry condition are forced through a SS-316 wire mesh of ASTM size (-) 30 and granules of the required size for compaction are extracted from the dried product by sieving using ASTM mesh size (-)

60 and (+) 100. The samples are compacted under optimized conditions using die assembly and hydraulic press (Fig 2.5). The green compacts were subjected to sintering as per the best sintering schedule employed shown in Fig 2.13 (a). Bulk density, porosity and water absorption of the sintered sample (third) was measured by following the ASTM C73 standard described above and XRD analysis are shown in Fig 2.13 (b).

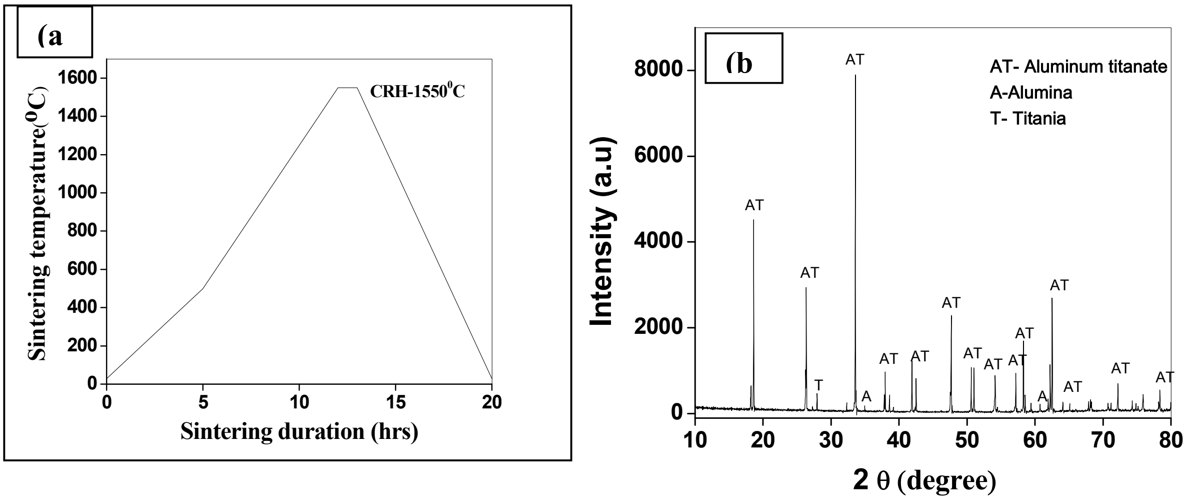

Fig 2.13 (a) Sintering schedule and (b) XRD pattern of Al_2TiO_5 preformed specimens

It is evident from the Table 2.6, though density was limited to 92.16% TD, needing alternatives route like additives which enhances the sintering. The XRD pattern of sintered AT preformed specimens, shows AT phase content about 97% (Fig 2.13(b)).

Table 2.6 Sintering parameters and results of the CRH sintered Al_2TiO_5 samples

Sr.No	Green density	Sintering temperature (°C)	Dwell Time (hr)	Density (g/cc)	%TD	Porosity (%)
1	51.3	1550	1	3.43	92.7	2.25
2	51.08			3.38	91.6	3.16
3	51.46			3.43	92.7	2.25
				3.41	**92.16**	**2.55**

2.3.2 Effect of Sintering Additives into Al_2O_3:TiO_2 Matrix

It is also well known that, densification of Al_2TiO_5 ceramics is a function of dopants and many attempts to dope with various oxide compounds such as MgO, ZrO_2, Fe_2O_3, SiO_2, $ZrSiO_4$ etc., are made so far [12-18]. These oxides are reported to be effective in densification and improving the thermal stability. However, they need to be doped in high volume fractions, deteriorating the

thermal properties and long term stability. Doping with spodumene ($LiAlSiO_4$), mullite ($3Al_2O_3.2SiO_2$), cordierite ($Mg_2Al_4Si_5O_{18}$) and feldspar have also been attempted, but no significant enhancement in thermo-mechanical properties were reported [20-22]. Studies have also been attempted to dope with SiO_2 (9 wt %) and co-doping with MgO (10 wt %) and SiO_2 (8 wt %), which have reported significant enhancement in stability and mechanical properties. However, doping of SiO_2 resulted in unreacted residual TiO_2 phase and the formation of additional phases such as $MgAl_2O_4$ and Mg_2SiO_4 with codoping [23]. In view of the above, the objective of the work is to elucidate systematically the effect of additives such as kaolinite and talc into Al_2O_3 : TiO_2 stoichiometric matrix with varying concentrations followed by the evaluation through DSC and dilatometric sintering studies. Sintered samples were characterized for their density and phase formation

2.3.2.1 Characterization of Additives

Kaolinite ($2Al_2O_3.3SiO_2.2H_2O$) and talc ($Mg_3Si_4O_{10}(OH)_2$) were used as additives for processing of the specimens. The powders were characterized for phase analysis using X-ray Diffraction Technique (XRD) and particle size by laser diffraction. The chemical analysis reported has specified by the supplier. The results are shown in Table 2.7 and the details of the measurements are discussed below.

Table 2.7 Characterization of Additives

Sr.No.	Attributes	Values Kaolinite	Values Talc
1	XRD phases	$2Al_2O_3.3SiO_2$	$Mg_3Si_4O_{10}(OH)_2$
2	Particle Size(µm)	4	12
3	Chemical analysis		
	SiO_2	44.0	60.0
	Al_2O_3	50.2	2.1
	TiO_2	0.4	0.08
	MgO	<0.1	31.1
	Na_2O	0.11	<0.01
	K_2O	<0.01	<0.01

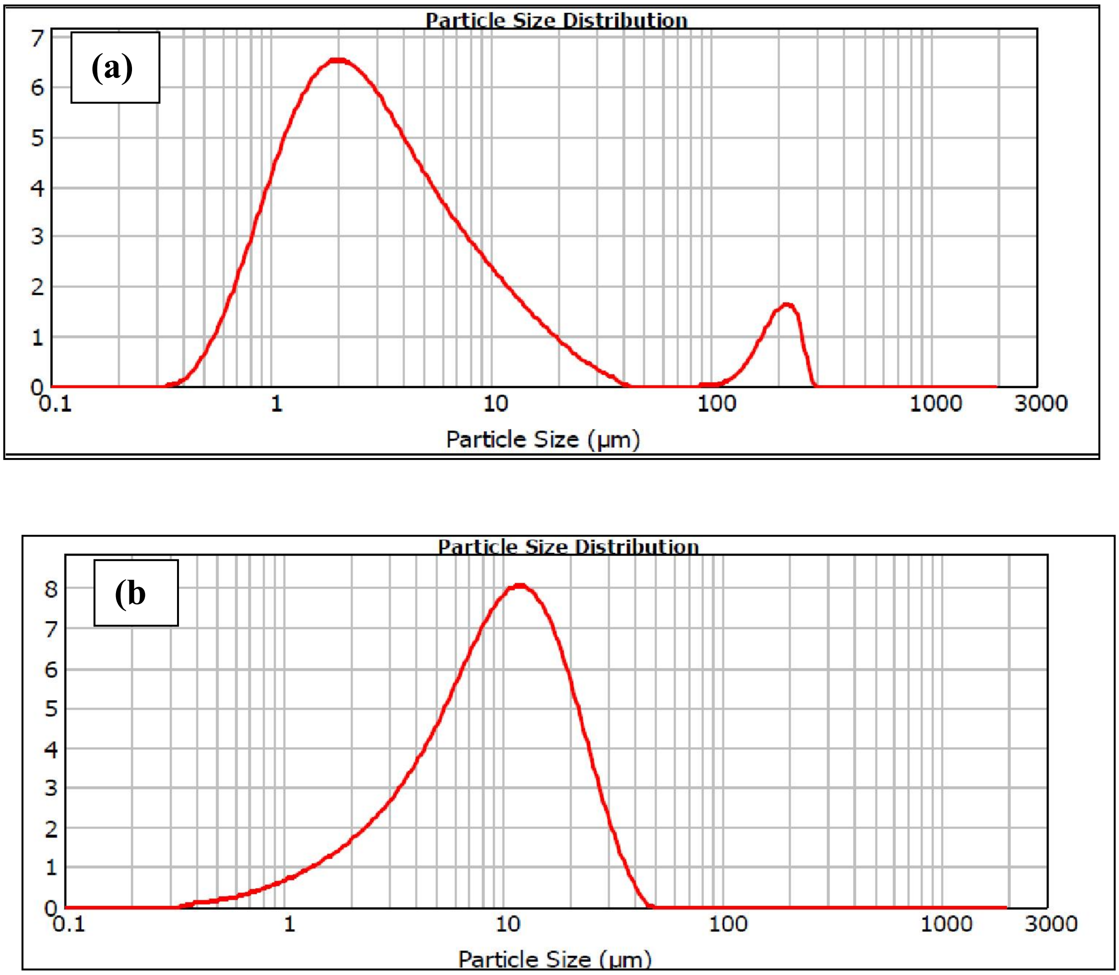

Fig 2.14 particle size distribution of (a) kaolinite and (b) talc powders

An average particle size of 3 µm with a particle size distribution ranging from 0.8 to 10 µm for clay and an average particle size of 12 µm with a particle size distribution ranging from 1 to 20 µm for talc are exhibited by the measurements (Fig. 2.14).

2.3.2.2 Compaction of alumina and titania powders granules with additives

The formulation were made with silica content of 1.5, 3 and 4.5 wt% and the concentration of both the additives are fixed based on their silica content. The sample ID's were depicted in Table 2.8. Compaction experiments are carried out with 0.8 gm of the granules filled in a compaction die (Die design and fabrication details are mentioned in chapter 2, section 2.2).

Sr. No.	**Sample. ID**	**Al_2O_3**	**TiO_2**	**Kaolinite**	**Talc**
1	AT	56	44	0	0
2	KAT-2.9	55.16	43.34	2.94% *(1.5wt% SiO_2)*	0
3	KAT-5.9	54.32	42.68	5.88% *(3 wt% SiO_2)*	0
4	KAT-8.8	53.48	42.02	8.82% *(4.5wt% SiO_2)*	0
5	TAT-2.5	55.16	43.34	0	2.5% *(1.5wt% SiO_2)*
6	TAT-5	54.32	42.68	0	5% *(3 wt% SiO_2)*
7	TAT-7.5	53.48	42.02	0	7.5% *(4.5wt% SiO_2)*

Table 2.8 Formulation investigated (wt %)

(where AT with kaolinite addition designated as KAT and AT with talc addition designated as TAT)

Granules were compacted at a constant ram rate of 1mm/min under pressure of 500MPa. Green densities of the pellets were calculated by dimensional method. Dimensions of the samples were measured using a digital Vernier caliper and weight of the pellets was determined using an analytical balance. Percentage theoretical density was calculated by the rule of mixtures (Table 2.9).

Table 2.9 Sample ID, specimen dimensions and green density of the samples

Sr.No	Sample Id	Dimensions (mm)		Weight (g)	Green density (g/cc)	Average green density (%TD)
		Diameter	Thickness			
1	KAT	10.00	4.4 4.3 4.3	0.8 0.8 0.8	2.4 2.4 2.4	58.64
2	TAT	10.00	4.3 4.3 4.3	0.8 0.8 0.8	2.4 2.34 2.38	58.31

2.3.2.3 Studies on Evolution of Al_2TiO_5 phase through Differential Scanning Calorimetry

Endothermic peak at ~ 1370°C indicate that, there is no significant shift in (KAT-8.8) $A1_2TiO_5$ phase formation compared to pure AT formulation (Fig 2.15). $A1_2TiO_5$ phase formation temperature is shifted to a lower temperature range of 1274°C in (TAT-5) compared to 1375°C observed with pure AT formulation as is evident from the DSC peak (Fig 2.15).

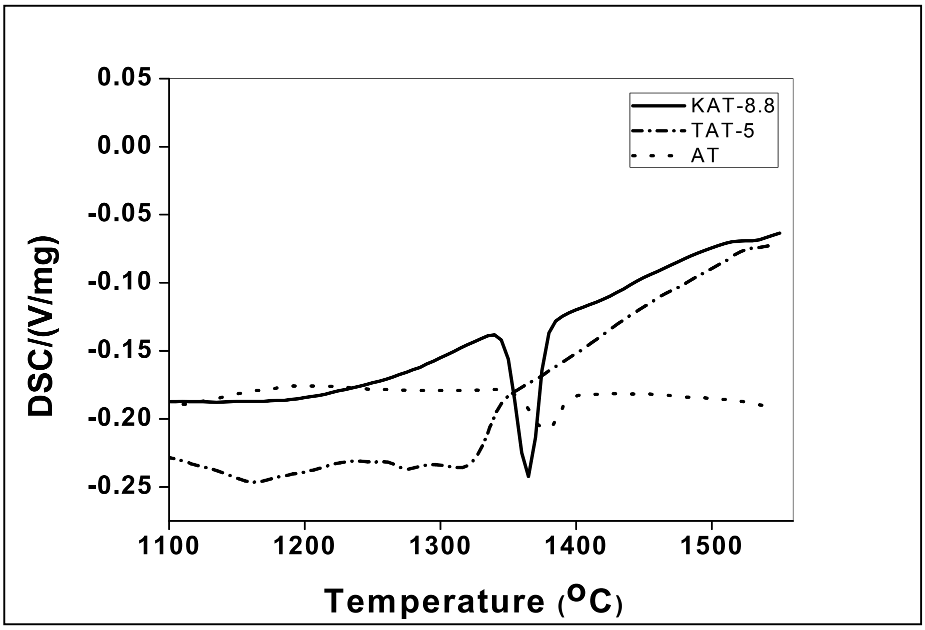

Fig 2.15 DSC curves of the AT, KAT-8.8 and TAT-5

2.3.3.4 Dilatometric studies

In order to study the effect of sintering additive on sintering behavior of AT, samples are subjected to dilatometry as discussed in 2.2.4.2 and corresponding shrinkage curve is shown in Fig 2.16. It is evident from Fig 2.16, sintering shrinkage starts around 1100°C in both cases and reach an early maximum at around 1280°C with talc addition.

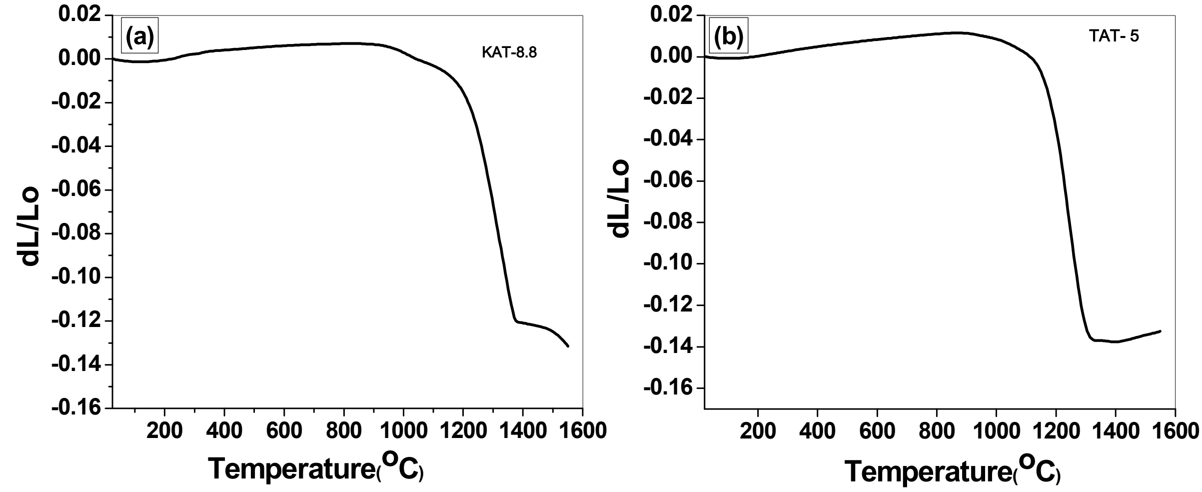

Fig 2.16 Dilatometry sintering curves of the (a) KAT-8.8 and (b) TAT-5

2.3.3.5 Sintering of compacts

The green compacts were subjected to sintering in a high temperature furnace with molybdenum disilicide heating elements (Nabertherm, Germany). Sintering schedule employed for the sample are shown in Fig 2.17.

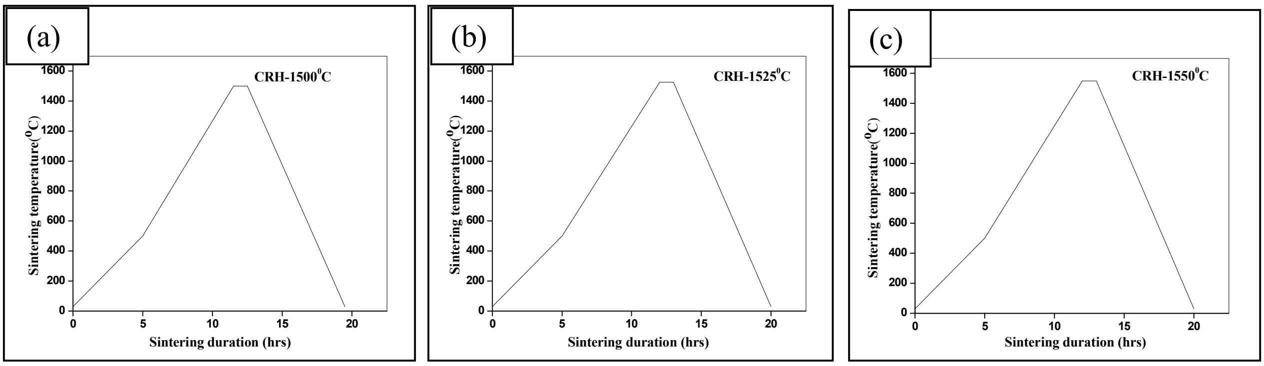

Fig 2.17 Sintering profiles employed to sinter pellet by CRH sintering method (a) 1500°C, (b) 1525°C, and (c) 1550°C

The low ramp rate of 90°C/hour was employed up to 500°C so as to eliminate the binder effectively without leading to the distortions of the compact. Further the heating rate is increased to 150°C//hour till it reaches the peak temperature of 1500, 1525 and 1550°C and further samples were soaked for 1 hour.

2.3.3.6 Densification of $A1_2TiO_5$ with and without additives

Composition, concentration and sintering temperature are found to have a significant effect on the final density values. Concentrations of both the additives are fixed based on their silica content (Table 2.7) in such a way that the final formulation corresponds to a silica addition of 1.5, 3 and 4.5% (Table 2.8). Variation of bulk densities with sintering temperature for all the compositions is shown in Fig 2.18 (a)-(b). The sintering parameters and corresponding density are given in Table 2.10. It is evident that the bulk density of $A1_2TiO_5$ formulation without additives has shown only a marginal increase from 84 to 85% of TD with increase of sintering temperature from 1500 to 1550°C. No significant increase in density is observed even at a sintering temperature of 1600°C.

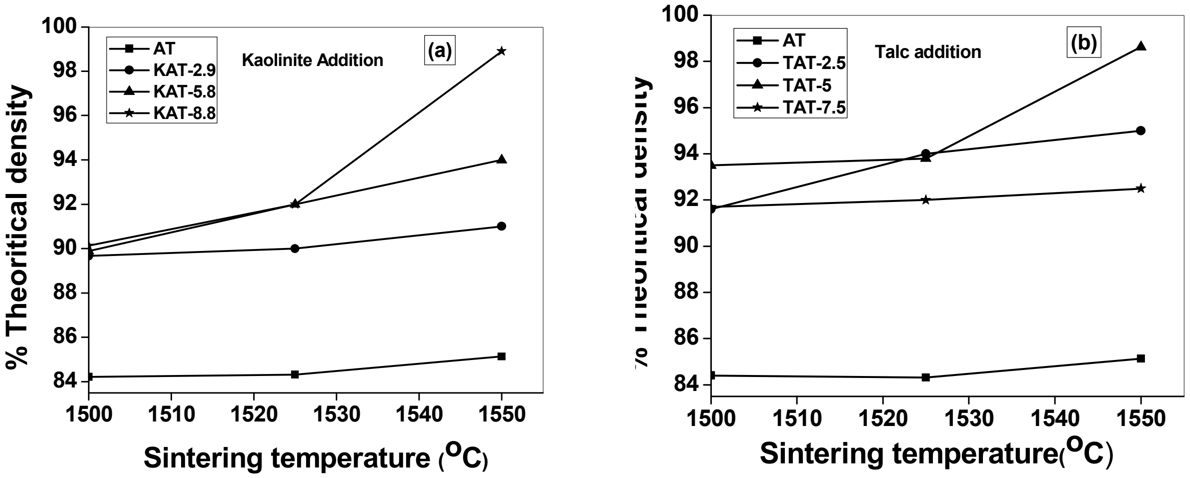

Fig 2.18 Density variation with temperature of (a)AT, KAT-2.88, KAT-5.8 and KAT-8.8 and (b) AT,TAT-2.5,TAT-5 and TAT-7.5

Kaolinite ($2Al_2O_3.3SiO_2.2H_2O$) addition from 2.9 to 8.8% has resulted in the consistent increase in density from 90% to a maximum density of 99% of TD. Talc ($Mg_3Si_4O_{10}(OH)_2$) addition from 2.5 to 5% increases the density from 92 to 98.7%% of

TD; however, unlike kaolinite, a higher concentration of talc (7.5%; TAT-7.5) has not shown any significant increase in density beyond 92 %.

Table 2.10 Sintering parameters and results of the CRH sintered samples

Specimen Identity	Sintering temperature (°C)	Dwell Time (hr)	Density (g/cc)	%TD	Porosity(%)
AT	1500	1	3.12	**83.71**	**21**
KAT-2.94			3.28	88.74	11.08
KAT-5.88			3.31	89.15	10.87
KAT-8.8			3.29	**90.40**	**10.54**
TAT-2.5			3.41	92.16	6.35
TAT-5			3.44	**93.98**	**1.91**
TAT-7.5			3.36	90.15	2.35
AT	1525	1	3.13	**84.21**	**20.25**
KAT-2.94			3.32	90.34	6.8
KAT-5.88			3.32	92.15	5.41
KAT-8.8			3.36	**92.05**	**4.98**
TAT-2.5			3.48	94.16	2.7
TAT-5			3.45	**94.26**	**148**
TAT-7.5			3.40	93.15	1.35
AT	1550	1	3.152	**85.03**	**12.93**
KAT-2.94			3.34	90.73	5.71
KAT-5.88			3.44	92.73	1.5
KAT-8.8			3.61	**98.9**	**0.3**
TAT-2.5			3.5	95.10	2.7
TAT-5			3.61	**98.63**	**0.67**
TAT-7.5			3.39	92.87	1.05

In order to elucidate the effect of additives in AT matrix, the samples which exhibited best density (TAT-5 and KAT-8.8) were subjected to XRD and microstructural studies.

Microstructural analysis of polished and thermally etched samples are carried out (procedure as discussed in section 2.2.2.3). Fig 2.23(a)-(c) showed the microstructures of AT, KAT-8.8 and TAT-5 samples. From the microstructure of KAT-8.8 and TAT-5 samples, it is clear that they possess single AT phase, where as in the case of AT some parent residual oxides still exist. Microstructural features do not show any significant variations in the grain size with both the additives (KAT-8.8 and TAT-5). The presence of additives enhanced the grain growth in AT ceramics.

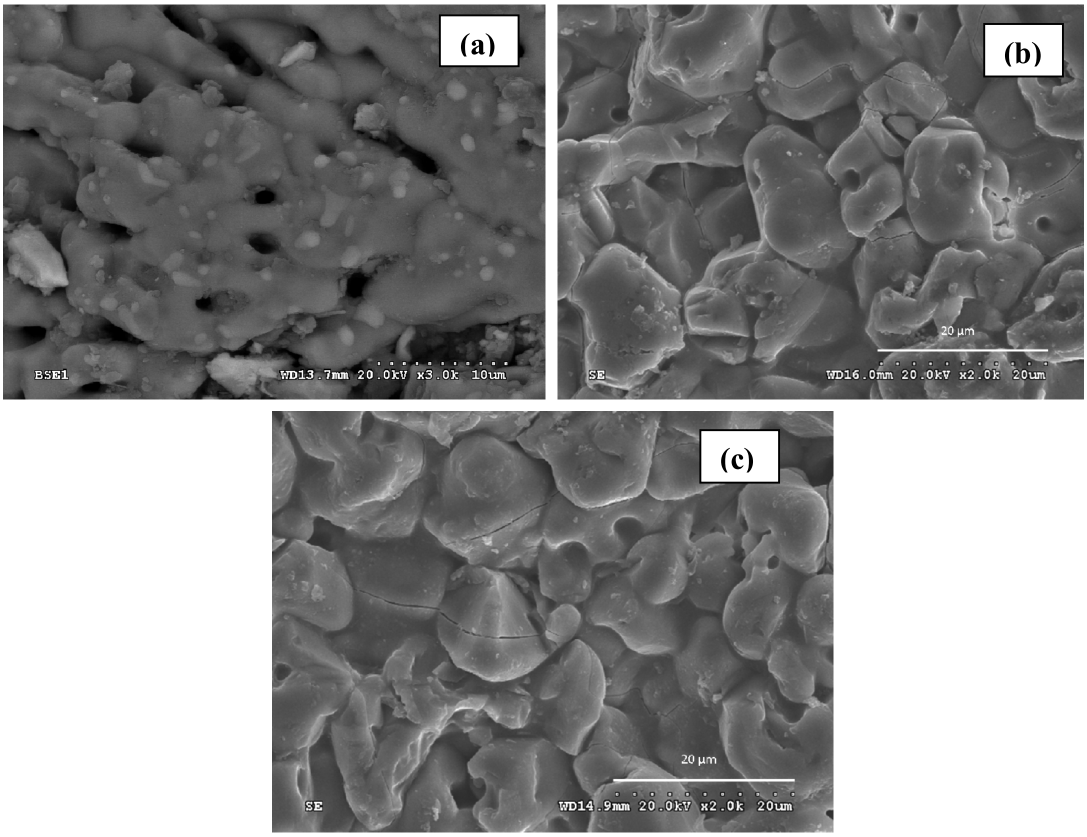

Fig 2.23 Microstructures of (a) AT, (b) KAT-8.8 and (c) TAT-5 samples

XRD pattern of the maximum dense samples TAT-5 and KAT-8.8 along with pure AT samples are shown in Fig 2.24 (a)-(c). It is evident that XRD patterns, unlike previous studies which is attempted to substitute MgO and SiO_2 simultaneously which generally

exhibited additional phases such as $MgAl_2O_4$ and Mg_2SiO_4 [23]. The present study have not resulted in significant additional phases, all the peaks in the XRD pattern could be indexed with standard Al_2TiO_5 phase except traces of precursors oxides.

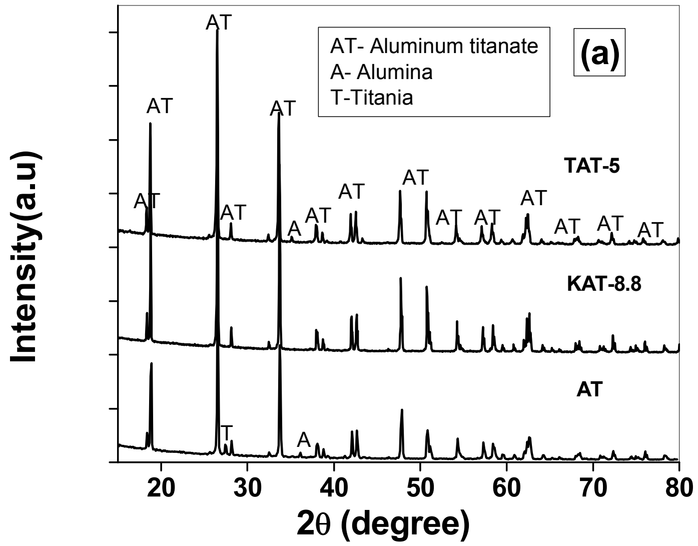

Fig 2.24(a) XRD patterns of sintered specimens 1550°C

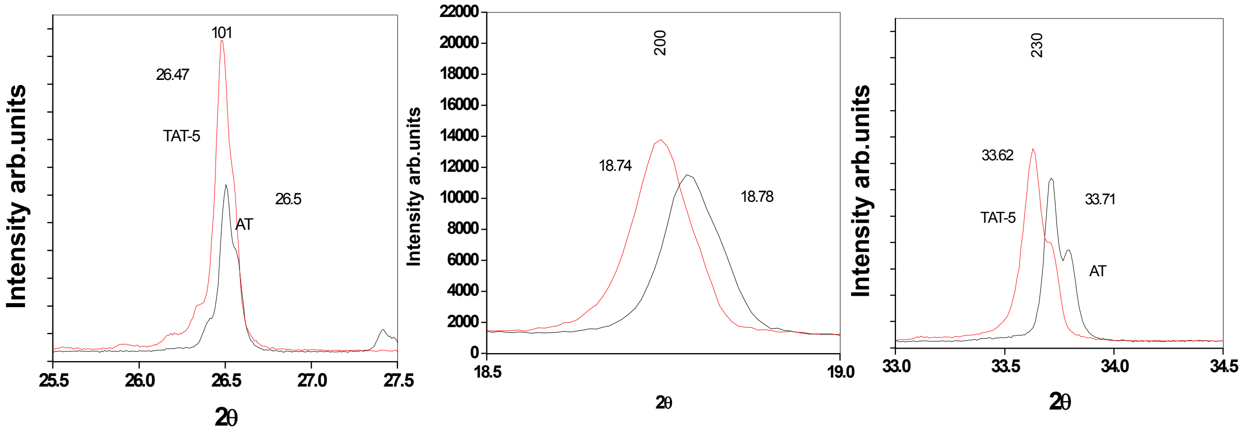

Fig 2.24 (b) XRD patterns of sintered specimens AT and TAT-5 at 1550°C

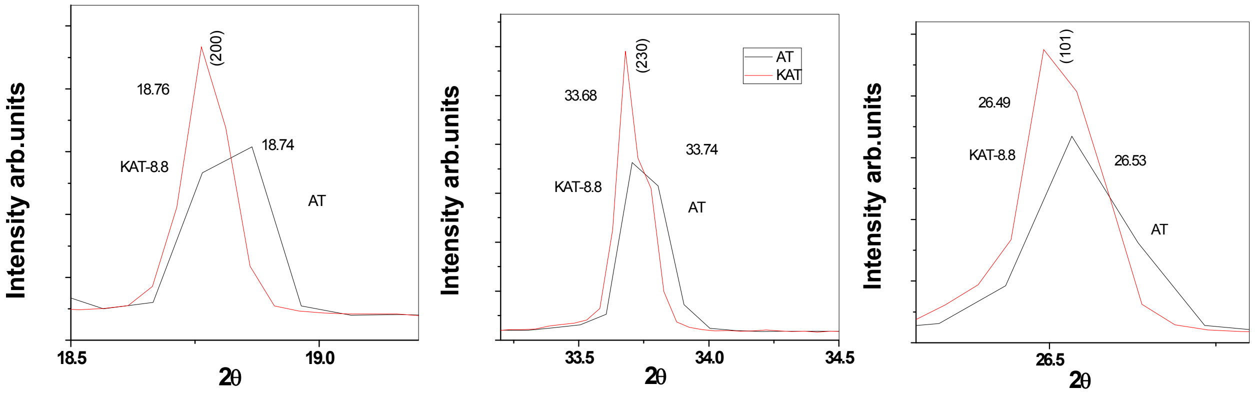

Fig 2.24 (c) XRD patterns of sintered specimens AT and KAT-8.8 at 1550^{o}C

Further, cell parameters and volume of AT sample are a=9.4315Å, b=9.6385 Å, c=3.590 Å and 326.35 (Å)^3, whereas cell parameters and volume of sample KAT-8.8 are a=9.4342 Å, b=9.6536 Å, c=3.5940 Å and 327.32 (Å)^3. The change in unit cell parameter is probably due to silicon (Si^{4+}, ionic radius = 0.41A^o) replacing Al^{3+} in the lattice of Al_2TiO_5 matrix. This may result in the multivalent state for titanium i.e., Ti^{3+}/Ti^{4+}, corresponding to a stoichiometry of $((Al^{3+},Ti^{3+})_2(Ti^{4+})_1(O^{2-})_5)$ which in turn enhances the sintering process. A closer look at the micrographs also reveals a change in the porous lamellar type of structure in to relatively dense faceted grains. Further, the micro-cracks are found visible and crack lengths are reduced to a greater extent in comparison to AT with no additives (Fig. 2.23).

XRD pattern of TAT-5 sample with maximum density depicted in Fig 2.24(a) has shown ~96% of Al_2TiO_5 phase with minor quantities of Al_2O_3 after sintering at 1550^{o}C. Further, the TiO_2 peaks are completely absent in the pattern. It is well known that talc ($Mg_3Si_4O_{10}(OH)_2$)transform to clinoenstatite ($MgSiO_3$) close to 1100^o C and at high temperatures, it decomposes to MgO and SiO_2. In the case of TAT-5 formulation, Mg^{2+} (MgO: 1.5 %) and Si^{4+} (SiO_2: 3 %) ions undergo simultaneous lattice substitutions for Al^{3+} to stabilize Al_2TiO_5 stoichiometry. This leads to change in unit cell parameters due to addition of talc.

The unit cell parameters and volume of sample AT are a=9.4315Å, b=9.6385 Å, c=3.590 Å and 326.35 (Å)^3. Whereas in sample TAT-5 unit cell parameters and volume are a=9.4651

Å, b=9.6715 Å, c=3.5981 Å and 329.37 (Å)^3, which displaces the inter planar spaces. The dilation along crystallographic c-axis in talc added samples, further expected to improve phase stability of AT [17]. A larger distortion from the AT composition can be attributed to the simultaneous substitution of Si^{4+} (ionic radius=0.41 Å) and Mg^{2+} (ionic radius=0.65 Å) replacing Al^{3+} in the lattice of Al_2TiO_5 matrix. Al_2TiO_5 formation process was led by nucleation and growth of grains and finally diffusion of reactant through the matrix and is controlled by the very slow reacting species. In addition to the multivalent state for titanium i.e., Ti^{3+}/Ti^{4+} as a result of Si^{4+} substitution, the presence of Mg^{2+} ions that replaces Al^{3+} may result in oxygen vacancy formation $((Al^{3+},Ti^{3+})_2(Ti^{4+})_1(O^{2-}{}_{5-\delta})$. These vacancies promote the diffusion in the solid state enhancing densification.

In order to get more clarity we have carried out a slow scan with a step size of 0.01°/ sec shown in Fig.2.24(b) and (c) for TAT-5 and KAT-8.8 respectively. In TAT-5 samples, a peak shift of 0.03° at 26.5 (100 % intensity peak), 0.09° at 33.71 (68% intensity peak) and 0.04°at18.78 (66% intensity peak) is observed. These observed shift can be attributed to the substitution of Mg^{2+} and Si^{4+} ions into Al_2TiO_5 lattice. In KAT-8.8 samples, a peak shift of 0.04° at 26.5 (100 % intensity peak), 0.06° at 33.71 (68% intensity peak) and 0.09°at18.78 (66% intensity peak) is observed. These observed shift can be attributed to the substitution of Si^{4+} ions into Al_2TiO_5 lattice.

Jiang et.al [23] studied the co-doping of higher concentrations of MgO (5.7wt %) and SiO_2 (8.5wt %) in AT lattice. An increase in c lattice parameter of 3.603Å against 3.589.1 Å for pure AT. The authors attributed the shift to the replacement of Al^{3+} by Mg^{2+} and/or Si^{4+}. In the present study on decomposition of talc is expected to produce MgO (1.5%) and Silica (3%) and correspondingly an increase of c-lattice parameter 3.5981 Å is observed with TAT samples, 3.590 for AT samples. In the present study, unlike co-doping with high concentration we have not observed any additional phases as a result of the talc substitution revealed by XRD pattern (Fig 2.24(a)). Hence, Mg^{2+} and Si^{4+} resulted in lattice substitution for Al^{3+} site, though the shift is minimal due to very low concentrations.

2.4 Conclusion

Precursor oxides were characterized for XRD phases, particle size and BET surface area. Al_2O_3 is found to be mixture of γ and α with γ as minor phase as extend of 15-20% and balance α as major phase. Particle size of 315 nm,(D_{50}) which is complementary with the measured surface area of 21.26 m^2/g. In case of titania, phase pure anatase with particle size of 355 nm,(D_{50}) and surface area of 10.57 m^2/g is observed.

Processing of precursor oxides and preformed Al_2TiO_5 through granulation and compaction has yielded a green density of 58.19 and 51.46 %TD on sintering at optimum temperature have resulted in the sintered density of 3.22 gm/cc (87.33%TD) and 3.41 gm/cc (92.16 %TD) respectively.

Addition of kaolinite ($2Al_2O_3.3SiO_2$) and talc ($Mg_3Si_4O_{10}(OH)_2)$) in relatively low concentration of 8.8 wt% and 5 wt% respectively resulted in enhanced densification leading to a substantial increase in percentage theoretical density to 99%TD in comparison with the maximum densities achieved for pure $A1_2TiO_5$ with 87%TD (Insitu) and 92%TD (Preformed) processed in the study. Kaolinite and/or talc substitution results in multivalent titanium (Ti^{3+}/Ti^{4+}) and oxygen vacancies in $A1_2TiO_5$ formulations promoting the enhanced diffusion and densification.

Microstructural evaluations revealed transformation of porous lamellar type of structure of pure $A1_2TiO_5$ into relatively dense grains with kaolinite and talc confirming higher density values. XRD studies have shown an improvement in $A1_2TiO_5$ phase content from 92 % to a maximum of 98% with the addition of kaolinite. The enhancement in phase content was moderate in case of talc with a maximum of 95.5%; however, DSC studies indicated a drop (~85°C) in phase formation temperature.

Addition of talc ($Mg_3Si_4O_{10}(OH)_2)$) in AT samples, resulted in a peak shift of 0.03° at 26.5 (100 % intensity peak), 0.09° at 33.71 (68% intensity peak) and 0.04° at 18.78 (66% intensity peak). Similarly addition of kaolinite ($2Al_2O_3.3SiO_2$) in AT samples a peak shift of 0.04° at 26.5 (100 % intensity peak), 0.06° at 33.71 (68% intensity peak) and 0.09° at 18.78 (66% intensity peak) is observed. These observed shift can be attributed to the substitution of Mg^{2+} and Si^{4+} ions into Al_2TiO_5 lattice.

2.5 References

1.S. Lang, C. Fillmore and L. Maxwell. The System Berillia-Alumina-Titania: Phase relations and general physical properties of three components porcelains, J. Res. Natl. Bur. Stand., 48 [4], 301-321(1952).

2.V. Buscaglia, P. Nanni, G. Battilana, G. Aliprandi and C. Carry. Reaction sintering of aluminium titanate: I - Effect of different alumina powder, J. Euro. Ceram. Soc., 13, 419-426 (1994).

3.M. Tahazaksi, M. Fukuda, H. Fukuda and T. Yoko. Preparation, structure, and properties of thermally and mechanically improved aluminium titanate ceramics doped with alkali feldspar, J. Am. Ceram. Soc., 85 [12], 3025-30 (2002).

4.H. C. Kim, K. S. Lee, O. S. Kweon, C. G. Aneziris and I. J. Kim. Crack healing, reopening and thermal expansion behavior of Al_2TiO_5 ceramics at high temperature, J. Euro. Ceram. Soc., 27, 1431-1434 (2007).

5.H.A.J. Thomas, R. Stevens, E. Gilbart. Effect of zirconia additions on the reaction sintering of aluminum titanate, J. Mater Sci., 26,3613-3616 (1991).

6.M. Nagano, S. Nagashima, H. Maeda, A. Kato, Sintering behavior of Al_2TiO_5 base ceramics and their thermal properties, Ceram Int., 25, 281-289 (1999).

7.A.M. Segadges, M.R. Morellib and R.G.A. Kiminam, Combustion Synthesis of aluminium titanate, J. Euro. Ceram. Soc., 18, 771-781 (1998).

8.M. Zaharescu, M. Crisan, M. Predaa, V. Fruth and S. Preda. Al_2TiO_5 -based ceramics obtained by hydrothermal process, J. Optoelec. & Adv Matrls., 5[5] 1411 - 1416 (2003).

9.Y. X. Huang and M. S. Senos, Effect of powder precursor characteristics in the reaction sintering of aluminium titanate, Mat. Res. Soc. Bull., 37, 99-111 (2002).

10. B. Morosin, R.W. Lynch. Structure studies on Al_2TiO_5 at room temperature and at 600°C, Acta cryst B 28, 1040-1046 (1972).

11. R.D. Skala, D. Li and I.M. Low, Diffraction, structure and phase stability studies on aluminium titanate, J. Euro. Ceram. Soc., 29, 67-75 (2009).

12. Y. Djambazo and A. Hristo. Effect of SiO_2 addition on thermal hysteresis of aluminum titanate, J. University of Chemical Technology and Metallurgy, 45(3) 269-274 (2010).

13. T. Korim, Effect of Mg^{2+} and Fe^{3+} ion on formation mechanism of aluminum titanate, Ceram. Int., 35, 1671-1675 (2009).

14. I.J. Kim and G. Cao, Low thermal expansion behavior and thermal durability of $ZrTiO_4$-Al_2TiO_5-Fe_2O_3 ceramics between 750°C and 1400 °C, J. Euro. Ceram. Soc., 22, 2627- 2632 (2002).

15. L. Giordano, M. Viviani, C. Bottino, M.T. Buscaglia, V. Buscaglia and P. Nanni. Microstructure and thermal expansion of Al_2TiO_5 - $MgTi_2O_5$ solid solution obtained by reaction sintering, J. Euro. Ceram. Soc,. 22, 1811-1822 (2002).

16. T. Shimada, M. Mizuno, K. Katou, Y. Nurishib, M. Hashibab, O. Sakuradab, D. Mizunob and T. Onob. Aluminum titanate-tetragonal zirconia composite with low thermal expansion and high strength simultaneously, Solid State Ionics 101-103, 1127-1133 (1997).

17. P. Oikonomou, Ch. Dedeloudis, C.J. Stournaras, Ch. Ftikos, Stabilized tialite-mullite composites with low thermal expansion and high strength for catalytic converters, J. Euro. Ceram. Soc., 27, 3475-82 (2007).

18. Tsetsekou. A comparison study of tialite ceramics doped with various oxide materials and tialite–mullite composites: microstructural, thermal and mechanical properties, J. Euro. Ceram. Soc., 25, 335–348 (2005).

19. H.F. Perera, A. Pajares and J.J. Melendez. Strength of aluminium titanate/mullite composites containing thermal stabilizers, J. Euro. Ceram. Soc., 31, 1695–1701 (2011).

20. G. Bruno, A. Efremov, B. Wheaton, I. Bobrikov, V. G. Simkin and S. Misture. Micro- and macroscopic thermal expansion of stabilized aluminium titanate, J. Euro. Ceram. Soc., 30, 2555–2562 (2010).

21. C.G. Shi and I.M. Low, Use of spodumene for liquid-phase-sintering of aluminium titanate, Mats. Ltrs. 36, 118–122 (1998).

22. C.G. Shi and I.M. Low, Effect of spodumene additions on the sintering and densification of aluminum titanate, Mat. Res. Bull., 33(6), 817–824 (1998).

23. J. Lan, C. Xiao-Yan, H. Guo-Ming and M. Yu. Effect of additives on properties of aluminium titanate ceramics, Trans. Nonferrous Met. Soc., 21, 1574-1579 (2011).

Chapter-III

Thermal Stability Studies on Preformed AT and TAT-5

3.0 Introduction

Al_2TiO_5 in pure form is not stable in the temperature range of 900 - 1280°C, where it tends to decomposes into corresponding precursor oxides of α-Al_2O_3 and TiO_2 due to the eutectoid reaction [1-2]. Hence this material loses its low thermal expansion behaviour leading to poor thermal shock resistance limiting its technological use. It is well known that Al_2TiO_5 exists in two allotropic forms, such as β-Al_2TiO_5, a low temperature phase stable from RT to 900°C and α-Al_2TiO_5, a high temperature phase stable above 1820°C (the inversion temperature). It is suggested that instability region exists between 900 to 1300°C, where two opposing phenomena compete in dynamic equilibrium, with tendency to shift the equilibrium towards right resulting in the decomposition, according to the reaction,

β-$Al_2TiO_5 \rightleftharpoons \alpha$-$Al_2O_3+TiO_2$

Beyond 1300°C the equilibrium shifts to the left forming β-Al_2TiO_5.

Molar free energy of Al_2TiO_5 formation can be estimated by a second-law of thermodynamics as follows:

$$\Delta G\,(Al_2TiO_5) = \Delta H - T\Delta S$$

For spontaneous reaction of α-Al_2O_3 & TiO_2

$\Delta G\,(Al_2TiO_5)$ should be equal to 0 or -ve, i.e

$$\Delta G\,(Al_2TiO_5) = 0 = 17{,}000 - 10.95T$$

$$\text{Thus, } T = 1553\text{ K } (1280^{\circ}\text{C})$$

This implies that above 1280°C the formation reaction is favoured based on the available heat capacity data and the equilibrium temperatures. It is well known that pseudobrookite structured oxides such as Al_2TiO_5 can be stabilised entropically due to the cation disorder [3]. Moreover, on selection of suitable dopants temperature regime of stabilisation can be modified.

Part of the work being published in Ceramic International, 40,[1],(2014) 659-666.

Earlier studies report that solid solutions of Al_2TiO_5 containing Fe^{3+} and Mg^{2+}, provide a lower decomposition temperature, which is exhibited to increase the temperature range of stability of AT ceramics. On the other hand, solid solutions with Cr^{3+} promote a greater temperature of decomposition[4]. Replacement of Ti^{4+} by Ge^{4+} and Al^{3+} by Ga^{3+} and Ge^{4+}solid solutions combined also with additions of MgO and Fe_2O_3, finding that the stabilizing effect of the additions decreased in the following order: Fe^{3+}, $Mg^{2+} > Ge^{4+} > Ga^{3+}$[5-7]. Additions, such as Fe_2O_3, MgO or SiO_2 were studied, the first two promoting structures of the pseudobrookites type Fe_2TiO_5 and $MgTi_2O_5$ giving complete solid solutions with Al_2TiO_5 [8-11]. SiO_2 has limited solubility [12], however additions up to 3 weight percent produce a slight increase in the mechanical resistance, due to small amounts of liquid phase that densify the material but, larger amounts cause excessive growth of the grain, which is detrimental to the mechanical resistance [13-14]. Thermal stability of Al_2TiO_5 with Fe_2TiO_5 and $MgTi_2O_5$ additions were studied by Liu et al. It has found that material with Fe^{3+}additions did not show any significant mechanical property degradation and the material with Mg^{2+} annealed at 1000 - 1100°C, showed decomposition to Al_2O_3 and TiO_2 [15-16].

This eutectoid reaction is also reported to be a function of processing conditions such as heating rate, soaking time and atmosphere of sintering [17-22]. Al_2TiO_5, being a candidate material for new generation diesel particulate traps, undergoes extreme environments while regeneration. Present study attempts to elucidate the effects of various thermal treatment parameters on eutectoid decomposition [23-26]. In addition to Conventional Ramp and Hold (CRH) sintering technique and cycling conditions, for the sake of scientific interest, preformed powders (~90% Al_2TiO_5) are also subjected to Spark Plasma conditions and were evaluated for extent of decomposition.

Al_2TiO_5 samples heated to 1400°C under SPS condition at 50MPa pressure and heating rates of 200°C/min and 50°C/min have shown eutectoid decomposition to an extent of 95% and 74%, respectively. On the contrary, compacts pressed out of the above powder, on conventional sintering (CRH) at a heating rate of 50°C/min and under pressureless conditions, have shown significantly low Al_2TiO_5 phase decomposition of 11%. Dilatometric studies have also exhibited a significant slope change in the temperature regime of 1000 – 1200°C. This correlates well with the high temperature XRD data, revealing appearance of high intensity peak at around $2\theta=40^{o}$ and further resulted in decomposition to precursor oxides, as is evident from the room temperature XRD peaks at 27.33° and 35.61° on heating beyond 1000°C.

Thermal cycling upto 10, 20 and 30 cycles from 28 to 1200°C at a heating rate of 100°C/min have resulted in the decomposition of 38%, 44% and 54% of ALT phases. A significant retention in eutectoid decomposition of Al_2TiO_5 phase is observed for 5wt% addition of magnesium silicate ($Mg_3Si_4O_{10}(OH)_2$) under identical treatment conditions, even with SPS heating rate of 200°C/min. Decomposition was limited to 30% under SPS condition and complete elimination under all CRH conditions, retaining the phase content unchanged. Magnesium silicate doping also inhibited ALT decomposition even with 30 thermal cycles. A comparative evaluation of microstructure is found to correlate well with the observed eutectoid decomposition. Hardness and thermal expansion measurements were also found to be in good agreement complementing the trend in decomposition.

3.1 Experimental Procedure

3.1.1 Sample Preparation

Raw materials and process parameters employed for the formation of stoichiometric preformed AT and TAT-5 formulations (designated as PAT and PTAT-5 formulations referred in this chapter) are shown in flow chart (Fig 3.1). Extents of AT phase formation in both samples were evaluated using X-Ray Diffractometer (D8 advanced, Bruker, Germany). Further, the particle size of the preformed powders was analyzed using DLS technique (Nanosizer, Malvern).

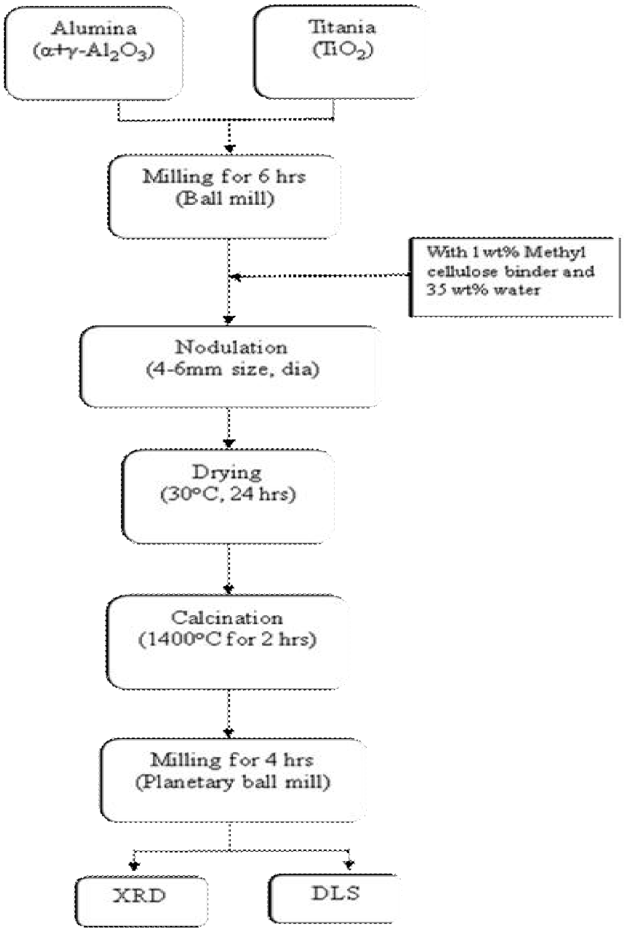

Fig 3.1. Flow chart for preformed formulation preparation

3.1.2 Characterization of Preformed PAT and PTAT-5 Formulations

The XRD patterns of the preformed PAT and PTAT-5 formulations are presented in Fig 3.2.(a)-(b). XRD patterns of the samples show Al_2TiO_5 as the predominant phase with minor quantities of α-Al_2O_3 and TiO_2. An increase in Al_2TiO_5 phase content from 92 % (in case of PAT) to 96% (in case of PTAT-5 samples) was observed with addition of 5% magnesium silicate.

It is well known that magnesium silicate ($Mg_3Si_4O_{10}(OH)_2$) transforms to clinoenstatite ($MgSiO_3$) at 1100^oC and decomposes to MgO and SiO_2 at high temperatures. In the case of PTAT-5 formulation, Mg^{2+} (MgO-1.5%) and Si^{4+} (SiO_2-3%) ions undergo simultaneous lattice substitutions for Al^{3+} to stabilize Al_2TiO_5 stoichiometry.

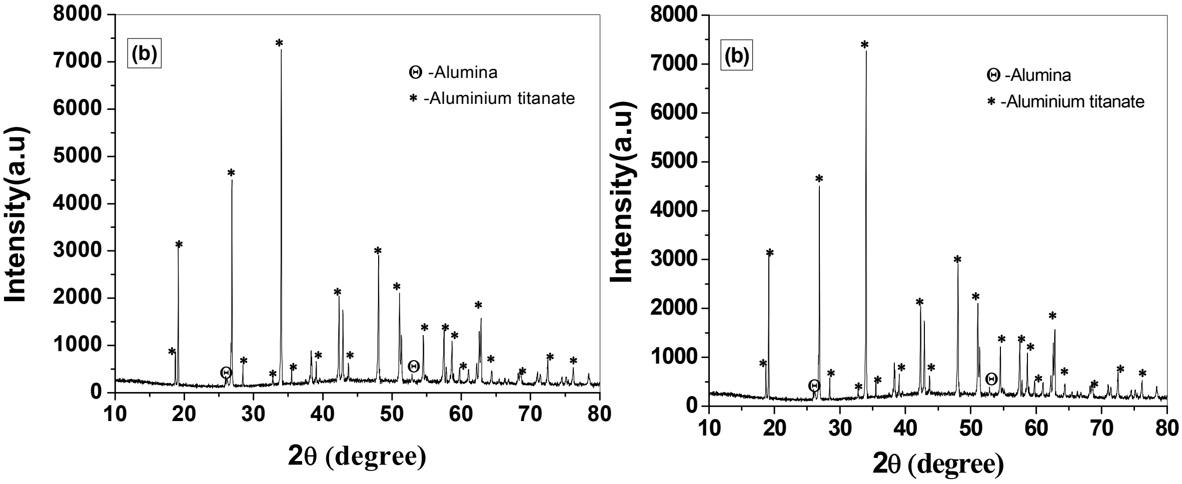

Fig 3.2 X-ray diffraction patterns of preformed (a) PAT and (b) PTAT-5 powders

Al_2TiO_5 nodules were crushed and milled in planetary ball mill at 150 rpm for 4 hrs, with powder to milling media of 1:2 ratio. Particle size reduction achieved through milling at an interval of 1 hr was measured and found no significant effect on milling beyond 4 hrs in both cases (Fig 3.3(a-b)). DLS pattern of the samples, after milling for 4 hrs are shown in Fig 3.4.(a)-(b) respectively. The average particle size of the PAT sample was found to be ~505 nm with distribution in the range of 300-800nm in comparison to PTAT-5 samples exhibiting mean size ~ 410 nm with a distribution in the range of 235-700nm.

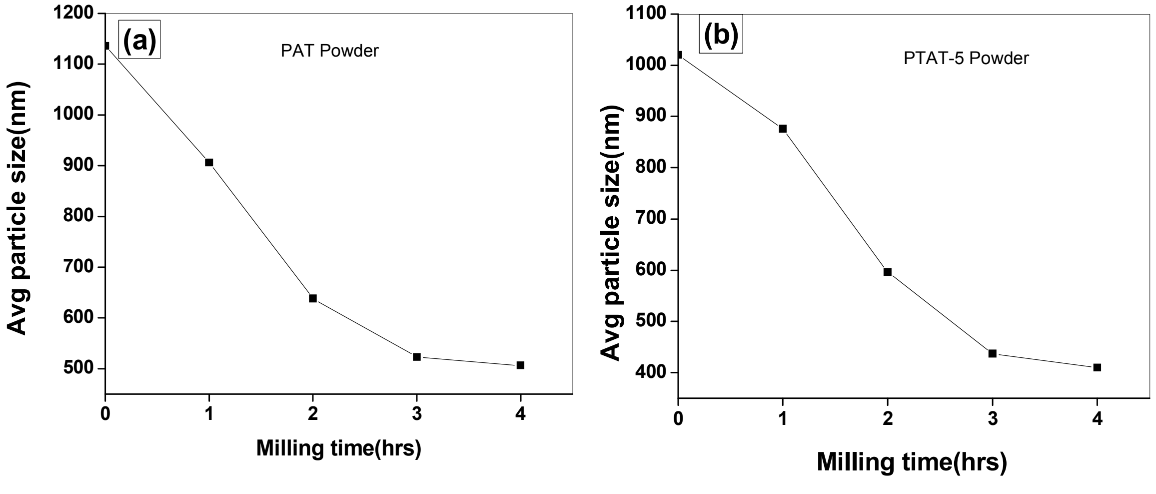

Fig 3.3 Average particle size as a function of milling time of (a) PAT and (b) PTAT-5 powders

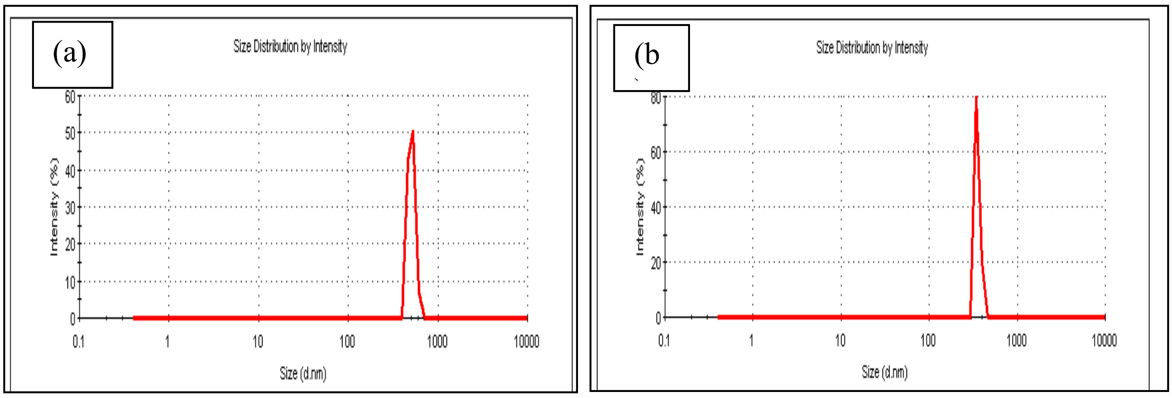

Fig 3.4 DLS patterns of (a) PAT and (b) PTAT-5 powders

3.1.3 Post Thermal Treatments

Preformed powders, PAT and PTAT-5 synthesised above were subjected to two post thermal treatment conditions such as Spark Plasma (SPS) and Conventional Ramp and Hold (CRH) as discussed below.

3.1.3.0 Spark plasma sintering (SPS)

Spark plasma sintering simultaneously applies pulsed electrical current and pressure directly on the sample leading to densification at relatively lower temperatures and short soaking times [27-28]. As both the die and sample are directly heated by the Joule effect extremely high heating rates are possible due to which non-densifying mechanisms like surface diffusion can be surpassed.

The versatility of SPS allows very quick densification to near theoretical density for a number of metallic, ceramic and multi-layer materials under a low vacuum/inert environment [29-30]. It is a novel hot pressing technique, where very high heating rates upto (~ 500°C/min) can be achieved by the application of pulsed electrical current and pressure (150MPa) simultaneously. In hot pressing, the precursor powder is loaded in a die and a uniaxial pressure is applied during the sintering. In the SPS technique, where a pulsed direct current is passed through an electrically conducting pressing die, working as the heating element, gives more rapid densification rate due to the use of pressure and rapid heating rate. The presence of a pulsed electrical field creates sparks during the initial part of the sintering, which clean the particles surface and thus facilitate grain boundary diffusion. Electrical field induced diffusion processes might also contribute to increased densification rate [31].

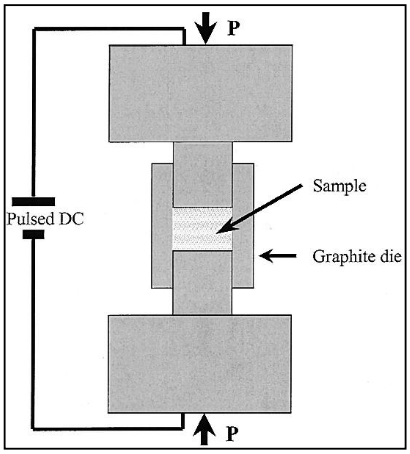

Fig 3.5 Schematic drawing illustrating the features of an SPS apparatus

The die acts as a heating source and the sample is heated from both outside and inside, as outlined in the schematic drawing in Fig 3.5. Rapid sintering by SPS makes it possible for the sample to skip over low temperature regime, where the non-densifying mechanism (surface diffusion) is active and to proceed directly to the elevated temperature regime where densifying mechanisms (grain boundary and volume diffusion) are predominant [27].

Plasma activated sintering (PAS) and spark plasma sintering (SPS) apparatus were developed in 1988 and 1990 respectively. Using SPS & PAS a variety of materials such as metallic materials, structural ceramics, oxide superconductors, ceramic composites, polymers, thermoelectric materials, and functionally graded materials have been prepared.

The unique features of the process are the possibilities of using very fast heating rates (~500°C/min) and very short soaking times (within few minutes) to obtain fully dense samples. Three factors that contribute to the rapid densification process are (i) the application of a mechanical pressure; (ii) the use of rapid heating rates; and (iii) the use of pulsed direct current, implying that the samples are also exposed to an electrical field. It is generally accepted that application of mechanical pressure is helpful in removing pores from compacts and enhancing diffusion. The heat transfer from the die to the compact is very efficient in this process because, the die itself acts as a heating element. However, it is frequently argued that the improved densification rates stem mostly from the use of direct current pulses of high energy. Thus, the process inventors originally claimed that the pulses generate spark discharges and even plasma between the powder particles, which explains why the process is named spark plasma sintering. During the initial stage of the sintering process the generated spark discharge and/or plasma is said to clean the surfaces from adsorbed species such as, CO_2, H_2O, and OH^-. In the later part of the process the clean surface is expected to enhance the grain-boundary diffusion processes that together with the proposed spark discharges and/or plasma processes, are assumed to promote transfer of material and thus, enhance the densification [32]. SPS has been demonstrated to enable the consolidation of ceramic materials within minutes. However, the use of a rapid densification process does not always guarantee that extensive grain growth can be avoided. The rapid densification of nanosized precursor powders under inappropriate sintering conditions can easily yield densified compacts composed of micrometer-sized grains. Various sintering conditions such as, the sintering temperature, holding time, heating rate, applied pressure, and pulse sequence, influence the densification and grain-growth rate. Spark plasma sintering (SPS), or field assisted sintering (FAS) combines these processing parameters needed for efficient densification of nanocrystalline compacts. These sintering conditions lead to superfast densification of nanocrystalline powder compacts and to retention of the nanostructure. This technique was found to be especially suitable for the densification of nanocrystalline powders. Many atomic transport mechanisms may be active during the sintering and densification of nanocrystalline oxide powders. Neglecting the evaporation–condensation and viscous sintering mechanisms that are limited to specific material systems, the main transport mechanisms are surface, grain boundary, and lattice diffusion. While surface diffusion during pressure-less sintering can change the pore shape, the corresponding pore volume is barely affected. Consequently, mass transport by surface diffusion is not considered as a densification mechanism. This is not valid for densification via SPS. The main advantage of SPS is the preservation of the particle specific surfaces during heating. Under applied load the compact densification may benefit from the low temperature mass transport mechanisms provided by the nanoparticle surfaces and interfaces. The short sintering durations at low temperatures are expected to limit the diffusion controlled grain growth.

In SPS process a graphite die set is filled with the raw material powder and placed between the lower and upper electrodes. A pressure is applied on the compact during sintering. A pulsed direct current (dc) is then applied to the sintering powder and the activation of powder particles is achieved by the application of electrical discharges. For electrically conductive powders heating up is mainly due to the Joule effect. For non-conductive powders heating is likely achieved through the heat transfer from the die and punches. For conductive powders electrical discharges can occur along the particle surfaces during the SPS process. For oxides ion conduction takes place at high temperatures. With the application of a altering pulse DC current thermal and electrical breakdown phenomena are most likely to occur at high temperatures for non-conductive ceramic powders and skin current can be formed [33-36]. With the alternative current powder contacts and gaps work like small capacitors and plasma may be generated by the electrical discharges across these capacitor gaps. The application of an external electric field leads to improved densification during sintering and requires a considerably shorter time cycle compared to conventional methods of sintering. The high-temperature sputtering phenomenon generated by spark plasma and spark impact pressure eliminates the absorbed gas and impurities present on the surface of the powder particles. There are several anticipated merits of SPS: 1. Generation of spark plasma; 2. Effect of electric field; 3. Effect of electric current on diffusion in conductor or skin current on the semiconductor and insulator; 4. Impact of spark plasma; 5. Rapid Joule heating and cooling.

R G Duan et.al [17] studied the consolidation of plasma-sprayed metastable Al_2TiO_5 powder and a mixture of nano-Al_2O_3 and TiO_2 powders with or without nano-MgO powder additive by SPS. The sintering temperatures were selected at 1000, 1150, and 1250°C, with a heating rate of 300°C/min and holding time of 3 min. During sintering the applied uniaxial pressure on the sample is 63MPa. It was found that the starting nano-Al_2O_3 reacted with nano-TiO_2 powder to form the Al_2TiO_5 phase after SPS consolidation at 1150°C under a pressure of 63MPa. The starting plasma-sprayed Al_2TiO_5 was stable above 1150°C after SPS under 63MPa, though in oxidizing atmospheres under the ambient air pressure, the stable temperature range of Al_2TiO_5 was above 1280°C. There was a fast decomposition rate for plasma-sprayed Al_2TiO_5 at 1000°C during SPS, whereas in oxidizing atmospheres under the ambient air pressure at 1000°C its decomposition is very slow. When the nano-Al_2O_3 and TiO_2 powders are consolidated by SPS at 1150°C, a small amount of Al_2TiO_5 phase was formed. The addition of MgO advanced the formation of $Mg_{0.3}Al_{1.4}Ti_{1.3}O_5$ along with $MgAl_2O_4$ in the ceramics prepared both from plasma-sprayed powder and from nano-powder.

3.1.3.1 Spark plasma processing of preformed PAT and PTAT-5 powders

SPS thermal treatment of the samples were carried out using the SPS facility (Dr. Sinter 1050). In the present study 8-10g of preformed Al_2TiO_5 powder was accurately weighed and the powder was poured into a conductive die made of high strength graphite and held between two graphite punches. Graphite foil is used as spacers between the powder and the punches to avoid the damage of the die. The die had an inner diameter of 20mm, an outer diameter of 50mm, and a depth of 50mm. A hole of 1.8mm diameter was drilled into the outside of the die for temperature measurements. A schematic of the die, punches, and spacers and furnace are shown in Fig 3.6(a).

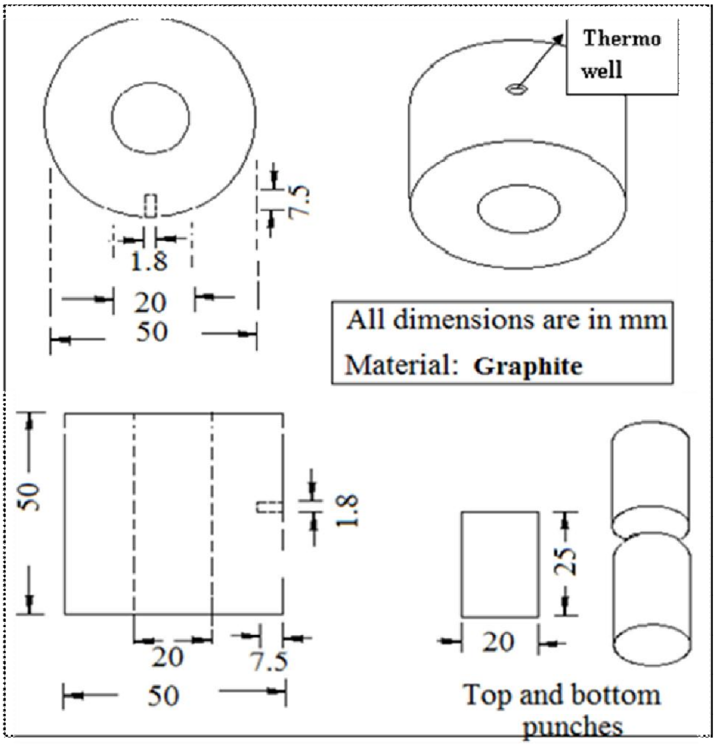

Fig 3.6(a) Schematic drawing to the scale and the dimensions of the die, punches, and spacers

The SPS system was evacuated to 5 Pa pressure and uniaxial pressure of 50 MPa was applied gradually at two different heating rates of 50 and 200°C/min to peak temperatures of 1400°C with dwell time of 3 minutes for PAT (Fig 3.6(b)-(c)). However, the SPS of PTAT-5 preformed powder was carried out under identical conditions but at heating rate of 200°C/min only (Fig 3.6(b)). The samples were furnace cooled to room temperature and the SPS pellets were soaked in air at 1300°C for 2hrs to remove carbon contamination.

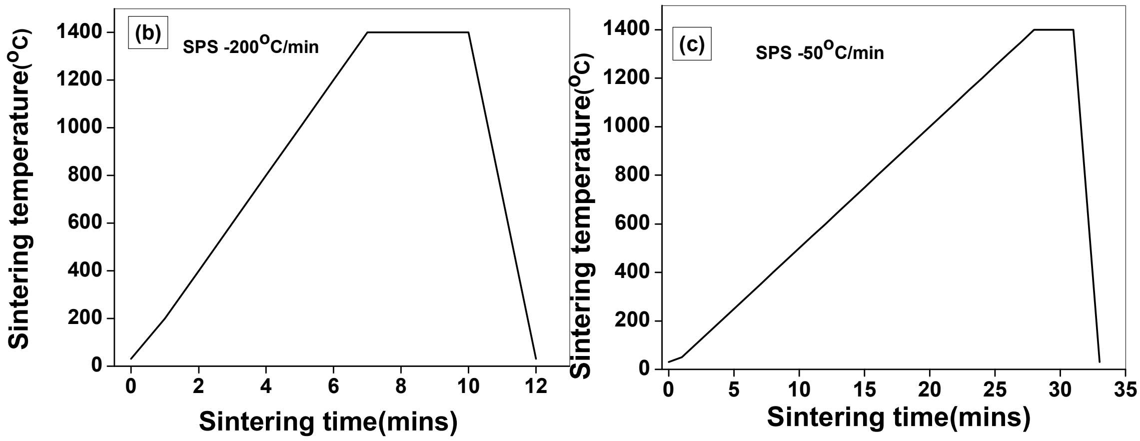

Fig 3.6(b)-(c) Temperature profile employed in SPS treatment

3.1.3.2 Conventional ramp and hold (CRH) processing of samples

CRH treatments were carried on compacts of preformed samples of same batches (PAT and PTAT-5). The compacts were conventionally heated to 1300°C for a dwell of 10 minutes in a PID controlled thermal cycling furnace (CMC, Industries) with two different heating rates of 50 and 100°C/min (maximum allowable heating rate) to 1300°C in order to limit the temperature to decomposition regime. The heat treatment schedules are shown in Fig 3.7(a)-(b).

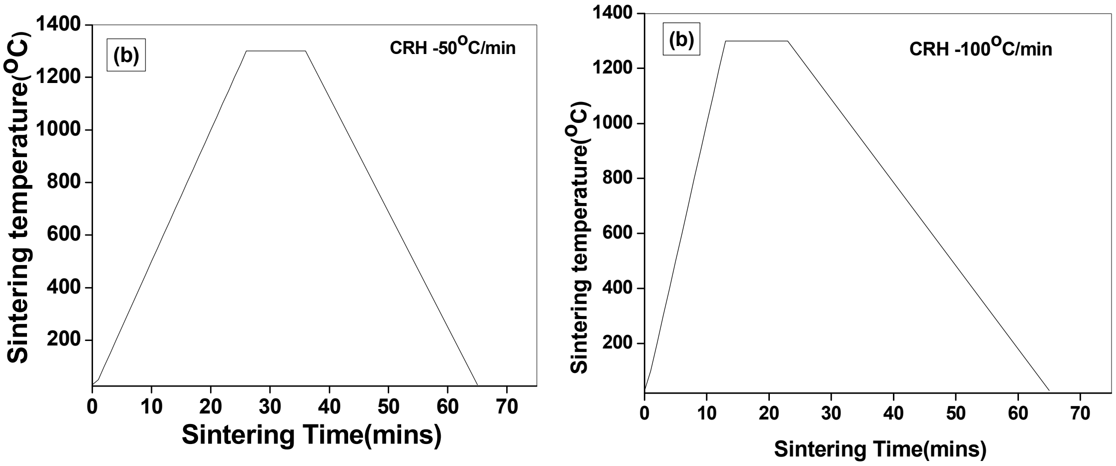

Fig 3.7 (a)-(b) Temperature profiles employed in CRH study

3.1.4 Characterisation of SPS and CRH Samples

3.1.4.1 XRD characterisation of SPS and CRH samples

X-ray diffraction patterns of the PAT and PTAT-5 samples sintered by SPS and CRH methods under different heating rates are shown in Fig 3.8 (a)-(d). Phase concentrations of Al_2TiO_5, α-Al_2O_3 and TiO_2 were calculated using the peak height intensity ratios and presented along with the XRD data. It is evident from the XRD pattern (Fig 3.8(a)) that PAT samples on exposure to spark plasma conditions, at a heating rate of 200°C/min has undergone the maximum decomposition retaining only 5% of Al_2TiO_5 phase. A corresponding increase in precursor oxide phases α-Al_2O_3 and TiO_2, are also evident from the XRD patterns. On decreasing the heating rate to 50°C/min (minimum possible with SPS facility), Al_2TiO_5 phase retention increased to 26% revealing that the heating rate plays a major role dictating the eutectoid decomposition.

Under SPS condition, at the initial stage of sintering as the powders are loosely packed the plasma will be generated between the graphite electrodes through the gaps in loose powders. The plasma generated in the initial stage is expected to clean the particle surfaces and results in nascent reactive surfaces leading to enhanced reactivity and more decomposition. It is important to point out that the decomposition of Al_2TiO_5 phase is strongly dependent on the reacting environments. As the SPS is carried out are under argon, the reduced partial pressure of oxygen also contributes to the enhanced decomposition. Decreased partial pressure of oxygen will increase the Ti^{3+} state which inturn increases Ti^{3+}/Ti^{4+} ratios and exchange of Al^{3+} against Ti^{3+} enhancing the Al_2TiO_5 phase decomposition. Even at 1400°C, AT could not be reformed due to partial oxygen pressure, no soaking (equilibrium is not achieved), inert atmosphere etc [14, 15, 37].

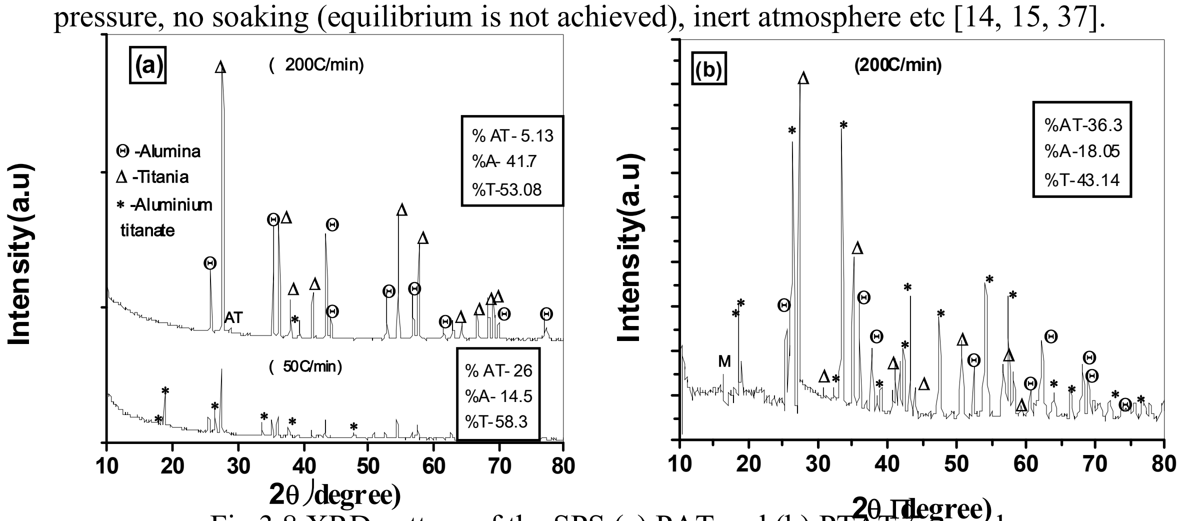

Fig 3.8 XRD pattern of the SPS (a) PAT and (b) PTAT-5 samples

However, magnesium silicate $(Mg_3Si_4O_{10}(OH)_2$ addition in PAT (i.e., PTAT-5) could substantially minimize the decomposition to 36% even with 200°C/min heating rate under SPS conditions against 5% retained with pure AT samples (Fig 3.8(b)). The crystallographic stabilization is responsible for the retention of 36% even with a heating rate of 200°C/min under SPS conditions. Simultaneous doping of MgO and SiO_2 in the Al^{3+} site, may lead to decomposition may result in crystallographic stabilization of the Al_2TiO_5 lattice [13]. XRD unit cell parameters and cell volume of PAT sample were a=9.4315Å, b=9.6385 Å, c=3.590 Å and 326.35 $Å^3$, which have increased to a=9.4651 Å, b=9.6715 Å, c=3.5981 Å and 329.37 $Å^3$ in case of PTAT-5 sample.

It is evident that, XRD pattern of the PAT sample exposed to CRH conditions of 50°C/min and 100°C/min has indicated significant retention of 85% and 80.9% Al_2TiO_5 phase respectively (Fig 3.8(c)). PTAT-5 samples, does not exhibited any significant decomposition in comparison to PAT samples under identical conditions.

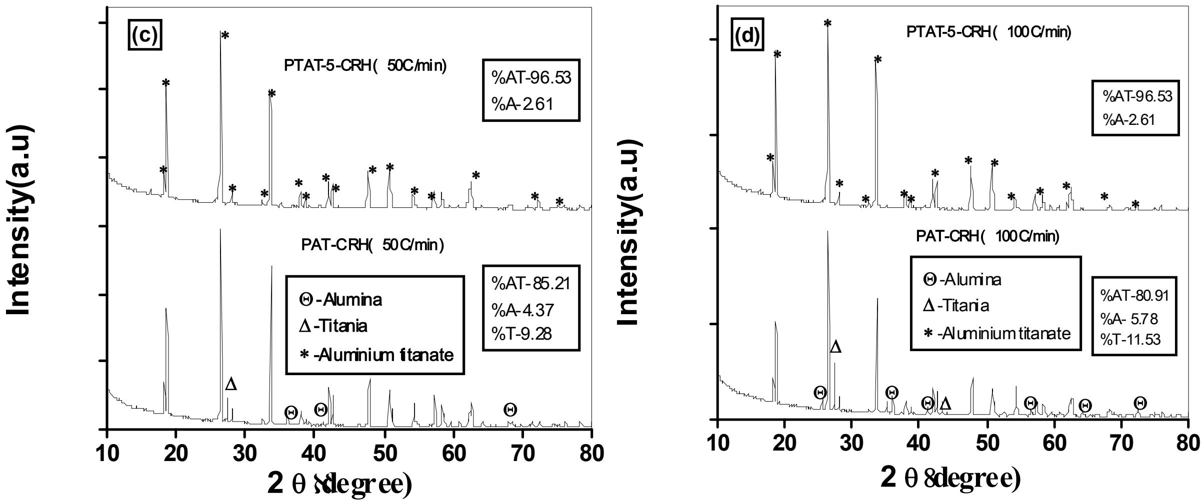

Fig 3.8 XRD pattern of the CRH treated (c) PAT and (d) PTAT-5 samples

3.1.4.2 Microstructural analysis

Microstructure of the PAT and PTAT-5 samples sintered by SPS method and different heating rates are shown in Fig 3.9. It was observed that PAT samples (from Fig 3.9 (a)-(b) exhibit a unique microstructure as a result of the non equilibrium heating and cooling experienced by sample in presence of plasma. The samples have shown a porous matrix with aggregates and elongated grains exhibiting unique texture.

It is evident from the micrograph of Fig 3.9 (a) that, in the case of partially decomposed AT samples there are particles on the surface of the grain and grain boundaries which are confirmed as alumina enriched composition through EDS analysis. These particles act as the nucleation sites resulting in the growth into elongated grains with average grain size of 0.8 µm with distributed porosity throughout the bulk in the case of fully decomposed (Fig 3.9 (b)) samples. The SPS treated PTAT-5 sample the microstructure is shown in Fig 3.9(c)

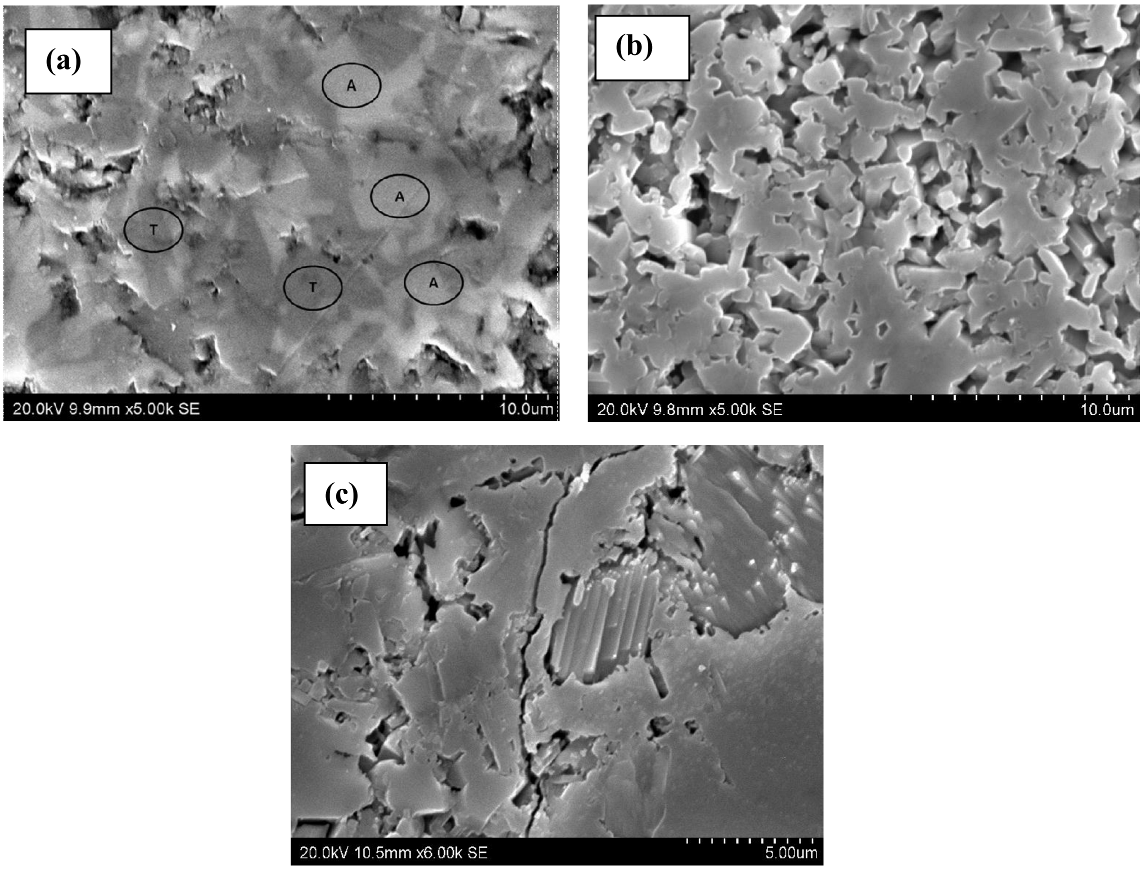

Fig 3.9. Microstructures of (a) Partially decomposed PAT sample (b) Fully decomposed PAT sample and (c) PTAT-5 sample under SPS condition (T and A corresponding to titania and alumina rich regions)

3.1.4.3 Dilatometric and high temperature XRD studies

In order to elucidate the decomposition, dilatometric measurements and high temperature XRD study were carried out for PAT and PTAT-5 samples. High temperature XRD facility (Ku Levenu, Belgium) used for the measurement of AT samples are shown in Fig 3.10(a). The dilatometric curves recorded for PAT and PTAT-5 samples at a heating rate of 5°C/min in air, using the facility already discussed before, are shown in Fig 3.10(b).

The AT samples were subjected to a heating rate of 20°C/min in high temperature XRD and patterns recorded for PAT samples at 30, 800 and 1000°C are shown in Fig 3.10(c).

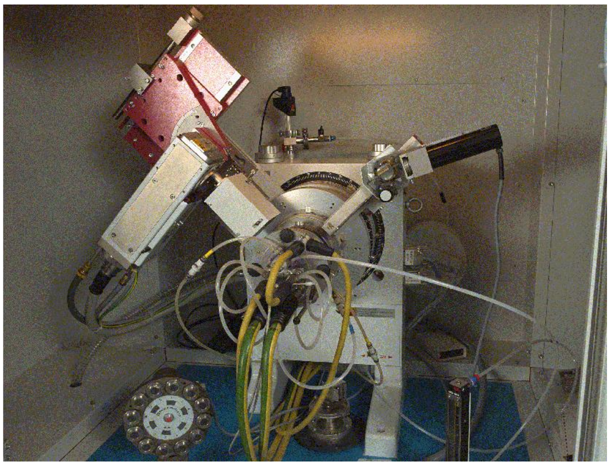

Fig 3.10(a) High temperature XRD facility (Ku Levenu, Belgium)

It is evident from dilatometric study that that PAT samples exhibited a negative slope change at ~ 1000°C indicating that the decomposition proceeds with a dimensional decrease. In Al_2TiO_5 structure, each Al^{3+} and Ti^{4+} cations are surrounded by six oxygen ions forming distorted AlO_6 or TiO_6 octahedra forming (001) oriented double chain.

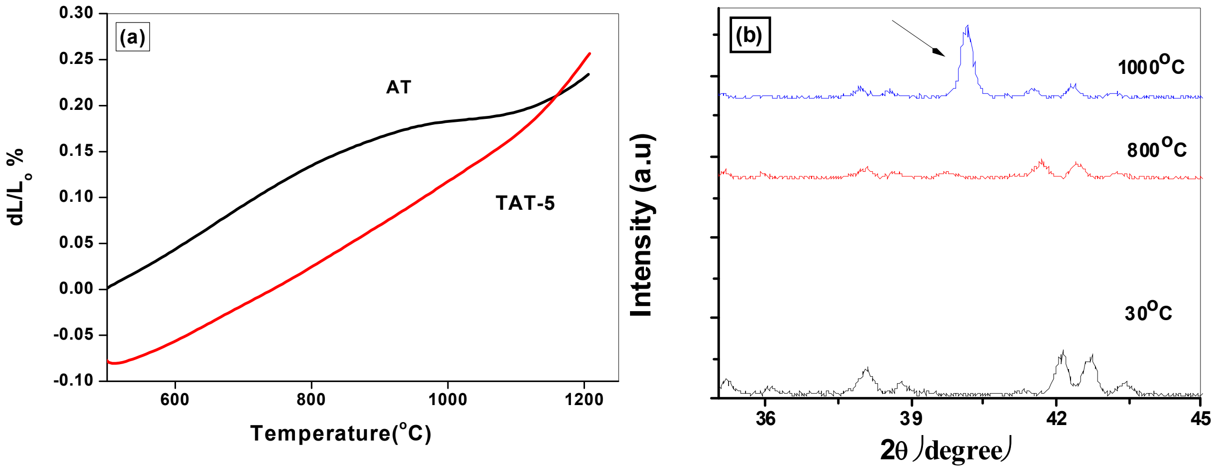

Fig 3.10 (b) Dilatometric curves of PAT and PTAT-5 samples and (c) XRD patterns recorded PAT sample at 800 and 1000°C with RT XRD

The dimensional decrease observed in the dilatometric study may impart elastic strain in the matrix. When the elastic strain energy surpasses the chemical driving force (ΔG) of decomposition, it results in dissociation into precursors oxides and is also dictated by the temperature ranges. It may be regarded as the strain energy surpasses the chemical driving force (ΔG) in the temperature regime of 1000°C–1200°C leading to spontaneous decomposition [3, 8, and 20].

High temperature XRD patterns recorded at 1000°C shows the appearance of a high intensity peak (Fig 3.10(c)) corresponding to a metastable phase at around sin2□=40° is observed. Probably the decomposition into α-Al_2O_3 and TiO_2 proceeds through this metastable phase.

3.1.5 Post Thermal CRH Cycling

Aluminum titanate samples on application as particulate trap practically undergoes several thermal cycles during the regeneration process. Incineration of carbon soot in presence of air may often results in temperature shoot up leading to hot spot formation and the temperature is reported to reach beyond 1200°C. Thermal cycling experiments for both PAT and PTAT-5 formulations were carried out in a Rapid thermal furnace. A typical cycle, from 28°C to 1200°C under a maximum heating rate of 100°C/min with a 10 minutes dwell time is shown in Fig 3.11. Thermal cycling was carried out for 10, 20 and 30 cycles under identical conditions. The samples with thermal cycling were subjected to flexure strength (45x 4x 3mm, as per type ASTM C 1161) and CTE measurements (25 x 4 x 4 mm).

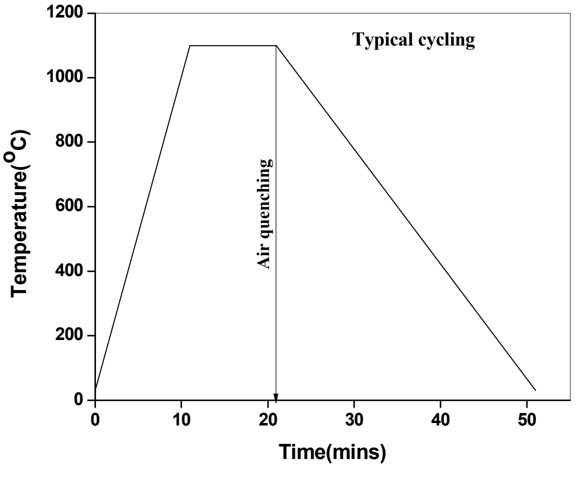

Fig 3.11 Thermal cycling schedule of the PAT and PTAT-5 samples

3.1.5.1 Characterization of post thermal cycled samples

Extent of decomposition of the samples, subjected to post thermal treatments, was evaluated using X-ray Diffraction technique. The polished samples were thermally etched and micro-structural observations were carried out using a scanning electron microscope

(S-4300SE/N, Hitachi, Tokyo, Japan). The XRD patterns of the thermally cycled PAT and PTAT-5 samples are depicted in Fig 3.12 (a)-(b). Further, a plot of retained Al_2TiO_5 phase and corresponding increase in precursor oxides against no. of thermal cycles is shown in Fig 3.12(c). It is evident from the XRD patterns that in case of PTAT-5 samples, the decomposition is completely eliminated and is also evident from the dilatometric curve (Fig 3.10(b)) showing no significant slope change imparting elastic strain in the matrix that leading to decomposition.

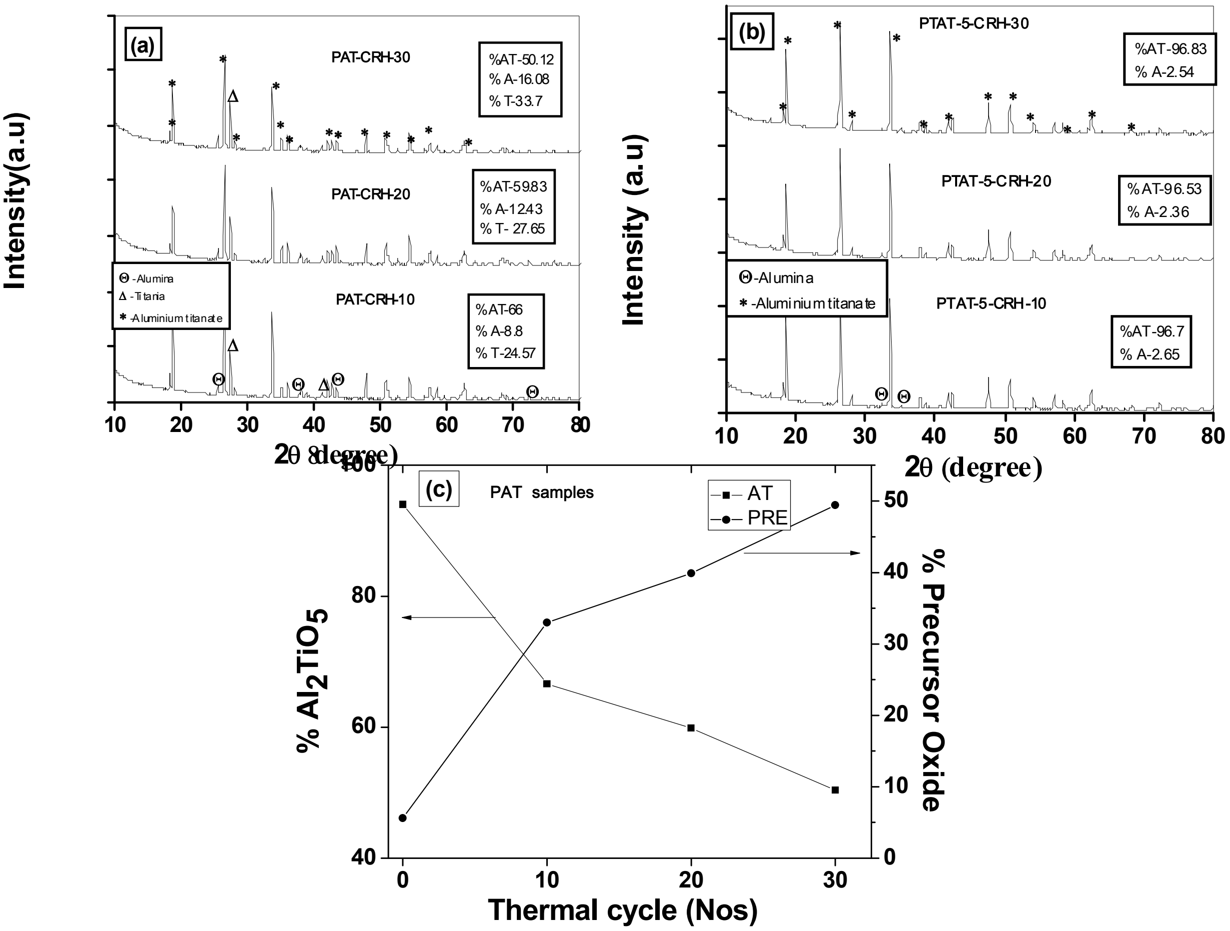

Fig 3.12 (a)-(b) XRD pattern of the thermal cycled (10, 20 and 30) PAT and PTAT-5 samples and (c) Plot of % Al_2TiO_5 phase retained and % of precursor oxide evolved under thermal cycling of PAT samples

It is interesting to note that (Fig.3.12(c)) the decomposition rate is maximum for first 10 cycles with decrease in decomposition rate exhibiting a non linear behaviour of the curves beyond 10 cycles. This can be attributed to the fact that unlike non equilibrium SPS conditions, CRH conditions follows chemical equilibrium and limits further decomposition of the bulk Al_2TiO_5 phase.

For the sake of comparison of the microstructures of PAT and PTAT-5 samples exposed to 30 cycles are also shown in Fig.3.13 ((a)-(b)). The CRH-PAT samples have shown a different microstructure in comparison to SPS-AT (Fig.3.9 (a-b)) with irregular grains and precursors precipitated occasionally. PTAT-5 samples under CRH conditions have shown occasional micro-cracking and no precipitations of precursor oxides could be seen.

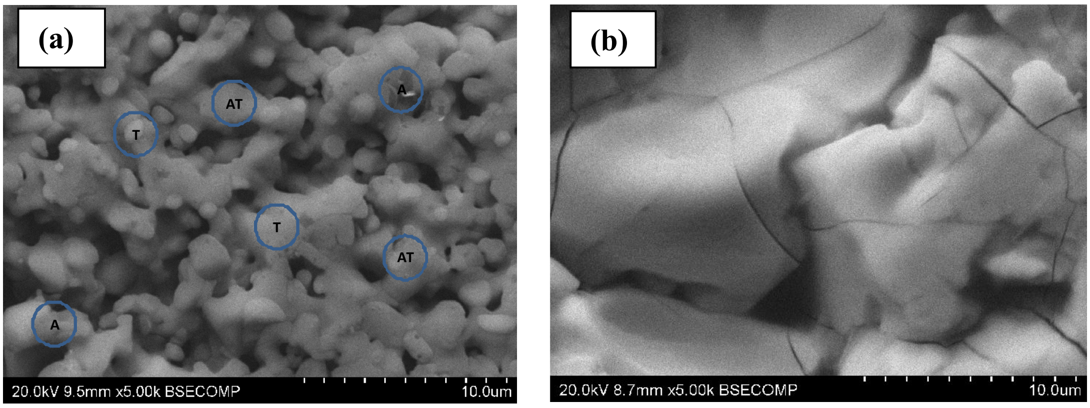

Fig 3.13 Microstructures of (a) PAT and (b) PTAT-5 samples exposed to 30 thermal cycles (AT, T and A corresponding to aluminium titanate, titania and alumina rich regions respectively)

Thermo-mechanical properties of thermal cycled PAT and PTAT-5 samples are represented in Table 3.1. It is evident that decomposition of AT in PAT samples results in composite matrix effect, precursor oxides are distributed in AT matrix which is responsible for improved mechanical properties like flexural strength and hardness. No significant change in thermo-mechanical properties of $Mg_3Si_4O_{10}$ $(OH)_2$ added Al_2TiO_5 (MSALT) samples.

Table 3.1 Flexural strength, hardness and CTE of PAT and PTAT-5 samples subjected to CRH thermal cycling conditions

Sample	**Flexural Strength (MPa)** $^{+}$	**Hardness(HV) ***	**CTE (x10^{-6}/^{o}C, 30-1000^{o}C)**
PAT-0cycling	11.83±1.5	170±20	1.09
PAT-30cycling	18.13±0.7	370±35	2.53
PTAT-5-0cycling	26.53±0.5	310±30	0.42
PTAT-5-30cycling	30.57±2	330±30	0.47

*($^{+}$ Avg of 5 readings, * Avg of 10 readings)*

3.1.6 Effect of Soaking on PAT and PTAT-5 Samples

The effect of soaking on decomposition was studied at the peak temperatures of 1000°C and 1100°C for 5 and 10 hours in a tubular furnace. PAT and PTAT-5 samples were heated to peak temperature at a heating rate 4°C/min and soaked for 5 and 10 hours, followed by furnace cooling to room temperature. XRD patterns and SEM micrographs of the PAT and PTAT-5 samples after soaking are shown in Fig. 3.14(a)-(e) and 3.14(f)-(i) respectively. Fig. 3.14(e) represents the plot of % of Al_2TiO_5 phase versus soaking time.

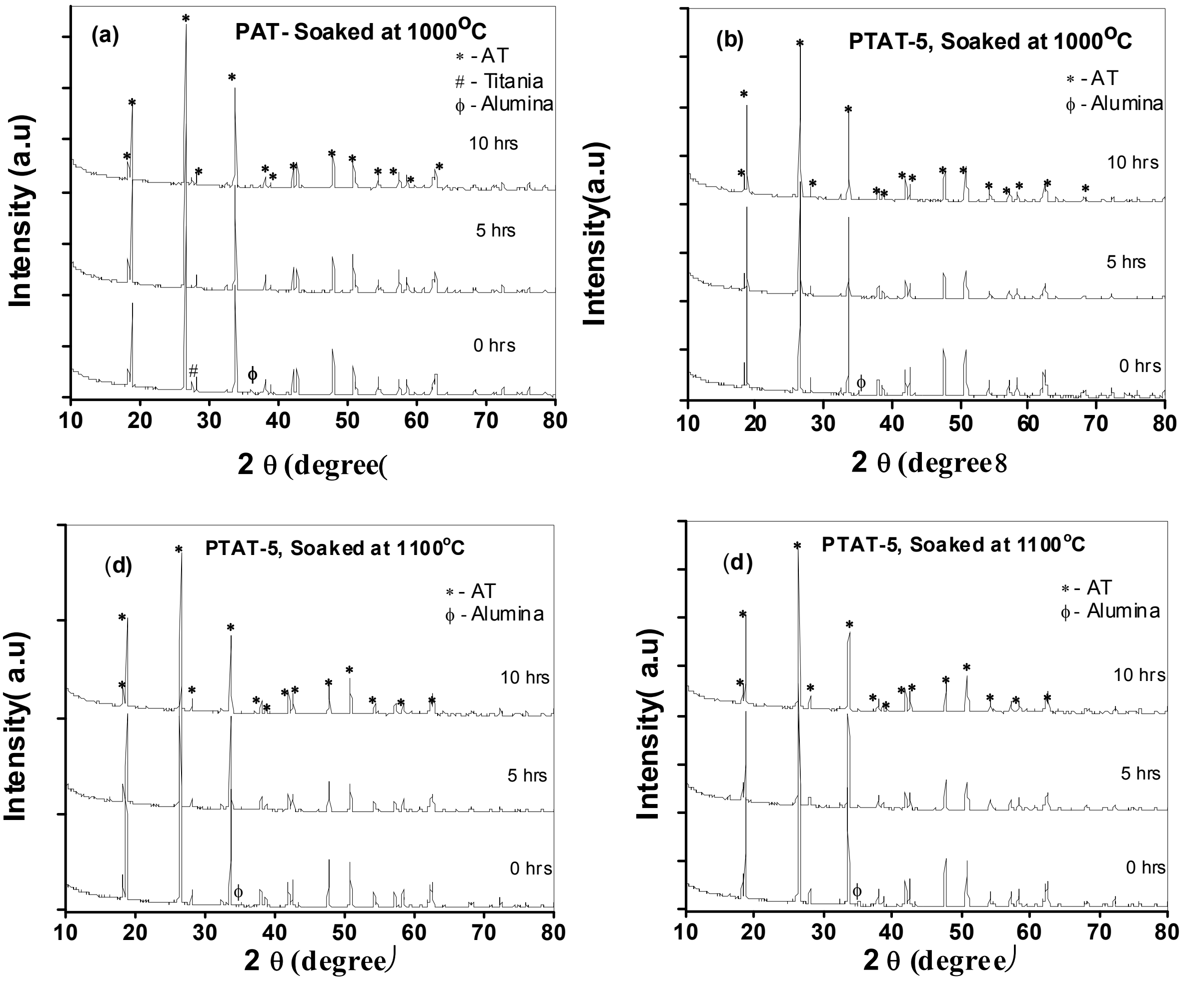

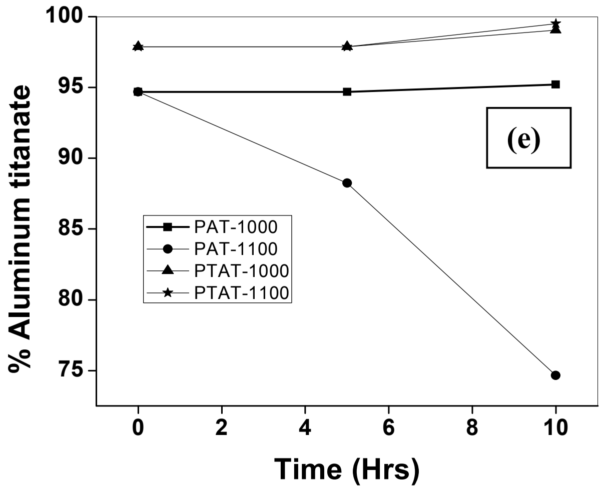

Fig 3.14 (a)-(d) XRD patterns of the PAT and PTAT-5 samples soaked at 1000 and 1100°C for 5 and 10 hrs and (e) represents the % AT as function of soaking time

Irrespective of initial concentration of Al_2TiO_5 phase and precursor oxides, there is no sign of eutectoid decomposition of Al_2TiO_5 phase till 5 h and 10 h at 1000°C for both PAT and TAT-5 samples. However, up to 7% decomposition has been observed for PAT samples soaked at 1100°C for 5 h and 21.13 % for 10 h with a corresponding increase in α-Al_2O_3 and rutile-TiO_2 phases. Decomposition is completely eliminated in PTAT-5 samples exhibiting thermal stability as a consequence of magnesium silicate addition. PTAT-5 samples observed in the present study can also correlates (lattice c–parameters 3.590 and 3.5981 Å calculated for PAT and PTAT-5 formulations) well with the earlier reports.

Further, SEM images show titania or alumina and alumina and titania (corresponding to AT) enrichment based on EDS elemental percentages as marked in the BSE images were shown in (Fig 3.14(f)-(i)), supporting the observations of XRD.

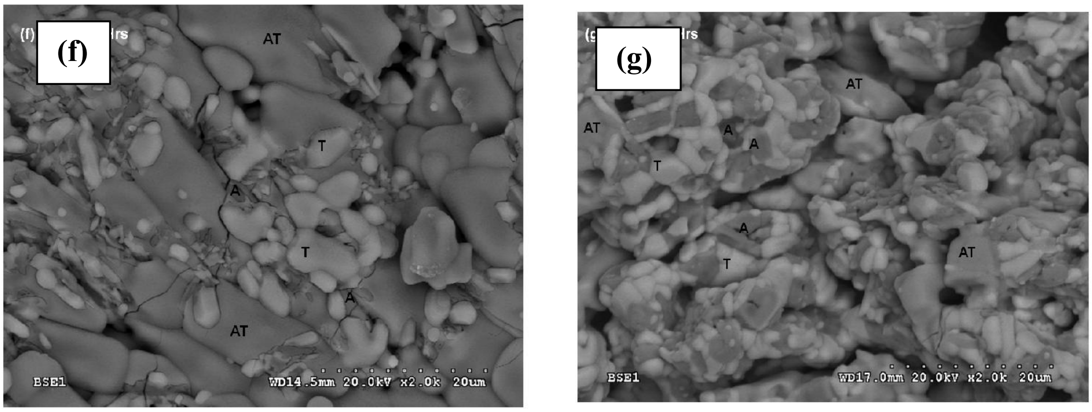

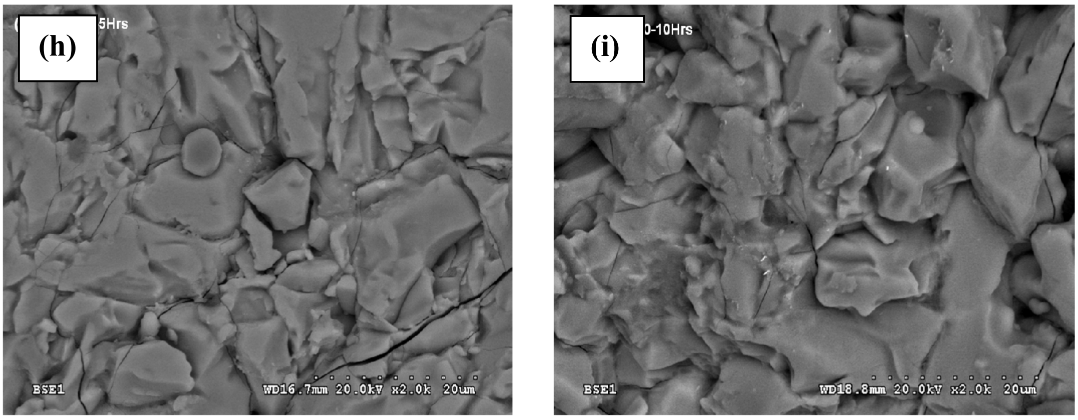

Fig 3.14 SEM micrographs of (f)-(g) PAT and (h)-(i) PTAT-5 samples soaked at 1100^oC for 5 and 10 hrs respectively

The enhancement of stability can be attributed to the larger c-constant which corresponds to the height of the distorted (MO_6) octahedra in the crystal structure of Al_2TiO_5, which minimises the distortion leading to the enhancement of stability.

3.2 Conclusion

Eutectoid phase decomposition of Al_2TiO_5 is studied under Spark Plasma (SPS) and Conventional Ramp and Hold (CRH) conditions. Decomposition of Al_2TiO_5 phase close to 100 % in the case of SPS conditions can be attributed to plasma generated in the initial stages of SPS condition that produces the reactive surfaces, extremely high heating rate of 200°C/min and argon atmosphere. $Mg_3Si_4O_{10}$ $(OH)_2$ addition in Al_2TiO_5 eliminated decomposition to considerable extent retaining the residual phase to 36% due to the crystallographic stabilization.

In Conventional ramp and hold heating with a heating rate of 100°C/min under pressure-less condition, PAT samples have shown Al_2TiO_5 phase decomposition to an extent of 54% after 30 thermal cycles and complete elimination of phase decomposition in case of $Mg_3Si_4O_{10}(OH)_2$ added Al_2TiO_5 (PTAT-5) samples has been observed.

A comparative evaluation of microstructure of samples is found to correlate well with the Al_2TiO_5 phase decomposition elucidated through XRD measurements and is further supported by micro-structural features exhibited irregular grains with precursors precipitated occasionally. Dilatometric measurements indicated slope changes in the temperature regime of decomposition and high temperature XRD at 1000°C exhibited an appearance of high intensity peak at around $\sin 2\theta = 40^\circ$ corresponding to a metastable phase. It can be concluded that decomposition into precursor oxides (α-Al_2O_3 and TiO_2) occurs through these metastable phase.

Thermal cycling exhibited the decomposition rate of maximum for initial 10 cycles with decrease in decomposition rate exhibiting a non linear behaviour of the curves beyond 10 cycles. A maximum decomposition is found to be 54% with PAT samples and complete elimination of decomposition with PTAT-5 composition. This can be attributed to the fact that unlike non equilibrium SPS conditions, CRH conditions follows chemical equilibrium and limits further decomposition of the bulk Al_2TiO_5 phase.

However, the enhancement of hardness and thermal expansion values were moderate in CRH thermally cycled ALT samples. Flexural strength values of CRH thermally cycled ALT samples also exhibited a marginal increase due to the composite matrix formation. No significant change in thermo-mechanical properties of $Mg_3Si_4O_{10}(OH)_2$ doped Al_2TiO_5 (MSALT) samples were observed.

On soaking at 1100°C for 5 hrs decomposition was limited to 7 % for PAT samples, which was increased to 21.13 % on soaking for 10 h with a corresponding increase in α-Al_2O_3

and rutile-TiO_2 phases. Decomposition is completely eliminated in PTAT-5 samples exhibiting thermal stability as a consequence of magnesium silicate doping.

In summary, $Mg_3Si_4O_{10}(OH)_2$ doping in Al_2TiO_5 has substantially increased the thermal stability under all CRH conditions including thermal cycling and soaking. Minimisation of decomposition even in extreme conditions under SPS is also evident from the study. Thus, PTAT-5 formulation provides possibility for technological exploitation.

3.3 References

1. S. Lang, C. Fillmore and L. Maxwell. The system berlia-alumina-titania: Phase relation and general physical properties of three components porcelain (1952).
2. L. Stanciu, J.R. Groza, M. Zaharescu. Microstructural investigations on aluminum titanate ceramics (1965).
3. E. Kato, K. Daimon, and J. Takahashi. Decomposition temperature of β- Al_2TiO_5, J.Am. Ceram. Soc. 63, 355-356 (1980).
4. A. Navrostky. Thermodynamics of formation of some compounds with the pseudobrookite structure of the $FeTi_2O_5$-Ti_3O_5 solid-solutions series, American Mineralogist, 60, 249-256 (1975).
5. B. Morosin and R.W. Lynch. Structure studies on Al_2TiO_5 at room temperature and 600ºC, Acta Crystallogr., B 28, 1040-1046 (1972).
6. J. Jung, A. Feltz and B. Freudenberg. Improved thermal stability of Al – Titanate solid solutions, *Cfi/ Ber. DKG* 70 No. 6, 299-301 (1993).
7. I. Brown and D. Mc Gavin. Effect of iron oxides additives Al_2TiO_5 on formation, Fourth Euroceramics. 4, 487-492 (1994). (Faenza editors. Italy)
8. V. Buscaglia, M. Alvazzi, P. Nanni, M. Leoni and C. Bottino. Factors affecting microstucture evolution during reaction sintering of Al_2TiO_5 ceramics. Ceramics Charting The Future. Edit. P. Vicenzini, Techna Srl., 1867-1875 (1995).
9. V. Buscaglia, F. Carracciolo, M. Leoni, P. Nanni, M.. Viviani, and J Lematre. Synthesis, sintering and expansion of Al0.8Mg0.6Ti2.1O5 low thermal expansion material resistent to thermal decomposition, J. Mater. Sci. 32, 6525-6531 (1997).
10. V. Buscaglia, R. Musenich, P. Nanni, and M. Leoni. Solid state reactions in ceramics systems in Proceedings of International Workshop on Advanced Ceramics, March 12-14, Inuyama, Japan, pp. 123-26 (1996).
11. M Ishitsuka, T. Sao, T. Endo and M. Shimada. Synthesis and thermal stability of aluminium titanate solid solutions. J. Am. Ceram. Soc., 70, 69-71 (1987).
12. H. Thomas and R. Stevens. Alumina titanate - A literature review. Part. Engineering properties and thermal stability, Br. Cer. Trans. J., 88, 184-190 (1989).
13. Z. Liu, O. Zhao and J.J. Yuan. The effects of additives on properties a structure of hot pressed aluminium titanate ceramics. J. Mater. Sci. Lett., 31, 90-94 (1996).

14. R. Naghizadeh and H.R. Rezaie, The influence of composition, cooling rate and atmosphere on the synthesis and thermal stability of aluminium titanate, Mater Sci & Engg B., 157, 20-25 (2009).

15. I.M. Low, Z. Oo and B. H. O. Connor, Effect of atmospheres on the thermal stability of aluminium titanate, Physica B., 385–386 [1] 502-504 (2006).

16. I.M Low and Z.Oo, Reformation of phase composition in decomposed aluminium titanate, Materials Chemistry and Physics 111, 9–12 (2008).

17. R.D. Duan, G.D. Zhana, J.D. Kuntz, B.H. Kear and A.K. Mukherjee, Spark plasma sintering (sps) consolidated ceramic composites from plasma-sprayed metastable Al_2TiO_5 powder and nano-Al_2O_3, TiO_2, and MgO powders, Mat. Sci & Engg A 373, 180–186 (2004).

18. L. stanciu, J.R. Groza , L. Stoica and C. Plapcianu, Influence of powder precursors on reaction sintering of Al_2TiO_5, Scrip. mater., 50, 1259–1262 (2004).

19. Y. Yang, Y. Wang, W. Tian, Z. Wang, Chong-gui li, Y. Zhaoa and H.M. Biana, In situ porous alumina/aluminum titanate ceramic composite prepared by spark plasma sintering from nanostructured powders, Scrip. mater., 60, 578–581 (2009).

20. L. Shou, R. Yu-Zhong, S. Yang and L. Jin-Rong, Crystalline phase and decomposition dynamics of aluminum titanate at different temperature, J. Struct.Chem, 79 [1] 79-84 (2012).

21. S. Djambazov, D. Lepkova and I. Ivanov, A study of the stabilization of aluminium titanate, J.Mater.Sci, 29, 2521- 2525 (1994).

22. T.S. Liu and D.S. Perera, Long-term thermal stability and mechanical properties of aluminium titanate at 1000-1200C, J.Mat.Sci, 35, 995-1001(1998).

23. R. Papitha, M.B. Suresh, D. Das, R. Johnson, Mineral oxide doped aluminum titanate ceramics with improved thermo-mechanical properties, J. Ceram., 214794,1-9 (2013).

24. R. Papitha, M.B. Suresh, D. Das and R. Johnson, High temperature flexure strength and thermal stability of near zero expanding doped aluminium titanate ceramics for DPF applications, Int. J. Appl. Ceram. Tech., (2013).

25. I.J. Kim, Thermal stability of Al_2TiO_5 ceramics for new diesel particulate filter applications- A literature review, J. Ceram. Pro. Res., 11[4] 411-418 (2010).

26. T. Boger, J. Jamison, J. Warkins, N. Golomb, C. Warren and A. Heibel, Next generation aluminum titanate filter for light duty diesel applications, SAE. Int., doi:10.4271/2011-01-0816 (2011).

27. K.A. Khor, L.G Yu, S.H. Chan and X.J. Chen, Densification of plasma sprayed YSZ electrolytes by spark plasma sintering (SPS), J. Eur. Ceram. Soc,. 20, 1855-1863 (2003).

28. K.A. Khor, L.G. Yu, S.H. Chan and X.J. Chen. Preparation yttria-stabilized zirconia electrolyte by spark-plasma sintering, Mater. Sci. Eng. A. 341, 43-49 (2003).

29. T. Takeuchi, M Tabuchi and H Kayeyam, Preparation of dense $BaTiO_3$ Ceramics with submicrometer grain by spark plasma sintering. J. Am. Ceram. Soc., 82, 939-943 (1999).

30. Z. Shen, M. Johnsson, Z. Zhao and M Nygren, Spark Plasma Sintering of Alumina. J. Am. Ceram. Soc,. 85, 1921-1927 (2002).

31. M.P. Harmer and R.J. Brook, Fast Firing - Microstructural Benefits, Tran. Br. Ceram. Soc. 80, 147-148 (1981).

32. M. Tokita, Trends in Advanced SPS Spark Plasma Sintering Systems and Technology, J. Soc. Powder Tech., Jpn. 30, 790-804 (1993).

33. L. Gao, Z. Shen, H. Miyamoto, M. Nygren, Superfast Densification of Oxide/Oxide Ceramic Composites, J. Am. Ceram. Soc., 82, 1061-1063 (1999).

34. J.R. Groza and A. Zavaliangos, Sintering activation by external electrical field, Mater. Sci. Engg. A. 287, 171-177 (2000).

35. M. Omori, Sintering and consolidation, reaction and crystal growth by the spark plasma system (SPS), Mater. Sci. Eng. A. 287,183-188 (2000).

36. M. Herrman, J. Rathel and I. Schulz, Spark Plasma Sintering/Field Assisted Sintering of ceramic materials, Inter. Ceram., 58, 109-114 (2009).

37. I.M. Low and W.K. Pang, In situ diffraction study of self-recovery in vacuum decomposed Al_2TiO_5, 49[1], 48 – 52 (2013).

Chapter-IV

Evaluation of Thermo-Mechanical Properties of AT and TAT-5 Specimens

4.0 Introduction

TAT -5 specimens have been found to exhibit superior physico-chemical properties. These formulations along with AT formulation were selected for the evaluation of thermomechanical properties. The formulations were prepared as per the procedure discussed in the previous chapter (section 2.2.1.5). Various ASTM standards and procedures were followed for the measurements as detailed below.

4.1 Experimental Procedure

4.1.0 Thermal Expansion Measurements

Thermo-dilatometry is a technique in which the dimension of a substance under negligible load is measured as a function of temperature, while the substance is subjected to a controlled temperature programmed heating (ASTM E 228-11). The dilatometer (Netzsch, 402 C) was used in the present study for thermal expansion measurements. The equipment is provided mainly with a sample holder, push rod, furnace, thermocouple and a data acquisition system for measuring temperature and change in dimension of the sample**.** The equipment is provided with an alumina sample holder, which is provided with a push rod, which transmits the change in length of the sample to the transducer and s-type thermocouple for measuring the temperature of the sample while heating. The furnace of dilatometer is equipped with silicon carbide with a PID which can be operated in air. In order to ensure the accuracy of the measurements sample temperature control (STC), thermocouple placed near the samples. The sample was subjected to predefined temperature program and the program is executed through a software in coordination with thermal analyser unit and data was acquiesced.

- **Part of the work being published in International Journal of Applied Ceramic Technology (JACT), DOI: 10.1111/ijac.12092, (2013)1-10.**
- **Part of the work being published in Journal of processing and application of ceramics, 7 [3] (2013) 143–146.**

The measured change in length includes both the sample holder expansion and the change in length of the specimen itself. The necessary correction (Δl_{system}) was applied by measuring the data with a standard reference sample under the same conditions of temperature program and heating rate, and then comparing the measured values with the tabulated reference data using the software.

$\Delta l_{system} = \Delta l_{std\ table} - \Delta l_{std\ measurement}$ *and* $\Delta l_{sample} = \Delta l_{sample\ measured} - \Delta l_{system}$,

where, Δl_{system} *- correction of the measuring system,* $\Delta l_{std\ table}$*-reference expansion value,* $\Delta l_{std\ measurement}$*-measured expansion of standard,* Δl_{sample}*- true expansion of sample,* $\Delta l_{sample\ measured}$*-measured uncorrected expansion of sample*

The mean coefficient of thermal expansion was calculated from the formula

$$\alpha_{av.} = \frac{L\ (T_1)}{[L\ (T_2) - L\ (T_1)] \quad (T_2 - T_1)}$$

Where, L- specimen length at room temperature

L (T_1) & L (T_2) – specimen lengths at T_1 & T_2 respectively.

4.1.1 Linear thermal expansion measurements of AT and TAT-5 samples

AT and TAT samples were cut into dimensions of 25 mm length x 6 mm width x 6 mm height as per the ASTM standards with both the sides polished to maintain the parallelism to achieve the close contact with the push rod during the measurements. The analysis was carried out under the following test parameters shown in Table 4.1.

Table 4.1 Test parameters used to measure thermal expansion of AT and TAT-5 specimens

Sr.No	Parameters	Ranges
1	Temperature range	30 to 1000°C
2	Heating rate	5°C/min
3	Atmosphere	Air
4	Sample holder	Alumina
5	Sample length	25mm
6	Sample cross section	6x6mm

Thermal expansion curves recorded for AT and TAT-5 samples are shown in Fig 4.1. Table 4.2 lists the thermal expansion values of AT and TAT-5 formulations from 30-1000ºC at an increments of 100ºC. It is evident that, TAT-5 samples have shown a lower CTE value of 0.42 x 10^{-6}/°C (30 -1000 °C) in comparison to 1.09 x 10^{-6}/°C (30 - 1000°C) observed with AT samples.

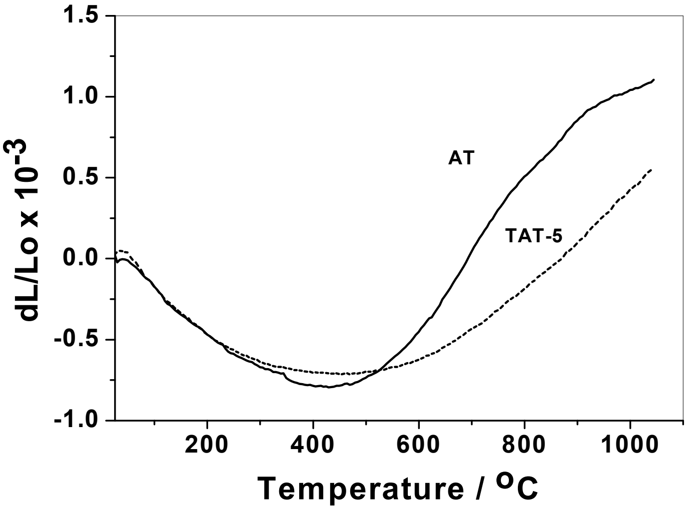

Fig 4.1 Thermal Expansion Curves of AT and TAT samples

It is evident from the plot that thermal expansion curves of both the samples initially exhibited shrinkage till 450ºC and followed by an expansion behaviour beyond 450ºC. Further, the curves exhibited a dissimilar behaviour, the curves corresponding to AT is tapered with a significant slope change beyond 900ºC unlike TAT-5 sample with a positive slope.

Table 4.2 Thermal expansion values of AT and TAT-5 formulations

Sr.No	**Sample Id**	CTE,10^{-6}/°C (30-600°C)	CTE,10^{-6}/°C (30-800°C)	**CTE,10^{-6}/°C (30-1000°C)**	**Hysteresis Area (cm^2)**
1	**AT**	-0.44	0.88	1.09	91
2	**TAT-5**	-0.624	-0.196	0.42	95

As the sample subjected to heating the microcrack healing takes places till 450ºC as marked by the platue. On further heating, the sample expands as monolithic since the microcrack healing is already completed. Low CTE value in the range of 30-450ºC, -

0.791 x 10^{-6}/°C corresponding to AT samples and -0.703 x 10^{-6}/°C for TAT-5 samples can be attributed to the compensation of expansion through healing of microcracks. Similar CTE values are also reported by several workers [1-4]. Kim et.al reported a coefficient of thermal expansion (CTE) value of 0.74 x 10^{-6}/°C in the temperature range of 30 to 1350°C for AT based ceramics[3].

4.1.2 Thermal hysteresis measurements

Heating and cooling curves of the AT and TAT samples during dilatometric analysis were recorded using the facility described above. Heating and cooling curves are depicted in Fig 4.2.

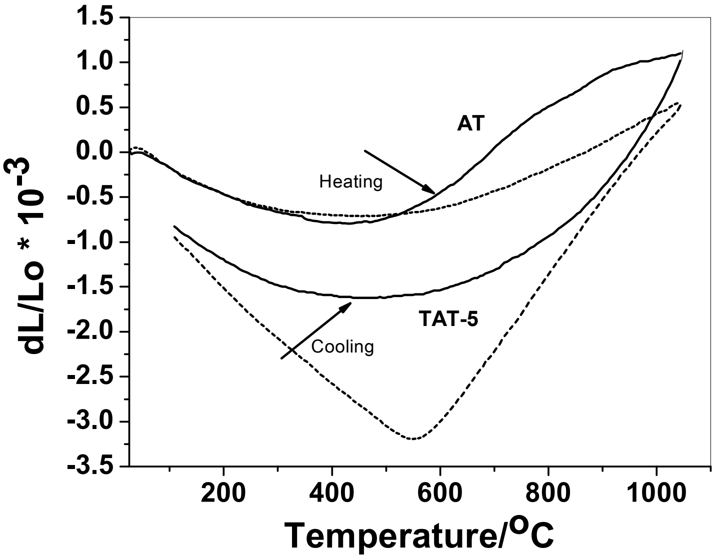

Fig 4.2 Thermal Hysteresis of AT and TAT samples

Though the heating curves have exhibited same similarity in AT and TAT samples, cooling curves are distinctly different for AT and TAT-5 formulations. TAT-5 specimen exhibited a deep well followed by a sharp expansion. Initial negative slope (1000–450°C) corresponds to the behaviour of a monolithic ceramic and expansion below 450°C can be attributed to the re-introduction of micro-cracks which were healed while heating. Significant variation in the heating and cooling curves can be attributed to the microcrack size and the density. Table 4.3 shows hysteresis area and estimated crack volume for AT and TAT samples.

Table 4.3 Comparison of Hysteresis area and estimated crack volume for AT and TAT-5 samples

Sr.No	Sample	CTE,10^{-6}/°C (30-1000°C)	Hysteresis area (cm^2)	Crack volume (%)
1	**AT**	**1.09**	**91**	**1.4**
2	**TAT-5**	**0.42**	**95**	**2**

A higher value of hysteresis area (95 cm^2) and crack volume (2 %) for TAT-5 samples in comparison to hysteresis area (91 cm^2) and crack volume (1.43 %) for AT samples is in good agreement with the low CTE value of 0.42 x 10^{-6}/°C (30-1000°C) observed for TAT-5 samples (as shown in Fig 4.3 and Fig 4.4). It is evident from Fig 4.4 that an increased in microcrack volume of 34% for TAT-5 samples, explains its low expansion behaviour [5-6].

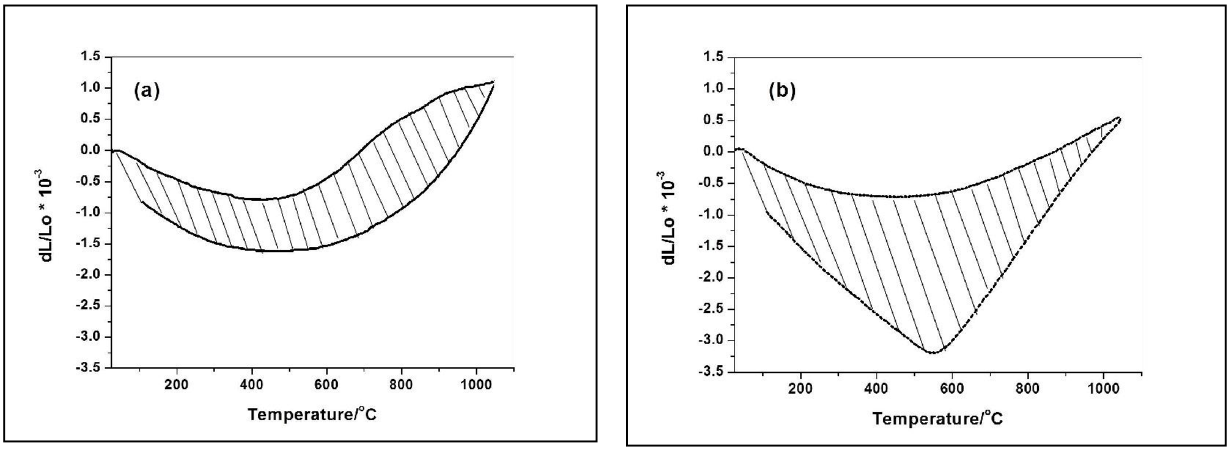

Fig 4.3 Thermal hysteresis area estimation (a) AT and (b) TAT-5 samples

A.Yoleva et.al has attempted to correlate thermal hysteresis behaviour of AT ceramics and demonstrated that a good correlation existing between thermal expansion value and thermal hysteresis [7].

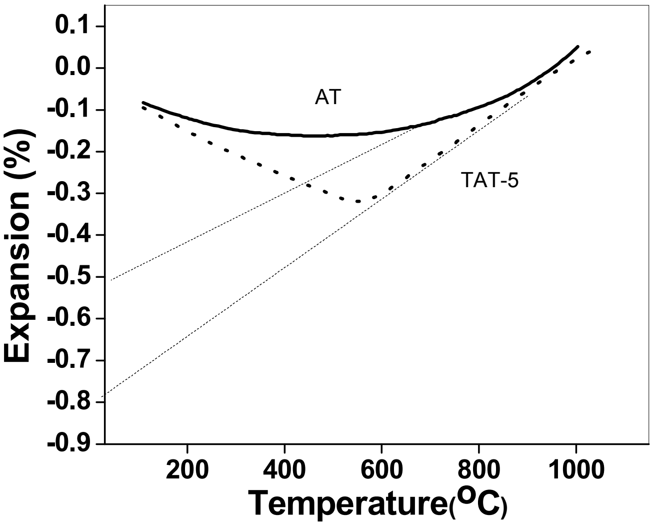

Fig 4.4 Crack volume estimation of AT and TAT-5 samples

4.2 Thermal Conductivity Measurements

Thermal conductivity measurements of AT and TAT-5 samples are carried out in NETZSCH LFA 429 Analyser shown in Fig 4.5. The sample is mounted on a carrier system, which is located inside a furnace of silicon carbide with S-type thermocouple. The furnace is held at a predetermined temperature. At this temperature the sample surface is then irradiated with a programmed energy pulse (laser). This energy pulse results in a homogeneous temperature rise at the sample surface. The resulting temperature rise of the sample on the other surface is measured by a high speed IR detector and thermal diffusivity values are computed from the temperature as a function of time.

The thermal diffusivity(a) is computed from the time/relative temperature increase data as follows,

$$\mathbf{a = 0.1388\ (l^2/\ t_{0.5})}$$

Where, l- sample thickness (mm) and $t_{0.5}$= time (s) at 50% of the temperature increase.

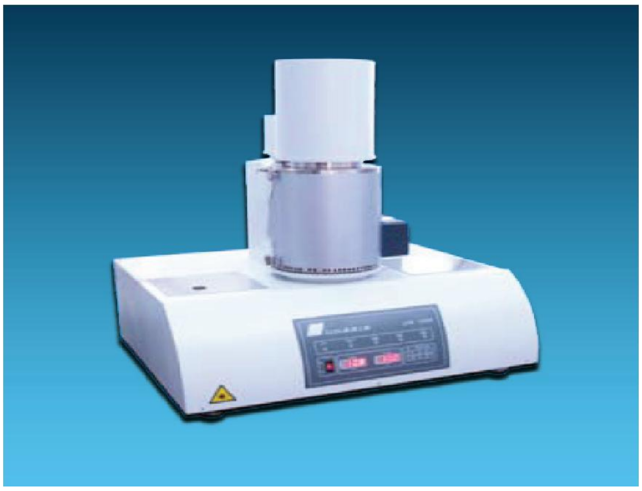

Fig 4.5 Thermal conductivity equipment

Thermal conductivity λ (T) is determined from thermal diffusivity (a), specific heat (C_p) and density (ρ) as a function of temperature as

$$\lambda(T) = a(T).\ C_p\,(T)\ .\rho(T)$$

The samples are ground into thin slabs of 10mmx10mmx3mm for thermal conductivity measurements. The samples are placed in alumina sample holder in the furnace. The analysis was carried out under the following test parameters shown in Table 4.4.

Table 4.4 Test parameters used for the measurements of the samples

Sr.no	Parameters	Ranges
1	Temperature range	30 to 700°C
2	Heating rate	10°C/min
3	Atmosphere	Argon
4	Sample holder	Alumina
5	Sample thickness	3 mm
6	Sample cross section	10x10mm

The samples are heated from 30-700°C at a heating rate of 10°C/min. Fig 4.6 ((a)-(b)) shows the thermal conductivity and thermal expansion values of AT and TAT-5 samples at high temperatures.

The plot of $dL/L_0 \times 10^{-3}/°C$ and thermal conductivity versus temperature of AT and TAT-5 samples are shown in Fig 4.6 ((a)-(b)) respectively. It is evident from Fig 4.6 ((a)-(b)) that the thermal expansion and thermal conductivity of both the samples have shown a decreasing trend till the temperature reaches 350 to 400°C. Beyond 400°C, a prominent slope change is evident in thermal conductivity. Where as, in the case of thermal expansion behavior the slope change is observed beyond 500°C. The observed decrease in thermal conductivity from room temperature to 400°C can be attributed to the low temperature phonon scattering in AT and TAT-5 samples [8]. In addition, the inherent microcracks in aluminum titanate ceramics are expected to play a major role in controlling the thermal behavior. However, the population of the microcracks and morphology (size and shape) of the microcracks are dependent on the micromechanical stresses generated at the grain boundaries due to the anisotropic expansion along the crystallographic axis [8-9].

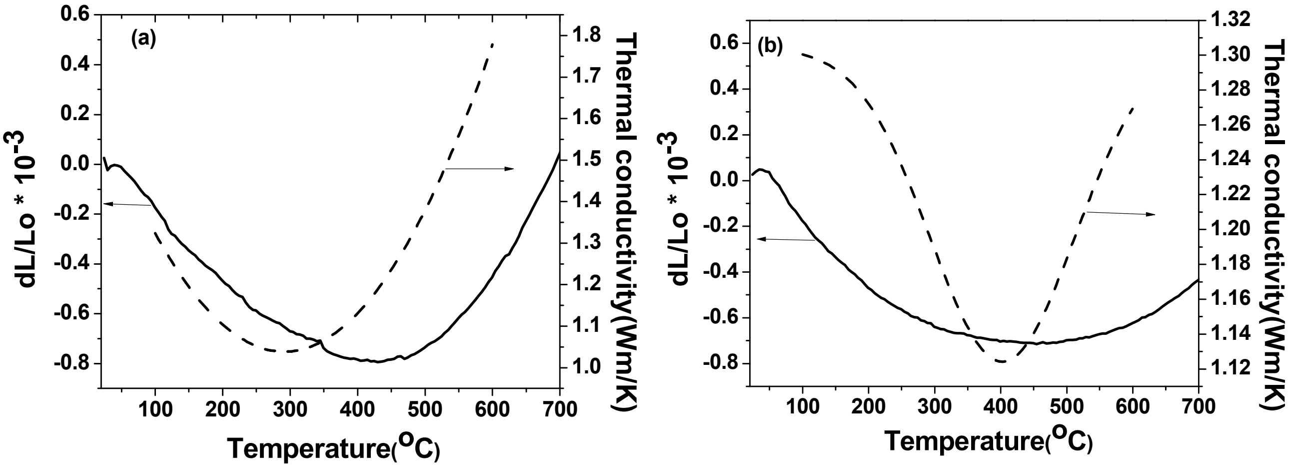

Fig 4.6 Thermal expansion and thermal conductivity values of (a) AT and (b) TAT-5 samples

Though phonon scattering is also operative which is responsible for the decrease in thermal conductivity, the observed increase in thermal conductivity beyond 400°C can be well correlated with the inherent microcracking healing which becomes more prominent. It can be understood that, as the temperature increases, inter and intra-granular cracks gets healed and provide paths for effective heat transfer through conduction. This observation also correlates well with the thermal expansion behavior. The inherent microcracks, which are open at room temperature, starts healing as the temperature increases and compensates for expansion till it reaches ~500°C. Above 500°C, the healing of the microcracks is almost complete and it expands as a monolith resulting in a plateau followed by a slope change indicating initiation of bulk expansion.

Relatively low thermal conductivity for TAT-5 samples in comparison to AT samples can be attributed to crystallographic substitution of Mg^{2+} and Si^{4+} to Al^{3+} site in Al_2TiO_5 generated as a result of the high temperature decomposition of magnesium silicate. Substitution of Mg^{2+} and Si^{4+} results in multivalent titanium (Ti^{3+}/Ti^{4+}) and oxygen vacancies and hopping of electrons in the vacant sites might promote the phonon scattering [10-11].

The low thermal expansion values observed in TAT-5 samples can be attributed to the increased crack density along with substanially low crack dimensions. However in case of , AT samples, the cracks were larger in dimensions depicted in Fig 4.7. Though distributed pores may arrest the crack propagation in case of AT samples low stress tolerance of the matrix leads to macro flaws. In the earlier sessions (Fig 4.2) the significant increase in crack volume is observed for TAT-5 samples through dilatometric hysteresis curves recorded during heating and cooling of samples. The study demonstrates a correlation of density and morphology of microcracks, which complements well with thermal expansion and thermal conductivity behaviour of tialite (AT) ceramics.

The study also reveals a significant decreases in coefficient of thermal expansion value estimated from the dilatometric curve, $-0.62 \times 10^{-6}/^{\circ}C$ (RT - 600°C) and a marginal decreases in thermal conductivity of 1.28 W/mK (at 600°C) for TAT- 5 samples in comparison to the thermal expansion of $-0.44 \times 10^{-6}/^{\circ}$ C (RT - 600°C) and thermal conductivity of 1.8 W/mK (at 600°C) for AT samples. There is a decrease in thermal properties of TAT-5 samples in comparison to the AT samples due to magnesium silicate addition. It is well known that on magnesium silicate addition, the cations ions substitutes for Al^{3+} in AT structure which significantly alter the microcracking due to the dilation along the crystallographic c-axis. The alternation in thermal properties can hence be attributed to the modifications in micro-crack density in combination with the morphology of the cracks resulting from magnesium silicate substitution [3, 7-8].

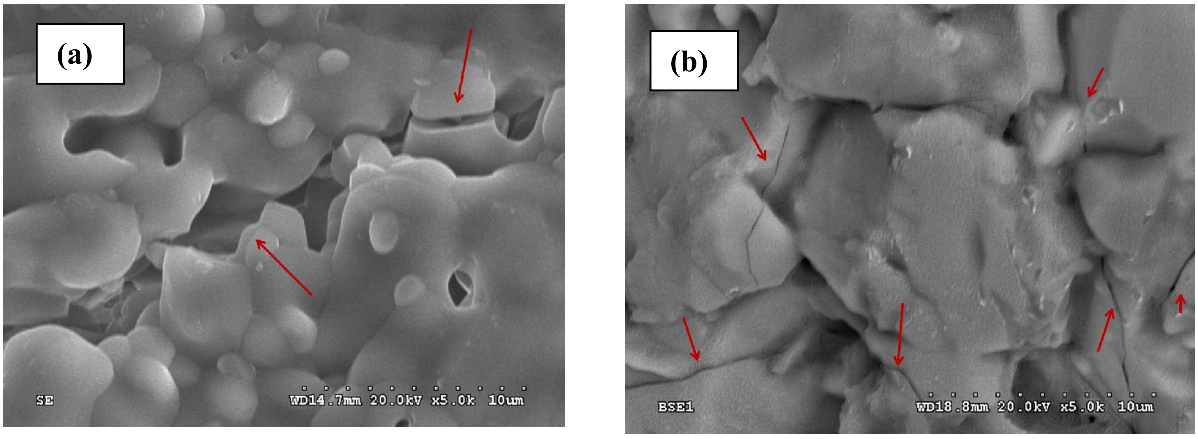

Fig 4.7 Microstructure of (a) AT and (b) TAT-5 samples

4.3 Flexural Strength Measurements

Flexural strength Measurements were carried out by 3-point bend measurement following ASTM C-1161-02C.

4.3.1 Preparation of the samples

AT and TAT -5 formulation were compacted into 63 x 63x 8mm using a hydraulic press and further sintered as per the procedure discussed in section 2.2.1.5. The samples were further machined to the rectangular specimens of 45 x 4 x 3 mm sizes and were ground and polished for the evaluation of the flexural strength. The flexural strength of AT and TAT-5 samples are tested at ambient temperature using a Universal Testing Machine (INSTRON -5584). Testing is carried out at cross head speed of 0.5mm/min and the sample span length was maintained at 40 mm. A typical load versus displacement curves are shown in Fig 4.8 (Though minimum of 5 samples were tested as the behaviour was almost identical only one curve is provided) and the flexural strength from 3-point bend test was calculated using the formula,

$$\boldsymbol{\sigma = \frac{3Pl}{2bd^2}}$$

Where, P is the maximum load, l is the span length, b is the breadth and d is the thickness of the sample.

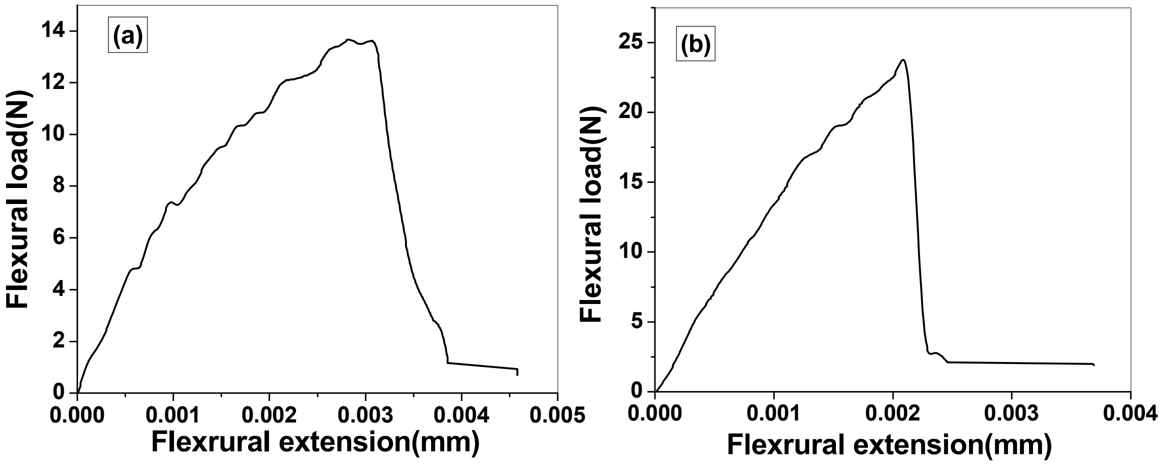

Fig 4.8 Load - displacement cure of (a) AT and (b) TAT-5 samples at room temperature

It is evident from Fig 4.8(a) that AT samples show a unstable crack extension with load drop after attaining peak flexural stress. A close look at the load–displacement curves obtained from the flexural loading of the AT samples (shown in Fig 4.8(a)) have shown several load excursions while on attaining peak load of 13N, corresponding to flexural strength of 16 MPa, depicting fracture over a wide range of strain followed by a gradual load drop. It is obvious that poor density (85%) and high porosity (shown in Fig 4.7(a)) are the factors that contributed, in addition to, the microcracks, to the fracture behavior observed with AT compositions. TAT-5 composition exhibited initial rapid increase in the stress, reaching a peak load of 23.5N, corresponding to flexural strength of 26 MPa, followed by the fracture (Fig 4.8(b)). It is clear that prior to the attainment of the peak flexural stresses, the material showed almost a linear increase in flexural stress with strain, indicating near-total elastic deformation, before final failure. This can be attributed to the existence of large number of micro cracks (Fig 4.7(b)). Microcracks are restricted within the grain, with maximum crack length < 10 μm, leading to the stable crack extension. Finally, the material fails with sudden load drop, which is an indication of rapid propagation of the macro cracks that resulted from coalescence of large number of micro cracks under local tensile loading [7-10].

SEM fractographs obtained from the specimens AT and TAT-5 tested till the failure under flexural (3–point bend loading) testing are shown in Fig 4.9 (a)-(b). These fractographs show an identical transgranular fracture. It is clear that TAT-5 specimen is associated with more microcracks and the crack paths. Hence crack initiated while propagation, encounters more microcracks needing alternative path. Such process needs higher fracture energy as compared to that required for AT, where microcrack densities are low [11-16].

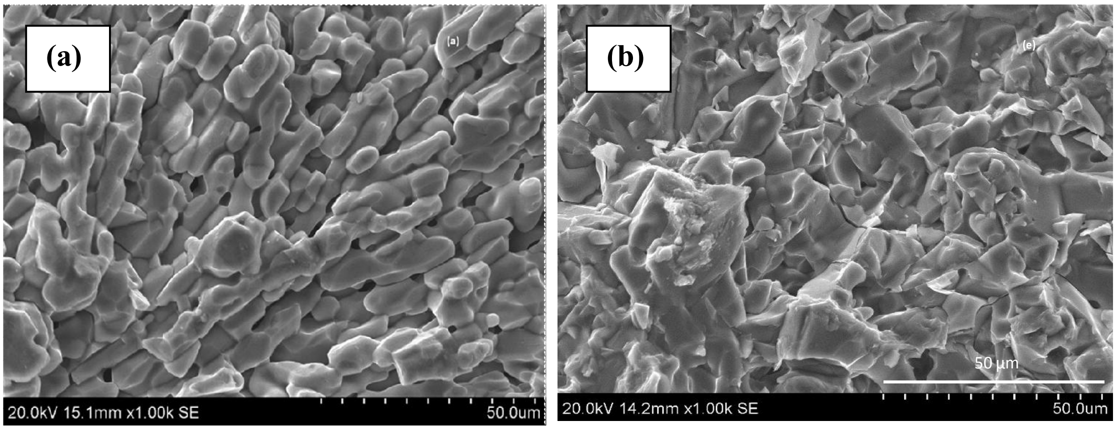

Fig 4.9 Fracture surfaces of (a) AT and (b) TAT-5 for room temperature testing

4.3.2 High temperature flexural strength of AT and TAT-5 specimens

High temperature flexural strength was measured at 600, 800, 1000 and 1200°C respectively using Hot MOR (OKAY, India) facility available at Defence Metallurgical Research Laboratory (DMRL), Hyderabad. The samples are heated at 5°C/min and load is applied at a rate of 0.005Kg/s. Fig. 4.10 ((a)-(b)) shows the flexure strength (MOR) at RT and at elevated temperatures for AT and TAT-5 specimens.

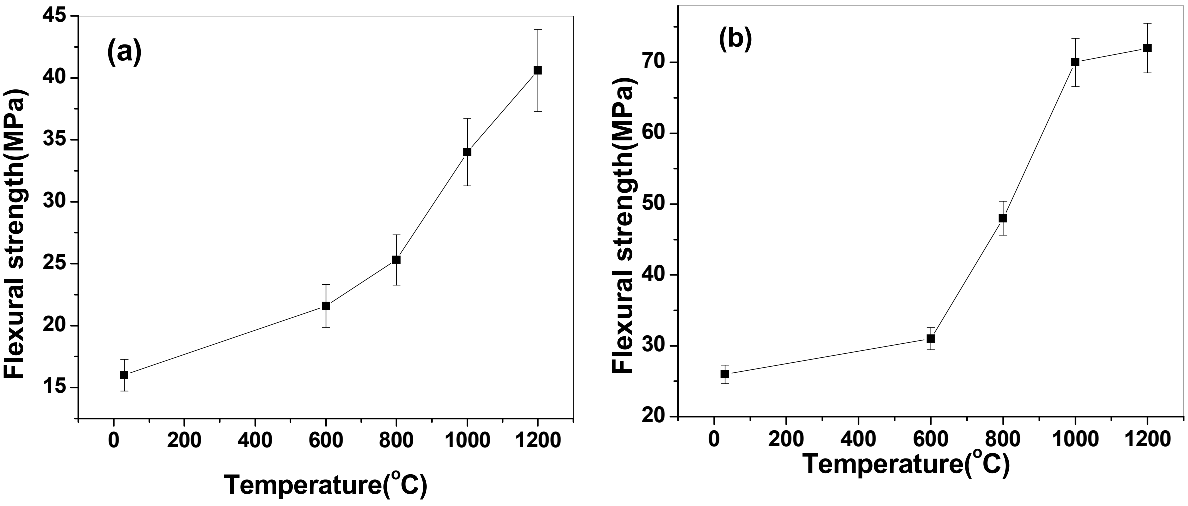

Fig 4.10 Flexure strength (MOR) at elevated temperatures for (a) AT and (b) TAT-5 specimens

The AT and TAT-5 specimens have shown almost identical behaviour till 1000°C, i.e., an increase in flexural strength with respect to temperature though the increase was substantial in case of TAT-5 samples at high temperature. Flexural strength of the TAT-5 specimen indicated a maximum improvement of 161.53% (68 MPa) at 1000°C in comparison to the room temperature flexural strength (26 MPa). Further increase in temperature from 1000°C to 1200°C indicated only negligible (~0.5%) increase exhibiting a stable behaviour. However, though there is a slope change in regimes of 1000°C - 1200°C in case of AT samples, saturation points are not achieved.

4.3.3 Correlation of thermal expansion and high temperature strength behaviour of AT and TAT-5 samples

Thermal expansion values estimated from the dilatometric curve (as per equation in section 3.11) and high temperature strength of AT and TAT-5 samples are shown in Table 4.5 and 4.6 respectively.

Table 4.5 Flexural strength and CTE values for AT at elevated temperatures

Temperature (°C)	***Flexural strength, (MPa)**	**Enhancement Flexural strength, (%)**	**Coefficient of Thermal Expansion, (10^{-6}/°C)**	**Enhancement in CTE, (%)**
30	16	-	-	-
600	21.6	20	-0.44,(30-600°C)	-
800	25.3	40.5	0.5, (30-800°C)	188
1000	34	88.8	1.09,(30-1000°C)	118
1200	41.6	131.1	-	-

(* *Avg of 5 readings)*

It is evident from Table 4.5 and 4.6 that trends in flexural strength exhibited a close similarity with thermal expansion behaviour at various temperatures for AT and TAT-5 samples confirming crack healing at these temperatures regimes. Enhancement in thermal expansion and flexural strength could be directly correlated to the proposed microcrack healing mechanism [20].

Enhancement of flexural strength, (σ_f) and CTE, (α) beyond 450°C can be attributed to thermally activated microcrack healing. Further, an identical increasing trend in both properties, (σ_f and α) at elevated temperatures reveals the increasing extent of thermally activated microcrack blunting mechanism. This is still operative at elevated temperatures upto 1000°C and a peak value at around 1200°C.

Table 4.6 Flexural strength and CTE values for TAT-5 at elevated temperatures

Temperature (°C)	***Flexural strength, (MPa)**	**Enhancement Flexural strength, (%)**	**Coefficient of Thermal Expansion, (10^{-6}/°C)**	**Enhancement in CTE, (%)**
30	26	-	-	-
600	31	19.2	-0.62, (30-600°C)	
800	48	84.6	-0.196, (30-800°C)	69.64
1000	68	161.5	0.42, (30-1000°C)	144.54
1200	70	169.2	-	-

(* *Avg of 5 readings)*

4.4 Hardness Measurements of AT and TAT-5 Samples

Vickers hardness was measured under a load of 4.9 N and at a dwell time of 15 s on the polished surface (as described in section 2.5) of the specimens sintered at 1550°C (ASTM F 1873-98). Table 4.7 shows that the TAT-5 specimen is 82.35 % more harder compared to AT specimens. A high hardness observed for TAT-5 samples can be attributed to the increased density value achieved through addition.

Table 4.7 Comparison of Vickers hardness value of AT and TAT-5 samples

Sr.No	**Sample**	**Hardness* (Kg/mm^2)**	**% increase in Hardness**
1	AT	170	-
2	TAT-5	310	82.35 %

(* *Avg of 10 readings)*

4.5 Compressive behaviour of AT and TAT-5 samples

Samples were cut into 10 mm^3 cubes for compressive strength determination and the load-displacement curves are shown in Fig 4.11(a)-(b). The samples were tested using compression testing setup attached with the Universal Testing Machine (INSTRON-5584), the strain rate was applied at a rate of 0.5 mm/min. The compressive strength values of AT and TAT-5 samples are 100 MPa and 178 MPa respectively.

The plots of compressive load versus strain show that in the case of TAT-5 samples, under compression, the critical stress increases to a peak value with a steep fall in flow stresses indicating more catastrophic failure in comparison to AT samples. Ceramic solids due to their inherent brittleness under compression generates micro cracks at the flaws or defects present in the solids, which propagates rapidly in the direction of the principal compressive stress. Curves for AT samples showing the spreading of the force of compression, though low, for longer period of time may be due to multiple crack initiation in presence of more flaws. A high compressive strength observed for TAT-5 sample even though contains high microcrack density, can be attributed to the significant reduction in size of microcrack, which may not lead to failure (Fig 4.7(b)).

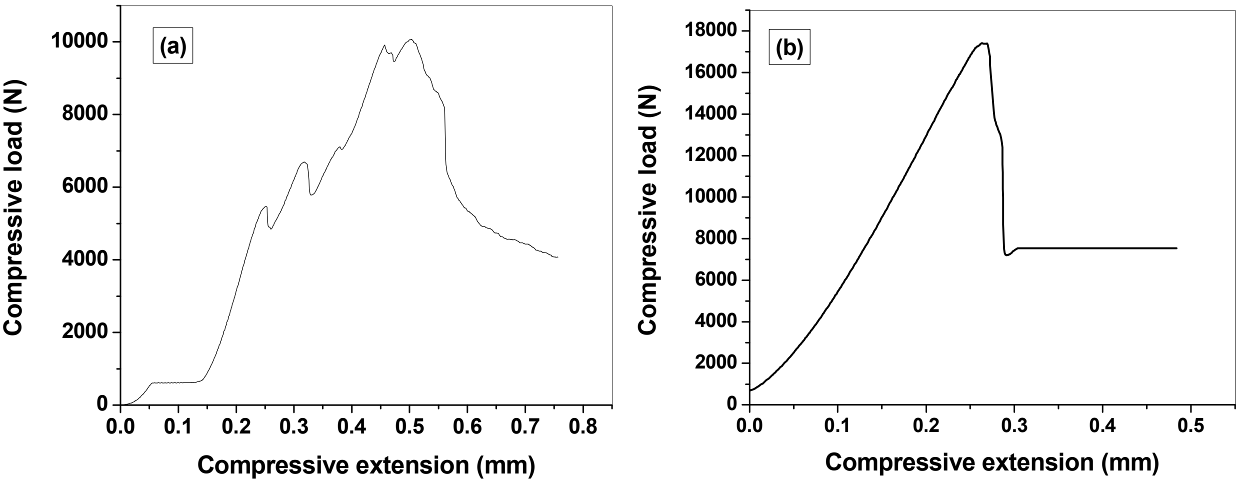

Fig 4.11 Load -displacement curves of (a) AT and (b) TAT-5 samples under compression testing

4.6 Conclusion

A significant decrease in thermal expansion values from 1.09 x 10^{-6}/°C to 0.42 x 10^{-6}/°C (30 -1000°C) is observed with magnesium silicate doping in AT. Thermal hysteresis area and crack volume estimation are found to be complementary with the observed thermal expansion values exhibited by AT and TAT-5 ceramics.

A correlation of density and morphology of microcracks has been established, which complements not only well with thermal expansion but also with thermal conductivity behavior of AT and TAT-5 ceramics as shown in the study. The study also reveals a significant decreases in the coefficient of thermal expansion value of -0.62 x 10^{-6}/°C (RT -600°C) and a marginal decreases in thermal conductivity of 1.28 W/mK (at 600°C) for TAT- 5 samples in comparison to the thermal expansion of -0.44 x 10^{-6}/° C (RT -600°C) and thermal conductivity of 1.8 W/mK (600 °C) for AT samples. The observed decrease in thermal properties of TAT-5 samples in comparison to the AT samples, due to magnesium silicate addition, can be attributed to the modifications in micro-crack density and the morphology of the cracks.

Flexural strength of the TAT-5 specimen clearly indicated an improvement of 161.53% (68 MPa) at 1000°C in comparison to the room temperature flexural strength (26 MPa). Enhancement of flexural strength, (σ_f) and CTE, (α) beyond 400°C can be attributed to thermally activated microcrack blunting. Further, an identical increasing trend in both properties, σ_f and α at elevated temperatures upto 1000°C reveal the increasing extent of thermally activated microcrack healing. The flexural strength remains almost constant at around 1200°C.

The enhancement in mechanical properties, such as flexural strength, hardness, fracture toughness and compressive strength of the TAT-5 ceramics can be attributed to the high sintered density of the samples as a result of magnesium silicate doping in AT samples.

4.7 References

1. S.M. Meybodi, H.B. Bafrooei, T.Y. Ohya and Z. Nakagawa. Grain boundary microcracking due to thermal expansion anisotropy in aluminium titanate ceramics, J. Am. Ceram. Soc., 70 [8] 184-186 (1987).
2. C.H. Chen and H. Awaji. Temperature dependence of mechanical properties of aluminium titanate ceramics, J. Eur. Ceram. Soc., 27, 13-18 (2007).
3. H.C. Kim, K.S. Lee, O.S. Kweon, G.C. Aneziris and I.J. Kim, Crack healing, reopening and thermal expansion behaviour of Al_2TiO_5 ceramics at high temperature, J. Eur. Ceram. Soc., 27, 1431-1434 (2007).
4. G. Bruno, A Efremov, B. Wheaton, I. Bobrikov, V.G. Simkin and S. Misture, Micro- and macroscopic thermal expansion of stabilized aluminum titanate, J. Eur. Ceram. Soc. 30, 2555–2562 (2010).
5. Y. Ohya. Measurement of crack volume by using dilatometer, J. Mater. Sci., 31, 1555-1559 (1996).
6. M. Milosevski, O. Ondracek, R. Milisevsk, D. Spasesk and A. Dimeska, Thermal expansion and mechanical properties of Al_2TiO_5 – SiO_2 System, Ceramics Charting the Future. (Edit. P. Vicenzini, Techna Srl.) 1875-1882 (1995).
7. Y. Djambazo and A. Hristo, Effect of SiO_2 addition on thermal hysteresis of aluminum titanate, Journal of University of Chemical Technology and Metallurgy, 45[3] 269-274 (2010).
8. T. Matsudaira, Y. Matsumura, S. Kitaoka and H. Awaji, Effect of microstructure on the fatigue behavior of aluminum titanate ceramics, J Mater Sci, 44, 1622–1632 (2009).
9. M. Milosevski, Thermal Diffusivity of Al_2TiO_5, $CaTiO_3$ and $BaTiO_3$, Science of Sintering, 29 [2] 105-112 (1997).
10. Y. Ohya and Z. Nakagawa, Grain boundary microcracking due to thermal expansion anisotropy in aluminium titanate ceramics, J. Am. Ceram. Soc., 70, 184-186 (1987).
11. G. Naderi, H.R. Rezaie, S.F. Ali, R. Naghizadeh and S. Atashgar, The effect of talc on the reaction sintering, microstructure and physical properties of Al_2TiO_5 based ceramics, J. Ceram. Process. Res., 10[1] 16-20 (2009).

12. K. Hamano, Y. Ohya and Zenbe, Crack propagation resistance of aluminium titanate, Int. J. High tech Cers., 1, 129-135 (1985).
13. J. Rodel, Crack closure forces in ceramics: Characterization and formation, J. Eur. Ceram. Soc., 9, 323-334 (1992).
14. T. Shimada, M. Mizuno, K. Katou, Y. Nurishib, M. Hashibab, O. Sakuradab, D. Mizunob and T. Onob, Aluminum titanate-tetragonal zirconia composite with low thermal expansion and high strength simultaneously, Solid State Ionics, 101-103 [2] 1127-1133 (1997).
15. P. Oikonomou, Ch. Dedeloudis, C.J. Stournaras and Ch. Ftikos, Stabilized tialite-mullite composites with low thermal expansion and high strength for catalytic converters, J. Eur. Ceram. Soc., 27, 3475-82 (2007).
16. A. Tsetsekou, A comparison study of tialite ceramics doped with various oxide materials and tialite–mullite composites: microstructural, thermal and mechanical properties, J. Eur. Ceram. Soc., 25, 335–348 (2005).
17. H. F. Perera, A. Pajares and J. J. Melendez, Strength of aluminium titanate/mullite composites containing thermal stabilizers, J. Eur. Ceram. Soc., 31, 1695–1701 (2011).
18. T. Matsudaira, S. Kitaoka , Y. Kuzushima , H. Awaji and D. Igimi, Temperature dependence of fatigue behavior of aluminum titanate ceramics, J Soc Mat Sci. 53,607-612 (2004).
19. L. Giordanoa, M. Viviania, C. Bottinoa, M.T. Buscagliaa, V. Buscagliaa and P. Nanni, Microstructure and thermal expansion of Al_2TiO_5–$MgTi_2O_5$ solid solutions obtained by reaction sintering, J. Eur. Ceram. Soc., 22, 1811–1822(2002).
20. M. Takahashi, M. Fukuda, M. Fukuda, H. Fukuda and T. Yoko, Preparation, structure, and properties of thermally and mechanically improved aluminum titanate ceramics doped with alkali feldspar. J. Am. Ceram. Soc., 85[12] 3025-3030 (2002).
21. I.J. Kim, Thermal stability of Al_2TiO_5 ceramics for new diesel particulate filter applications-a literature review. J. Ceram. Pro. Res. 11, 411-418 (2010).

22. H. Morishima, Z. Kato, K. Uematsu, K. Saito, T. Yano and N. Ootsuka, Synthesis of aluminium titanate - mullite composite having high thermal shock resistance, J. Mater. Sci. Lett., 6, 389-390 (1987).
23. C.A. Botero, E. Jimenez-Pique, C.B. Ebadzadeh and M. Tazike, Microstructure and mechanical properties of Al_2O_3–20 wt% Al_2TiO_5 composite prepared from alumina and Titania nanopowders. Ceram Int. 39, 977–982 (2013).

24. B. Freudenberg and A. Mocellin, Aluminum titanate formation by solid-state reaction of fine $Al_2O_3$and TiO_2 Powders, J. Am. Ceram. Soc., 70[1] 33-38 (1987).

Chapter-V

Shaping of TAT-5 Formulation into Components

The emerging applications of aluminum titanate ceramics due to their inherent combination of thermo-mechanical properties are presented in Fig. 5.1. In the present study an attempt has been made with newly developed TAT-5 ceramics to extrusion form honeycomb structures. It is well known that honeycomb structures are used for Diesel Particulate Filter (DPF) in automobiles.

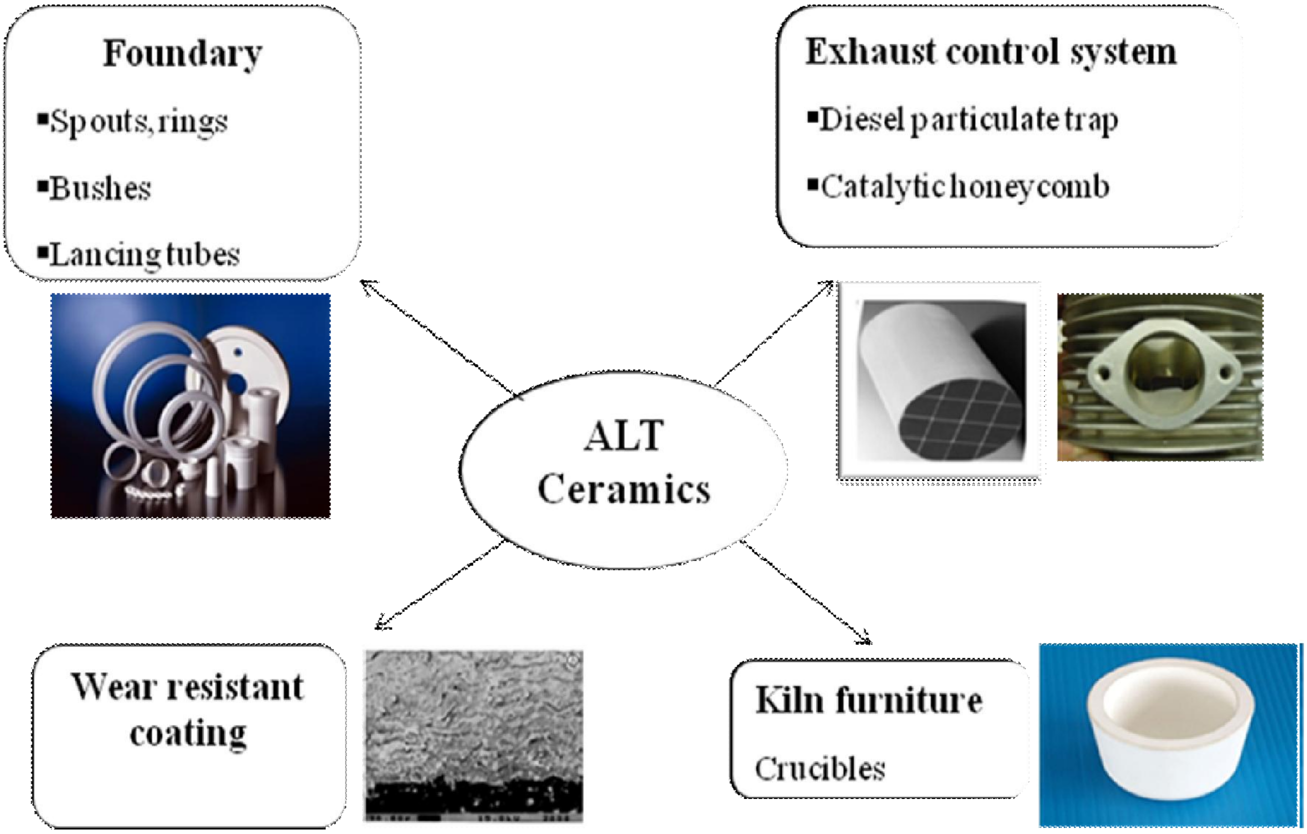

Fig 5.1 Aluminum titanate ceramics: Applications [Courtesy Ceram Tec, USA and NGK Insulators](Fracture surface of ALT ceramics coating on engine parts)

Part of the work being, published in Trans Indian Inst Metals. DOI 10.1007/s12666-011-0096-3 (2011)

5.1.0 Exhaust Emission Control

Diesel engine emissions are highly complex mixtures consisting of a wide range of organic and inorganic compounds distributed among the gaseous and particulate phases. Public health concern has arisen about these emissions for the following reasons:

- Particulates in diesel emissions are respirable
- Particles have hundreds of chemicals adsorbed onto their surfaces, including many carcinogens
- Gaseous phase contains many irritants and toxic chemicals.

Out of the various options to control these pollutants after treatment devices such as catalytic control using honeycomb supported catalyst and particulate traps with wall flow filters is gaining importance. Silicon carbide (SiC) and Cordierite are the two material in use for these applications. Cordierite ($2MgO-2Al_2O_3-5SiO_2$) with it's low coefficient of thermal expansion and high thermal shock has specific advantages but is limited by its low heat capacity and low melting point 1450°C. SiC, though satisfies most of the requirements, it exhibits lower thermal shock resistance and thus needs to be segmented leading to substantial increase in cost. Aluminum titanate with novel additives is considered as the new generation DPF material due to its inherent high refractoriness with high melting point [1-6]. A comparative evaluation of candidate materials in use is shown in Table 5.1.

A typical after treatment device with continuous soot regeneration is shown in Fig. 5.2. Monolithic honeycomb filters are generally processed by extrusion.

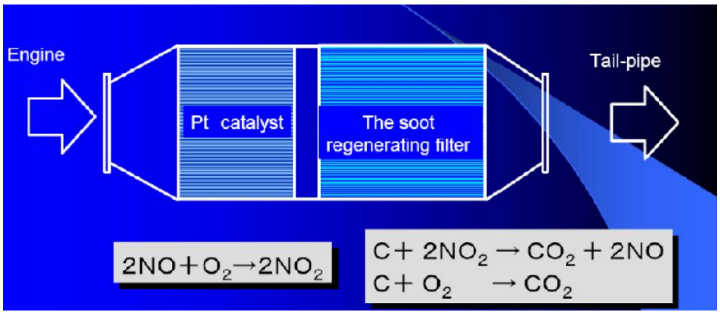

Johnson Matthey CRT™

Fig 5.2 Continuous soot regeneration device consisting of low thermal expanding honeycombs

Table 5.1 Candidate materials for exhaust control and their critical properties

Properties	**SiC**	**Cordierite**	**AT**
Density(g/cm^3)	3.1-3.2	2.1	3.3
CTE(x10^{-6}/°C) (30-1000 °C)	4.7-5.2	0.9-2.5	-0.5- 2.5
Thermal conductivity (W/mK)	90	1-3	1.5-3
Thermal application limit (°C)	1500	1350	1500
Corrosion resistance	acceptable	poor	acceptable

[Ref: J. Alder, Int. J. Appl. Ceram. Technol., 2 [6], (2005)]

5.1.1 Extrusion Processing of Ceramics

Extrusion forms one of the prominent techniques for the manufacture of ceramic parts with complex and symmetric shapes, especially honeycomb structures. This process involves forming plastic, easily deformable dough of the fine ceramic powder, by mixing the powder with suitable binders, additives and solvent [7-9]. The dough thus formed is subsequently extruded, that is forced through a die so as to form the desired shapes, followed by drying and sintering to get the product. To achieve defect free honeycomb structures it is necessary to ensure that (a) the dough extrudes neatly and homogeneously at the operating pressure without deforming the die, and (b) the extrudate has green strength sufficient enough to maintain its shape integrity during extrusion and subsequent operation [10-13].

An extrusion mix is a two-phase material system consisting of a solid and a liquid phase. With an optimum quantity of liquid medium along with binder, plastizier the solid phase can be deformed into the desired shape as per the dimensions of the die. Generally for extrusion, the rheological behaviour of this paste is preferred to be pseudoplastic or shear thinning. This is mainly because the shear produced by the extrusion process reduces the viscosity, so that the material can flow easily through the die and immediately after extrusion from the die, due to the loss of shear, the high viscosity can be regained for better rigidity of the extrudate [14]. The quality of extrusion requires a balance of the materials, additives and processing to achieve the desired properties of the extrudates. The rheology of the batch and extrusion parameters needs to be well controlled to prevent the extrusion defects [15]. This necessitates the use of an effective screening tool to evaluate the effect of additives so that the compositions can be formulated as per the required specifications. The various parameters on which the dough rheology depends and which in turn effect the quality of the extrudate are shown in Fig. 5.3.

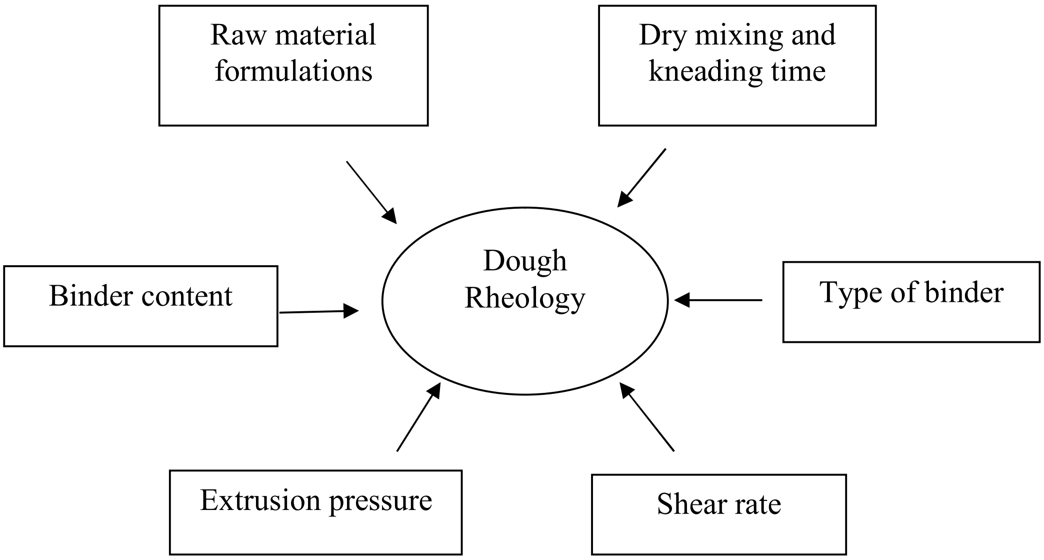

Fig 5.3 Dough rheology: Critical parameters

5.1.1.1 Extruders

An extruder forces the semisolid dough through a die under pressure in order to form green desired components. Extruder can be of two types such as: the ram (piston) and the screw (auger). The ram extruder is mainly consists of a barrel, a piston and a die (Fig. 5.4). During the extrusion process the contact between the tool parts and the dough are minimal in case of ram type extruder which inherently minimizes the contamination related issues. One of the main limitation of ram type extrusion process is being batch type, no more dough fed into barrel till completes the extrusion cycle is finished. Further, homogenization of the dough through mixing is also very minimal in this process as it occurs only during the extrusion section of the barrel to the die. Generally, the extrusion defect originate in ram extrusion due to the nonuniform flow of dough through the spider. Application of ram extruder is limited to pilot or lab scale production.

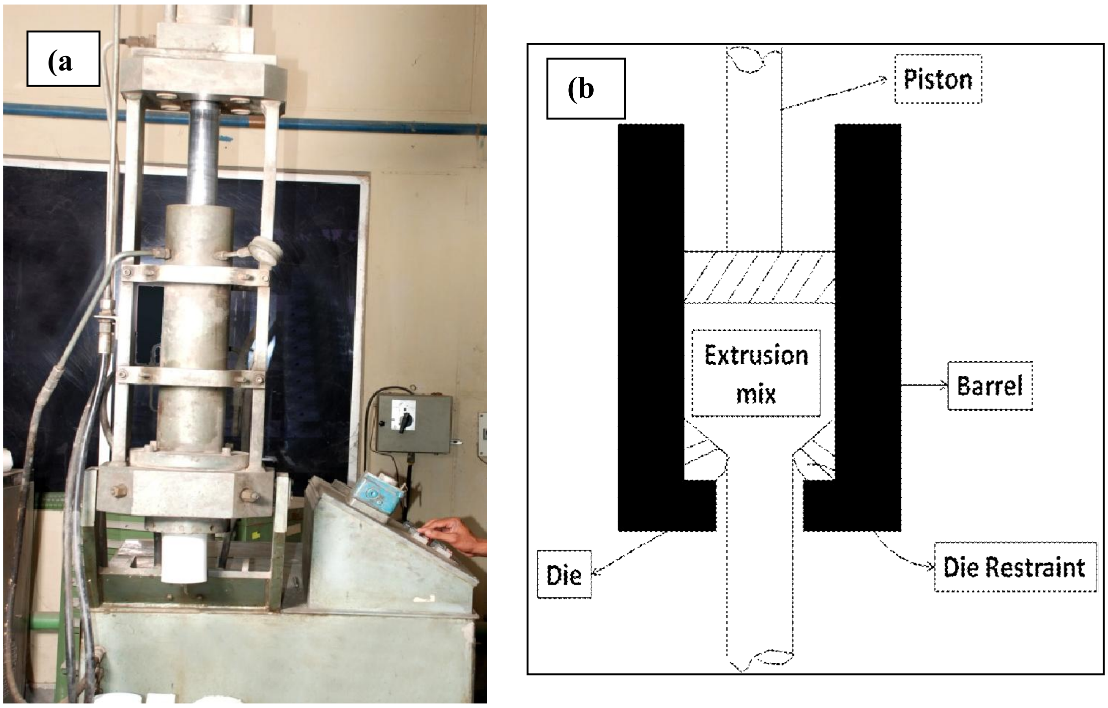

Fig 5.4 (a) Ram type extruder [Loomis, USA] and (b) a cross sectional view of extruder

The screw extruder is rather complex design (A typical screw type extruder is shown in Fig. 5.5) and the transportation of the dough mainly takes through rotation of the screw and quantity transported is depend on the pitch of the screw. Due to the excessive dough contact, wear is the problem and may drastically reduce the durability of the service in case of materials with high hardness. Main advantage of the screw type extruder is that process can be continuous with intensive and homogeneous mixing throughout the extrusion process. Hence, generally screw type extruder are used in production of traditional ceramics as well as refractories, whitewares etc [16-19].

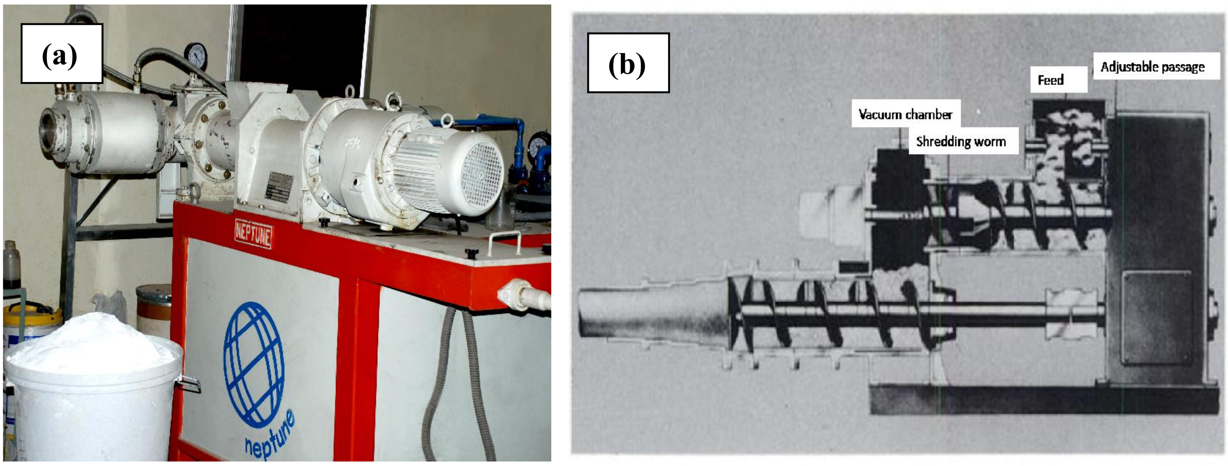

Fig 5.5 (b) Screw type extruder [Neptune, India] and (b) a cross sectional view: [Scheffler M, Colombo P (Eds)., Cellular ceramics, Wiley-Vch , USA, 59-63(2004)]

5.1.1.2 Mechanics of flow

(a) Rheological models

The rheological models are generally employed to define the extrusion bodies in ceramics. Fig. 6.6 shows the four plastic rheological models: (a) perfect plastic, (b) Bingham plastic, (c) shear-thining plastic and (d) dilatant plastic as designated as Fig. 5.6 (a)-(d). The perfect plastic body is purely a theoretical concept and is useful only for describing the behaviour of a material at vanishingly small strain rates. The Bingham plastic body is widely observed experimentally and provides a useful starting point for many theoretical analyses. The shear thining and dilatant plastic bodies are refinements on the Bingham model and observed commonly as well. The shear-thining plastic bodies is generally composed of anisotropic particles which exhibits greater alignment of the particles under higher the degree of shear resulting in lower resistance to the flow. On increasing shear rate of the bodies with high viscosity binder system, it shows a strong decrease in viscosity binder system. The dilatant behaviour is generally associated with high solid loading and also with bodies having inhomogeneous mixing leading to pockets of binder system that makes the poor flowability [20,21]. Plug flow is one of the characteristics of a plastic body and Fig. 5.7 shows schematically the flow of a plastic body through a cylindrical cross section. As the flow progress central region of the flow front advances faster which experiences no plastic flow. However, drag on the wall induces slip at the boundaries and hence entire column experiences plug flow [22, 23].

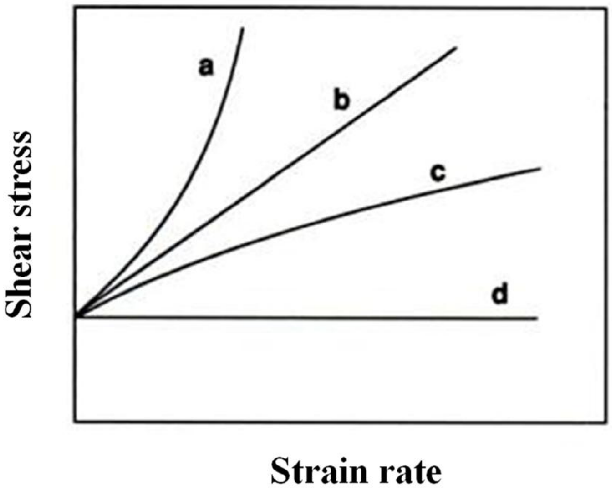

Fig 5.6 The four rheological models ((a) dilant plastic, (b) Bingham plastic, (c) shear-thining plastic and (d) perfect plastic)

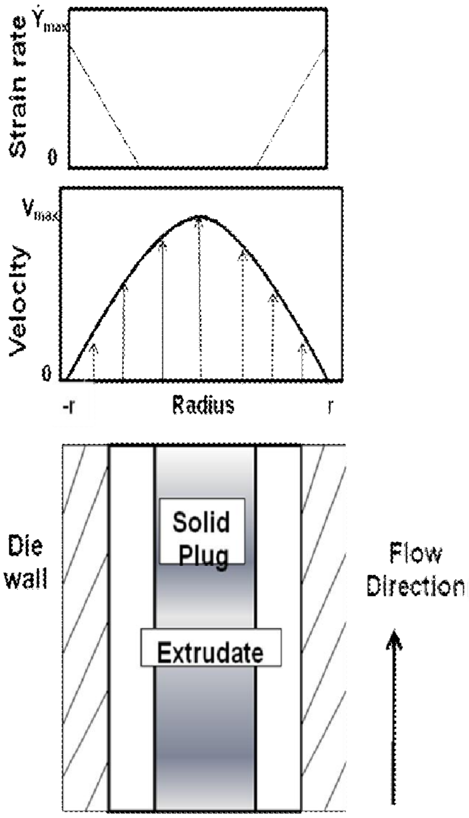

Fig 5.7 Schematic flow behavior of a plastic body through a cylindrical die

(b) Pressure variations in the die and the barrel

A typical pressure profile generated as the dough is extruded from the barrel through the die, a pressure is shown in Fig. 5.8. There are three distinct components of the pressure drop designated as dP_{etn}, dP_{die} and dP_{exit}, where dP_{ent} is the die entry pressure, dP_{die} is the die land pressure and dP_{exit} is the pressure condition. The entrance drop, dP_{ent}, measure of work required to deform the dough from the barrel to the die diameter. dP_{die}, indicates the work required to overcome the frictional force of making the dough proceeds through the section. dP_{exit}, reflects the release of pressure as the material exits from the die. In practice, dP_{ent} and dP_{die} are large and of similar magnitude, however dP_{exit} is relatively small. Spring back or elastic rebound of the extrudate is strong function of the dP_{exit} and hence, it is important to minimize the dP_{exit} within the limits by controlling the extrusion rate. Another way to control the spring back is to increase the die land region. The spring back generally introduces the defects such as axial cracks and warpage to the green body [24,25].

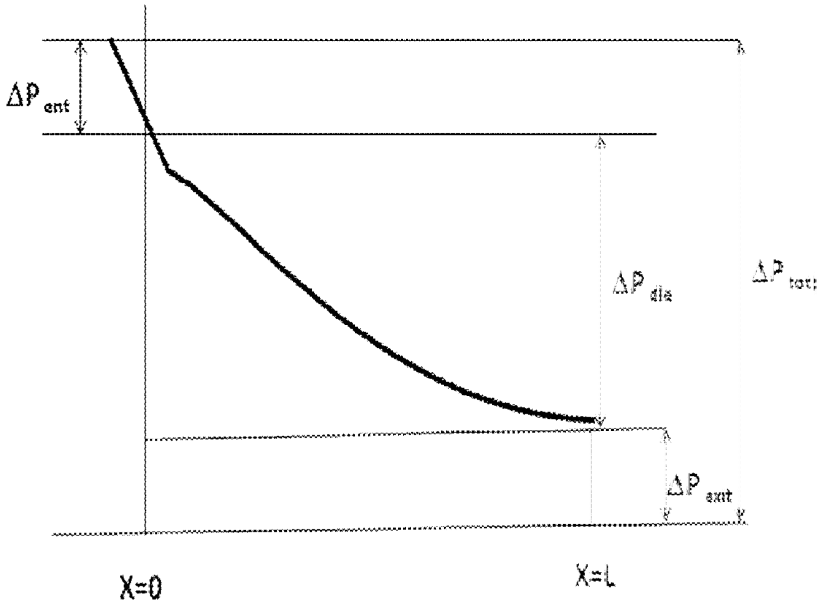

Fig 5.8 The pressure profile in the barrel and the die.

5.1.1.3 Dies

A well designed, complex die will take a long time to design, test and get into production. Typical die used for the extrusion of honeycomb structures are shown in Fig. 5.9 [7,8,26-28]. As it is evident from Fig. 5.9, the die consists of large number of holes on one side and parallel and perpendicular slits on the other side. Die should allow lateral flow of the dough followed by the knitting with adjacent cross section within the die to form the honeycomb structures. Most common extrusion defects such as tearing and segregation are mainly originated from improper die designs [29-31]. Tearing is mechanical defect caused by the interaction of the die with the extrusion mix. Poor die design and/or/low plasticity in the extrusion mix can lead to tearing. Segregation may be caused by the differential flow of water (or other solvent) upon application of pressure.

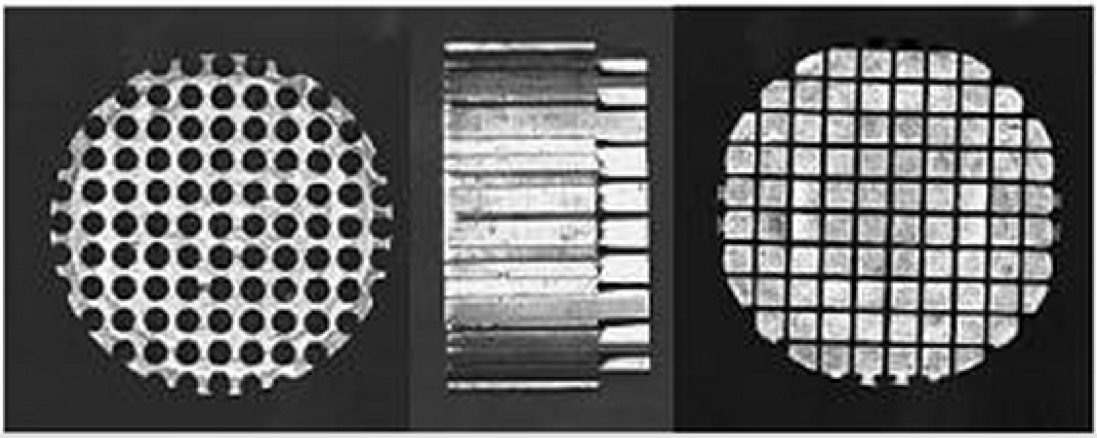

Fig 5.9 Honeycomb extrusion die schematic: [Scheffler M, Colombo P (Eds)., Cellular ceramics, Wiley-Vch , USA, 59-63(2004)]

5.1.2 Extrusion Processing of Honeycomb Structures

Based on the critical parameters the experimental scheme followed for the estimation of the dough rheology in the present study is shown in the flow chart depicted in Fig. 5.10 and has been discussed below.

5.1.2.1 Dry mixing in ball mill

The raw mix of 500g was weighed according to the stoichiometry and was ball milled for 1-2 hours to ensure a uniform mix. The average particle size and the particle size distribution of the mix after the dry mixing were measured using the particle size analyzer and the average particle size was found to be ~350 nm.

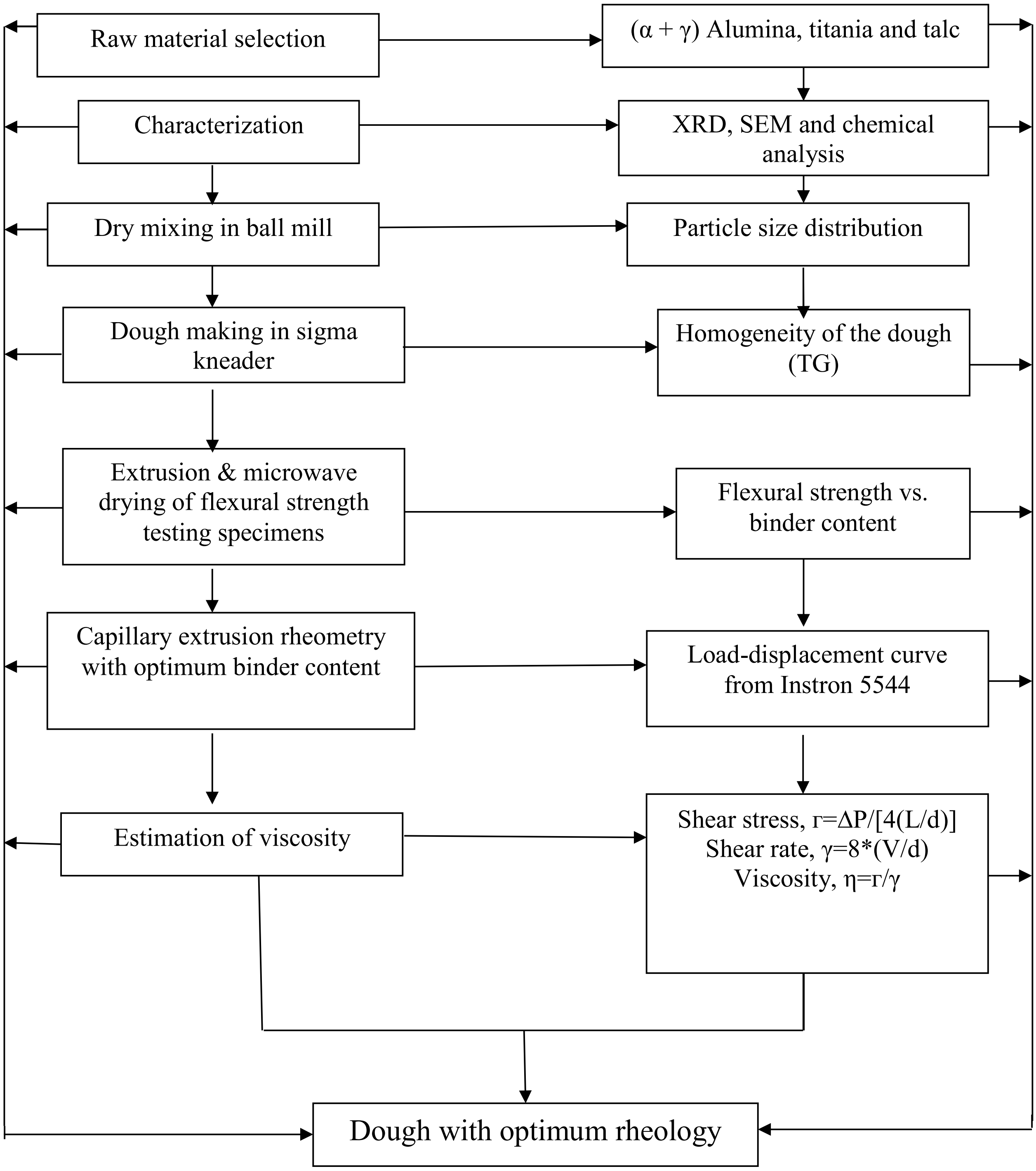

Fig 5.10 Flow chart for estimation of dough rheology

5.1.2.2 Dough Making and Kneading Time

Dough making is the most critical step in the extrusion batch formulation. Poor distribution of additives in the extrusion batch results in many problems during extrusion as well as during further processing. In the present study a vacuum sigma kneader, as shown in Fig. 5.11, was utilized for optimization of time of mixing for obtaining the uniform extrusion batch. The raw mix was kneaded for 10-20 minutes in the vacuum sigma kneader depending on the raw material along with the necessary additives (Methyl cellulose as binder and poly ethylene glycol as plasticizer) needed. The optimization of the kneading time 20 minutes is arrived at by collecting the samples at different points from the monolithic dough. These samples were subjected to thermo gravimetric estimation analysis until consistent weight loss was obtained.

Fig 5.11 Sigma kneader used for dough preparation

5.1.2.3 Optimization of binder content based on green flexure strength

Binder system basically provides the green strength to the extrudate, which determines the handlability after extrusion. In order to study the strength, the dough was extruded into standard specimens of 45 x 4 x 3 mm and dried. These samples are further subjected to the 3-point bend test to estimate the modulus of rupture (MOR) using a universal testing machine (Instron 5584). The minimum binder content will be always desirable in ceramic processing not only because of economic point of view but also because of the processing difficulties encountered with higher binder contents. Hence, the minimum organic binder content that provides the maximum strength with respect to the various formulations is optimized. Fig. 5.12 shows a plot of the modulus of rupture versus the binder content for extruded and dried rectangular bars. It clearly indicates that the strength of the samples increases as the binder content is increased from 1 to 3%. The strength does not improve further beyond 3% and rather shown a decreasing trend. Hence, a binder content of 3% is selected for the preparation of the dough used in this study.

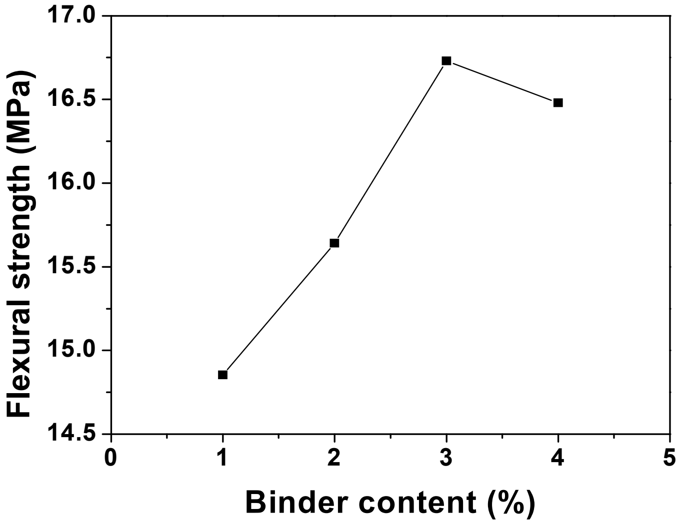

Fig 5.12 Variation of flexural strength for extruded specimens after drying as a function of binder content

5.1.3 Rheological Characterization through Capillary Extrusion Rheometry

The ceramic dough prepared with the optimum binder content was characterized for their rheological properties using an indigenously designed and fabricated extrusion rheometer. The extrusion rheometer designed and fabricated at ARCI under this project is depicted in Fig. 5.13 along with the detailed drawing of the extrusion dies.

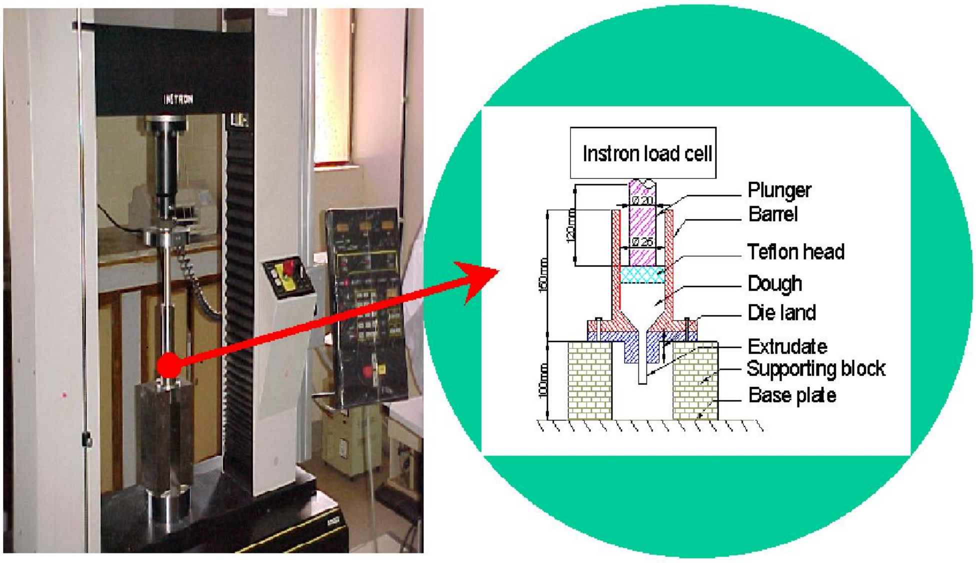

Extruder set up mounted on Instron

Fig 5.13 Extruder setup mounted on Instron 5584 for the rheological characterization of the dough.

The extrusion capillary rheometer is composed of a piston, extrusion barrel fitted with a detachable capillary at the end and the complete assembly, which can be attached to the crosshead of the Instron machine (model no. 5584,UK) The specifications of the dies are detailed in Table 5.2.

Table 5.2 Specification of the dies

Sr. No	Length of the die (L), mm	Diameter of the die (d), mm	L/d ratio
1	70	3.5	20
2	52.5	3.5	15
3	35	3.5	10

Initially, the dough was rammed continuously several times to remove the entrapped air and then loaded into the extrusion barrel. The dough was further extruded at preset ram rates of 10,25 and 50mm/min, and the load versus displacement curves were recorded for various L/d ratios. Extrusion pressures, P, required for maintaining stable flow through the capillary die were calculated from the steady state load values corresponding to the plateau region of the load displacement curve, as load per unit cross sectional area of the barrel, ($4L/\pi.D^2$), where L is the load and D is the diameter of the barrel (25 mm). Similarly, the extrusion velocities, V, corresponding to these pressures were calculated from the ram rates scaled for the relative change in the cross sectional area from the barrel to the capillary, as $v.(D^2/d^2)$, where v is the ram rate and d is the diameter of the capillary die [32-36].

The typical load versus displacement curves recorded for TAT-5 formulations during extrusion at 50 mm/min is shown in Fig. 5.14. It is clear from the graph that the load steeply rises to attain a peak value. Subsequently, the load decreases rather sharply, though by a small value, before attaining a steady state value. Such behaviour is typical for all the ram speeds examined. As the dough gets compressed in the barrel because of the movement of the piston, the load builds up and peaks. If this load is sufficient enough to overcome the inertial resistance to flow through the capillary, the mix starts to extrude out. The observed peak load value has been considered as the yield value by some researchers [34-35].

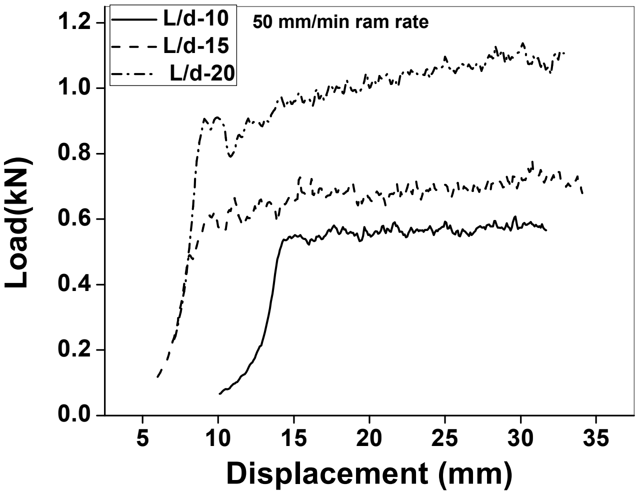

Fig 5.14 Typical load versus displacement curves for TAT-5 formulations during extrusion at 50 mm/min

In that case, the flow can be expected to start once the same minimum load value is reached, and therefore the peak load should remain independent of the rate of extrusion. However, it is observed that this value increases asymptotically with the extrusion velocity. This indicates that the peak results from the inertial resistance of the dough to initiate flow through the capillary, rather than any yield phenomenon inherent of the mix.

Viscosity is calculated from the corrected shear stress – shear rate data. Fig. 5.15 shows the variation of the viscosity as a function of the shear rate. The viscosity tends to decrease with the shear rate, suggesting a shear thinning behaviour of the extrudate.

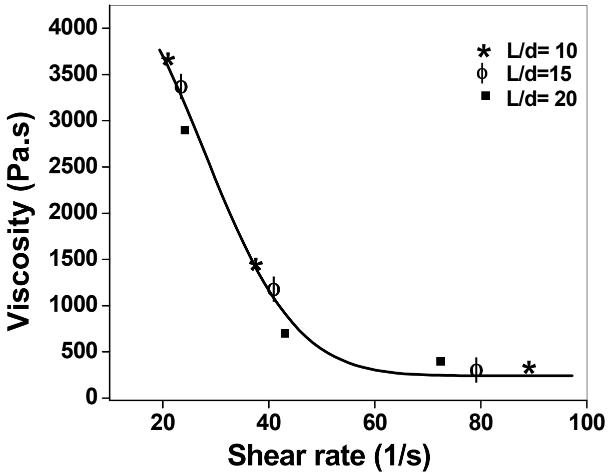

Fig 5.15 Variation of the viscosity as a function of the shear rate for different L/d ratio of

5.1.4 Shaping of Optimised Dough into Honeycomb Structures

Based on the optimized flow chart (as shown in Fig. 5.10) the TAT-5 formulations were made into extrudable dough and extruded into the honeycomb structures with the proprietary techniques of ARCI. The honeycomb is dried in microwave oven and subjected to sintering as per the sintering schedule shown in Fig. 5.16. The low ramp rate of 90ºC/hour was employed up to 500ºC and 30 minutes soaking at 500ºC, so as to remove the binder effectively without leading to the distortions of the honeycomb. Further, the heating rate is increased to 150ºC//hour till it reaches the maximum temperature of 1550°C and further samples were soaked for 1 hour at peak temperature.

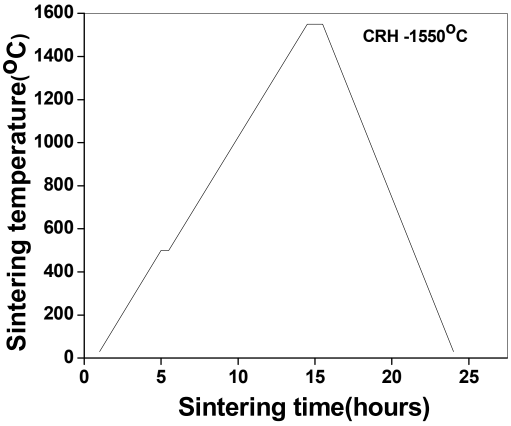

Fig 5.16 Sintering schedule employed for TAT-5 honeycombs

5.1.5 Characterization of Honeycombs

5.1.5.1 Physico-chemical properties

Densities of the sintered honeycomb samples were estimated by Archimedes principle. Cellular properties of the honeycombs were calculated using the unit cell dimensions and wall thickness. Open frontal area (OFA), relative density (ρ^*/ρ_s) and surface area/unit volume (S) of honeycomb with square channel configuration is estimated in the present study using equations (5.1), (5.2) and (5.3)[31,36].

Open frontal area (OFA):

$$OFA=(l-t)^2 / l^2 \quad \ldots . (5.1)$$

Where, t - wall thickness (mm) and l - edge length (mm)

Relative density:

$$\rho^*/\rho_s = 2t/l\{1-0.5(\rho/l)\} \quad \ldots . . (5.2)$$

Where, ρ^* - density of honeycomb and ρ_s - density of solid, which is made up of AT

Surface area:

$$S = (k.l)/(t+l)^2 \qquad \ldots\ldots (5.3)$$

Where, k- dimension less parameter (k=2, for square configuration)

A typical honeycomb with 625 channels/square inch (as-sintered) in the sintered condition are shown in Fig. 5.17 and also the properties of all the honeycombs produced have been shown in Table 5.3.

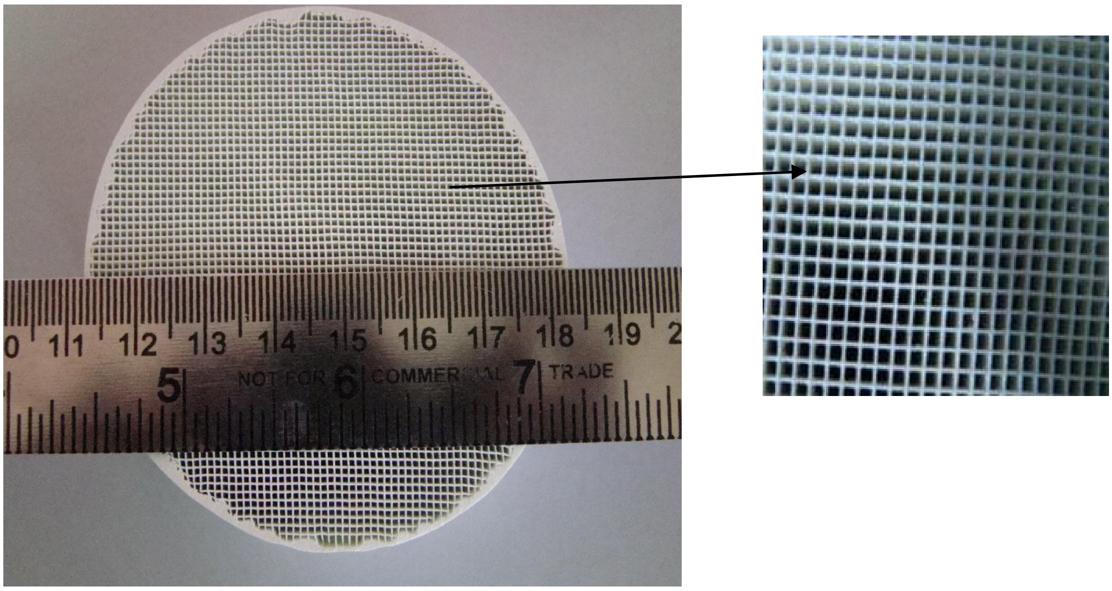

Fig 5.17 Sintered TAT-5 honeycomb

Table 5.3 Physio-chemical cellular properties of TAT-5 honeycomb

Sr.No	Cellular properties	Nominal values
1	Channel Density (CPSI)	625
2	Density (gm/cc)	3.35
3	Wall thickness (t) (average) (mm)	0.14
4	Edge length (l) (mm)	0.69
5	Open frontal area	0.614
6	Surface area (cm^2/cm^3)	1.96
7	Relative Density	0.38

5.2 Conclusion

Honeycomb structure being a potential candidate for various applications especially automobile pollution control, the developed formulation of TAT-5 has been explored successfully for the fabrication of the honeycomb structures.

The TAT-5 composition was formulated into a extrudable dough with methyl cellulose as the binder and poly ethylene glycol as the plasticizer based on the strength measurement on the green bodies.

Kneading parameters, microwave drying parameters, binder removal and sintering parameters were optimized and crack free fully integrated honeycomb structure with thin walls (0.14mm) are obtained.

Honeycomb samples characterized for cellular properties such as open frontal area (OFA), relative density (ρ^*/ρ_s) and surface area/unit volume (S) are found to be 0.614, 0.38 and 1.96(cm^2/cm^3) respectively.

5.3 References

1. J. Adler, Ceramic diesel particulate filters, Int. J. Appl. Ceram. Technol., 2 [6] 429–439 (2005).
2. W.A. Cutler, Overview of ceramic materials for diesel particulate filter applications, Ceram. Eng. Sci. Proc., 25 [3] 421–430 (2004).
3. T. Boger, J. Jamison, J. Warkins, N. Golomb, C. Warren and A. Heibel, Next generation aluminum titanate filter for light duty diesel applications, SAE. Int., doi:10.4271/2011-01-0816 (2011).
4. S. Ogunwumi, P. Tepesch, T. Chapman and C. Warren, Aluminum titanate compositions for diesel particulate filters, SAE. Int., doi:10.4271/2005-01-0583 (2005).
5. K. Ogyu, K. Ohno, S. Hong, and T. Komori, Ash storage capacity enhancement of diesel particulate filter, SAE 2004-01-0949 (2004).
6. S. Bardo, B. Bouteiller, N. Bonnail, P. Girot, V. Gleize and L. Oxarango, Asymmetrical channels to increase DPF lifetime, SAE 2004-01-0950 (2004).
7. R.D. Bagley, Extrusion method for forming thin walled honeycomb structures, U.S. Patent 3790654 (1974).
8. I.M. Lachman and R.M. Lewis, U.S. Patent No.3885977 (1975).
9. J.S. Reed, Extrusion and plastic deformation forming, Principles of ceramic processing, Wiley, New York (1995).
10. L.J. Gibson and M.F. Ashby, Cellular solids: Structure and properties – Second Edition, Cambridge University, 34-40 (1997).
11. M. Vijayakumar, Loading of solids in a liquid medium: The concept of CBVC. Met. Mater. Pro. 7: 139 (1995).
12. A.J. Moulson and J.M. Herbaert. Electroceramics, 2nd Edition, John Wiley & Sons Ltd, England. 95 (2003).
13. F. Handle (Ed.), Extrusion in ceramics, Springer, New York (2007).
14. F.J. Goodson. Experiments in extrusion. Trans. Br. Ceram. Soc., 58, 158-187 (1959).
15. G.C. Robinson, R.H. Kizer and J.F. Duncan, Raw material parameters determining extrudability. Am. Ceram. Soc. Bull., 47, 822-832 (1968).

16. J.G. Seanor and W.P Schweltzer, Basic theoretical factors in extrusion screws. Am. Ceram. Soc. Bull., 41, 560-63 (1962).
17. H.H. Lund, S.A. Bortz and A.J. Reed, Screw design for clay extrusion. Am. Ceram. Soc. Bull., 41, 554-59 (1962).
18. J.R. Parks and M.J. Hill, Design of extrusion screws and the characteristic equation of ceramic extrusion mechanics. J. Am. Ceram. Soc., 42, 1-6 (1950).
19. M. Arakawa, S. Banerjee and W.O. Williamson, Extrusion behaviour of hard shale, Am. Ceram. Soc. Bull., 50, 933-35 (1971).
20. M.A. Janney, Plasticity of Ceramic Particulate systems, Ph.D Dissertation, University of Florida (1982).
21. J.H. Atkinson and P.L. Bransby, Mechanics of soils, McGraw-Hill, maidenhead, UK (1978).
22. A.N. Schofield and C.P. Wroth, Critical state soil mechanics, McGraw-Hill, Maidenhead, UK (1968).
23. R. Russel and Jr.C.F. Hanks, Stress-strain characteristics of plastic clay masses, J. Am. Ceram. Soc., 25, 16-28 (1942).
24. C.D. Han, Rheology in polymer processing, Academic Press, New York (1976).
25. E. Mosthaf, Long extrusion dies cut losses. Ceram. Ind (serves, France) 53, 70 (1949).
26. B. Butterworth, L.W Baldwin and S.G Coley, Dies for extruding perforated bricks. J.By.Ceram.Soc.,3, 563-583 (1966).
27. E.F. Kelm, Manufacture of Multiple Flow Path Body, US 4041592, published (1977).
28. I.M. Lachman, R.D. Bagley and R.M. Lewis, Thermal expansion of extruded cordierite ceramics. Am. Ceram. Soc. Bull., 60, 202 (1981).
29. G. Robinson, Extrusion defects, in Ceramic Processing Before firing (eds G.Y. Onoda Jr and L.L.Hench) J.Wiley and Sons, New York (1978).
30. A. Zamperi , P. Colombo , G.T.P Maba de, T Selvam , W Schweiger and, F Scheffler , Adv. mater, 16, 819-823 (2004).
31. M. Scheffler and P Colombo (Eds)., Cellular ceramics, Wiley-Vch , USA, 59-63 (2004).
32. R.N. Das, C.D. Madhusoodana and K. Okada, Rheological studies on cordierite honeycomb extrusion, J. Eur. Ceram. Soc., 22, 2893-2900 (2002).

33. M. Swathi, R. Papitha, U. S. Hareesh, B. P. Saha, R. Johnson and M. Vijayakumar. Rheological Studies on Aqueous Alumina Extrusion Mixes. Trans Indian Inst Met, DOI 10.1007/s12666-011-0096-3
34. S.Chacko, R. Johnson, B.P. Saha, I. Ganesh and Y.R. Mahajan. Rheometric studies on cordierite-mullite honeycombs, Trans. Ind. Ceram. Soc., 63[2] 119-123(2004).
35. A.J.J. Reddy, M. Vijayakumar, R.R.T. Mohan and P. Ramakrishnan, J. Eur. Ceram. Soc., 16, 567-574 (1990).
36. R. Holder, A global reaction mechanism transient simulation by three way catalytic converters, Cuivillier verlag, 8-12 (2008).

Chapter- VI

Pressure Assisted and Conventional Slip Casting of TAT-5 Formulation based Green Components

6.0 Introduction

Defect free near net shaping of advanced ceramic powders into engineering components in large scale manufacturing has always been a challenge to ceramic engineers [1]. Among the powder compaction processes isostatic pressing under cold (CIP) or hot (HIP) conditions are expected to provide parts with high density as well as isotropic properties [2]. Colloidal processing techniques such as injection moulding and slip casting are two existing large fabrication process generally practiced, however the application is limited by several factors [1-5]. Injection moulding essentially requires large amount of binders or polymers and pyrolysis of the organic polymers becomes cumbersome especially for larger components [6]. Slip casting proceeds by capillary forces at 0.1 to 0.2 MPa pressure for longer formation time and drying durations. Plasters of paris mold contamination of advanced ceramics as well as solid waste generation due to frequent mold rejections are other issues in slip casting [7-8]. Main issue of productivity of slip casting can be overcomed substantially by the application of external pressure. It is well known that the fluid flow through the porous medium with inter connected pores under pressure obeys Darcy's differential equation [$S^2 = (2 \times \Delta P / \eta . \rho_p . R_s) \times ((\O_c / \O_c - \O_s) t)$] where, S : the cake thickness, ΔP : Pressure of slurry , η: viscosity of the slurry, ρ_p : particle density , R_s : permeability of the cake, $\O_c$: solid volume fraction of the cake, $\O_s$: solid volume fraction in the slurry and t: the casting time. Practically, casting rate is controlled by the resistance of cast layer and the mold. Mold resistance being negligible, considering the interaction of particles and particle size distribution, while cake formation under pressure, the cake is expected to grow at a faster rate to a peak value followed by the decrease exhibiting a parabolic behavior with respect to other variables [9-12].

Part of the work being published in Journal of processing and application of ceramics, 7 [4] (2013) 159–166.

However, recent developments in durable polymer mold with average pore size of ~10 µm do not operate on capillary forces but on external pressure applied to slurry isostatically upto 6 MPa which substantially enhances the isotropy of properties and productivity. This innovative tool also permits the mechanization of the process providing high efficiency. Pressure casting is presently well established in the traditional ceramic processing with respect to hollow and solid articles. The pressure cast parts are demonstrated for the additional advantages of reduced water content of the cast, better handilability and green strength [13-15].

In the area of advanced ceramics attempts are now in progress however, achieving suitable rheology of the slurry for pumpability, filtration behavior under pressure and demoulding. For eg., unlike traditional clay based ceramics, advanced ceramics pose improper alignment of particles and mechanical interlocking resulting in collapse of the cast while demoulding [16].

Current chapter describes comparative evaluation of the conventional slip casting (CSC), pressure slip casting (PSC) and cold isostatic dry pressing (CIP) of a mixture of alumina with varying particle sizes and titania in Al_2TiO_5 stoichiometry with 5 wt % talc as additive for suppressing the eutectoid decomposition [17-19]. Properties exhibited by the cast parts under pressure (PSC) and pressure-less condition (CSC) is compared with isostatically dry formed CIP specimens and were further correlated with the processing parameters.

6.1 Experimental Procedure

6.1.1 Characterization of raw materials and formulation

Alumina powder obtained from two different sources (CRF-30, Baikowski, France and MR-01 and MR-06, NALCO, India) and titania (TiO_2, Qualigens, India) and stabilizing additive magnesium silicate ($Mg_3Si_4O_{10}(OH)_2$, India). The powders were characterized for phase analysis by XRD, particle size and morphology by SEM as described earlier in section 2.3. XRD patterns, particle size distribution curves and the morphology of the powders are shown in Figs 6.1 to 6.5 respectively.

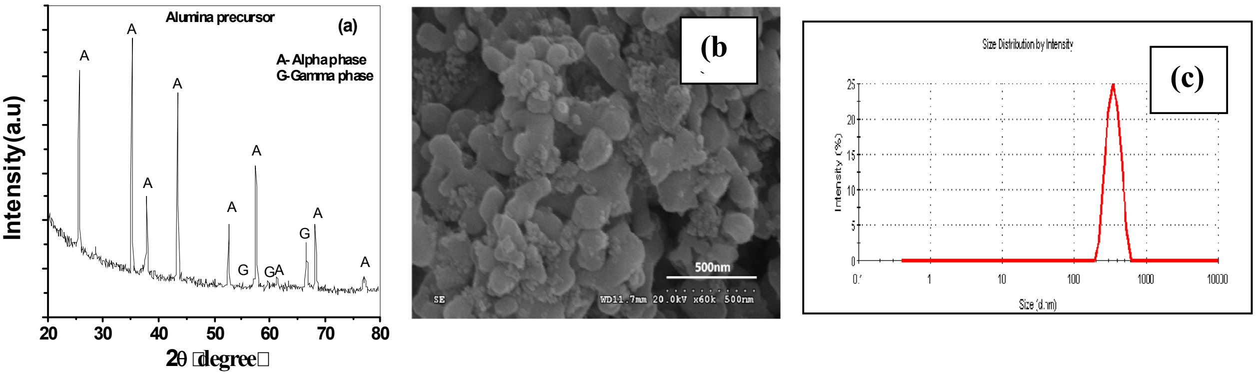

Fig 6.1 (a) XRD pattern, (b) SEM morphology and (c) particle size distribution of CRF-30 alumina powder

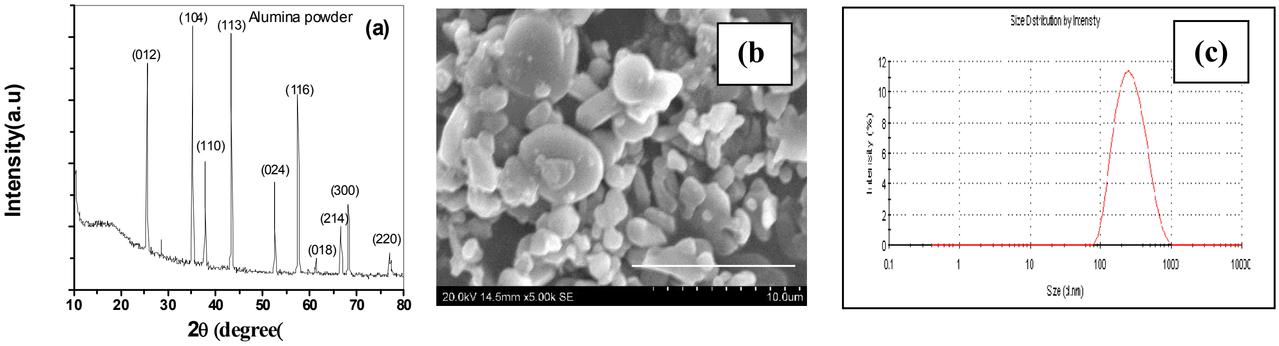

Fig 6.2 (a) XRD pattern, (b) SEM morphology and (c) particle size distribution of MR-01 alumina powder

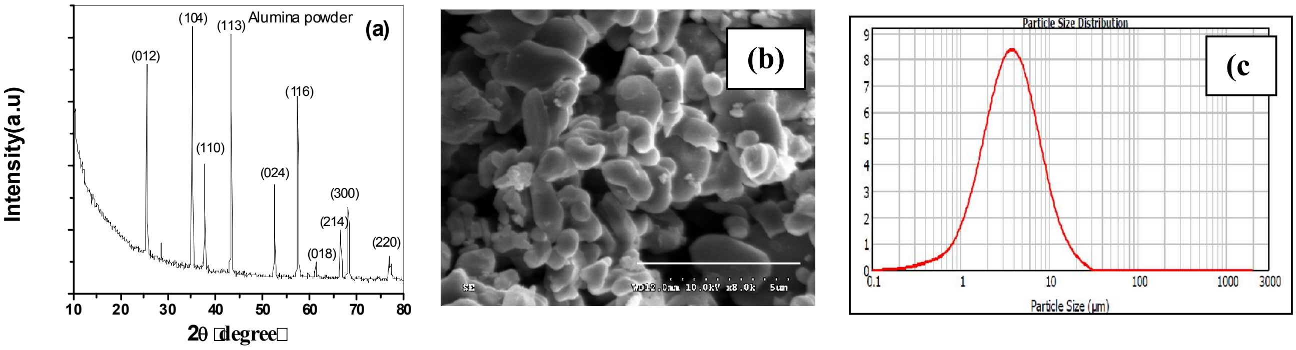

Fig 6.3 (a) XRD pattern, (b) SEM morphology and (c) particle size distribution of MR-06 alumina powder

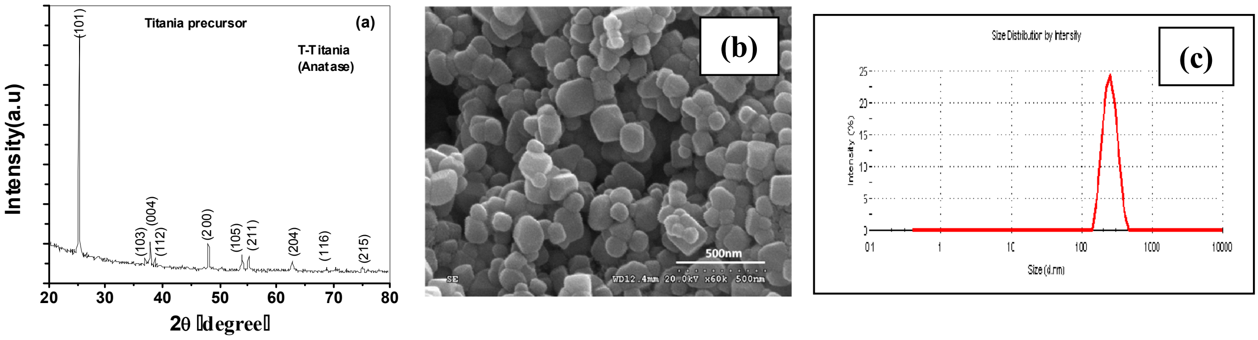

Fig 6.4 (a) XRD pattern, (b) SEM morphology and (c) particle size distribution of titania powder

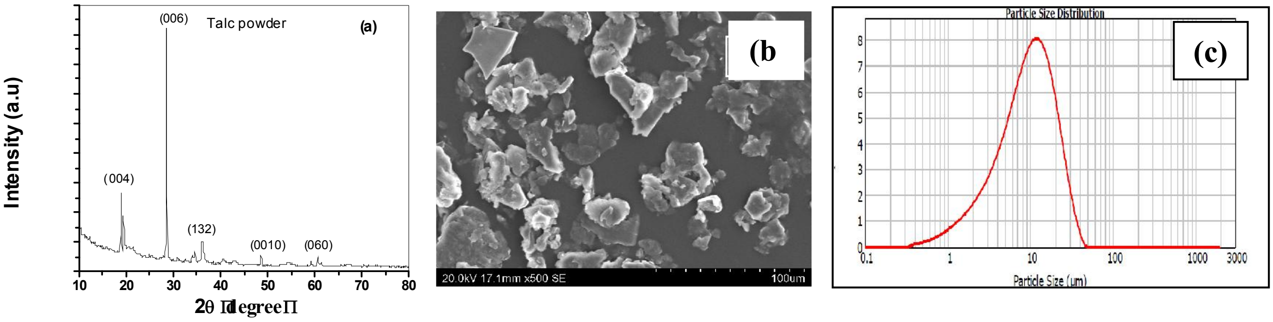

Fig 6.5 (a) XRD pattern, (b) SEM morphology and (c) particle size distribution of talc powder

Average particle size (D_{50}), phases anaysis from XRD data and morphology of the raw materials are mentioned in Table 6.1. As discussed earlier CRF-30 alumina confirms the presence of α and γ phase of alumina with α-Al_2O_3 as the major phase with an average particle size of 0.3μm and an irregular morphology. MR-01 and MR-06 alumina have shown 100% α-Al_2O_3 with the particle size of 1.0 and 6.0 μm respectively and irregular particle morphology. Titania exhibited single phase of anatase with average particle size of 0.3 μm. Magnesium silicate was used as a common additive for all the formulations.

Table 6.1 Specification of raw materials used to prepare TAT-5 by CSC and PSC

Formulation designation	**Average Particle size (D_{50}) μm**	**XRD Phases**	**Morphology**
ALT-1			
CRF-30	0.3	>85 % α +15% γ- alumina	Irregular
TiO_2	0.3	100% Anatase	Irregular
ALT-2			
MR-01	1.0	100% α-alumina	Irregular
TiO_2	0.3	100% Anatase	Irregular
ALT-3			
MR-01 (50%)	1.0	100% α- alumina	Irregular
MR-06 (50%)	6.0	100% α- alumina	Irregular
TiO_2	0.3	100% Anatase	Irregular

*All the formulations were formulated with 5 wt% of Magnesium Silicate as an additive

The formulation in the Al_2TiO_5 stoichiometry was prepared in the molar ratio of 1:1 with optimized concentration of 5 wt% of $Mg_3Si_4O_{10}(OH)_2$ as reported in section 2.3. The formulations are designated as shown in Table 6.2.

Table 6.2 Designations of raw mix

Formulation designation	**Alumina (Al_2O_3)**	**Titania (TiO_2)**	**$Mg_3Si_4O_{10}(OH)_2$**
ALT-1	CRF-30 (Baikowski)	Qualigens	Becham
ALT-2	MR-01 (NALCO)	Qualigens	Becham
ALT-3	MR-01+MR-06 (NALCO)	Qualigens	Becham

6.1.2 Preparation of slurry for CSC and PSC

Formulations of ALT-1, ALT-2 and ALT-3 were made into aqueous slurries in distilled water using Darvan 821A (R. T. Vanderbilt Co., Inc., Norwalk, CT, USA) as a dispersant. The suspensions were then milled for 2 hrs in a rubber lined ball mill using alumina balls with 1:1 charge to balls ratio to achieve optimum solid loading of precursor ALT in the range of 63 – 65 wt% depending upon the formulation. ALT-1, ALT-2 and ALT-3 slurries with optimum solid loadings, as depicted in Table 5.3, are characterized for the rheological behavior at varying shear rates using a Rheometer (MCR 51, Anton Paar, rheometer).

Optimum solid loading and viscosity at constant shear rate for slurries ALT-1, ALT-2 and ALT-3 are shown in Table 6.3. Fig. 6.6 ((a) – (c)) presents the viscosity measurements with varying shear rates of the slurries ALT-1, ALT-2 and ALT-3 respectively. It is evident that all the slurries have shown a pseudoplastic behavior at lower shear rates and as the shear rate is increased beyond 100 s^{-1} the slurries exhibit close to Newtonian behavior adaptable for casting of the slurry.

Table 6.3 Solid loading and viscosity

Formulation designation	**Solid loading (%)**	**Viscosity(Pa.s^{-1})**
ALT-1	63	1.3
ALT-2	65	1.7
ALT-3	65	0.93

A low viscosity of the slurry results in long casting rate and cracks however, a high viscosity slurry results in pin holes and poorly drained surfaces generally in case of CSC. In case of PSC the mechanism is being pressure filtration, although shear rheology is also important though the suspensions are subjected to isostatic compression shear forming.

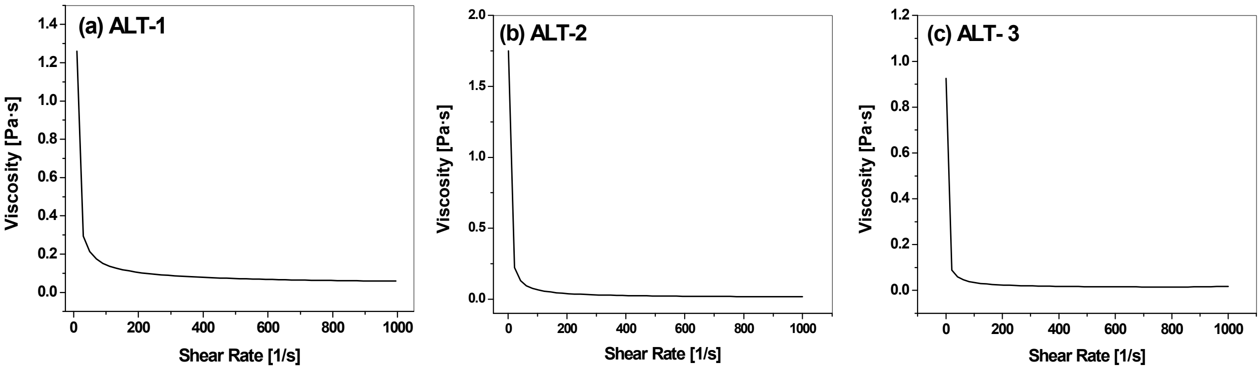

Fig 6.6 (a)-(c) Viscosity versus shear rates of the ALT-1, ALT-2 and ALT-3 slurries

6.2 Conventional Slip Casting (CSC)

Slip casting is a ceramic shaping process in which the partial separation of liquid from a particulate-liquid suspension contained in a permeable mold forms a condensed deposit with the general conformity of the working surface of the mold. In conventional casting, the capillary suction of the mold creates a pressure gradient across the deposit, and the kinetics of casting are a function of the capillarity of the mold.

In the slip casting process the ceramic powder is suspended in a fluid vehicle, usually water. These suspensions have to fulfill several requirements such as the particles should not settle fast under the effect of gravity to minimize the segregation leading to density in-homogeneities in the cast objects. These slurries should have high solids content to achieve reasonable casting rates and to reduce energy consumption in the subsequent drying stage due to the lower moisture content of the cast [20-21]. Furthermore, the prevailing trend in ceramic processing is the development of very fine particles in order to enhance sintering rates as well as to reduce the size scale for mixing uniformity in powder blends. However, the combination of high solid loading and small particles leads to a viscosity increase because of the increased particle-particle interactions and consequently to difficulties in slurry handling [22-24].

Ceramic powders have the tendency to agglomerate due to the attractive interparticle Van der Waals forces. This tendency can be eliminated with the addition of appropriate dispersants which alter the powder surface properties so that repulsive forces – either due to electrostatic repulsion resulting from the overlapping of electrical double layers or due to steric hindrance resulting from absorption of large molecules- become higher than the attractive ones and the particles can remain suspended in the slurry [25]. Dispersants that functions both via the electrostatic and the steric mechanism are called polyelectrolytes, which usually consist of a hydrocarbon chain and a polar head group (COO^-, SO_3^-) [26-27]. Dispersant addition can dramatically reduce the viscosity of slurries with very high solid content [28-29].

Fabrication of the mold is critical in the slip casting process. A suitable mold is prepared using plaster of paris and is made by casting around the pattern of the required shape designed based on shrinkage allowance for drying and firing. The inner surface of the plaster of paris mold should have very smooth finish; free from any holes originates from air bubbles in the plaster so that the cast article is removed without damage. The mold is dried and the slip is poured into it. Water passes into the porous plaster leaving a layer of the solid on the wall of the mold. This is continued until the part is solid, or is interrupted to make a thin walled part and the cast is allowed to dry. Schematic of the slip casting process employed in the present study is shown in Fig. 6.7.

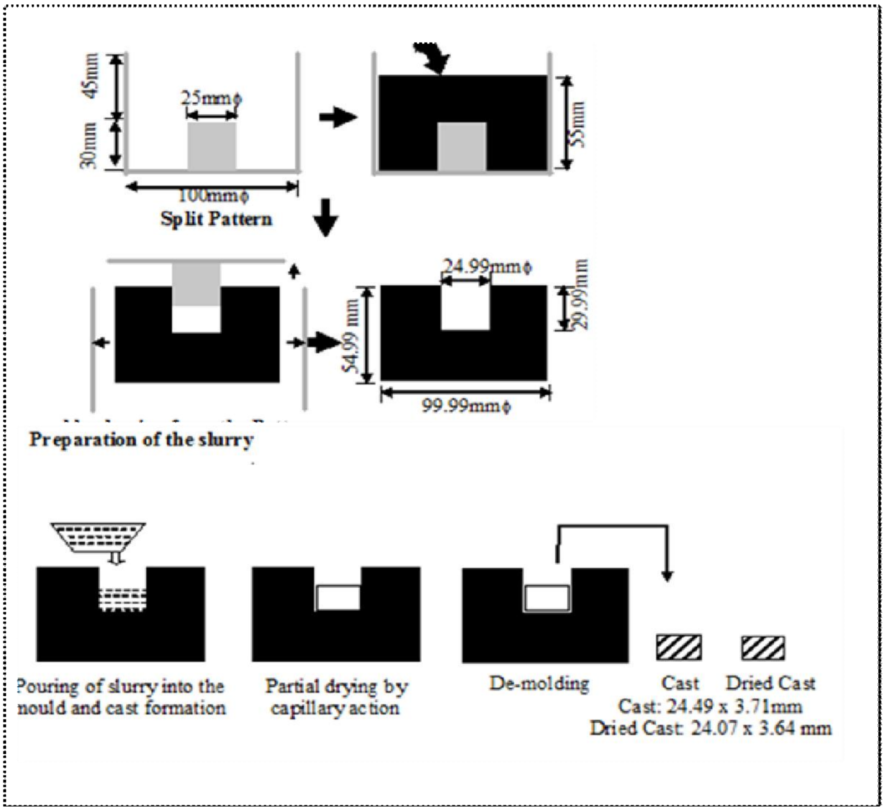

Fig 6.7 Slip casting process (schematic) for the TAT-5 casting

6.2.1 Design and Fabrication of Pattern

Slip casting of aluminum titanate precursor starts with the pattern fabrication. In the present study patterns are fabricated with stainless steel with circular core rod and a casing with the dimensional tolerance of 0.05% and 0.1% for the drying and sintering shrinkage allowance, respectively, based on the initial trials. The casing was made into a split design in order to have an easy release of the mold. The pattern was also buffed to achieve proper surface finish of the mold surface.

6.2.2 Fabrication of Plaster of Paris Mould

Plaster of Paris ($CaSO_4.H_2O$) procured from the commercial sources (Khushi Premium Quality, New Vinyl Chemicals. Hyderabad, India) is mixed with 35% of water by weight and the slurry was poured into the casing placing the core rod located at the centre and was left for 30 minutes under laboratory conditions. During this process the plaster of paris crystallizes and hardens, releases heat, and increases in volume slightly. The plaster mold was removed after drying and the inconsistencies or imperfections of the mold are slowly scraped off using a small craft knife. After scrapping of the excess material the mold was laid out on a plate or rack overnight to harden. Fig. 6.8 shows the photograph of the mould fabricated for the slip casting in the present study.

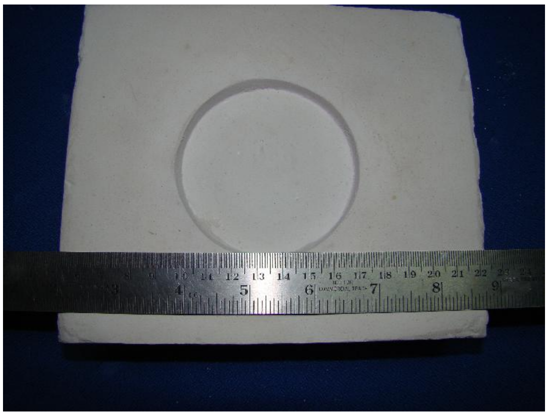

Fig 6.8 The photograph of the mould fabricated for the slip casting of TAT-5 formulation

6.2.3 Conventional Slip Casting of the Slurry

Slurry with 63-65 wt% of solid loading were thoroughly stirred with a glass rod without introducing any air bubbles (observed with naked eye) and casted into the porous plaster of paris molds fabricated under laboratory conditions. The slurry is found to have good flowability while casting. After the slip is poured in to the mold the wall thickens, the plaster mold absorbs water and the level of the slip went inside the mold, and was dropping continuously, which was compensated by adding small amounts of slip into the mold and was left for drying. The mold absorbs water from the cast, which gets dried causing shrinkage of the cast piece.

6.2.3.1 Drying of cast piece

The cast samples were subjected to drying in a laboratory oven at 60°C. Drying curves obtained with respect to duration of drying of the cast samples are shown in Fig. 6.9 and the dried samples are shown in Fig. 5.10. It is evident that the water content in ALT-1 cast is maximum ~ 30.3% which has reduced to less than 2% in a period of 7 hours of drying. In case of ALT-2 and ALT-3, the water contents were 25.6% and 23.6% respectively, which have reduced to less than 2% in 6 hours of drying.

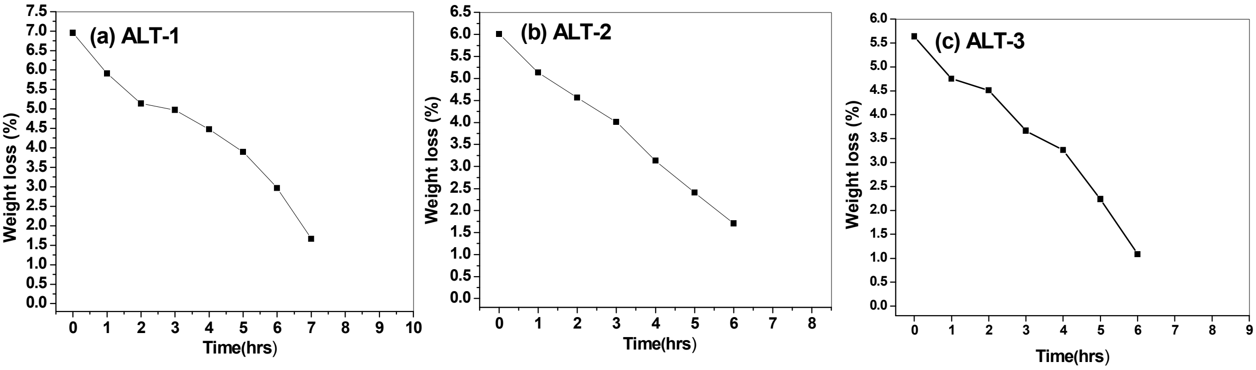

Fig 6.9 Drying curves obtained for the cast (a) ALT-1, (b) ALT-2 and (c) ALT-3 samples

The time of drying is found to be related with the water content even for high densities samples, where the capillary action is still effective.

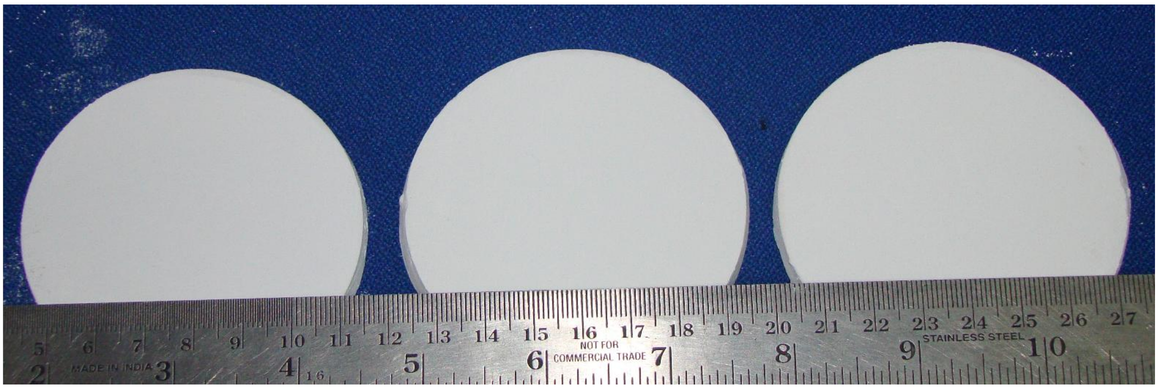

Fig 6.10 Dried samples of CSC

6.3 Pressure Casting of the Slurry

6.3.1 Fabrication of Pattern and Mold

Heart of the pressure casting is the polymer mould with engineered porosity produced through proprietary techniques. A prefabricated SS-316 pattern of 100 mm diameter x 8 mm thickness with shrinkage allowance of 20% for the cast part and proper release angle was used to produce polymer (SAMA-pore) macro porous moulds. Polymer (SAMA-pore) macro porous molds were fabricated by proprietary techniques of M/s. SAMA MASCHINENBAU GmbH. The split mold has two parts with a cross section each of 200 mm ^{3} capable of casting a specimen of 100 mm diameter.

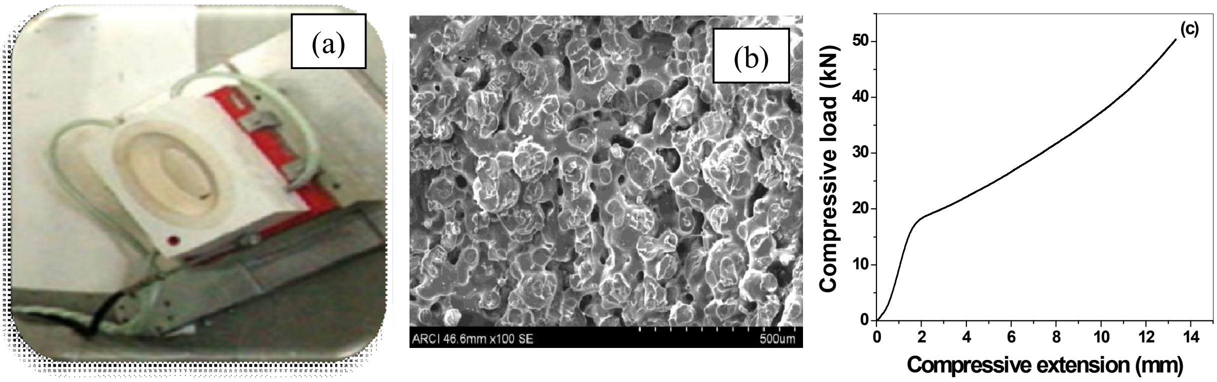

Fig 6.11 (a) Polymer mold (b) SEM Micrograph and (c) Load – displacement curve of polymer mold

Fig. 6.11(a) shows the polymer mold and SEM micrographs of the mold is shown in Fig. 6.11(b). SEM micrographs clearly exhibit the interconnected pores which are responsible for the permeability of water under pressure. The initial cake formation along with the interconnected pores results in effective particle separation from the slurry leading to the cast formation. A typical Load displacement curve showing deformation behavior of the mold is shown in Fig. 6.11(c).

6.3.2 Slurry Casting

Pressure Casting Machine PCM-100 (SAMA) used for pressure casting is shown in Fig. 6.12(a) and the typical pressure casting cycle carried out using a PLC based casting cycle as per the programme pre-set parameters is shown in Fig. 6.12(b). Slurry was pumped into the mold, at a feed pressure of 5 bar and a filling time of 15 seconds. After filling a slip pressure of 10 – 35 bar (i.e., 1-3.5 MPa) was applied with an increment of 5 bar and was maintained for 60 seconds to determine the effect of the pressure on build up of the cast.

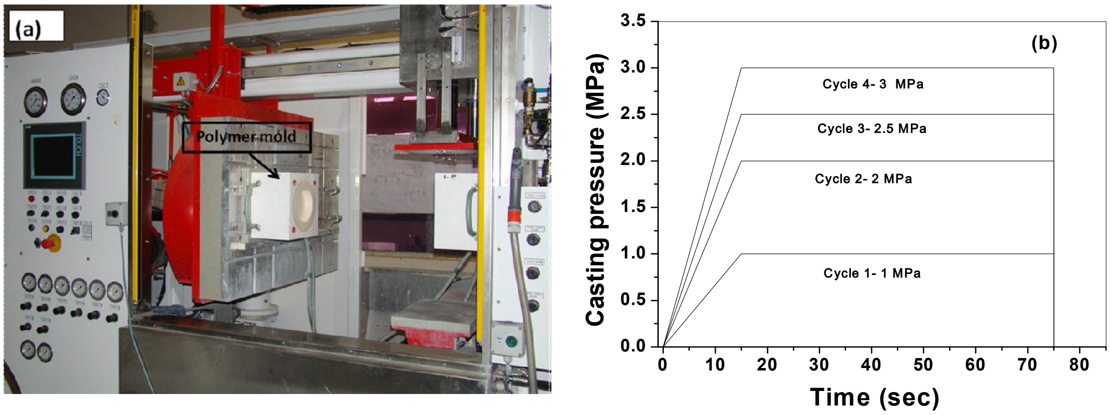

Fig 6.12 (a) Pressure casting machine and (b) Pressure casting cycle employed for TAT-5 formulations

6.3.2.1 Mold release of cast part

After opening of the mold the cast part formed within the mold is shown in Fig. 6.13(a) and the cast part is removed instantly by vacuum holder.

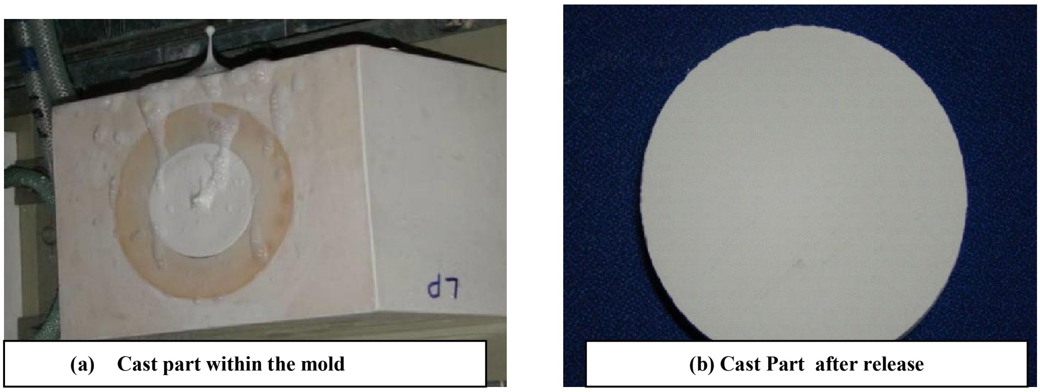

(a) Cast part within the mold

(b) Cast Part after release

Fig 6.13 (a) Cast part within the mold and (b) Cast part (Typical) after mold release

6.3.2.2 Drying of cast piece

The cast samples were subjected to drying in a laboratory oven at 60°C. Drying curves obtained with respect to duration of drying is shown in Fig. 6.14 and the dried samples are shown in Fig. 6.15.

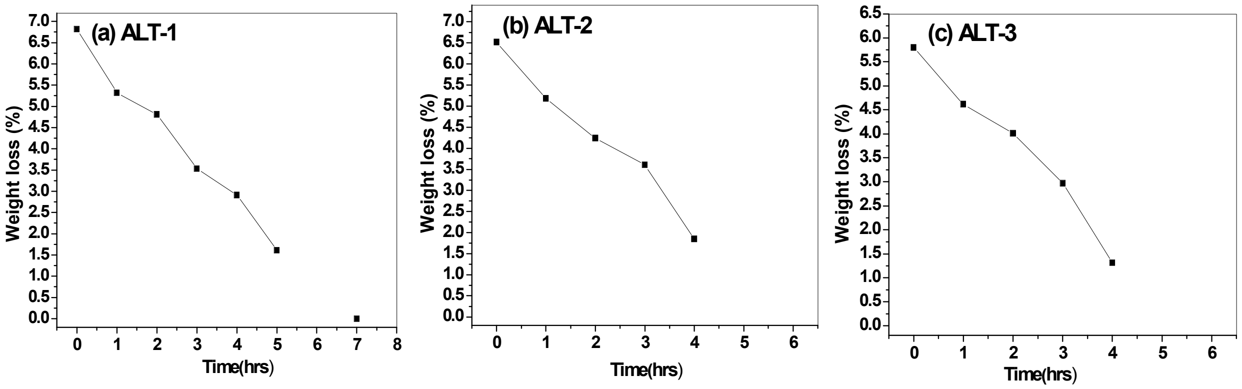

Fig 6.14 Drying curves obtained for the cast samples

The pressure cast samples have exhibited lower water content for all the formulations with a significant variation observed in case of ALT-2 and ALT-3 samples, which can be attribute to effective filtration under pressure. The water content in the cast and its removal have a significant effect in the quality of the dried product especially interms of warpage, cracks, rejections etc. Hence PSC in comparison to CSC has the advantage of processing cast with lesser water content and hence higher green densities.

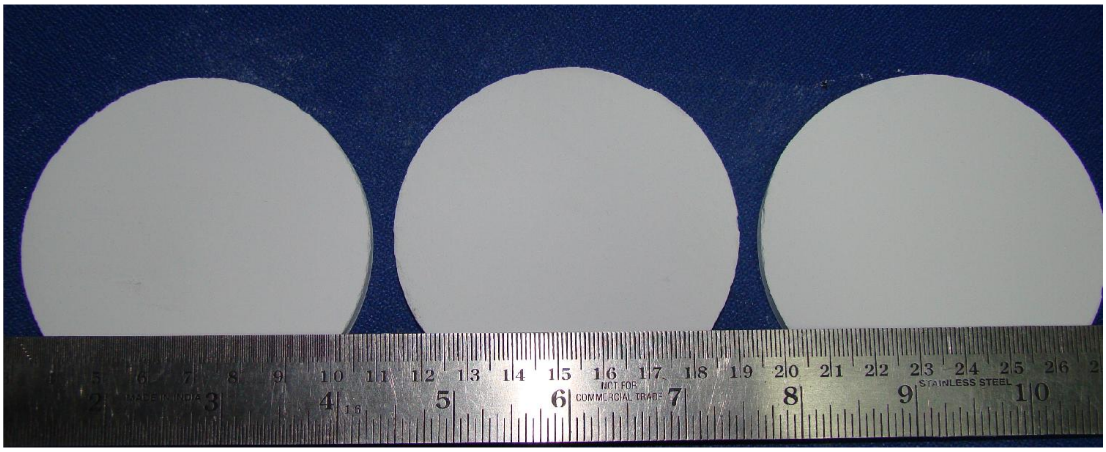

Fig 6.15 Dried samples of PSC samples

6.4 Cold Isostatic Pressing

6.4.1 Granulation and Flow Behavior

Formulations were made into semi solid dough with polyvinyl alcohol (PVA) as binder (2 wt %). The powder was granulated and powder flow measurement was carried out using an analyzer attached to a Texture Analyzer (Stable Micro System, UK), which utilizes a rotating blade moving down and up through the granules achieving the controlled flow. In order to measure powder flow characteristics 50 g of the granules of ALT-1, ALT-2 and ALT-3 are placed in the cylinder and blade moves in a cylinder, which confines the movement of the granules, thus eliminating any dissipation of the force as depicted in Fig. 6.16. As is evident from the figure that the helical shape of the blade helps to eliminate the torque on the blade; additionally if the linear motion of the blade is in the same direction as the rotation and equal to the lead distance, then the axial force performed on the blade will be negligible. Thus the programmed motion of the blade could be generated according to the rotational and vertical speeds applied by the blade. If the blade is moving clockwise and downwards a compression action is generated, whereas for downwards and anti clockwise, a slicing effect occurs. If the blade is moving upwards and with a clockwise motion, it will cause a slicing action, and if upwards and anticlockwise, lifting of the material above the blade will occur [30-32].

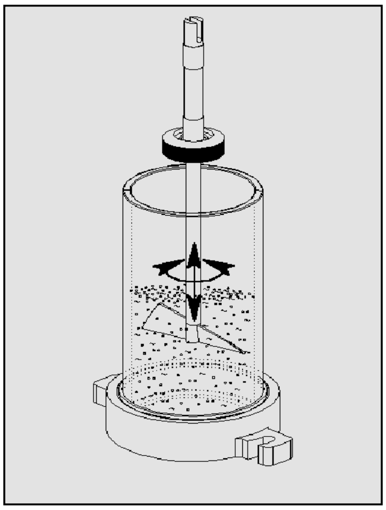

Fig 6.16 Combination of rotational (clockwise or anticlockwise) and linear (up or down) movement of the blades leading to four controlled flow modes

Cohesion Index is regarded as the ratio of cohesion coefficient and the weight of the sample evaluated and is calculated by integrating the negative areas under the force versus displacement curves shown in Fig. 6.17.

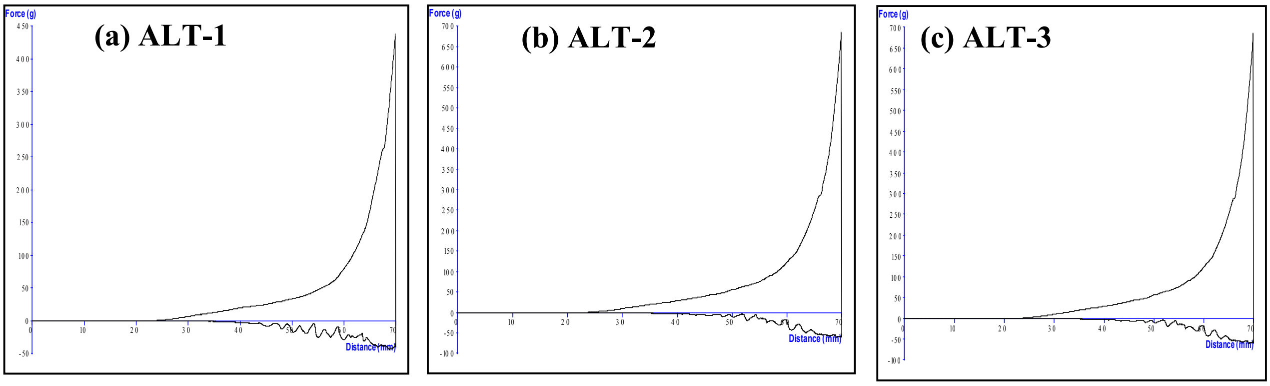

Fig 6.17 Force and distance curves for powder and granules of (a) ALT-1, (b) ALT-2 and (c) ALT-3 samples

A cohesion Index of 11-14 for all samples of ALT-1, ALT-2 and ALT-3 corresponds to free flowing behavior and the categorization is shown in Table 6.4 and is suitable for compaction.

Table 6.4 Powder categorization scale based on cohesion index

Category	Cohesion Index	Flow Behaviour
I	19+	Hardened, extremely cohesive
II	16-19	Very cohesive
III	14-16	Cohesive
IV	11-14	Easy flowing
V	11	Free flowing

6.4.2 Cold Isostatic Pressing of ALT formulation

Granules with acceptable flow behavior were compacted by uniaxial pressing using a hydraulic press. Typical pressure cycle carried out in CIP)and the compacted samples are shown in Fig. 6.18 (a)-(b). The samples were vacuum sealed in plastic bags and isostatically pressed at 50, 100 and 140 MPa using a Cold Isostatic Press (Avure Technologies, USA). The samples after drying were characterised for the moisture content and found be a maximum 1-2 % irrespective of the formulation and hence drying curves are not recorded.

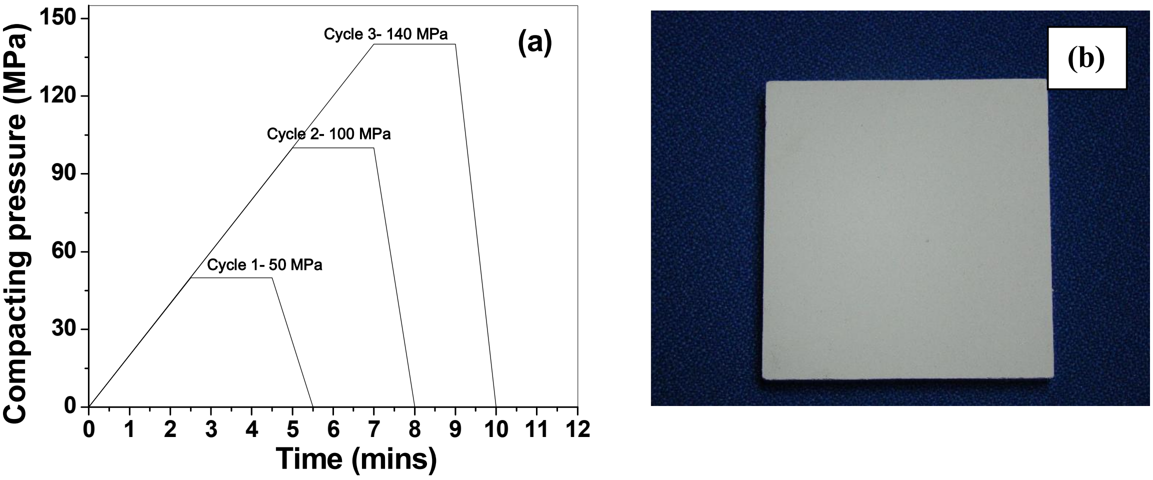

Fig 6.18 (a) Pressure cycle in CIP and (b) Compact part (ALT-1) after mold release

6.5 Characterization of Green Specimens

Pressure applied to achieve the maximum green density for ALT-1, ALT-2 and ALT-3 and the maximum green density achieved for these samples with respect to pressure slip casting (PSC) and cold isostatic pressing (CIP) are shown in Table 6.5. Further, a comparative evaluation of percentage increase in pressure corresponding to the process and increase in green density is also shown in Table 6.5. Plots of pressure versus green density (GD) in case of ALT-1 samples for PSC and CIP conditions are shown in Fig. 6.19.

Table 6.5 Comparison of PSC and CIP Specimens

Sample ID	**Pressure slip casting (PSC)**		**Cold Isostatic Pressing (CIP)**		**Increase in green density CIP Vs PSC** (%)
	Pressure corresponding to maximum % GD (MPa)	Maximum Green density Achieved (%)	Pressure corresponding to maximum % GD (MPa)	Maximum Green density Achieved (%)	
ALT-1	3	44	100	58.5	33
ALT-2	3	51.8	100	58.7	13.2
ALT-3	2	60.1	100	65	8

However, CIPing of uni-axially pressed ALT-1 samples at a pressure of 50 MPa has shown an increase in percentage green density by 30 % in comparison to PSC. On increasing the pressure to 100 MPa the increase in green density is around 33 % and further increase to 140 MPa has shown only negligible effect in percentage increase in green density.

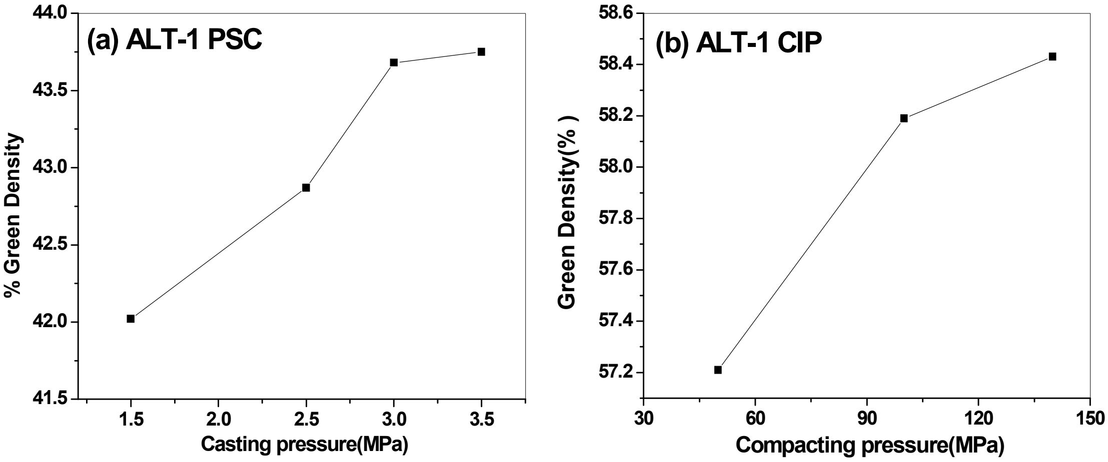

Fig 6.19 Plots of GD versus Pressure for ALT-1 under (a) PSC and (b) CIP condition

Table 6.6 shows a comparison of slip casting with pressure slip casting. It is evident that in case of ALT-1 sample, percentage green density has shown no significant effect on CSC and PSC samples even at a pressure of 3 MPa. On the contrary, ALT-2 and ALT-3 samples have exhibited an increase of 7.3 % and 19.4 % increase in green density on application of

3 MPa and 2 MPa pressures respectively while PSC processing in comparison to CSC. Increase in percentage green density for ALT-2 and ALT-3 samples on CIPing at 100 MPa (optimum pressure based on CIPing of ALT-1 sample) is found to be less significant in with respect to ALT-1 samples. ALT-2 and ALT-3 samples on CIPing exhibited 13.9 % and 8 % only in comparison to PSC samples achieving green densities of 58.7 and 65 % TD respectively.

Table 6.6 Comparison of PSC and CSC Specimens

Sample ID	**Pressure slip casting (PSC)**		**Conventional Slip casting (CSC)** Maximum Green density Achieved at atmospheric Pressure (%)	**Increase in green density CSC Vs PSC** (%)
	Pressure corresponding t maximum % GD (MPa)	Maximum Green density Achieved (%)		
ALT-1	3	44	43	-
ALT-2	3	51.8	48.3	7.3
ALT-3	2	60.1	50.3	19.4

Plot of GD versus pressure for ALT-1 are already presented in Fig. 6.19 (a) and ALT-2 and ALT-3 samples under PSC condition are shown in Fig. 6.20 (a)-(b). ALT-1 samples achieved a maximum green density of 43.8% TD at 3 MPa however; ALT- 2 and ALT-3 samples have shown a maximum density of 51.8% TD and 60.1% TD respectively at a lower pressure of 2 MPa. On further increasing the pressure beyond 3 MPa in the case of ALT-1 and 2 MPa in the case of ALT-2 samples no significant effect on green densities are observed. Unlike ALT-1 and ALT-2 beyond 2MPa pressure ALT-3 samples have clearly indicated a percentage decrease in green density. It is evident that highest density is observed for the ALT-3 sample with a collection of particles with a variety of sizes irrespective of the shaping techniques employed such as CIP- (65%TD), PSC-(60.1 %TD) and CSC-(50.3 % TD).

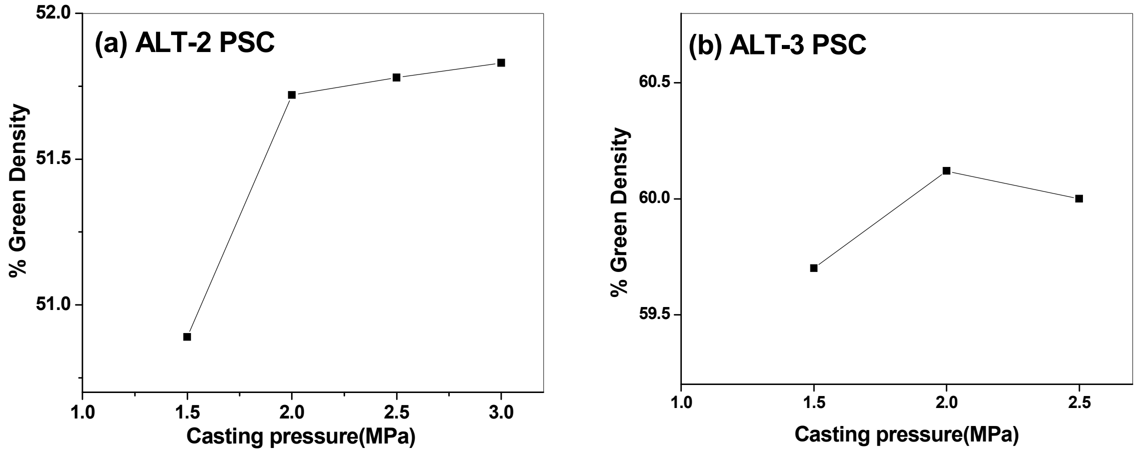

Fig 6.20 Plots of GD versus Pressure for (a) ALT-2 and (b) ALT-3 samples under PSC condition

SEM micrograph of the fracture surfaces were examined using scanning electron microscope and the representative micrographs of the samples ALT-1, ALT-2 and ALT-3 processed through CIP, PSC and CSC with highest green densities are shown in Fig. 6.21. There is clear distinction between the surfaces depending on the forming process. All CIP ALT samples have shown (Fig. 6.21(a)-(c)) high degree of roughness with significant particle agglomeration and lesser pores. ALT-3 samples have shown less agglomeration and absence of larger flaws and more homogeneity complementing high green density of the (65% TD) observed for the sample.

A more homogeneous and uniform distribution of particle and homogeneity in comparison to CIP is evident for PSC samples. PSC and CSC samples exhibited more of a layered structure and seem like glued together with interlayer voids. A more prominent effect of pressure is evident with PSC ALT-3 (Fig. 6.21(f)) in comparison to CSC ALT-3 samples (Fig. 6.21(i)) which correlates well with high green density.

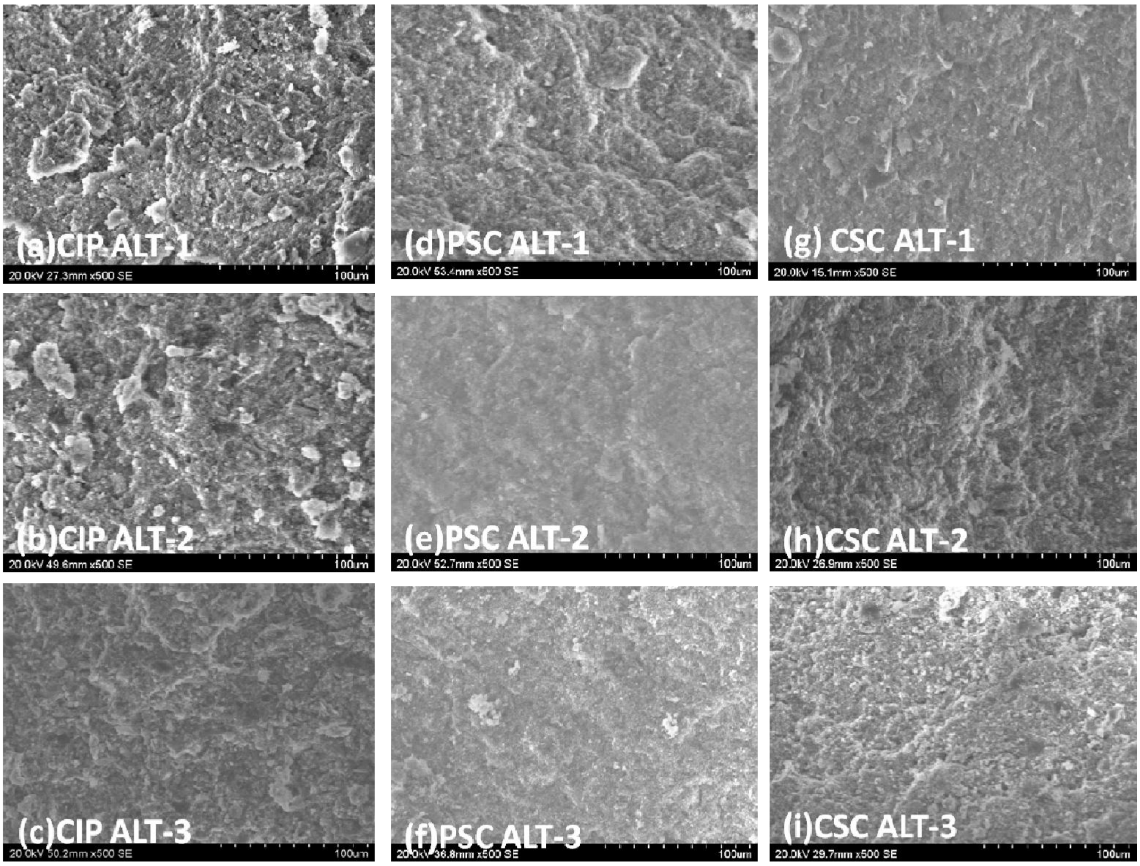

Fig 6.21 SEM of CIP of (a) ALT-1, (b) ALT-2 and (c) ALT-3, PSC of (d) ALT-1, (e) ALT-2 and (f) ALT-3 and CSC of (g) ALT-1, (h) ALT-2 and (i) ALT-3 samples

6.6 Conclusions

Titania and alumina precursor oxide formulations in the aluminum titanate stoichiometry with varying particle sizes were subjected to slip casting under pressureless (CSC) and pressure (PSC) conditions along with cold isostatic pressing (CIP).

The slurries prepared for CSC and PSC processing have exhibited shear thining behaviour due to optimum dispersion achieved through proper dispersant selection and optimum concentration of dispersant, which is suitable for casting process.

The cohesion index of the granules in the range of 11-14 exhibited a free flowing behaviour which can be attributed to the optimum binder concentration and selection of granules size distribution in the raw mix, suitable for compaction processing.

The duration of drying is found to have a clear effect on initial water content and becomes critical as the water content increases in the cast samples. CIP samples do not require any drying followed by lesser duration PSC and maximum for CSC samples.

Conventional slipcasting (CSC) with the ALT-1, ALT-2 and ALT-3 slurries having similar solid loadings with pseudoplatic behavior achieved densities of 43, 48 and 50 % of TD for ALT-1, ALT-2 and ALT-3 samples respectively revealing the particle size distribution of alumina plays a key role in achieving the green densities.

Pressure slipcasting (PSC) with the same batch of CSC slurries enhanced the green densities to 44, 51 and 60 % of TD for ALT-1, ALT-2 and ALT-3 samples respectively. Application of pressures from 2 to 3 MPa under PSC conditions reveals the combined effect of particle size distribution and applied pressure on green densities. However, ALT-1 has shown only minimal effect on green densities on application of pressure in comparison to CSC due to the repulsive interparticle Vander waals forces associated with 0.3 μm alumina in the colloidal state.

CIPing with applied pressure of 100 MPa being below the yield strength of the alumina particles, applied pressure goes to overcome the inter-particle friction with the decrease of porosity as the pressure approaches 100 MPa. At these pressures, the rearrangement of the particles takes place through rolling, twisting and interlocking.

Higher densities of 60 % of TD through PSC and a maximum 65 % of TD through CIP with ALT-3 samples attributed to the collection of particles with a variety of sizes 0.3, 1 and 6 μm achieving a close packing under applied pressure.

6.7 References

1. J.S. Reed, Principles of Ceramic Processing, A Wiley –Interscience Publication (1995).

2.N. Shinohara, M. Okumiya, T. Hotta, K. Nakahira, M. Naito and K. Uematsu, Variation of the microstructure and fracture strength of cold isostatically pressed alumina ceramics with the alteration of dewaxing procedures. J. Euro. Ceram. Soc., 20, 843-849 (2000).

3.A.K. Mallik, S. Gangadharan, S. Dutta and D. Basu, Micrometer size grains of hot isostatically pressed alumina and its characterization, Bull. Mater. Sci., 33 [4] 445–449 (2010).

4.M.J. Edirisinghe and J.R.G. Evans, Review: fabrication of engineering ceramic by injection molding II techniques, Int. J. High. Tech. Ceram., 2, 249-278 (1986).

5.A. Tsetsekou, C. Agrafiotis and A. Milias, Optimisation of the rheological properties of alumina slurries for ceramic processing applications Part I: Slip-casting, J.Euro.Ceram.Soc. 21, 363-369 (2001).

6.C.H. Schilling and I.A. Aksay, Slip casting- In Engineered Materials Handbook, Ceramics and Glasses. American Technical Publishers, Herts. 5, 153 (1991).

7.S. Schaffoner and C.G. Aneziris, Pressure slip casting of coarse grain oxide ceramics, Ceram. Int., 38, 417–422 (2012).

8.S. Maleksaeedi, M.H. Paydar, S. Saadat and H. Ahmadi, In situ vibration enhanced pressure slip casting of submicrometer alumina powders, J. Euro. Ceram. Soc., 28, 3059–3064 (2008).

9.J.M F. Ferreira and H. M. M. Diz, Influence of pH on the pressure slip casting of silicon carbide bodies, J. Euro. Ceram. Soc., 17, 259-266 (1997).

10. R. Morenoay, A. Salomoni, I. Stamenkovic and S.M. Castanh, Colloidal filtration of silicon nitride aqueous slips, Part II: Slip casting and pressure casting performance, J. Euro. Ceram. Soc., 19, 49-59 (1999).

11. T.J. Fennelly and J.S. Ree, Compression permeability of Al_2O_3 cakes formed by Pressure casting. J Am. Ceram. Soc,. 55 [8], 381-383 (1972).

12. T.J. Fennelly and J.S. Reed, Mechanics of pressure slip casting, J Am. Ceram. Soc., 55 [5], 254-288 (1972).

13. A. Solomoni , R. Moreno , E. Rastelli , I. Stamenkovic and L. Esposito, Correlation between rheological behaviour of alumina slip and characteristics of pressure cast bodies, J. Euro. Ceram Soc., Conf No.5 Versailles, France, 132-136, 346-349 (1997).

14. A.W. Hey, A. Bresciani, L. Correia and R. Moren, Industrial pressure casting of alumina ceramics. Euro. Ceram. Soc., Conf No.5 Versailles, France, 132-136, 350-353 (1997).

15. Y.S. Rao, and R. Johnson, Pressure Slip Casting: A Novel Process for Producing Alumina Bodies with Superior Green Density. Interceram., 62, 3, 218-221 (2013).

16. A. Solomoni, L. Esposito, A. Tucci and I. Stamenkovi, Homogeneity of thick ceramic bodies obtained by pressure casting, World Ceramic Congress Florence Italy (14-19 June 1998).

17. R. Papitha, M.B. Suresh, D. Das and R. Johnson, High temperature flexure strength and thermal stability of near zero expanding doped aluminium titanate ceramics for DPF applications, Int. J. Appl. Ceram. Tech. doi: 10.1111/ijac.12092, 1-10 (2013).

18. R. Papitha, M.B. Suresh, D. Das and R. Johnson, Mineral oxide doped aluminum titanate ceramics with improved thermo-mechanical properties, J. Ceram. 214794, 1-9 (2013).

19. R. Papitha, M.B. Suresh, D. Chakravarty, A. Swarnakar, D. Das and R. Johnson, Eutectoid decomposition of aluminum titanate (Al_2TiO_5) ceramics under spark plasma (SPS) and conventional (CRH) thermal treatments. Ceram. Int., 40,[1], 659-666 (2014).

20. M.N. Rahaman, Ceramic processing and sintering, Marcel Dekker Inc., New York. (1995).

21. R.A.Terpstra, P.P.A.C.Pex and A.H.De Vries, Ceramic processing, Chapman and Hall publication (1995)

22. C.D. Hans, Rheology in polymer processing, Academic Press, New York (1976).

23. R.A. McCauley, Rheology. In Ceramic Monographs – Hand book of Ceramics, Verlag Schmid GmbH, Freiburg. (1983).

24. R.G. Horn, Surface forces and their action in ceramic materials, J. Am. Ceram. Soc. 73**,** 1117-1135 (1990).

25. A.E. McHale, Processing additives. In Engineered Materials Handbook, Ceramics and Glasses. American Technical Publishers, Herts. 4, (1991).

26. C. Brinker and G. Scherer, Sol-Gel Science, The Physics and chemistry of Sol-Gel Processing. Academic Press (1990).

27. R.J. Pugh and L. Bergstrom. Surface and colloid chemistry in advanced ceramic processing. surfactant science series. Marcell Dekker, New York. (1994).

28. C.M. Lambe, preparation and use of plaster mold in Ceramic fabrication process, W.D. Kingery (eds), MIT press, Cambridge MA 31-40(1963).

29. F.F. Lange, Powder processing science and technology for increased reliability. J. Am. Ceram. Soc. 72, 3-15(1989).

30. P. Ramavath, M. Swathi, M. B. Suresh and R. Johnson, Flow properties of spray dried alumina granules using powder flow analysis technique. Adv. Powd. Tech., 24, 667–673 (2013).

31. A. Choudhary, P. Ramavath, P. Biswas, N. Ravi and R. Johnson, Experimental investigation on flowability and compaction behavior of spray granulated submicron alumina granules, ISRN Ceramics, 2013, 264194, 1- 6 (2013).